

Remote Sensing of Active Periglacial Landforms Within the Western Nyainqêntanglha Range, Tibetan Plateau

Von der
Fakultät Architektur, Bauingenieurwesen und Umweltwissenschaften
der Technischen Universität Carolo-Wilhelmina
zu Braunschweig

zur Erlangung des Grades eines
Doktor-Ingenieurs (Dr.-Ing.)
genehmigte

Dissertation
kumulative Arbeit

von
Eike Reinosch
geboren am 26.03.1991
aus Karlsruhe

Eingereicht am: 3. Mai 2021
Disputation am: 30. Juni 2021

Berichterstatter: Prof. Dr. Markus Gerke
PD Dr. Jussi Baade

2021

Zusammenfassung

Einige der größten Flusssysteme der Welt entspringen dem Tibetischen Plateau. Diese versorgen 1,65 Milliarden Menschen in Großasien mit Frischwasser. Auf dem Tibetischen Plateau befindet sich außerdem mehr Gletschereis als in jeder anderen Region außerhalb der Pole, weshalb es auch als der *Dritte Pol* bezeichnet wird. Der Klimawandel hat diese wichtigen Frischwasserreserven stark verringert und die Hydrologie von Flüssen, Seen und vergletscherten Gebirgsketten verändert. Den Auswirkungen auf Seen und Eisgletscher wurde in den letzten Jahrzehnten viel Aufmerksamkeit geschenkt. Weniger im Fokus standen großflächige Studien der periglazialen Landschaft, die die Gletscher umgibt. Periglaziale Landformen, wie beispielsweise Blockgletscher, spielen jedoch eine wichtige Rolle in der Hydrologie von Hochgebirgen. Blockgletscher entwickeln sich aus einer Mischung aus gefrorenem Schutt und Eis, die bei ausreichender Feuchtigkeit zu kriechen beginnt. Sie sind auf optischen Satellitenbildern schwerer zu erkennen als Eisgletscher, da sich das Eis hauptsächlich im Inneren der Landform befindet und somit nicht an der Oberfläche sichtbar ist. Wir können jedoch das Kriechen dieser Landformen durch Techniken der Radarfernerkundung überwachen. In dieser Dissertation nutzen wir die Satellitenfernerkundung ergänzt durch geophysikalische Feldmessungen um die Aktivität von periglazialen Landformen im westlichen Nyainqêntanglha Gebirge, südliches Tibetisches Plateau, zu untersuchen. Zuerst konzentrieren wir uns auf die Untersuchung zweier Einzugsgebiete, bevor der Umfang erweitert wird, um ein großflächiges Inventar der Blockgletscher in der Gebirgskette zu erstellen.

Die Radarinterferometrie (InSAR) ist eine Technik der Fernerkundung, die es ermöglicht, je nach Sensor und Methodik, Oberflächenbewegungen von einigen Millimetern bis Dezimetern zu erkennen. Um diese hohe Genauigkeit zu erreichen, wird der Phasenunterschied der rückgestreuten Wellen zwischen zwei oder mehr Satellitenaufnahmen berechnet. Die daraus berechnete Oberflächenbewegung ist eindimensional und nur Bewegung entlang der Sichtlinie des Sensors kann erkannt werden. Die Bewegung der untersuchten Landformen ist vorrangig von der Schwerkraft getrieben. Folglich wird angenommen, dass die Bewegungsrichtung entlang der größten Hangneigung erfolgt. Die eindimensionale Bewegung entlang der Sichtlinie wird deshalb in die Richtung der größten Hangneigung projiziert, wodurch eine repräsentativere Geschwindigkeitsschätzung erzielt wird.

Unsere Ergebnisse zeigen, dass InSAR eine geeignete Technik ist um sowohl saisonale als auch mehrjährige Oberflächenbewegungen in dieser Region zu untersuchen. Das trockene Winterklima sorgt für eine relativ dünne Schneedecke und die hohe Lage verhindert das Wachstum großer Vegetation. Dies ermöglicht eine gute flächenhafte Abdeckung der Oberflächenbewegungsdaten. Eingeschränkt wird die Genauigkeit von InSAR-basierten Methoden in dieser Region hauptsächlich durch (1) die Hochgebirgslage, (2) die niedrige

Sensitivität bei Bewegungen orthogonal zur Sichtlinie des Sensors und (3) die maximale Bewegungsrate die erkannt werden kann. Ersteres kann zu saisonalen atmosphärischen Artefakten in den Zeitreihen führen. Die zweite Einschränkung verursacht eine Unterschätzung der erkannten Oberflächengeschwindigkeit bei Landformen, die sich nach Norden oder Süden bewegen. Die dritte Einschränkung führt zu einer Unterschätzung der Oberflächengeschwindigkeit bei Landformen, die sich schneller als ~ 10 cm/Jahr bewegen.

Das lockere Material führen zu einem Kriechen der Oberfläche von 1 bis 5 cm/Jahr auf vielen spärlich bewachsenen schuttbedeckten Hängen. Einige Hangrutschungen bewegen sich schneller als 10 cm/Jahr. Das Kriechen auf diesen Hängen beschleunigt sich stark vom Spätsommer bis Frühherbst, wenn der Boden aufgetaut und durch den Monsunregen aufgeweicht ist. Flaches Terrain, wie Talböden oder alte Seeterrassen, sind weitgehend stabil. Bereiche um Flüsse und Feuchtgebiete folgen einem saisonalen Heben-Senken Zyklus, der durch das Frieren des Bodens im Herbst und dem Tauen im folgenden Frühling verursacht wird.

Blockgletscher sind die schnellsten häufig vorkommenden periglazialen Landformen im westlichen Nyainqêntanglha Gebirge, jedoch erreichen einige Hangrutschungen vergleichbare Geschwindigkeiten. Es wurde ein Inventar aller bewegenden Blockgletschertypen in diesem Gebirge erstellt. Eine automatische Landschaftserkennung basierend auf ausschließlich optischen Daten ist nicht ausreichend um Blockgletscher zuverlässig zu erkennen, da Blockgletscher einen sehr ähnliche Reflexionsgrad aufweisen wie die umgebene Landschaft. Aus diesem Grund verbinden wir einen manuellen Ansatz mit einer semi-automatischen Landschaftserkennung. Beide Ansätze basieren auf optischen Satellitendaten, Ableitungen des Höhenmodells TanDEM-X und der Oberflächengeschwindigkeiten von 2016 bis 2019 berechnet mittels InSAR Zeitreihenanalyse. Der manuelle Ansatz folgt den Richtlinien vom internationalen Permafrostverband (IPA) um Blockgletscher zu identifizieren und ihre Aktivität anhand der Oberflächengeschwindigkeit zu klassifizieren. Dies stellt eine gute Vergleichbarkeit mit zukünftigen Blockgletscherinventaren sicher. Die semi-automatischen Landschaftserkennung nutzt die gleichen Datensätze um Blockgletscherflächen mit einer pixelbasierten Wahrscheinlichkeitsfunktion zu erkennen.

Das Inventar umfasst 1433 Blockgletscher mit einer Gesamtfläche von 124.9 km². Davon werden 265 als aktiv eingestuft mit Oberflächengeschwindigkeiten von meist 10 bis 30 cm/Jahr. Die anderen 1168 Blockgletscher bewegen sich langsamer als 10 cm/Jahr. Die semi-automatische Landschaftserkennung konnte 87.8 % der Blockgletscher korrekt identifizieren, mit einer richtig-positiven Rate von 69.5 %. Außerdem wurden 18 zuvor übersehene Blockgletscher erkannt. Allerdings überschätzt die automatisierte Landschaftserkennung die tatsächliche Blockgletscherfläche in hohem Maße. Diese Methode sollte

deshalb unterstützend zum manuellen Ansatz eingesetzt werden und nicht um diesen zu ersetzen.

Der Einfluss des Monsunklimas auf die Entstehung von Blockgletschern ist klar ersichtlich in dieser Region. Die dem Wind zugewandte Südseite der Gebirgskette erhält mehr Feuchtigkeit als die dem Wind abgewandte Nordseite. Dies spiegelt sich in der höheren Anzahl und Aktivität von Blockgletschern auf der Südseite wider. Diese stellt ~59 % des Studienbereichs dar, beinhaltet jedoch 91.3 % aller aktiven Blockgletscher. Aufgefächerte und zungenförmige Blockgletscher sind die größten und aktivsten Blockgletschertypen. Zusammen repräsentieren sie 29.4 % der Blockgletscherfläche und 29.1 % aller aktiven Blockgletscher. Die Verteilung der Blockgletscher weist auf eine untere Grenze des diskontinuierlichen Permafrosts auf ungefähr 5200 m Höhe hin.

Weitere Forschung dieser periglazialen Landschaft sollte sich auf die Hydrologie und den Sedimenttransport dieses Hochgebirges konzentrieren. Sowohl das Kriechen von Blockgletschern, als auch von schuttbedeckten Hängen trägt zum Sedimenttransport bei. Allerdings ist es schwierig deren Beitrag einzuschätzen, ohne weitere Studien über Sedimentsenken und Sedimentdicke durchzuführen. Großflächige Analysen der Bodenfeuchte mittels Fernerkundung oder weitere Untersuchungen des Eisgehalts von Blockgletschern würden unser Verständnis dieser Landschaft weiter verbessern.

Abstract

The Tibetan Plateau is the source region of some of the world's largest river systems. These supply around 1.65 billion people in greater Asia with fresh water. The Tibetan Plateau also contains more glacial ice than any other region outside of the poles, which has earned it the title of *Third Pole*. Climate change has greatly depleted these vital storages of fresh water and significantly altered the hydrology of its rivers, lakes and glaciated mountain ranges. The effects on lakes and ice glaciers have received a lot of attention in past decades. Less attention has been given to the large-scale study of the periglacial landscape surrounding these glaciers. Nonetheless, periglacial landforms, such as rock glaciers, play an important role in high mountain hydrology. Rock glaciers evolve from mixtures of frozen debris and interstitial ice, which begins to creep if sufficient moisture is available. They are harder to identify on optical satellite images than ice glaciers, as the ice is contained within the landform and generally not exposed to the surface. We can, however, monitor the creeping of these landforms with microwave remote sensing techniques. In this thesis we use satellite remote sensing supplemented by geophysical field measurements to study the activity of periglacial landforms in the western Nyainqêntanglha Range on the southern Tibetan Plateau. Initially, we focus on the study of two sub-catchments, before expanding our scope to generate a large-scale inventory of rock glaciers in this mountain range.

Radar interferometry is a remote sensing technique which can be used to monitor surface displacements of several millimeters to decimeters depending on the sensor and the methodology. To achieve this high accuracy, we calculate the phase difference of backscattered microwaves between two or more satellite acquisitions. The resulting surface displacement is one-dimensional and only displacement along the sensor's line-of-sight can be observed. The surface velocity of the landforms studied in this thesis is predominantly gravity-driven. We therefore assume the inter-annual displacement to be directed along the direction of the steepest slope. The one-dimensional surface velocity along the line-of-sight is projected along the direction of the steepest slope to produce more representative estimations for the surface velocity.

Our research shows that Interferometric Synthetic Aperture Radar (InSAR) techniques are suitable to study surface displacements of both seasonal and inter-annual processes in this region. The relatively thin snow cover associated with the dry winter climate and the absence of large vegetation due to the high altitude, result in a good spatial coverage of surface displacement data. The main limitations affecting the accuracy of InSAR-based techniques in this area are (1) the high mountain environment, (2) the insensitivity towards displacement moving orthogonal to the line-of-sight of the sensor and (3) the maximum detectable surface velocity. The first limitation may lead to seasonal

atmospheric artefacts in the time series. The second limitation causes an underestimation of the apparent surface velocity of landforms creeping towards the north or south. The third limitation leads to an underestimation of the surface velocity of landforms faster than $\sim 10 \text{ cm yr}^{-1}$.

The unconsolidated material of sparsely vegetated, debris-covered slopes displays surface creeping of mostly 1 to 5 cm yr^{-1} and above 10 cm yr^{-1} on some landslides. The creeping on these slopes accelerates greatly during late summer to early autumn, when the ground thaws and becomes inundated by the monsoonal rains. Flat terrain, such as valley floors or old lake terraces, is mostly stable on an inter-annual scale. Areas surrounding river areas or wetlands display a seasonal heave-subsidence cycle associated with the freezing of the ground in autumn and subsequent thawing in spring.

Rock glaciers are the fastest common periglacial landforms in the western Nyainqên-tanglha Range, though a small number of landslides reach comparable velocities. We created an inventory of all actively moving rock glacier types in the mountain range. An automated landscape classification based solely on optical imagery is not sufficient to detect rock glaciers reliably, as rock glaciers display a very similar surface reflectance as the surrounding landscape. We therefore combine a manual approach with a semi-automatic detection. Both approaches are based on optical satellite imagery, derivatives of the surface elevation model TanDEM-X and the surface velocity estimation of 2016 to 2019 calculated with InSAR time series analysis. The manual approach follows the guidelines of the International Permafrost Association (IPA) to identify rock glaciers and classify their activity according to their surface velocity. This ensures a good comparability with future rock glacier inventories. The semi-automatic detection approach uses the same data sets as the manual approach to detect rock glacier areas with a maximum likelihood algorithm.

The inventory contains 1433 rock glaciers in total with a combined surface area of 124.9 km^2 , 265 of which are considered active with surface velocities of mostly 10 to 30 cm yr^{-1} . The other 1168 rock glaciers display velocities below 10 cm yr^{-1} . The semi-automatic classification correctly identified 87.8 % of all rock glaciers, including 18 previously overlooked rock glaciers, at a true positive rate of 69.5 %. However, the automated approach greatly overestimates the actual rock glacier area. It should therefore be seen as a supplement to the manual approach rather than a replacement.

We can clearly see the influence of the monsoon climate on the formation of rock glaciers in this region. The southern windward side of the mountain range receives more moisture than the leeward northern side. This is reflected by the more numerous and more active rock glaciers on the southern side. It represents ~ 59 % of the study area but

contains 91.3 % of all active rock glaciers. Spatulate and tongue-shaped rock glaciers are the largest and most active rock glacier types. Together they represent 29.4 % of the rock glacier area and 29.1 % of all active rock glaciers. The rock glacier distribution suggests a lower boundary of discontinuous permafrost at around 5200 m.

Further research into the high mountain hydrology and the sediment transport of this periglacial landscape are required. Both the creeping of rock glaciers and of debris-covered slopes contributes to sediment transport. However, it is difficult to quantify their contributions without further study of sediment sinks and the thickness of the transported sediment. Large-scale soil moisture analysis with remote sensing and further studies on the subsurface ice content of rock glaciers would further improve our understanding of this environment.

Acknowledgements

Like most achievements, this dissertation would not have been possible without the help of many others. I would like to thank all my colleagues in the TransTiP project and at the Institute of Geodesy and Photogrammetry for their support and many interesting discussions. I would like to specifically thank Johannes Buckel for our successful collaboration on many projects and publications. I also thank the DFG for financing this project and my supervisors, Prof. Markus Gerke and Dr. Björn Riedel, for guiding me through my work and supporting me during the field expeditions. Furthermore, I thank the Chinese colleagues who helped us during our field expeditions and those who made my stay in Wuhan memorable and enjoyable. Finally, I want to express my gratitude to my partner Ayelén Lapiana, who supported and encouraged me throughout the entirety my PhD.

Contents

1	Introduction	11
1.1	Motivation and problem statement	11
1.2	Aims and Research Questions	14
1.3	Study area	16
1.4	Thesis outline	17
2	Permafrost Detection with Remote Sensing and Geophysics on the Ti- betan Plateau	25
2.1	Introduction	26
2.2	Study area	26
2.3	Data and methods	28
2.3.1	ERT data acquisition	28
2.3.2	ISBAS Processing	29
2.3.3	InSAR Postprocessing	29
2.4	Results and discussion	30
2.5	Summary and Outlook	34
3	Insights into a remote cryosphere: a multi-method approach to assess permafrost occurrence at the Qugaqie basin, western Nyainqêntanglha Range, Tibetan Plateau	37
3.1	Introduction	38
3.2	Study area	41
3.3	Data and methods	44
3.3.1	Inventory of cryospheric mesoscale landforms	46
3.3.2	Ice detection by ERT	47
3.3.3	Creeping rates by InSAR analyses	49
3.4	Results and interpretation	52
3.4.1	The cryosphere of the Qugaqie basin	52
3.4.2	ERT-based ice detection	55
3.4.3	Creeping rates of periglacial landforms	58
3.4.4	Assessment of the lower permafrost limit of the Qugaqie valley . . .	61

3.5	Discussion	61
3.6	Conclusion and future work	64
4	InSAR time series analysis of seasonal surface displacement dynamics on the Tibetan Plateau	79
4.1	Introduction	80
4.2	Study area	82
4.3	Data	84
4.4	Methods	86
4.4.1	ISBAS Processing	86
4.4.2	Selection of reference areas	87
4.4.3	Surface displacement models	88
4.4.4	Linear velocity model (LVM)	90
4.4.5	Heave-subsidence model (HSM)	91
4.4.6	Seasonal slope process model (SSM)	92
4.5	Results	92
4.5.1	Linear surface velocity derived from LVM	92
4.5.2	Heave-subsidence cycle derived from HSM	95
4.5.3	Seasonally accelerating slopes derived from SSM	98
4.6	Discussion	100
4.6.1	Multiannual displacements in flat terrain	101
4.6.2	Seasonal displacements in flat terrain	101
4.6.3	Multiannual displacements in steep terrain	103
4.6.4	Seasonal displacements in steep terrain	105
4.7	Conclusion	106
5	Rock glacier inventory of the western Nyainqêntanglha Range, Tibetan Plateau, supported by InSAR time series and automated classification	116
5.1	Introduction	117
5.1.1	Importance of rock glacier inventories	117
5.1.2	Rock glacier morphology	118
5.1.3	Rock glacier activity	118
5.1.4	Creating rock glacier inventories	118
5.1.5	Purpose of this study	119
5.2	Study area: The western Nyainqêntanglha Range	120
5.2.1	Climate	120
5.2.2	Glaciers and lakes	121
5.2.3	Permafrost and periglacial landforms	122
5.3	Data and Methods	123
5.3.1	InSAR processing	124

5.3.2	Removal of large-scale phase delay	126
5.3.3	Downslope projection	126
5.3.4	Optical satellite and DEM products	127
5.3.5	Manually generating the rock glacier inventory	128
5.3.6	Supervised maximum likelihood classification	130
5.4	Results	132
5.4.1	Accuracy of surface velocity	132
5.4.2	Manual Rock glacier inventory	132
5.4.3	Maximum likelihood estimation	135
5.5	Discussion	137
5.5.1	InSAR limitations	137
5.5.2	Rock glacier inventory	139
5.5.3	Semi-automatic classification	140
5.6	Conclusion	142
6	Summary and conclusions	152
6.1	Potential and limitations of InSAR remote sensing to study the periglacial landscape	153
6.2	Different surface displacement patterns and their contribution to sediment transport	155
6.3	Rock glacier distribution and the implications for permafrost extent	158
6.4	Effect of the monsoonal climate on surface displacement	163
6.5	Influence of climate change on the study area	164
6.6	Outlook	165

Chapter 1

Introduction

1.1 Motivation and problem statement

The Tibetan Plateau (TP) is the largest alpine plateau on earth and provides around 1.65 billion people and many ecosystems with fresh water (Cuo and Zhang, 2017). The effects of climate change on the TP’s hydraulic cycle are complex and spatially heterogeneous (Jiang et al., 2017). Its large scale and poor accessibility make the study of climate change challenging. Models estimating precipitation and permafrost extent often rely on sparse field data, making it difficult to assess their accuracy. Remote sensing appears to be the solution to overcome these issues of scale and accessibility. It describes the study of objects, areas or phenomena by analyzing data collected by devices that are not in contact with the investigated subject (Lillesand et al., 2015). This includes data collected on the ground with terrestrial devices such as laser scanners, from the air with unmanned aerial vehicles (i.e. drones) and by spaceborne sensors on satellites. This thesis focuses on satellite remote sensing. It allows us to study the earth’s surface on a large scale and at regular time intervals, even in remote regions such as the TP. Many studies in recent years have used remote sensing techniques to assess changes to the extent of lakes on the TP (e.g. Jiang et al., 2017; Song et al., 2015) and the rate of glacier retreat (e.g. Zhang et al., 2013a; Wu et al., 2016). Lake and glacier extents can be detected with automated classification algorithms on cloud-free optical satellite acquisitions. This is due to the strong difference in spectral reflectance of visible and infrared light between water, glaciers and the surrounding landscape such as vegetation, rock or soil. Periglacial landscapes have received considerably less attention than lakes or glaciers (Anslan et al., 2020). This is partly due to the spectral similarity of periglacial landforms, such as rock glaciers, compared to their surrounding environment. They can therefore not be detected well with automated classification algorithms based on optical data alone. Recently, considerable success has been achieved to automatically detect rock glaciers. Other parameters, such as digital elevation models, were incorporated alongside optical data during the classification process (Robson et al., 2020; Marcer, 2020).

Many surface processes in periglacial landscapes are associated with freezing and thawing of the ground (French, 2017). These landscapes and their associated landforms are an integral part of the water budget of many high mountain areas around the globe (Jones et al., 2018). Rock glaciers are mixtures of frozen debris and interstitial ice, which evolve through gravity-driven creep (Haerberli et al., 2006). They form under permafrost conditions and may extend multiple kilometers in length, several hundred meters in width and are often several tens of meters high. They store fresh water in the form of interstitial ice and may act as buffers to the fresh water supply during dry seasons (Rangecroft et al., 2015). As large visible expressions of permafrost conditions, rock glaciers are invaluable to understanding the current state of the periglacial landscape of our study area. The response of glaciers and lakes to climate change on the TP can be assessed very well with optical remote sensing approaches. The distribution and water storage of periglacial landforms is harder to assess as the ice is stored within the landform and is not visible at the surface. Furthermore, it is often difficult to distinguish landforms with significant ice storage from those without, which makes extensive field work necessary to determine the ice stored in periglacial landscapes. Consequently, rock glacier inventories are less extensive on a global scale compared to inventories of ice glaciers, especially in remote regions such as the TP.

Microwave remote sensing allows us to study the activity (i.e. surface motion) of rock glaciers and other periglacial landforms on a regional scale. Interferometric Synthetic Aperture Radar (InSAR) techniques exploit the phase difference of backscattered microwaves between two or more acquisitions to determine the relative displacement of an area over time (Osmanoğlu et al., 2016). The debris surface of active rock glaciers make their identification difficult on optical imagery but make them suitable for InSAR, which benefits from the stable backscatter properties of the vegetation-free debris. Assessing rock glacier activity with InSAR can provide us with a better understanding of their subsurface ice content, as their gravity-driven motion is enabled by subsurface ice. However, rock glaciers may also be inactive (i.e. unmoving) while still containing ice (Barsch, 1996). Furthermore, various limitations of the InSAR techniques, such as their insensitivity to motion towards the north or south, necessitate a thorough evaluation of their potential for the study of periglacial landforms. In this thesis we evaluate optical and microwave remote sensing techniques as well as an automated classification approach to study the distribution and activity of periglacial landforms in the western Nyainqêntanglha Range on the TP.

- **Chapter 1:** First we present our aims and pose the associated research questions. We then introduce our study area and the main chapters of this dissertation.
- **Chapter 2:** A conference contribution to the *Geomonitoring* conference of March 2020 with the title *Permafrost Detection with Remote Sensing and Geophysics on the Tibetan Plateau* by (Reinosch et al., 2020b). My contribution as the 1st author is very significant and includes processing of most data, writing the majority of the manuscript and creating most of the figures.
- **Chapter 3:** An article published in the journal *The Cryosphere* titled *Insights in a remote cryosphere: A multi method approach to assess permafrost occurrence at the Qugaqie basin, western Nyainqêntanglha Range, Tibetan Plateau* by Buckel et al. (2021a). My contribution, though listed as 2nd author, is significant and the contents are relevant to the topic of this dissertation. My contribution includes writing a significant portion of the manuscript, processing and evaluating parts of the published data and aiding significantly during the review process. The first author has given permission to use this article in this dissertation.
- **Chapter 4:** Another article published in the journal *The Cryosphere* titled *InSAR time series analysis of seasonal surface displacement dynamics on the Tibetan Plateau* by Reinosch et al. (2020a). My contribution as the 1st author is very significant and includes processing all data, writing the majority of the manuscript and creating all of the figures.
- **Chapter 5:** An article published in the journal *Permafrost and Periglacial Processes* titled *Rock glacier inventory of the western Nyainqêntanglha Range, Tibetan Plateau, supported by InSAR time series and automated classification* by Reinosch et al. (2021). My contribution as the 1st author is very significant and includes processing of most data, writing the majority of the manuscript and creating most of the figures.
- **Chapter 6:** We discuss the most important findings in relation to our research questions, present our conclusions and provide an outlook to potential future research.

This thesis focuses on intermediate and large-scale remote sensing of periglacial landforms within the study area. One of the core principles of the TransTiP project is to encourage scientific exchange and cooperation between different cultures and research backgrounds. Johannes Buckel and I worked closely together to evaluate geomorphological, geophysical and remote sensing methods and their combination to achieve a better understanding of periglacial landforms in our study area (Fig. 1.1). Johannes Buckel

focuses on the geomorphological and geophysical analysis of different rock glacier types on a small to intermediate spatial scale. His research is supplemented by my analysis of surface displacements derived from InSAR data. This dissertation focuses on different remote sensing approaches to study the activity of periglacial landforms on an intermediate to large spatial scale. Johannes Buckel greatly aided my research by providing the geomorphological interpretation and context of the observed surface displacements.

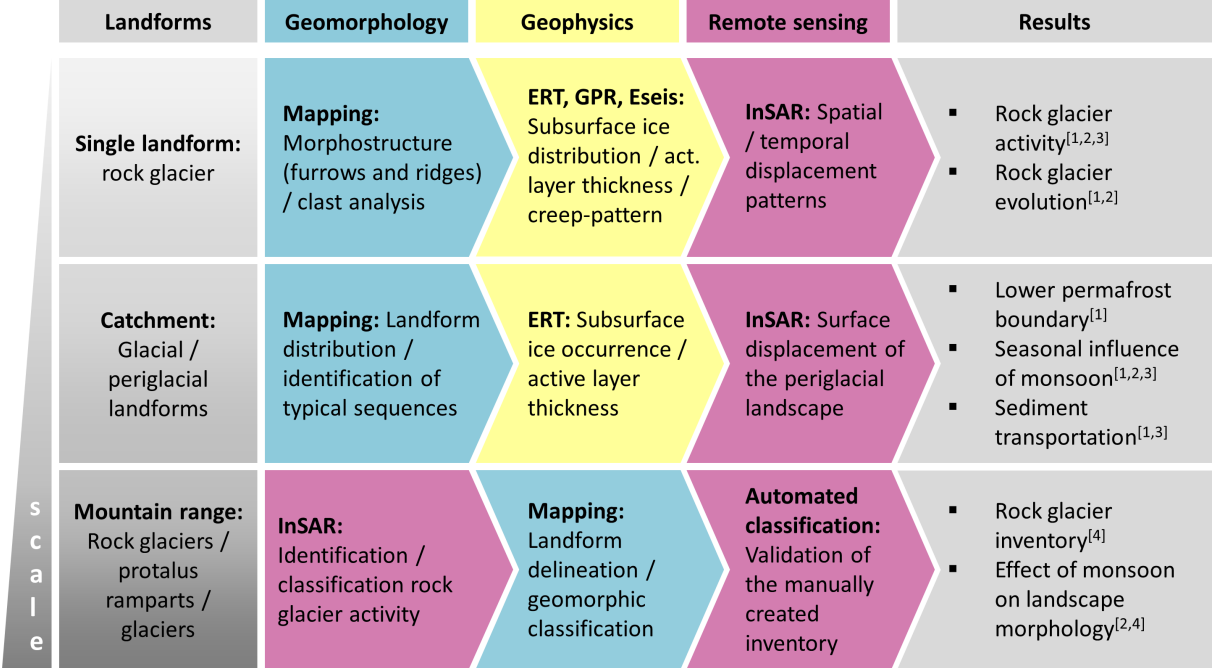


Figure 1.1: Schematic overview of our interdisciplinary approach to study the cryosphere of the western Nyainqêntanglha Range. We combined techniques of geomorphology, geophysics and remote sensing to study various landforms on different spatial scales. The numbers in parenthesis denote where the individual results are published: [1] Buckel et al. (2021a); [2] Buckel et al. (2021b); [3] Reinosch et al. (2020a); [4] Reinosch et al. (2021).

1.2 Aims and Research Questions

The aim of this thesis is to fill the current gap in knowledge regarding the distribution and the activity of periglacial landforms, especially rock glaciers, in the western Nyainqêntanglha Range on the TP. Knowing their spatial distribution and temporal variability helps us to assess the influence of the summer monsoon, their contribution to sediment transport and the potential impact of climate change on this environment. To reach our aims we need to answer the following research questions:

1. How potent is InSAR time series analysis for the study of periglacial landforms? Remote sensing allows us to study surface processes, such as the creep of periglacial landforms, on a large scale, even in remote regions. Evaluating the strengths and limitations of these methods is vital to choose the most potent method to achieve our aims and to produce reliable results for our evaluations.
2. Which displacement patterns can we observe via remote sensing and how are they related to sediment transport? Not all surface displacements directly cause sediment transport observable with remote sensing. Seasonal heaving and subsiding of the ground due to freezing and thawing of pore water is an example of this. This process may lead to changes in the sediment transport but the observed displacement does not directly transport sediment. It is therefore vital to separate them from processes such as solifluction, which transports sediment through gravity-driven creep.
3. Where are rock glaciers distributed and how active are they? Most actively moving rock glaciers display surface displacement of centimeters to multiple decimeters per year. Their motion is facilitated by the ice within the ice-debris mixture, which requires permafrost conditions within the rock glacier. They are therefore visible expressions of permafrost conditions. Assessing their distribution and activity with both optical and microwave remote sensing techniques provides us with more detailed information about the distribution of permafrost in this region.
4. How does the monsoon climate affect surface displacements on different landforms? The summer monsoon delivers the majority of the annual precipitation within a period of four months. This is also the only time when the average daily temperature exceeds freezing for higher elevation areas. Different landforms and their surface velocity are potentially affected differently, which could provide us with information about their subsurface.
5. Can we assess the influence of climate change on this periglacial environment? Increasing ground temperature and precipitation are expected consequences of climate change in this region. This affects not only glacial retreat but also permafrost distribution and the activity of the periglacial landscape. Periglacial landforms on the TP have received less attention compared to lakes and glaciers. Understanding their response to climate change will therefore help to fill a crucial knowledge gap.

1.3 Study area

The western Nyainqêntanglha Range is located in the south-eastern center of the TP (Fig. 1.2B). It strikes from the south-west to the north-east, with a median elevation of around 5350 m a.s.l. and reaches a maximum elevation of 7162 m a.s.l. (geoid elevation of TanDEM-X, ©DLR 2017). It acts as a climate divide between the Indian Summer Monsoon system (ISM) from the south and the dry continental climate of the north and east (Wünnemann et al., 2018). Most regions above 5700 m a.s.l. are glaciated and they are surrounded by a periglacial landscape (Keil et al., 2010). The free ice sections of the glaciers cover an area of 575.7 km² (Reinosch et al., 2021) and currently retreat at a rate of 0.3 to 0.5 % yr⁻¹ (Anslan et al., 2020). The ISM brings most of the annual precipitation from June to September of about 300 to 600 mm. Lake Nam Co (4735 m a.s.l.) on the northern side receives less precipitation (annual mean of 406 mm) than the Damxung Valley (460 mm at 4275 m a.s.l.) to the south (Fig. 5.2; Anslan et al., 2020; Zhang et al., 2013a). The highest precipitation (528 mm) was measured within the mountain range itself (Zhang et al., 2013b). The mean annual air temperature is around 1°C for the Nam Co and Damxung areas and around -6 °C near the glaciated parts. Permafrost and periglacial landscapes are less well studied in this region, though permafrost is likely present above an elevation of 5300 to 5450 m (Buckel et al., 2021a).

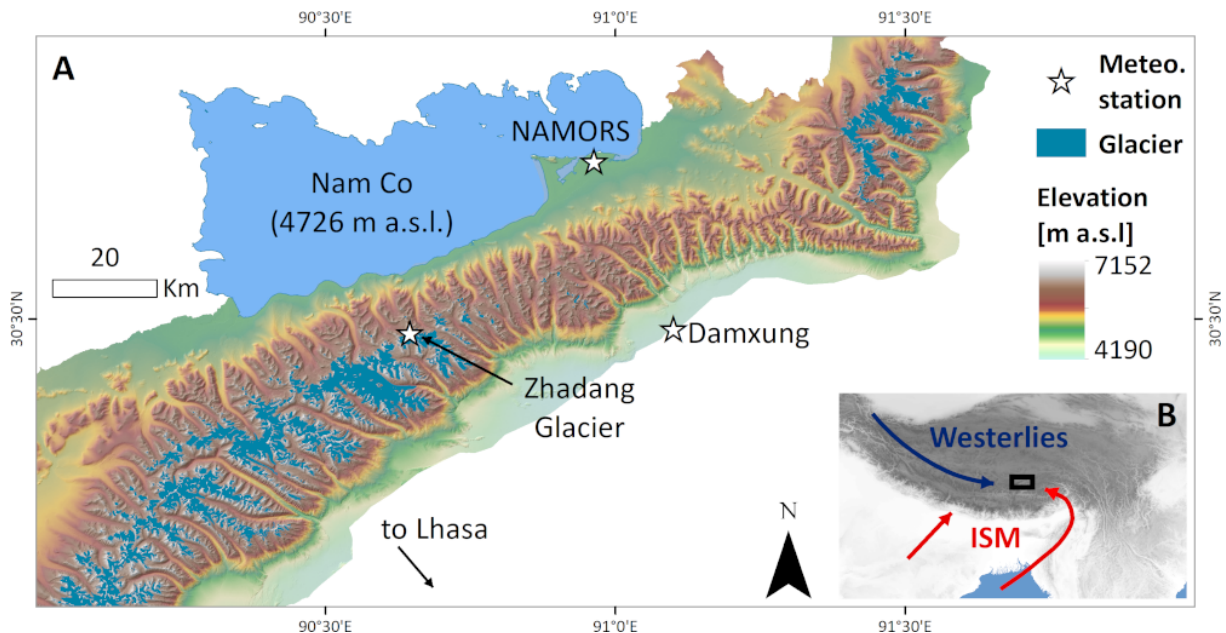


Figure 1.2: (A) Overview of the study area within the western Nyainqêntanglha Range (Geoid elevation according to TanDEM-X ©DLR 2017; glacier extent according to Reinosch et al., 2021). (B) Location on the Tibetan Plateau, including the major climatic systems active in summer (Indian Summer Monsoon – ISM) and winter (Westerlies) (Wünnemann et al., 2018).

The western Nyainqêntanglha Range is a suitable study area due to the following reasons:

1. The high elevation makes the presence of permafrost and periglacial landforms very likely. Large-scale permafrost distribution maps predict a near 100 % likelihood for permafrost occurrence in most of the study area (e.g. Obu et al., 2019).
2. Active periglacial landforms were not studied in detail in this area before, especially not on a large scale. This ensures the novelty of our work there (Anslan et al., 2020).
3. The lack of large vegetation (trees, bushes, crops) and the dry winter climate create good conditions to apply microwave remote sensing techniques to study the surface motion of this landscape.
4. Its good accessibility compared to other parts of the TP enable field studies to verify our remote sensing results. The infrastructure of the Institute for Tibetan Plateau Research of the Chinese Academy of Sciences (ITP CAS) is well prepared for field work in this region. Equipment can be stored at the research station NAMORS at the Nam Co (Fig. 1.2) and relatively short distance to Lhasa make its transport easier.

1.4 Thesis outline

To study the permafrost and periglacial landscape of our study area, we begin our investigations on an intermediate scale and then expand to a large scale. Initially, we focus on two sub-catchments within the Nyainqêntanglha Range: The Niyaqu basin and Qugaqie basin (Fig. 3.1). These sub-catchments were chosen to represent the non-glaciated (Niyaqu) and the glaciated catchments (Qugaqie) surrounding the Nam Co. Two consecutive field campaigns to the study area in the summers of 2018 and 2019 provide us with field measurements and field observations to corroborate our remote sensing results. Field observations are vital to identify small scale processes, which may be difficult to assess with remote sensing. They also help us to identify potential sources of errors, such as strong weather events. On the intermediate scale, we focus on the seasonal variation of surface displacements near the flat valley bottom and in steeper terrain. Our aim is to identify differences in the displacement patterns of varying landscapes and to understand the underlying processes. Finally, we expand our investigations to cover the majority of the western Nyainqêntanglha Range. On this large scale, we focus exclusively on rock glaciers as the clearest representation of permafrost conditions in this periglacial landscape. Both optical and microwave remote sensing techniques are used at this scale. We combine manually generated outlines and an automated detection approach to create an

inventory of actively moving rock glaciers. We study their distribution, surface velocity patterns and geomorphological parameters to assess the influence of the monsoon climate on these landforms.

We use Sentinel-1 microwave satellite data to determine the surface velocity of this landscape. The surface velocity is calculated with Interferometric Synthetic Aperture Radar (InSAR) techniques. These techniques exploit the phase difference of backscattered microwaves between two acquisitions to determine the relative displacement of an area over time (Osmanoglu et al., 2016). Repeating this process with many subsequent satellite acquisitions allows us to create time series of the surface velocity over multiple years. Only 1-dimensional surface displacement along the satellite's line-of-sight (LOS) can be observed. The larger the angle between the LOS and the direction of the surface displacement, the less sensitive InSAR is towards that displacement. The Sentinel-1 constellation observes the earth obliquely (Yagüe-Martínez et al., 2016). It acquires data every 12 days both during its ascending and descending orbits. The LOS of Sentinel-1 and its orbit make it sensitive towards motion with a predominantly vertical or east-west direction. Displacement towards the north or south is strongly underestimated and may even be overlooked completely. To compensate for this limitation we have to assume the motion direction of the observed displacement. In flat terrain we assume the displacement to be predominantly vertical, as the slope is too small to enable gravity-driven horizontal displacement (Matsuoka, 2001). The vertical displacement is calculated from both ascending and descending time series results. We use a decomposition function, where the north component of the displacement is assumed to be negligible, which allows us to determine the vertical and the east-west component (Fialko et al., 2001). In steeper terrain and for rock glaciers we assume displacement to be gravity-driven and therefore directed along the direction of the steepest slope. In those areas we follow the approach described by Notti et al. (2014) to project the LOS velocity of ascending and descending time series results along the direction of the steepest slope.

This dissertation focuses on the intermediate to large scale study of periglacial landforms, especially rock glaciers. Rock glaciers move at relatively slow velocities of mostly centimeters to decimeters per year. InSAR works well for this velocity range and the sparsely vegetated surface of active rock glaciers (Cannone and Gerdol, 2003) ensures stable backscatter properties. The motion of rock glaciers is enabled by the subsurface ice contained within the landform (Haeberli et al., 2006). Detecting motion of several centimeters to decimeter per year on a rock glacier is therefore a strong indication of ice in the subsurface. Electrical resistance tomography and InSAR are two methods to assess the presence of ice in rock glaciers. Performing both methods on the same rock glacier allows us to compare their capabilities and limitations in great detail (Chapter 2; Reinosch

et al., 2020b). Buckel et al. (2021a) study multiple periglacial landforms, including rock glaciers, with a combination of geophysical field measurements, field observations and InSAR surface velocity (Chapter 3; Buckel et al., 2021a).

On the intermediate scale we focus on surface displacement processes in the Niyaqu basin and the Qugaqie basin. We use InSAR to study both seasonal and inter-annual displacements and evaluate the impact of the monsoonal climate on the underlying processes. The ISM controls the summer climate of the western Nyainqêntanglha Range. The mean annual air temperature in these catchment ranges from around 0 °C at the lake to around -6 °C at the glaciers of Qugaqie basin. Average daily summer temperatures reach 10 °C and 2 °C respectively. The summer monsoon also delivers the majority of the annual precipitation to an otherwise semi-arid region (Anslan et al., 2020). This climate controls many processes associated with surface displacement in permafrost and periglacial landscapes. Seasonal freezing in autumn and subsequent thawing of the ground in spring leads to soil creep, so-called solifluction. Many slopes in the Qugaqie basin and the upper Niyaqu basin are covered in unconsolidated debris and are mostly free of vegetation, making them prone to debris movement. Rock glaciers may seasonally increase their velocity with increasing ground temperature and precipitation (Wirz et al., 2016). The climate also causes heaving and subsiding of the ground by freezing and thawing the moisture within the ground (Daout et al., 2017). Not all of these displacements are associated with sediment transport. We use different displacement models to study seasonal variations and the inter-annual surface velocity of different periglacial landforms. We then compare the surface displacement patterns with field observations to determine the underlying processes (Chapter 4; Reinosch et al., 2020a).

After investigating the various surface displacement patterns on an intermediate scale, we focus on rock glaciers for our large-scale study. The study area covers the majority of the western Nyainqêntanglha Range (4622 km²). Processing and analyzing displacement time series data on this scale is time consuming. The previous studies on smaller scales were necessary to select the best processing parameters, identify potential error sources and to determine the focus of this final study. We focus on rock glaciers, as our previous studies show InSAR to be well suited to study these landforms in this region. Furthermore, they play an important role in the hydraulic cycle of high mountain areas (Jones et al., 2018) but are not well studied on the TP compared to ice glaciers and lakes (Anslan et al., 2020).

Inventories of ice glaciers can be created from optical satellite imagery with automated classification algorithms by taking advantage of large spectral difference between glacial ice and the surrounding landscape (e.g. Rastner et al., 2013). Their reflectance differ

greatly both on the visible and the shortwave infrared spectrum, which can be exploited to calculate indexes, such as the normalized difference snow index, to aid the identification of glacial ice. Ice within rock glaciers is mainly stored in the subsurface making, it unfeasible to employ the same techniques. The debris of rock glaciers originates from rock walls and debris-covered slopes adjacent to them and is therefore spectrally very similar to the surrounding rock. Optical imagery alone is therefore not sufficient to automatically detect rock glaciers. Automated classification algorithms show promising results to detect rock glaciers by combining optical imagery with other parameters such as InSAR coherence, digital elevation models (DEM) and vegetation indices (Robson et al., 2020; Marcer, 2020). These algorithms are not yet able to generate sufficiently accurate inventories by themselves and rock glacier inventories still have to be created manually. This makes rock glacier inventories rather subjective and creates problems in the comparability of rock glacier inventories. Rock glaciers identified and outlined by different analysts often vary greatly in both number and surface area (Brardinoni et al., 2019). The recently formed action group on rock glacier inventories and kinematics of the International Permafrost Association (IPA) aims to reduce this subjectivity (Delaloye et al., 2018). They created detailed guidelines for the generation of rock glacier inventories, which also incorporate InSAR surface displacement information (Delaloye and Echelard, 2020). To create the most accurate and reliable rock glacier inventory possible we combine a manual approach with an automated classification. For the manual approach we follow the IPA guidelines to identify, outline and classify rock glaciers. This is done by three analysts who review and adjust each other's work. We use optical satellite data, the DEM of the TanDEM-X mission (©DLR 2017) and the InSAR surface velocity of 2016 to 2019 based on Sentinel-1 data to identify actively moving rock glaciers. Two subsets of the manual rock glacier outlines act as training and validation areas for a pixel based automated classification. The purpose of the automated classification is to identify areas where rock glaciers are likely, to ensure none were missed during the manual identification process (Chapter 5; Reinosch et al., 2021).

Bibliography

- Anslan, S., Azizi Rad, M., Buckel, J., Echeverria Galindo, P., Kai, J., Kang, W., Keys, L., Maurischat, P., Nieberding, F., Reinosch, E., et al. (2020). Reviews and syntheses: How do abiotic and biotic processes respond to climatic variations in the Nam Co catchment (Tibetan Plateau)? *Biogeosciences*, 17(5):1261–1279.
- Barsch, D. (1996). *Rockglaciers: indicators for the present and former geocology in high mountain environments*, volume 16. Springer Science & Business Media.
- Brardinoni, F., Scotti, R., Sailer, R., and Mair, V. (2019). Evaluating sources of uncertainty and variability in rock glacier inventories. *Earth Surface Processes and Landforms*, 44(12):2450–2466.
- Buckel, J., Reinosch, E., Hördt, A., Zhang, F., Riedel, B., Gerke, M., Schwalb, A., and Mäusbacher, R. (2021a). Insights in a remote cryosphere: A multi method approach to assess permafrost occurrence at the Qugaqie basin, western Nyainqêntanglha Range, Tibetan Plateau. *The Cryosphere*, 15:149–168.
- Buckel, J., Reinosch, E., Voigtländer, A., Dietze, M., Bücken, M., Krebs, N., Schroeckh, R., Mäusbacher, R., and Hördt, A. (2021b). Rockglacier evolution by ground-truthing the state and possible fate in semiarid climate in the Nyainqêntanglha range, Tibetan Plateau. in preparation.
- Cannone, N. and Gerdol, R. (2003). Vegetation as an ecological indicator of surface instability in rock glaciers. *Arctic, Antarctic, and Alpine Research*, 35(3):384–390.
- Cuo, L. and Zhang, Y. (2017). Spatial patterns of wet season precipitation vertical gradients on the Tibetan Plateau and the surroundings. *Scientific reports*, 7(1):1–10.
- Daout, S., Doin, M.-P., Peltzer, G., Socquet, A., and Lasserre, C. (2017). Large-scale InSAR monitoring of permafrost freeze-thaw cycles on the Tibetan Plateau. *Geophysical Research Letters*, 44(2):901–909.
- Delaloye, R., Barboux, C., Bodin, X., Brenning, A., Hartl, L., Hu, Y., Ikeda, A., Kaufmann, V., Kellerer-Pirklbauer, A., Lambiel, C., et al. (2018). Rock glacier inventories and kinematics: A new IPA Action Group. In *Proceedings of the 5th European Conference on Permafrost (EUCOP5-2018), Chamonix, France*, volume 23.
- Delaloye, R. and Echelard, T. (2020). Towards standard guidelines for inventorying rockglaciers – Baseline concepts (Version 4.1). <https://www3.unifr.ch/geo/geomorphology/en/research/ipa-action-group-rock-glacier/>. [Accessed November 13, 2020].

- Fialko, Y., Simons, M., and Agnew, D. (2001). The complete (3-D) surface displacement field in the epicentral area of the 1999 Mw7. 1 Hector Mine earthquake, California, from space geodetic observations. *Geophysical research letters*, 28(16):3063–3066.
- French, H. M. (2017). *The periglacial environment*. John Wiley & Sons.
- Haerberli, W., Hallet, B., Arenson, L., Elconin, R., Humlum, O., Kääb, A., Kaufmann, V., Ladanyi, B., Matsuoka, N., Springman, S., et al. (2006). Permafrost creep and rock glacier dynamics. *Permafrost and periglacial processes*, 17(3):189–214.
- Jiang, L., Nielsen, K., Andersen, O. B., and Bauer-Gottwein, P. (2017). Monitoring recent lake level variations on the Tibetan Plateau using CryoSat-2 SARIn mode data. *Journal of Hydrology*, 544:109–124.
- Jones, D., Harrison, S., Anderson, K., and Betts, R. (2018). Mountain rock glaciers contain globally significant water stores. *Scientific reports*, 8(1):2834.
- Keil, A., Berking, J., Mügler, I., Schütt, B., Schwalb, A., and Steeb, P. (2010). Hydrological and geomorphological basin and catchment characteristics of Lake Nam Co, South-Central Tibet. *Quaternary International*, 218(1-2):118–130.
- Lillesand, T., Kiefer, R. W., and Chipman, J. (2015). *Remote sensing and image interpretation*. John Wiley & Sons.
- Marcer, M. (2020). Rockglacier evolution by ground-truthing the state and possible fate in semiarid climate in the Nyainqêntanglha range, Tibetan Plateau. *Permafrost and Periglacial Processes*, 31(4):561–566.
- Matsuoka, N. (2001). Solifluction rates, processes and landforms: a global review. *Earth-Science Reviews*, 55(1-2):107–134.
- Notti, D., Herrera, G., Bianchini, S., Meisina, C., García-Davalillo, J. C., and Zucca, F. (2014). A methodology for improving landslide PSI data analysis. *International journal of remote sensing*, 35(6):2186–2214.
- Obu, J., Westermann, S., Bartsch, A., Berdnikov, N., Christiansen, H. H., Dashtseren, A., Delaloye, R., Elberling, B., Etzelmüller, B., Kholodov, A., et al. (2019). Northern Hemisphere permafrost map based on TTOP modelling for 2000–2016 at 1 km² scale. *Earth-Science Reviews*, 193:299–316.
- Osmanoğlu, B., Sunar, F., Wdowinski, S., and Cabral-Cano, E. (2016). Time series analysis of InSAR data: Methods and trends. *ISPRS Journal of Photogrammetry and Remote Sensing*, 115:90–102.

- Rangecroft, S., Harrison, S., and Anderson, K. (2015). Rock glaciers as water stores in the Bolivian Andes: an assessment of their hydrological importance. *Arctic, Antarctic, and Alpine Research*, 47(1):89–98.
- Rastner, P., Bolch, T., Notarnicola, C., and Paul, F. (2013). A comparison of pixel- and object-based glacier classification with optical satellite images. *IEEE Journal of Selected Topics in Applied Earth Observations and Remote Sensing*, 7(3):853–862.
- Reinosch, E., Buckel, J., Dong, J., Gerke, M., Baade, J., and Riedel, B. (2020a). InSAR time series analysis of seasonal surface displacement dynamics on the Tibetan Plateau. *The Cryosphere*, 14(5):1633–1633.
- Reinosch, E., Buckel, J., Gerke, M., Hördt, A., Baade, J., and Riedel, B. (2020b). Permafrost-Detektion mittels Fernerkundung und Geophysik auf dem tibetischen Plateau.
- Reinosch, E., Gerke, M., Riedel, B., Schwalb, A., Ye, Q., and Buckel, J. (2021). Rock glacier inventory of the western Nyainqêntanglha Range, Tibetan Plateau, supported by InSAR time series and automated classification. *Permafrost and Periglacial Processes*.
- Robson, B. A., Bolch, T., MacDonell, S., Hölbling, D., Rastner, P., and Schaffer, N. (2020). Automated detection of rock glaciers using deep learning and object-based image analysis. *Remote Sensing of Environment*, 250:112033.
- Song, C., Ye, Q., and Cheng, X. (2015). Shifts in water-level variation of Namco in the central Tibetan Plateau from ICESat and CryoSat-2 altimetry and station observations. *Science bulletin*, 60(14):1287–1297.
- Wirz, V., Gruber, S., Purves, R. S., Beutel, J., Gärtner-Roer, I., Gubler, S., and Vieli, A. (2016). Short-term velocity variations at three rock glaciers and their relationship with meteorological conditions. *Earth Surface Dynamics*, 4(1):103–123.
- Wu, K.-p., Liu, S.-y., Guo, W.-q., Wei, J.-f., Xu, J.-l., Bao, W.-j., and Yao, X.-j. (2016). Glacier change in the western Nyainqentanglha Range, Tibetan Plateau using historical maps and Landsat imagery: 1970-2014. *Journal of Mountain Science*, 13(8):1358–1374.
- Wünnemann, B., Yan, D., Andersen, N., Riedel, F., Zhang, Y., Sun, Q., and Hoelzmann, P. (2018). A 14 ka high-resolution $\delta^{18}\text{O}$ lake record reveals a paradigm shift for the process-based reconstruction of hydroclimate on the northern Tibetan Plateau. *Quaternary Science Reviews*, 200:65–84.
- Yagüe-Martínez, N., Prats-Iraola, P., Gonzalez, F. R., Brcic, R., Shau, R., Geudtner, D., Eineder, M., and Bamler, R. (2016). Interferometric processing of Sentinel-1 TOPS data. *IEEE Transactions on Geoscience and Remote Sensing*, 54(4):2220–2234.

Zhang, G., Kang, S., Fujita, K., Huintjes, E., Xu, J., Yamazaki, T., Haginoya, S., Wei, Y., Scherer, D., Schneider, C., et al. (2013a). Energy and mass balance of Zhadang glacier surface, central Tibetan Plateau. *Journal of Glaciology*, 59(213):137–148.

Zhang, G., Kang, S., Fujita, K., Huintjes, E., Xu, J., Yamazaki, T., Haginoya, S., Wei, Y., Scherer, D., Schneider, C., et al. (2013b). Energy and mass balance of Zhadang glacier surface, central Tibetan Plateau. *Journal of Glaciology*, 59(213):137–148.

Chapter 2

Permafrost Detection with Remote Sensing and Geophysics on the Tibetan Plateau

Eike Reinosch¹, Johannes Buckel², Markus Gerke¹, Andreas Hördt², Jussi Baade³, Björn Riedel¹

¹ Institute of Geodesy and Photogrammetry, Technische Universität Braunschweig, Braunschweig, Germany

² Institute of Geophysics and extraterrestrial Physics, Technische Universität Braunschweig, Braunschweig, Germany

³ Department of Geography, Friedrich-Schiller-Universität Jena, Jena, Germany

Corresponding author: Eike Reinosch (e.reinosch@tu-braunschweig.de)

Abstract

In this study we combine geophysical techniques in the form of microwave remote sensing and Electrical Resistance Tomography (ERT) to study the extent of permafrost in the catchment of Lake Nam Co on the Tibetan plateau. Interferometric Synthetic Aperture Radar (InSAR) is a powerful technique to monitor permafrost related surface displacement processes on a large scale. However, the insensitivity of InSAR data regarding northward or southward directed motion and its inability to detect permafrost when no displacement occurs, impose significant limitations to its application in permafrost study. We highlight those limitations on a rock glacier within Qugaqie basin, a sub-catchment within the Nyainqêntanglha range, and show how ERT can be used to compensate for them. With this combined approach we will create an inventory of rock glaciers and constrain the extent of permafrost areas within the Nyainqêntanglha range.

2.1 Introduction

Studying permafrost landscapes and their related processes is of immense importance as they act as both carbon sinks and water storages (Hock et al., 2019). The degradation of permafrost is a severe problem, as this releases the stored carbon to the air to accelerate climate change and destabilizes the ground, leading to soil erosion and slope collapses in mountain regions (Haeberli et al., 2010). The air temperature on the Tibetan Plateau has been shown to rise significantly faster than the global average (Yao et al., 2000), which has contributed to permafrost degradation throughout the plateau (Wu et al., 2010). Interferometric Synthetic Aperture Radar techniques make it possible to study even remote permafrost landscapes and their related surface displacement processes on vast spatial scales. These observed motion patterns include seasonal signals induced by thawing of the ground in spring and subsequent refreezing in autumn, as well as multiannual creeping motions on the order of millimeters to decimeters per year. However, despite the obvious potency of InSAR to study these landscapes, this technique has some limitations. Heavy snowfall in winter can hide the surface from the satellite, making continuous monitoring impossible. In addition, InSAR data allows only to analyze motion towards the satellite or away from it and the multitude of atmospheric interference prevalent especially in high mountain areas creates noise. It is therefore crucial, to validate remote sensing data with field observations and measurements.

In this study we assess the potential of combining geophysical techniques, such as Electrical Resistance Tomography, with InSAR remote sensing analysis to detect long-term subsurface ice content and permafrost related landscapes on the Tibetan Plateau. To that end we highlight their interaction on a rock glacier within our study area, the Qugaqie basin at Lake Nam Co, and show how this approach can be used to detect other permafrost related landscapes on a larger scale.

2.2 Study area

Our study area, the Qugaqie basin, covers 58 km² within the western Nyainqêntanglha range and features elevations of 4722 m to 6117 m a.s.l (Fig. 2.1a). This catchment was formed by glacial processes and as such is largely covered by unconsolidated glacial and periglacial deposits interspersed with grassland where soil has accumulated (Fig. 2.1b). Higher order vegetation is almost nonexistent and many slopes are not vegetated and prone to seasonal sliding (Reinosch et al., 2020). The higher reaches of the catchment feature both active and inactive periglacial landforms, such as rock glaciers. Rock glaciers are steadily creeping permafrost landforms of ice-rich debris in mountainous valleys (Haeberli et al., 2006). The main river is fed by hanging valleys, some containing the remnants

of small glaciers, as well as the two main glaciers Zhadang and Genpu to the south. The sparse snow cover in winter and the lack of vegetation make this region a suitable study site for periglacial processes using InSAR technology, as this reduces the risk of temporal decorrelation. However, temporal decorrelation remains a large issue during the thawing and freezing periods, when surface characteristics change rapidly over a few weeks, especially in areas with significant soil and grassland. Sentinel-1 is a suitable satellite system to study this region, due to its large footprint, relatively short revisit time and C-Band (5.6 cm) wavelength, which is less prone to decorrelation than shorter wavelengths (Crosetto et al., 2016).

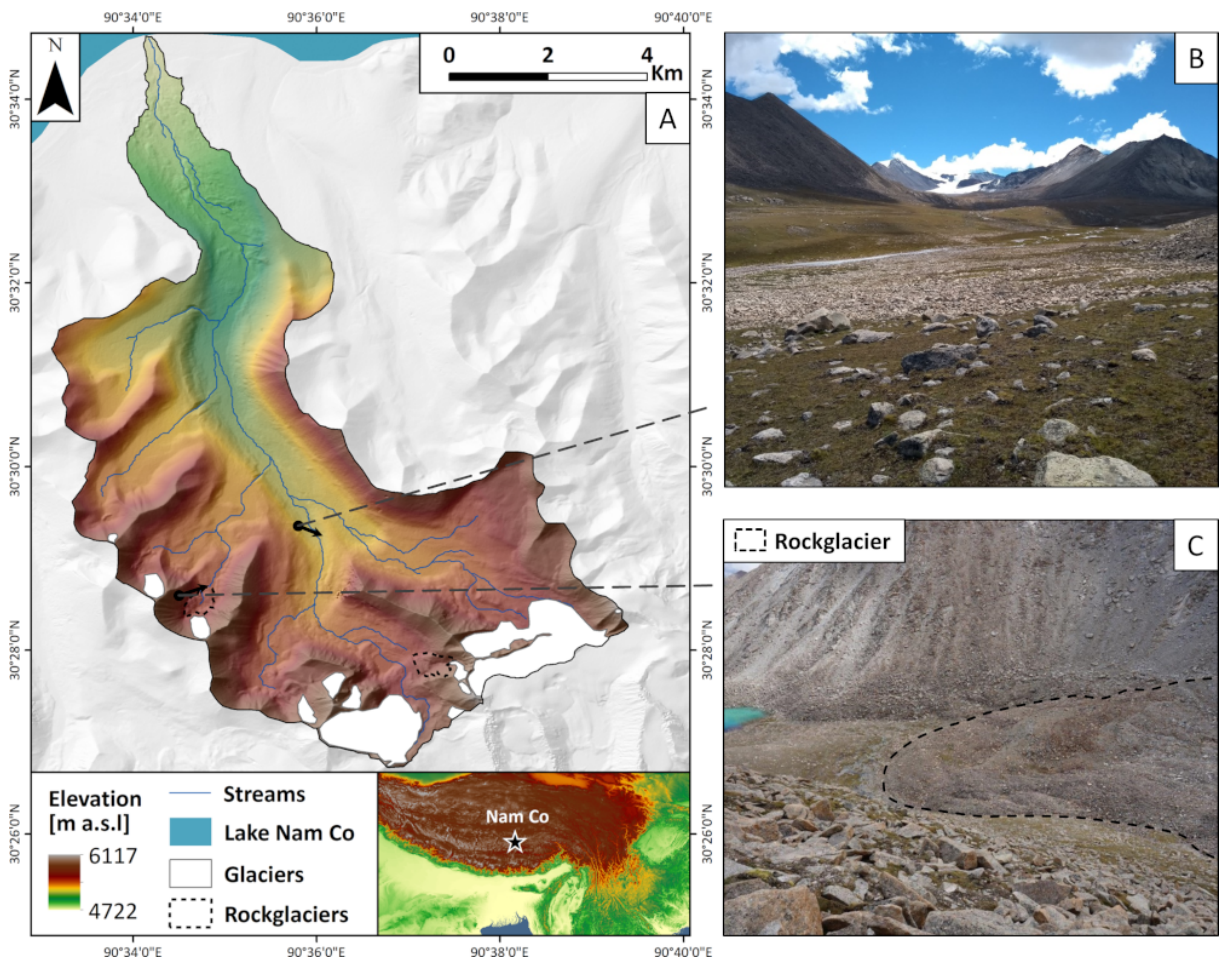


Figure 2.1: (A) Overview map of the Qugaqie catchment at Lake Nam Co including the location of the study area on the Tibetan Plateau. Elevation data based on SRTM v4 (Jarvis et al., 2008) and TanDEM-X 0.4" DEM (©DLR, 2017). The location and viewing direction of the images B and C are shown as black arrows. (B) Image of the main valley of Qugaqie basin with the Zhadang glacier in the background. (C) Image of the studied rock glacier (Fig. 2.2).

2.3 Data and methods

Here we use Sentinel-1 Level-1 single look complex data for all InSAR analysis, both from ascending and descending orbits from the interferometric wide swath mode with a ground resolution of 20 m azimuth and 5 m in range direction (Fletcher, 2012) and a 12 day repeat interval in this region. Due to the unreliability of early Sentinel-1a data, we decided to start our time series analysis of our study area in May and November 2015 for ascending and descending acquisitions respectively. The latest data acquisitions included in the analysis are from December 2018. We used a total of 74 acquisitions in ascending and 63 acquisitions in descending orbit for our 3 year time series analysis. We carefully analyzed all individual interferograms and excluded those with long temporal or geometric baselines, unwrapping errors and overall low coherence and therefore poor spatial coverage. This especially excluded many acquisitions from spring to autumn, as freezing and thawing of the ground changes surface characteristics and overall surface change, including surface motion, is strongest during this time period. We chose a coherence threshold of 0.3 for our analysis.

Electrical resistivity tomography (ERT) is a widely used method in geoscience. It is especially potent for the detection of subsurface ice under permafrost conditions. It has been used to detect permafrost in loose sediments, including rock glaciers, since the end of the 1990s (Hauck and Vonder Muhll, 2003; Kneisel et al., 2008; Mewes et al., 2017; Vonder Muhll et al., 2002). Geoelectric exploit the different electrical resistivities (or electrical conductivity as their reciprocal value) in the subsurface. The resistivity is generally higher in sediments interspaced by ice than in unfrozen bedrock and decreases significantly with increasing moisture content. The simplest iteration of this technique works with as little as four electrodes. Two electrodes feed current into the underground and generate an electric field in the subsurface, while two potential probes in between register the drop in voltage. These multi-channel geoelectric measurements result in two-dimensional depth sections (so-called pseudo-sections), which show the distribution of the apparent resistances in the subsurface.

2.3.1 ERT data acquisition

The shown ERT results were acquired during the field trip in July 2018. We worked with multi-electrode equipment (50 electrodes), a maximum spacing of 2 meters and applied the roll-along procedure. Blocky surfaces like rock glaciers have difficult characteristics due to their instability and a lack of fine material required for the electricity feed to reach the ground. The best connection was accomplished in areas where sandy soil material filled the gaps between boulders. The ends of the electrodes were pushed through sponges into the

fine material. We saturated the sponge with salted water, which kept the fine material wet due to desiccation through high solar radiation and supported a better electrode coupling and current-flow. We processed our ERT-data with the Res2Dinv-Software.

2.3.2 ISBAS Processing

We chose a modified version of the Small BAseLine Subset (SBAS) method (Berardino et al., 2002) for our time series analysis, as tests showed that results from this approach are superior in terms of spatial coverage and noise level to Persistent Scatterer Interferometry (PSI). The SBAS method generates interferograms between SAR acquisitions with a short temporal and geometric baseline and stacks them to estimate surface displacement and velocity over a time period. Interferograms are a spatial representation of the phase difference of two SAR acquisitions and can be used to determine the relative surface displacement between them. The modified SBAS approach we employed, referred to as Intermittent SBAS (ISBAS) (Bateson et al., 2015), produces a significantly improved spatial coverage by allowing limited interpolation of temporal gaps for areas, where the coherence is intermittently below the chosen threshold. Areas where at least 75 % of interferograms feature a coherence above a threshold of 0.3 will be retained in the final result. Those time periods when the coherence fell below the threshold were interpolated based on spatial and temporal parameters. This helped us to compensate for the lower coherence in spring to autumn, while still producing a reliable result. The topographic phase was removed from the interferograms with the TanDEM-X 12 m resolution DEM and the orbital phase was corrected via a polynomial function prior to unwrapping.

2.3.3 InSAR Postprocessing

The relative nature of InSAR results can make it difficult to interpret the results, especially in a dynamic mountainous setting. It is therefore desirable to derive absolute displacement signals by combining different data sets, such as ascending and descending orbits or field measurements, and by making a number of assumptions regarding the expected direction of the surface motion. The decomposition method combines ascending and descending acquisitions to derive absolute east-west and vertical displacement vectors but assumes north-south displacements to be negligible (Fialko et al., 2001), due to the low sensitivity of SAR acquisitions in those directions. This popular technique is therefore not useful to us as it does not produce representative data for slopes with a north or south aspect. We instead employed a different method to estimate absolute surface velocity. Areas with a slope $>5^\circ$ were projected in the direction of the steepest slope (after Notti et al., 2014), as most surface displacement is assumed to be caused by sliding processes transporting material parallel to the slope. This technique originates in landslide studies, where the direction of the landslide generally follows the steepest slope.

We calculate a coefficient (C) in order to estimate the downslope velocity (V_{SLOPE}). C receives a value between 0.2 and 1, based on the cosine of the LOS (n_{LOS} , h_{LOS} and e_{LOS}) of the satellite, calculated from the incidence angle (α) and the azimuth (Θ) in radians, and the aspect (A) and slope (S) of the surface area. The LOS velocity (V_{LOS}) is divided by C to produce the slope velocity. The following equations describe the necessary calculations to estimate the slope velocity (Notti et al., 2014):

$$V_{SLOPE} = \frac{V_{LOS}}{C}$$

$$C = (n_{LOS} \times \cos(S) \times \sin(A - 1.571)) + (e_{LOS} \times (-1 \times \cos(S) \times \cos(A - 1.571)) + (h_{LOS} \times \sin(S)));$$

$$h_{LOS} = \cos(\alpha); n_{LOS} = \cos(1.571 - \alpha) \times \cos(\eta); e_{LOS} = \cos(1.571 - \alpha) \times \cos(\omega);$$

$$\eta = 3.142 - \Theta; \omega = 4.712 - \Theta$$

The larger the difference between the LOS vector and the downslope vector, the smaller and therefore stronger C becomes. We excluded data points with a strong coefficient if a slope has a strong coefficient in only one LOS but not the other, as a strong coefficient is associated with a larger uncertainty. The maximum strength of C is set to 0.2 to avoid producing unrealistically large slope velocities caused by a coefficient close to zero. We used a smoothed version of the TanDEM-X DEM (with a 90×90 m moving mean) to determine the motion direction. We did this as we assume, that structures such as rock glaciers and landslides move a larger amount of sediment in a similar direction and we wanted to avoid outliers caused by single pixels with different slope aspects. This is a simplified approach to estimate the slope velocity and it does not take into account rotational and compressional motion within the moving structure. This approach is therefore likely to lead to an overestimation of the actual velocity in many areas.

2.4 Results and discussion

We can clearly see from the results of our time series analysis, that the studied rock glacier is active. It shows clear creeping motion on the order of 5 to 15 cm yr^{-1} after our projection along the steepest slope (Fig. 2.2c). The outline of the rock glacier was derived from optical satellite data (©Bing, 2019) and a 12 m resolution TanDEM-X DEM (©DLR, 2017). We observe strong differences in velocity between different parts of the rock glacier but it is likely that this is not only a reflection of different levels of activity but rather due to varying surface aspects. When we compare the velocities to the surface aspect, we can clearly see that those parts of the rock glacier with strong north or south aspects appear significantly less uniform and with more noise. This is connected to the low sensitivity of SAR acquisitions in the north-south direction due to the polar orbit

of the satellite. The sensitivity coefficient we use to project our velocity models from LOS to the downslope direction, is strongest for slopes with a north or south aspect. Therefore the precision of our data is also lowest on those slopes, making the results more noisy in comparison to slopes with better sensitivity coefficients. Slopes with a strong coefficient also display overall lower slope velocities, like in the frontal region of the rock glacier, which again is more indicative of the insensitivity of the satellite, rather than actually reduced velocities. This is corroborated by the ERT profile, which displays a cross-section of the frontal part of the rock glacier (Fig. 2.3, profile 2). Red and purple areas represent high resistivity ($>100 \text{ k}\Omega\text{m}$), associated with subsurface ice content, while blue areas feature lower resistivity ($<100 \text{ k}\Omega\text{m}$), associated with unfrozen ground. We positioned profile 1 (Fig. 2.3, profile 1) in front of the rock glacier in order to highlight the difference between frozen sediment of the rock glacier and partly frozen glacial till. In profile 1 we observe only individual ice lenses with similar high resistivity values ($>70 \text{ k}\Omega\text{m}$).

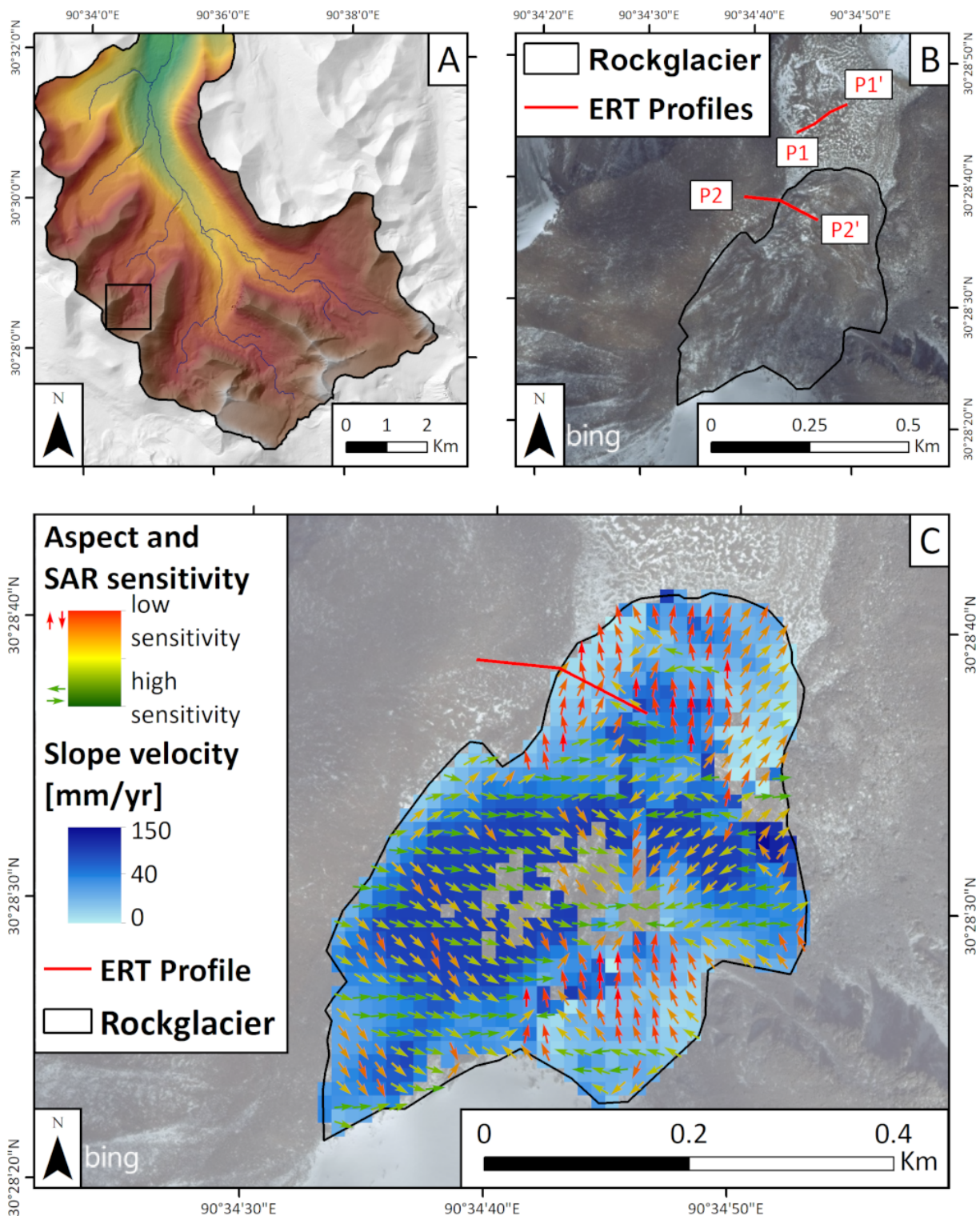


Figure 2.2: (A) Overview of the study area (©DLR, 2017) featuring the location of the rock glacier displayed in B and C. (B) Extent of a rock glacier within the study area and the locations of our ERT profiles (Fig. 2.3) superimposed over an optical satellite image (©Bing, 2019). (C) Surface velocity of the rock glacier from 2015 to 2018 derived from ascending and descending Sentinel-1 satellite data (©Copernicus, 2017). The velocity has been projected into the direction of the steepest slope after (after Notti et al., 2014). The aspect of the surface is shown by arrows, colour coded according to the sensitivity of SAR acquisitions to those directions. The missing velocity values in the center of the rock glacier are likely caused by rotation of the surface material, which leads to decorrelation of the data.

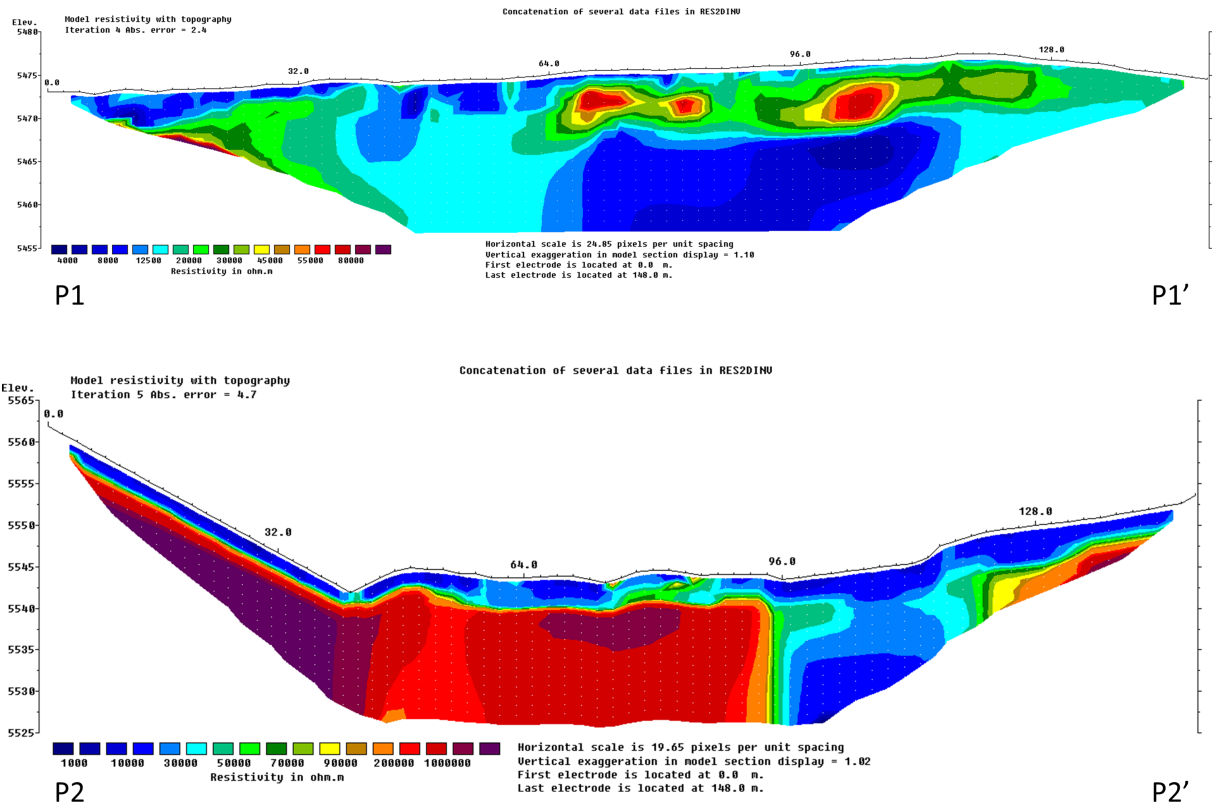


Figure 2.3: ERT profiles near the rock glacier shown in Fig. 2.2 B/C. Top: Profile 1 is characterized by low resistivity values ($<20 \text{ k}\Omega\text{m}$) associated with unfrozen ground dominated by conductive material. Three areas of higher resistivity values ($>70 \text{ k}\Omega\text{m}$) are interpreted as ice lenses. Below: In profile 2 the uppermost, unfrozen layer represents the active layer ($<20 \text{ k}\Omega\text{m}$), which thaws in summer. The black dashed line indicates frozen bedrock, while the high resistivity values ($>70 \text{ k}\Omega\text{m}$) outside of the dashed line represent the frozen sediment of the rock glacier.

Another limitation is that absence of permafrost related creep does not mean absence of subsurface ice. Areas with a small slope ($<5^\circ$) rarely display surface creep (Daanen et al., 2012), yet they may still contain ice lenses and be categorized as permafrost. This is the case for the valley bottom in front of the rock glacier, where no significant creep takes place but where our ERT measurements nonetheless display ice content (Fig. 2.3, profile 1). Seasonal freezing and thawing cycles can also be observed in flat terrain but we could not observe a significant difference between cycles in areas with permafrost compared to areas with seasonally frozen ground, as both produce a similar freeze-thaw signal. It is therefore possible to use InSAR to detect permafrost where measurable creep takes place but using it to identify permafrost on flat ground or on north- or south-facing slopes is problematic.

Despite these limitations InSAR time series analysis is still a capable tool when it comes to studying permafrost creep, as it can be used to identify rock glaciers and other periglacial landforms with sufficiently large motion over extended areas. It should therefore be used in combination with optical satellite data and geomorphological maps to

determine the extent of such landforms after they have been detected with InSAR. We aim to expand our approach to a larger region, in this case the northern Nyainqêntanglha range, to assess its viability on a regional scale (Fig. 2.4).

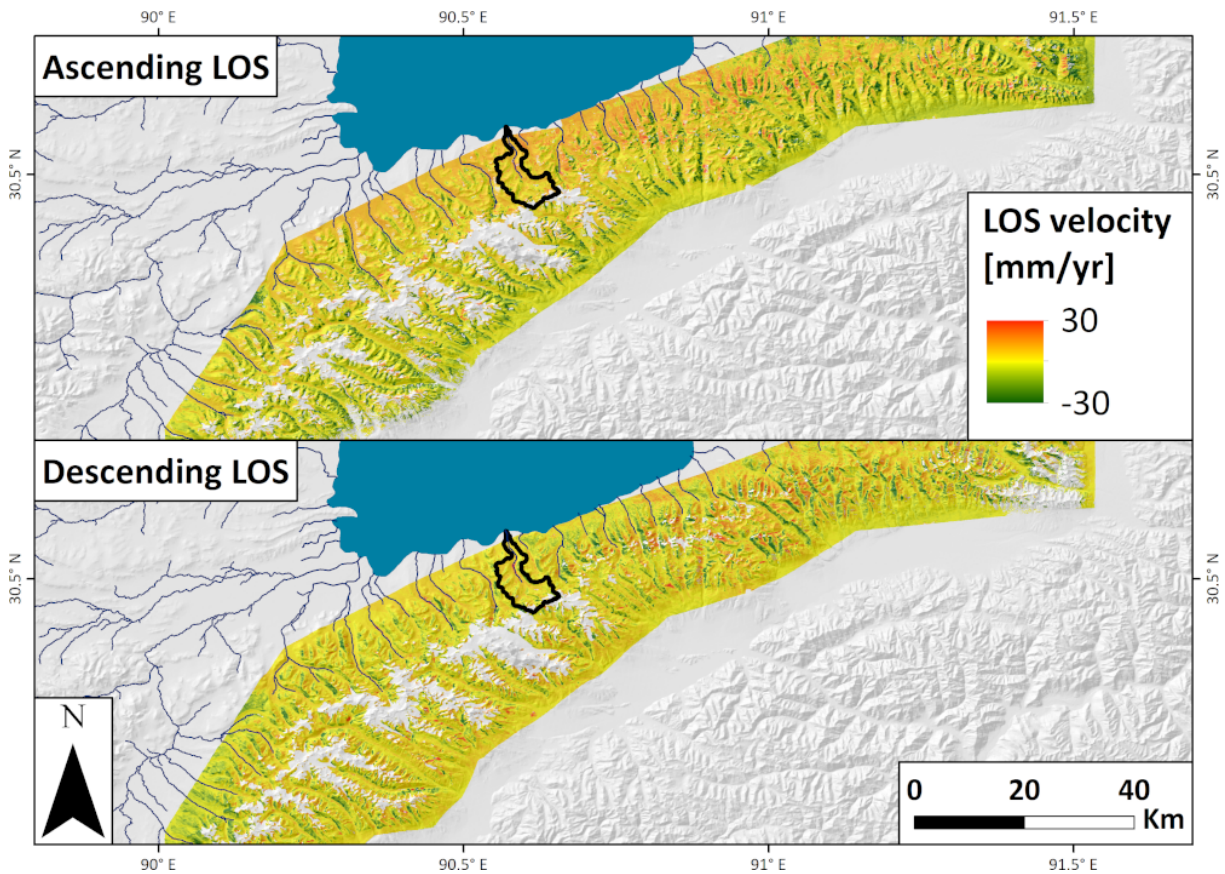


Figure 2.4: Preliminary results of InSAR time series analysis of the Nyainqêntanglha mountain range from 2015 to 2019 based on Sentinel-1 data (©Copernicus, 2017). The outline of Qugaqie basin (Fig. 1) is shown in black.

2.5 Summary and Outlook

Our combination of geophysical field measurements and microwave remote sensing highlights the capabilities of each technique and how they can be used in combination to compensate for their limitations for permafrost investigation. InSAR time series analysis allows us to detect surface motion induced by permafrost creep on a large scale, while ERT measurements add information about permafrost areas without significant surface creep and slopes where InSAR sensitivity is low i.e. with a strong north or south aspect. We studied a rock glacier within the Qugaqie basin extensively with both techniques, with the goal of applying this detailed information to the entire Nyainqêntanglha range to create an inventory of permafrost related creep processes and to better constrain the permafrost extent in this area. Further validation with TerraSAR-X satellite data and ground-truth through terrestrial laser scans will be added to our models to improve their

precision and reliability.

Acknowledgements

We would like to thank the DLR for providing us with the high-resolution TanDEM-X DEM for our data processing (Proposal ID DEM_HYDR1727) and the ESA and Copernicus for making Sentinel-1 and Sentinel-2 data freely available to the public. We are especially grateful to the ‘Deutsche Forschungsgemeinschaft’ (DFG) for funding our work as part of the Sino-German project ‘Geo-ecosystems in transition on the Tibetan Plateau’ (TransTiP; GRK 2309/1). We thank our Chinese colleagues, especially at the NAMORS research station, who have worked tirelessly to support us before and during our field work.

Bibliography

- Bateson, L., Cigna, F., Boon, D., and Sowter, A. (2015). The application of the Intermittent SBAS (ISBAS) InSAR method to the South Wales Coalfield, UK. *International Journal of Applied Earth Observation and Geoinformation*, 34:249–257.
- Berardino, P., Fornaro, G., Lanari, R., and Sansosti, E. (2002). A new algorithm for surface deformation monitoring based on small baseline differential SAR interferograms. *IEEE Transactions on geoscience and remote sensing*, 40(11):2375–2383.
- Crosetto, M., Monserrat, O., Cuevas-González, M., Devanthéry, N., and Crippa, B. (2016). Persistent scatterer interferometry: A review. *ISPRS Journal of Photogrammetry and Remote Sensing*, 115:78–89.
- Daanen, R., Grosse, G., Darrow, M., Hamilton, T., Jones, B. M., et al. (2012). Rapid movement of frozen debris-lobes: implications for permafrost degradation and slope instability in the south-central Brooks Range, Alaska. *Natural Hazards and Earth System Sciences*, 12(5):1521–1537.
- Fialko, Y., Simons, M., and Agnew, D. (2001). The complete (3-D) surface displacement field in the epicentral area of the 1999 Mw7. 1 Hector Mine earthquake, California, from space geodetic observations. *Geophysical research letters*, 28(16):3063–3066.
- Fletcher, K. (2012). *SENTINEL 1: ESA’s Radar Observatory Mission for GMES Operational Services*. European Space Agency.
- Haeberli, W., Hallet, B., Arenson, L., Elconin, R., Humlum, O., Käab, A., Kaufmann, V., Ladanyi, B., Matsuoka, N., Springman, S., et al. (2006). Permafrost creep and rock glacier dynamics. *Permafrost and periglacial processes*, 17(3):189–214.

- Haerberli, W., Noetzli, J., Arenson, L., Delaloye, R., Gärtner-Roer, I., Gruber, S., Isaksen, K., Kneisel, C., Krautblatter, M., and Phillips, M. (2010). Mountain permafrost: development and challenges of a young research field. *Journal of Glaciology*, 56(200):1043–1058.
- Hauck, C. and Vonder Mühl, D. (2003). Evaluation of geophysical techniques for application in mountain permafrost studies. *Zeitschrift für Geomorphologie, NF Suppl., Bd.*, 132:161–190.
- Hock, R., Rasul, G., Adler, C., Cáceres, B., Gruber, S., Hirabayashi, Y., Jackson, M., Kääh, A., Kang, S., Kutuzov, S., et al. (2019). High mountain areas.
- Jarvis, A., Reuter, H. I., Nelson, A., Guevara, E., et al. (2008). Hole-filled SRTM for the globe Version 4. *available from the CGIAR-CSI SRTM 90m Database (<http://srtm.csi.cgiar.org>)*, 15:25–54.
- Kneisel, C., Hauck, C., Fortier, R., and Moorman, B. (2008). Advances in geophysical methods for permafrost investigations. *Permafrost and periglacial processes*, 19(2):157–178.
- Mewes, B., Hilbich, C., Delaloye, R., and Hauck, C. (2017). Resolution capacity of geophysical monitoring regarding permafrost degradation induced by hydrological processes. *The Cryosphere*, 11(6):2957–2974.
- Notti, D., Herrera, G., Bianchini, S., Meisina, C., García-Davalillo, J. C., and Zucca, F. (2014). A methodology for improving landslide PSI data analysis. *International journal of remote sensing*, 35(6):2186–2214.
- Reinosch, E., Buckel, J., Dong, J., Gerke, M., Baade, J., and Riedel, B. (2020). InSAR time series analysis of seasonal surface displacement dynamics on the Tibetan Plateau. *The Cryosphere*, 14(5):1633–1633.
- Vonder Mühl, D., Hauck, C., and Gubler, H. (2002). Mapping of mountain permafrost using geophysical methods. *Progress in Physical Geography*, 26(4):643–660.
- Wu, Q., Zhang, T., and Liu, Y. (2010). Permafrost temperatures and thickness on the Qinghai-Tibet Plateau. *Global and Planetary Change*, 72(1-2):32–38.
- Yao, T., Liu, X., Wang, N., and Shi, Y. (2000). Amplitude of climatic changes in Qinghai-Tibetan Plateau. *Chinese Science Bulletin*, 45(13):1236–1243.

Chapter 3

Insights into a remote cryosphere: a multi-method approach to assess permafrost occurrence at the Qugaqie basin, western Nyainqêntanglha Range, Tibetan Plateau

Johannes Buckel¹, Eike Reinosch², Andreas Hördt¹, Andreas Hördt², Fan Zhang³, Björn Riedel², Markus Gerke², Antje Schwalb⁴, Roland Mäusbacher⁵

¹ Institute for Geophysics and Extraterrestrial Physics, Technische Universität Braunschweig, 38106 Braunschweig, Germany

² Institute for Geodesy and Photogrammetry, Technische Universität Braunschweig, 38106 Braunschweig, Germany

³ Key Laboratory of Tibetan Environment Changes and Land Surface Processes, Institute of Tibetan Plateau Research, Chinese Academy of Sciences, Beijing, 100101, China

⁴ Institute of Geosystems and Bioindication, Technische Universität Braunschweig, 38106 Braunschweig, Germany

⁵ Geographical Institute, Friedrich Schiller University of Jena, 07743 Jena, Germany

Corresponding author: Johannes Buckel (j.buckel@tu-braunschweig.de)

Abstract

Permafrost as a climate-sensitive parameter and its occurrence and distribution play an important role in the observation of global warming. However, field-based permafrost distribution data and information on the subsurface ice content in the large area of the southern mountainous Tibetan Plateau (TP) are very sparse. Existing models based on boreholes and remote sensing approaches suggest permafrost probabilities for most of the Tibetan mountain ranges. Field data to validate permafrost models are generally lacking because access to the mountain regions in extreme altitudes is limited. The study provides geomorphological and geophysical field data from a north-orientated high-altitude catchment in the western Nyainqêntanglha Range. A multi-method approach combines (A) geomorphological mapping, (B) electrical resistivity tomography (ERT) to identify subsurface ice occurrence and (C) interferometric synthetic aperture radar (InSAR) analysis to derive multi-annual creeping rates. The combination of the resulting data allows an assessment of the lower occurrence of permafrost in a range of 5350 and 5500 m above sea level (a.s.l.) in the Qugaqie basin. Periglacial landforms such as rock glaciers and protalus ramparts are located in the periglacial zone from 5300-5600 m a.s.l. The altitudinal periglacial landform distribution is supported by ERT data detecting ice-rich permafrost in a rock glacier at 5500 m a.s.l. and ice lenses around the rock glacier (5450 m a.s.l.). The highest multiannual creeping rates up to 150 mmyr^{-1} are typically observed on these rock glaciers. This study closes the gap of unknown state of periglacial features and potential permafrost occurrence in a high-elevated basin in the western Nyainqêntanglha Range (Tibetan Plateau).

3.1 Introduction

Information on permafrost (defined as a thermal state of perennially cryotic ground, frozen for at least 2 consecutive years; (Ballantyne, 2018; Washburn, 1980) distribution is of great importance in times of global warming, especially in high-mountain areas (Hock et al., 2019), because these areas are climatically sensitive (Barsch, 1996; Mollaret et al., 2019). The International Panel on Climate Change (IPCC) reported the strongest observed increase in permafrost temperature (globally averaged across polar and high-mountain regions) since 2007 in 2019 (Hock et al., 2019). Periglacial landforms, like rock glaciers and protalus ramparts in this study, are features “resulting from the action of intense frost, often combined with the presence of permafrost” (French, 2012). If permafrost as perennial frozen ground ice is available, periglacial landforms are particularly well suited to detect and to study changes of permafrost and the related ice content (Kneisel and Kääh, 2007; Kääh, 2013; Knight et al., 2019). These changes have an increasing impact on people and

their livelihood (Gruber et al., 2017), e.g., due to the importance of long-term ground ice as a water resource (Jones et al., 2019) in arid/semiarid regions like the Andes (Azócar and Brenning, 2010; Rangecroft et al., 2015) or the Tien Shan (Bolch et al., 2009). The frozen water storages have a strong impact on water budgets by permafrost degradation and glacier melt (Bibi et al., 2018; Song et al., 2020), especially at the so-called Asian water tower, which provides water for more than 1.4 billion people (Immerzeel et al., 2020). The occurrence of natural hazards increases due to thawing permafrost (Zhang and Wu, 2012; Yu et al., 2016), for example by destabilizing mountain slopes and rock walls (Deline et al., 2015). The scientific and social importance leads to a stronger focus on permafrost areas, especially on the Tibetan Plateau (TP) where permafrost conditions react fast to atmospheric warming (Cheng and Wu, 2007; Lu et al., 2017).

Permafrost research in engineering has a 60-year-long tradition on the TP (Chen et al., 2016; Yang et al., 2010). The continuous use and life span of infrastructure depends on stable surface conditions which are strongly deteriorated by permafrost degradation. The engineering corridors for infrastructure projects like the Qinghai-Tibetan highway/railway and pipelines (Yang et al., 2010; Yu et al., 2016) were accompanied by monitoring permafrost sites based on borehole temperature (Hu et al., 2020; Li et al., 2009a), ground temperature data (Cheng and Wu, 2007; Ma et al., 2006) and geophysics: small-scaled ground ice distribution was investigated by ground-penetration radar (Wang et al., 2020; Wu et al., 2005; You et al., 2017) and by electrical resistivity tomography (ERT) (You et al., 2013, 2017) close to the important highways/railways. Compared to the central and eastern parts of the TP, permafrost surveys in the western and southern TP are very scarce (Yang et al., 2010). Additional permafrost studies outside the engineering corridors are limited to modelling results and large-scale permafrost distribution maps (Ran et al., 2012; Cao et al., 2019; Obu et al., 2019). Implications of a temperature warming followed by permafrost degradation for the entire TP are hard to deduce due to inadequate distribution and a small number of stations recording air temperature (Yang et al., 2010). Therefore, modelling approaches are gaining increasing importance in order to estimate the consequences of the current temperature rise on the TP. This warming temperature trend is reconstructed by $\delta^{18}\text{O}$ records in four spatially well-distributed ice cores back to the beginning of the last century (Yao et al., 2006). Sun et al. (2020) confirm the relationship between the temperature increase and permafrost degradation on the TP by a slow adaptation until the year 2100 based on a numerical heat conduction permafrost model. New statistical and machine learning approaches suggest that the permafrost extent on the entire TP is 45.9 % (2003-2010), and they predict future permafrost degradation of 25.9 % by the 2040s and 43.9 % by the 2090s (Wang et al., 2019). Cheng and Wu (2007) also conclude that more than “half of the permafrost may become relict and/or even disappear by 2100”.

This study aims to supplement the previously summarized studies with an assessment of probable occurrence of permafrost in remote high-mountain regions unbiased by the location of the Tibetan corridors and to provide a ground truthing for existing permafrost studies and maps on the TP. The use of the term “probable” is motivated by the fact that we do not have ground-truthed temperature data for geophysical data validation. Furthermore, no small-scaled modelled permafrost distribution is available, and therefore we assess its occurrence indirectly. The spatial heterogeneity of our data (mapping, InSAR and ERT) and of topographic variations in permafrost occurrence also prevents us from providing precise elevational limits; thus we provide an assessment of probable occurrence of permafrost in a range according to the findings of the three methods.

Our study area (Fig. 3.1b and c) is located at the interface between continuous permafrost and seasonally frozen ground according to large-scale modelling results of permafrost conditions on the TP (Sun et al., 2020). The location makes it a suitable environment to validate such large-scale models and to precisely define the interface with ground-truthed data. The validation is important, because the final conclusion would be that some higher region on the TP is not completely underlying permafrost conditions, unlike expected and modelled at other places at the TP (Cao et al., 2019; Ran et al., 2012).

The identification of periglacial landforms, subsurface ice and surface creeping rates on these landforms leads to an assessment of the probable occurrence of permafrost. The combination of field investigations and remote sensing techniques is a useful tool to detect permafrost occurrence (Bolch et al., 2019; Dusik et al., 2015; Monnier et al., 2014). Periglacial landforms such as active (creeping) rock glaciers and protalus ramparts can contain ice (Barsch, 1996; Scapozza, 2015; Schrott, 1996) and are considered indicators of permafrost occurrence (Frauenfelder et al., 1998; Haeberli et al., 2006; Kneisel and Kääh, 2007; López-Martínez et al., 2012). Especially on the TP only sparse literature is found that describes periglacial landforms in detail in combination with permafrost occurrence (Fort and van Vliet-Lanoë, 2007; Ran and Liu, 2018; Wang and French, 1995). However, these periglacial landforms as an indicator for permafrost occurrence are essential for creating large-scale permafrost distribution maps (e.g., Schmid et al., 2015).

We present a multi-method approach to provide a reliable prediction of subsurface ice and permafrost occurrence to answer the following research questions:

1. How are periglacial landforms distributed?
2. Do the investigated periglacial landforms like rock glaciers and protalus ramparts show an active status?
3. Which creeping rates do the periglacial landforms indicate?

We created (A) an inventory of periglacial landforms indicating potential subsurface ice occurrence, we (B) acquired electrical resistivity tomography (ERT) data to validate the ice occurrence of selected landforms and we (C) then used multi-annual surface creeping rates from InSAR time series analysis to corroborate the hypothesis of long-term ice occurrence due to permafrost conditions above a special elevation. As a result, the study provides probable occurrence of permafrost by combining these three methods for a catchment in a high-altitude mountain range of the TP.

3.2 Study area

The western Nyainqêntanglha Range (Fig. 3.1) was formed during the Himalayan-Tibetan orogenesis as part of the central Lhasa block (Kapp et al., 2005; Keil et al., 2010). From Tertiary to Quaternary, the Nyainqêntanglha area was controlled and compressed by a fracture belt which folded and rose violently, forming the Nyainqêntanglha Mountains, with the highest peak of 7162 m a.s.l. (Kidd et al., 1988; Keil et al., 2010). Our study area, the Qugaqie catchment, is characterized by Cretaceous red beds and sandstone in the northern part and by early tertiary granodiorites in the centre. The bedrock of the southern part consists of biotite adamellites and glaciers in the highest zone (Kapp et al., 2005; Yu et al., 2019). The atmospheric circulation pattern and the topographic characteristics are responsible for a similar glacier distribution pattern in all north-oriented catchments of the western Nyainqêntanglha range, including the Qugaqie basin (Kang et al., 2009; Zhang et al., 2013a). On the lee side of the main western Nyainqêntanglha crest and therefore at the lee site of the moisture of the Indian summer monsoon (ISM) the glaciers are smaller in area and length (Zhang et al., 2013a) (Fig. 3.1b). Zhang et al. (2013a) also investigated the glacier shrinkage based on satellite data. They observed a glacier retreat of about -9.9 ± 3.1 % between 1976 and 2009. Zhang and Zhang (2017) observe a melting rate -0.30 ± 0.07 myr⁻¹ over the entire western Nyainqêntanglha range from 2000 to 2014. The Zhadang glacier located in the Qugaqie head lost an area of almost 0.4 km² in the same time span and covered an area of 2.36 km² in 2009. The

corresponding retreat rate is 14 %, slightly larger than the regional average, which could indicate a slightly faster deglaciation of the smaller, north-orientated glaciers in the western Nyainqêntanglha range.

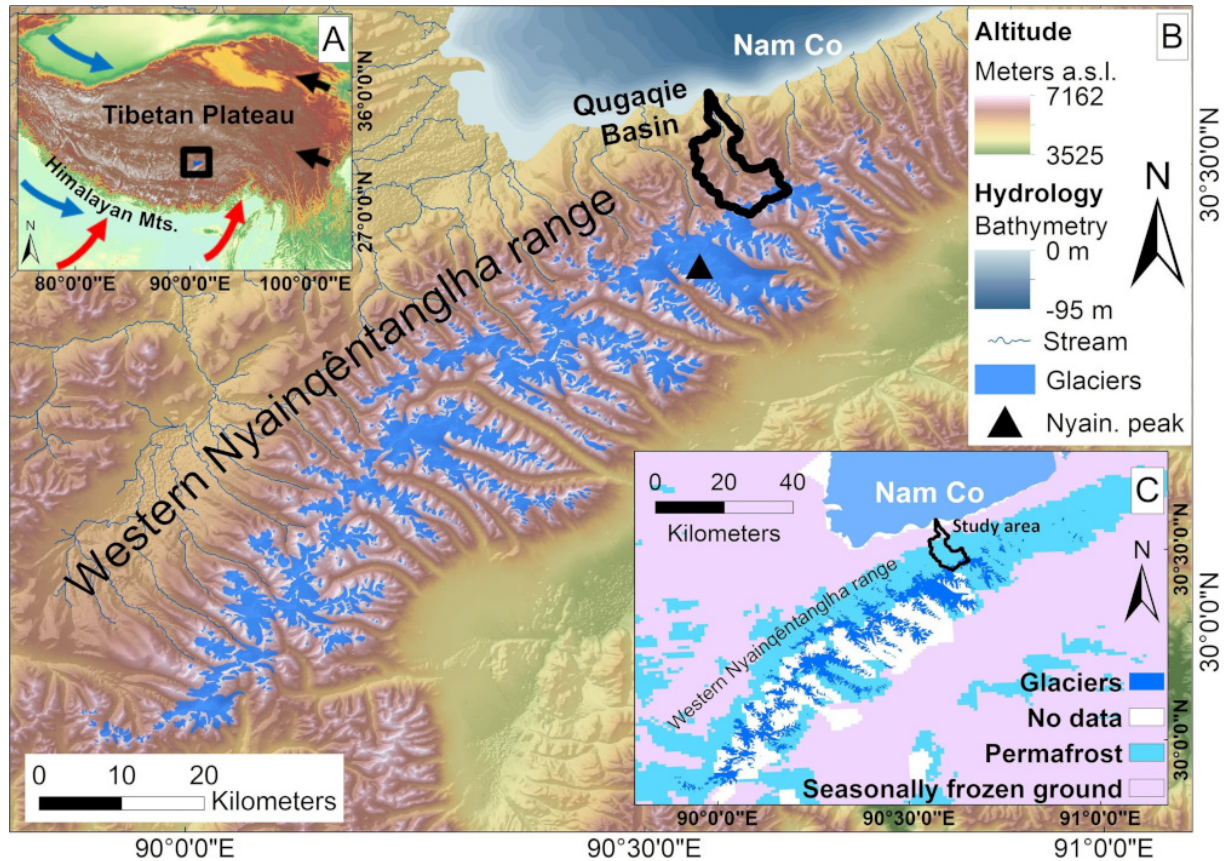


Figure 3.1: (A) Location of the study area within the Tibetan Plateau (TP) (background on SRTM DEM v4, Jarvis et al., 2008). Different wind systems influencing climate of the TP are shown by blue (westerlies), red (Indian summer monsoon) and black (East Asian monsoon) arrows based on Yao et al. (2012). (B) Overview map of the Nam Co catchment with the altitude colours and the study area of the Qugaqie catchment (thick black lines). Note the greater glacier extents on the south-oriented mountain range. Bathymetric data originated from Wang et al. (2009) (hillshade and DEM background based on SRTM DEM v4, Jarvis et al., 2008). Glacier extents originated from the GLIMS database (Cogley et al., 2015; Guo et al., 2015; Liu and Guo, 2014). (C) Permafrost distribution in the western Nyainqêntanglha range based on Zou et al. (2017).

The Qugaqie catchment is a sub-catchment of the Nam Co catchment, which is influenced by a strong climate seasonality driven by different wind systems throughout the year (Yao et al., 2013): westerlies dominate in the winter months and provide cold, dry continental air from east to northeast (Fig. 3.1a, blue arrows), with temperature minima below $-20\text{ }^{\circ}\text{C}$. The dry season ends with the onset of the ISM (Fig. 3.1a, red arrows), which provides moisture from May to September (Mügler et al., 2010). A total of 80 % of the annual precipitation ($295\text{-}550\text{ mmyr}^{-1}$) occurs during the monsoon-dominated summer months (Wei et al., 2012). The influence of the East Asian monsoon on our

study area is minor but it is an important source of moisture for the eastern TP (Fig. 3.1a, black arrows). Consequently, the study area of the Qugaqie basin, situated in the western Nyainqêntanglha Range (Fig. 3.1b), is characterized by semiarid climate and a large amount of solar radiation due to the high elevation and reduced cloud cover (Li et al., 2009b). With an area of almost 60 km², the basin drains into the dimictic lake Nam Co (Fig. 3.1b), and the relief extends from 4722 m a.s.l. to an elevation up to 6119 m a.s.l.

Detailed information about permafrost occurrence and distribution in the study area is very scarce. Tian et al. (2006) determined a lower limit of permafrost based on soil probes at an elevation of around 5400 m a.s.l. along the northern slopes of Mt. Nyainqêntanglha (Fig. 3.1b). This is generally higher than in other regions (>4500 m a.s.l.) of the TP (Ran et al., 2012). Schütt et al. (2010) sampled lacustrine sediments from a permafrost lens in an outcrop at the Gangyasang Qu's entry into the northwestern end of the lake Nam Co at 4722 m a.s.l. Zou et al. (2017) distinguish between seasonally frozen ground and permafrost on their distribution map over the TP (Fig. 3.1c). According to their map permafrost is existent at elevation higher than 5000 m a.s.l. and covers more than 90 % of the study area. The visible data gaps were not further discussed by Zou et al. (2017). A coarse overview including a distinction between glacial and periglacial processual states around the lake Nam Co is given by Keil et al. (2010). A 2-year temperature dataset on the Zhadang glacier, recorded at 5680 m a.s.l. by an automatic weather station (2009-2011) at 2 m height, shows a mean annual air temperature (MAAT) of -6.8 °C (Zhang et al., 2013b) and suggests permafrost conditions for the surrounding periglacial landscape.

3.3 Data and methods

We have used three different methods (A-C) to gain insights into permafrost-indicating periglacial landforms and to assess the lower occurrence of probable permafrost in the Qugaqie catchment. The following methods (Fig. 2) indicate information about permafrost conditions.

- (A) Geomorphological mapping. A map visualizes the distribution and characteristics of periglacial landforms and geomorphometric features.
- (B) Geophysical methods. Electrical resistivity tomography (ERT) identifies ice content and reveals the subsurface structure of periglacial landforms.
- (C) Microwave remote sensing. Interferometric synthetic aperture radar (InSAR) time-series analysis of ESA’s Sentinel-1 satellite data detects perennial, constant creeping rates of active periglacial landforms.

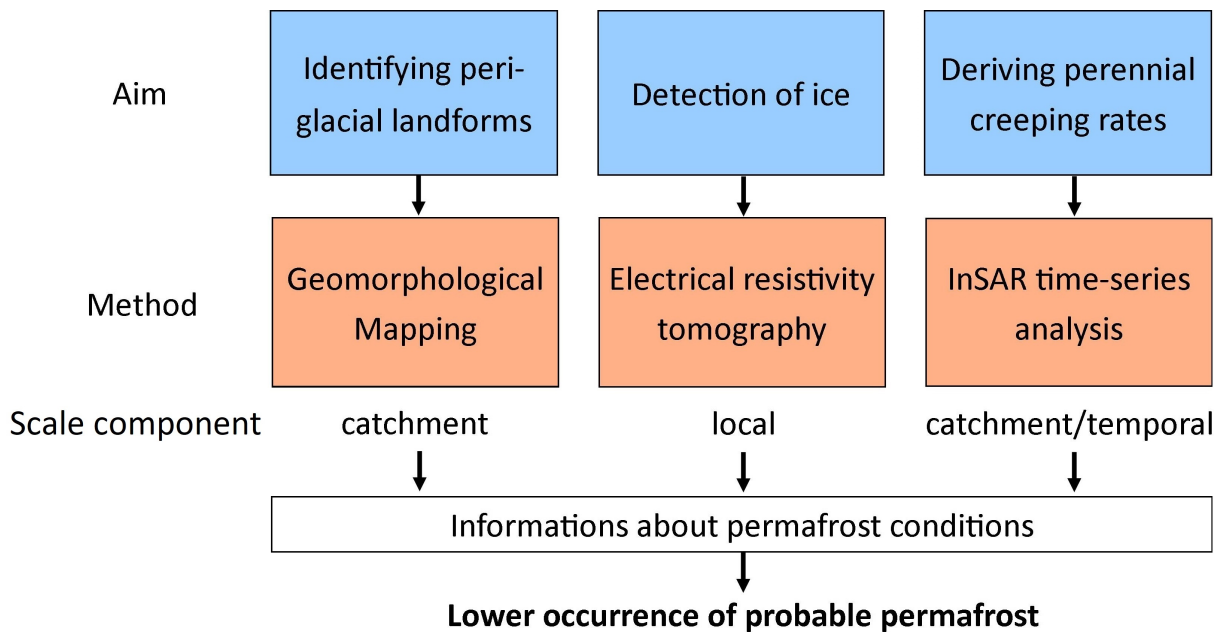


Figure 3.2: Schematic workflow of applied methods to assess lower occurrence of probable permafrost.

(A) A geomorphological map visualizes the distribution and characteristics of landforms and geomorphometric features with the focus on periglacial landforms on a catchment-wide/regional scale. Periglacial landforms like rock glaciers (Barsch, 1996) and protalus ramparts (Scapozza, 2015) can potentially preserve ice over a long period of time (Balantyne, 2018), and their activity and perennial creeping are an indicator for permafrost

occurrence (Delaloye et al., 2010; Eckerstorfer et al., 2018; Angillieri, 2017). This circumstance is validated (B) by ERT to detect subsurface ice on a local scale. (C) InSAR time series analysis detects perennial creeping which is typical of active periglacial landforms. The permafrost occurrence is indicated by activity of landforms and the corresponding surface structures like bulges, furrows, ridges or lobes. We make use of the fact that the deformation of debris supersaturated with ice causes surface displacement by downwards permafrost creep (Barsch, 1996; Delaloye et al., 2010). Therefore, we concretize surface displacement (rates) as permafrost creep (creeping rates) in this study. Although the continuous movement of periglacial landforms and the presence of ice can be implied from InSAR data alone, ground truth at selected locations by ERT is essential to exclude other possible interpretations.

We assess the lower occurrence of probable permafrost by the mean altitudinal distribution of periglacial landforms, by the subsurface ice occurrence which has been validated with geophysics and by the active status which is indicated by perennial surface creeping rates (Fig. 3.3). An occurrence of sporadic permafrost is not excluded in lower elevation but cannot be validated by the used methods and due to scale issues.

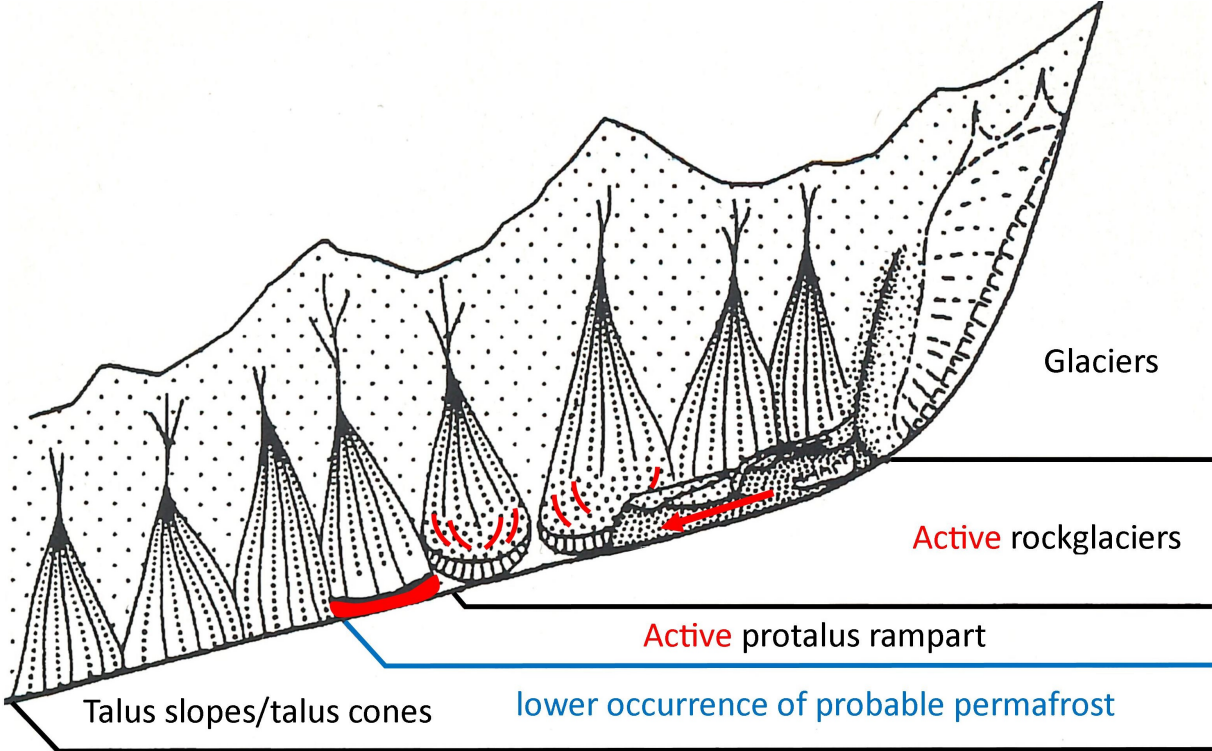


Figure 3.3: Schematic, hypsometric distribution of mapped landforms. Red features show active, multiannual creeping structures (furrows, lobes, bulges, ridges) of periglacial landforms indicating the lower occurrence of probable permafrost. Modified from Barsch (1996) after Höllermann (1983).

3.3.1 Inventory of cryospheric mesoscale landforms

The mapping procedure consists of the elementary mapping steps, described by Knight et al. (2011) and Otto and Smith (2013). Pre-mapping includes analyses of digital elevation models (DEMs) and mapping of landforms on optical images at a scale of 1:10000 (named mesoscale here following Höllermann, 1983). The DEM used in this study originates from TanDEM-X data (2015) with a resolution of 12 m (©DLR). The optical images are based on Digital globe, BING maps (2013) and Google Earth data (2007-2012). Geomorphological symbols were used after Kneisel et al. (1998) for field mapping and after Otto and Dikau (2008) for the digitized visualization in ArcGIS. During the field campaign, the main focus was on the mapping of periglacial landforms at the mesoscale (Höllermann, 1983). These landforms are components of the periglacial zone which is defined by seasonally frozen and perennally frozen ground (French, 2017). A differentiation between seasonally frozen and perennally frozen movement behaviour is given by the InSAR data and a derived model by Reinosch et al. (2020). These data were used for the preparation of the cryospheric landform identification. Next to optical and InSAR data, the periglacial landforms were identified in the field by an inspection of the form, the substrate, the catchment and the potential process which formed the landform. The Results section describes the inventory statistically and includes morphological field observations which could not be included in the map due to scale issues. For example, small-scaled dead ice holes were not included in the mesoscale geomorphological map. During post-mapping we integrated the field-mapped information into ArcGIS. Additional features like a stream network, lakes, ridges, glacier extents and moraines were delineated with the help of the mentioned DEM, a hillshade map (azimuth 315°, altitude 45°) and the mentioned optical images. Glacier extents were digitized based on optical images of the year 2013 (BING maps). Rock glaciers were identified following the comprehensive description by Barsch (1996): if the form shows a tongue or a lobate shape in the field and the optical images, we classified the landform as a rock glacier. Additionally, field observations like coarse clasts at the surface and at the front indicate typical rock glacier substrate. Protalus ramparts are classified by a coarse debris accumulation in front of a rock wall. A small depression occurs between the non-lobate bulge and the weathering rock wall. We followed the geomorphological mapping approach based on the baseline concepts (V 4.0) of the IPA Action Group “Rock glacier inventories and kinematics” (Delaloye et al., 2018; Delaloye and Echelard, 2020) and mapped the extended geomorphological footprint of the rock glaciers. Additional mapping criteria of rock glaciers in the field were visible creeping structures on the surface (ridges, furrows and lobes as those shown in Fig. 3.4a).

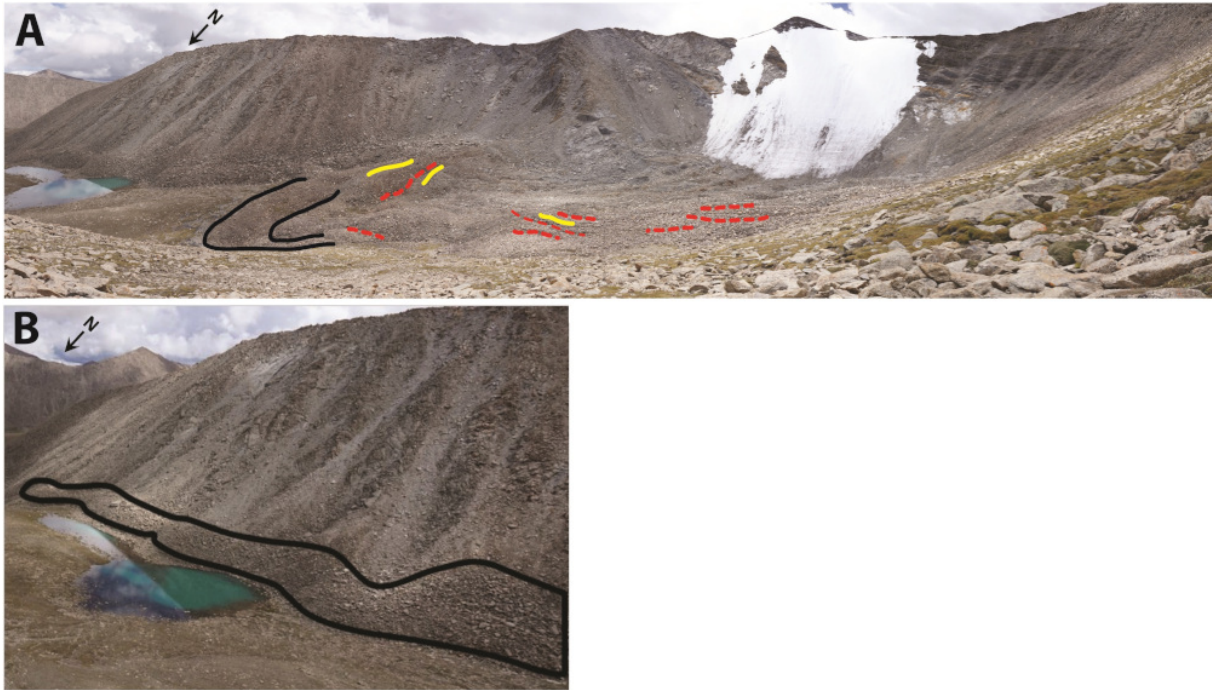


Figure 3.4: (A) Panorama view on a rock glacier (no. 1) with marked creeping structures (lobe in black, ridges in yellow and furrows in dashed red) in the Qugaqie basin in hanging valley 3. (B) Example of a protalus rampart in hanging valley 3 of the Qugaqie basin. A bulge (in black) formed through creeping of rockfall deposits. The length of the bulge is approximately 500 m. The location of the photos can be found in Fig. 3.6b. (photos: J. Buckel)

Protalus ramparts (Fig. 3.4b) were mapped as periglacial features or permafrost-related landforms as suggested by Scapozza (2015). A straight headwall for the sediment source is required, as the sediment originated by rockfalls and is accumulated at the foot of the rock wall. Infiltrating moisture originating from precipitation and snowmelt freezes the sediment deposit and creates a bulge parallel to the rock wall. These ice-permeated rockfall deposits creep downwards. Scapozza (2015) also noted the challenge to differentiate protalus ramparts from initial talus rock glaciers in the sense of Barsch (1996). Protalus ramparts mapped in the present study show no ridges, furrows or lobes at the surface, but the mapped rock glaciers do. It is pertinent to point out that our mapping procedure both in the field and during post-mapping consistently differentiates between rock glaciers and protalus ramparts based on the above-mentioned criteria. An incorrect determination as pronival ramparts can be minimized by the absence of longer existing snow fields due to arid climate conditions during the winter and the strong solar radiation and less cloud cover due to the extreme altitude (compare Hedding, 2016).

3.3.2 Ice detection by ERT

Electrical resistivity tomography (ERT) is a widely used method in geomorphology (Schrott and Sass, 2008). The application works especially well for subsurface ice detection due

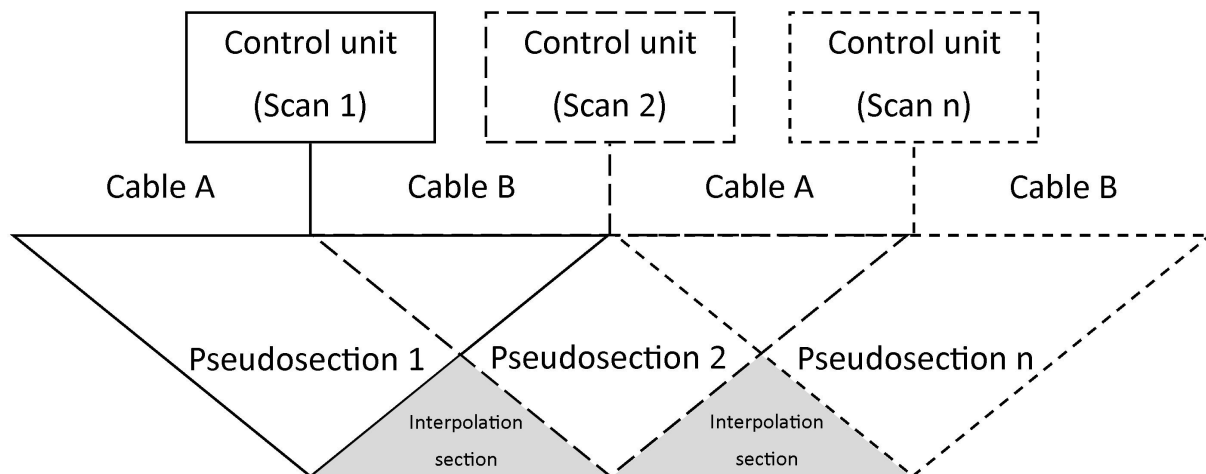


Figure 3.5: *Measurement setup for the roll-along procedure (adapted from El Sayed et al., 2017).*

to strong differences between frozen (high resistivity values) and unfrozen ground (low resistivity values) (Hauck and Vonder Mühll, 2003; Hauck and Kneisel, 2008). Since the end of the 1990s the method has been established for permafrost detection in solid rock (Krautblatter et al., 2010; Hartmeyer et al., 2012) and in debris-ice mixtures, like rock glaciers (Vonder Mühll et al., 2002; Kneisel et al., 2008; Rosset et al., 2013; Emmert and Kneisel, 2017; Mewes et al., 2017).

For the usual four-point measurement of the ground electrical resistivity, two electrodes feed current into the ground, which establishes an electric field in the subsurface. Another pair of electrodes is used to measure the voltage drop between two other locations on the surface. In order to obtain information on the two-dimensional distribution of electrical resistivity in the subsurface, a linear arrangement of the four electrodes is used to measure at different positions along the profile and with varying distances between the electrodes (Wenner array). The apparent resistivity (Ωm) of each measurement can be calculated from the injected current, the applied voltage and a factor, which takes the geometry of the arrangement into account. Subsequently, inverse modelling techniques are used to reconstruct the resistivity structure of the subsurface from the measured apparent resistivity data (Loke and Barker, 1995).

We performed ERT measurements during a field campaign in July 2018. We worked with multi-electrode (50) equipment “GeoTom-MK” (GEOLOG2000, Augsburg, Germany) and a maximum spacing of 2 m, allowing a maximum profile length of 98 m with a single measurement. To obtain longer sections, we used the roll-along procedure illustrated in Fig. 3.5. For this procedure, two cables were available (denoted A and B), each equipped with 25 channels. First, both are connected with the control unit to obtain pseudosection number 1 (Fig. 3.5). Next, cable B (and all connected electrodes) remains

at the same location, whereas cable A is moved to the right of cable B to measure pseudo-section number 2, and so on. The location of the ERT profiles was partly constrained by logistical conditions. Due to the high altitude, the crew had to stay at one level for 3 d to get adapted to altitude. The measurement locations were not accessible by vehicles, and a few hours were needed every day to reach the sites, resulting in limited productivity. Therefore, we tried to locate the profiles efficiently to obtain a representative data set of the valley. We covered different landform features (moraine, valley bottom, rock glacier) where permafrost conditions were assumed. Blocky surfaces constitute a challenge for ERT measurements due to instability and a lack of fine material necessary to provide sufficient contact for the electrodes. In cases where no soil material could be found that closed the gaps between the boulders, we inserted the end of each electrode into a sponge saturated with salt water to improve connectivity to the fine material. The saturated sponge kept the fine material wet and diminished desiccation through high solar radiation. The ERT data were processed with the Res2Dinv software (©Geotomo Software).

3.3.3 Creeping rates by InSAR analyses

InSAR time series analysis is an active microwave remote sensing technique, which can exploit the phase change of the backscattered microwaves to determine relative surface displacement on the order of millimetres to centimetres (Osmanoğlu et al., 2016). Both the amplitude and the phase of the microwave backscatters are used for InSAR. After precisely co-registering all acquisitions, it is possible to calculate the average phase change of each resolution cell over time, which contains a number of different signals, including whether a resolution cell moved closer to the receiver, i.e. the satellite, or further away from it. These images of phase change are called interferograms. The accuracy of the derived motion is dependent on a number of different factors, including the frequency of the emitted wave, the atmospheric delay, the accuracy of its modelling, the topographic data used to correct the images, the choice of reference points, the surface characteristics of the observed structure and the frequency of the data acquisitions (Hu et al., 2014).

The reliability of an interferogram is often described by its so-called coherence. Coherence is a measure of phase stability with a value near zero representing poor reliability and values near 1 representing high reliability (Crosetto et al., 2016). If the backscatter characteristics of the observed surface change too much between two acquisitions, e.g. due to snow cover, vegetation or events occurring between the acquisitions like rockfalls, the coherence is poor and no phase change can be determined reliably. Coherence also decreases with increasing displacement, and displacements larger than half the SAR wavelength (~ 2.8 cm for Sentinel-1) cannot be determined accurately. For this study we chose

a coherence threshold of 0.3 and discarded areas with coherence values below 0.3. This threshold is similar to the one chosen by Sowter et al. (2013) and provides good spatial data coverage while also excluding unreliable data. The issue of low coherence or decorrelation is exacerbated for interferograms with a long temporal baseline, i.e. a long time period between data acquisitions. No Sentinel-1 data are available for a period of 48 to 96 d during the summers of 2016 and 2017. These longer temporal baselines cause decorrelation during the summer months on some of the faster landforms. Freezing and thawing of the ground leads to reduced coherence values in autumn and spring. The coherence over periglacial landforms in the Qugaqie basin is relatively good, due to the lack of high vegetation on actively moving landforms and the relatively sparse snow cover in winter visible on optical Sentinel-2 acquisitions.

Exploiting the phase change with InSAR provides only relative surface motion towards the satellite or away from it. The line of sight (LOS) of the satellite is therefore very important, as motion with a very different direction compared to this LOS is severely underestimated (Hu et al., 2014). The severity of this underestimation depends on the angle between the LOS and the direction of the surface displacement. An angle close to 0° will cause only minor underestimation, while displacement with a direction near 90° to the LOS will be severely underestimated or even completely overlooked. The Sentinel-1 satellites follow a circumpolar orbit and observe the Earth obliquely with an incidence angle of $33\text{-}43^\circ$ (Yagüe-Martínez et al., 2016). Both ascending (satellite travelling south to north) and descending (satellite travelling north to south) acquisitions are therefore sensitive to vertical surface displacement and towards the east or west but very insensitive to displacement towards the north or south. We always select the geometry with the highest sensitivity towards the expected displacement direction to calculate our displacement and velocity results.

The surface displacement data presented in this study represent a spatial subset of a surface displacement model originally based on Reinosch et al. (2020). For our analysis of the Qugaqie basin, we processed 278 interferograms from 74 ascending acquisitions (June 2015 to December 2018) and 257 interferograms from 63 descending acquisitions (November 2015 to December 2018) (Table 3.1). The temporal baselines, i.e. the time period between two data acquisitions, of individual interferograms is mostly 12 to 36 d with a maximum of 72 and 96 d for ascending and descending orbits respectively. All data acquisitions originate from ESA’s Sentinel-1A/B satellite constellation. Both ascending and descending datasets were processed using small baseline subset (SBAS) time series analysis (Berardino et al., 2002), with a coherence threshold of 0.3. Mean velocities were calculated by dividing the cumulative displacement observed during the observation period by the length of the observation period (2015-2018).

Table 3.1: *Summary of ISBAS processing parameters.*

Geometry	Observation period	Acquisitions	Interferograms	Temporal baseline	Coherence threshold
Ascending	2015-06-05 to 2018-12-22	74	278	12 to 72 d	0.3
Descending	2015-11-15 to 2018-12-29	63	257	12 to 96 d	0.3

All surface velocity data of periglacial landforms have been projected along the direction of the steepest slope under the assumption that the motion of the described landforms is mainly gravity-driven by an ice-debris mixture. Hereafter we will refer to the mean surface velocity of periglacial landforms projected along the steepest slope as “creeping rates” to reflect this assumption. We calculate a sensitivity coefficient to compensate for the underestimation of the displacement signal caused by the disparity between the LOS and the assumed displacement direction. We followed an approach developed for the study of landslides (Notti et al., 2014), as the displacement of landslides is gravity-driven, which we also assume to be true for the periglacial landforms investigated in this study. Creeping rates presented in this study were not verified by independent measurements (GPS measurements, laser scans, optical remote sensing, etc.), as no such data sets exist for our study area. Reference points are located on bedrock whenever possible and on ridges or stable, vegetated moraines with good coherence if no coherent bedrock was available (compare Fig. 3.9a). Areas which are likely unmoving on a multiannual scale, such as the old moraines at the entrance of the Qugaqie basin, display LOS velocities of ± 2.4 mmyr^{-1} during our observation period. This does not provide information regarding the accuracy of the seasonal variations in our surface displacement results but it indicates that the multiannual LOS velocity results are reliable. We use this variation of ± 2.4 mmyr^{-1} over likely stable areas as the precision of the mean LOS velocity during our observation period. The precision of the creeping rates was determined by dividing the precision of the LOS velocity by the sensitivity coefficient. It therefore varies between 2.4 and 12.0 mmyr^{-1} for areas with a sensitivity coefficient of 1 and 0.2 (Reinosch et al., 2020).

3.4 Results and interpretation

3.4.1 The cryosphere of the Qugaqie basin

The geomorphological map in Fig. 3.6 shows features of the mesoscale cryosphere in the Qugaqie basin: glaciers, moraines, proctalus ramparts and rock glaciers. The moraine distribution suggests that former glaciers extended to the present shoreline of the Nam Co at their largest size during Marine Isotope Stage (MIS) 3 (Dong et al., 2014). Multiple smaller moraines are displayed in closer proximity to today's glaciers (Fig. 3.6). Glacial landforms like valley glaciers, cirque and wall glaciers increase in number and size towards the south due to a higher elevation and shorter distance to the main ridge (Fig. 3.6). Only the Genpu (1.56 km²) and the Zhadang (1.41 km²) glaciers are considered valley glaciers; most of the other glaciers are located in the head of the hanging valleys as cirque glaciers. The northward orientation of all glaciers is a result of the lee effect towards incoming moisture from the southern direction. The topographic barrier of the western Nyainqêntanglha Range detains precipitation and causes an asymmetric and uneven north-south distribution of glacier extents expressed by smaller extents in the northern catchments draining in the Nam Co like Qugaqie (compare Zhang et al., 2013a). The glacial zone with a cumulative glacier area of 4.07 km² (Bing maps, 2013) extends from 5500 m a.s.l. to the highest elevation (6086 m a.s.l.) with a mean elevation of 5770 m a.s.l.

The altitudinal (mean) landform distribution illustrates the statistical analyses and displays a typical high-mountain pattern (Fig. 3.7). Debris and talus cones can be found in lower altitudes. The periglacial landforms (i.e. proctalus ramparts and rock glaciers) are located between elevations of 5300 and 5600 m a.s.l., and the average number of periglacial landforms is situated around 5500 m a.s.l. We conclude from this altitudinal distribution a probable occurrence of permafrost higher than 5300 m a.s.l., which has to be supported by validating ice occurrence and the status of activity of these landforms.

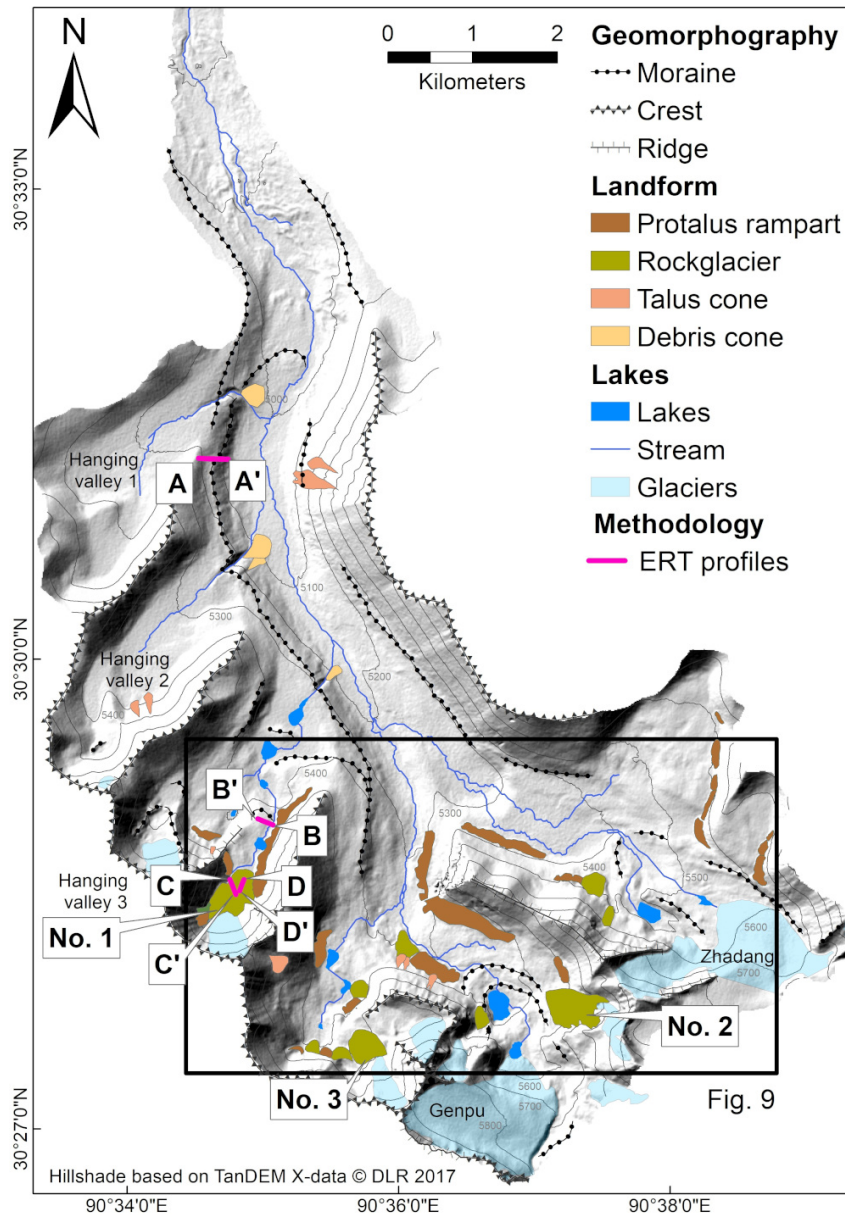


Figure 3.6: Geomorphological map of the Qugaqie basin. The locations of the ERT profiles are shown with purple lines. Periglacial landforms are greenish (rock glaciers and protalus ramparts). The black rectangle represents the boundary of the map shown in Fig. 3.9.

Table 3.2: Statistical description of cryotic landforms based on DEM analyses.

	No.	Cumulative area [m ²]	Area (mean)	Elevation (min, max)	Elevation (mean)
Protalus rampart	22	1018014	46273	5292, 5685	5530
Rock glacier	10	830185	83019	5363, 5789	5523
Glacier	11	4075580	370507	5504, 6086	5771

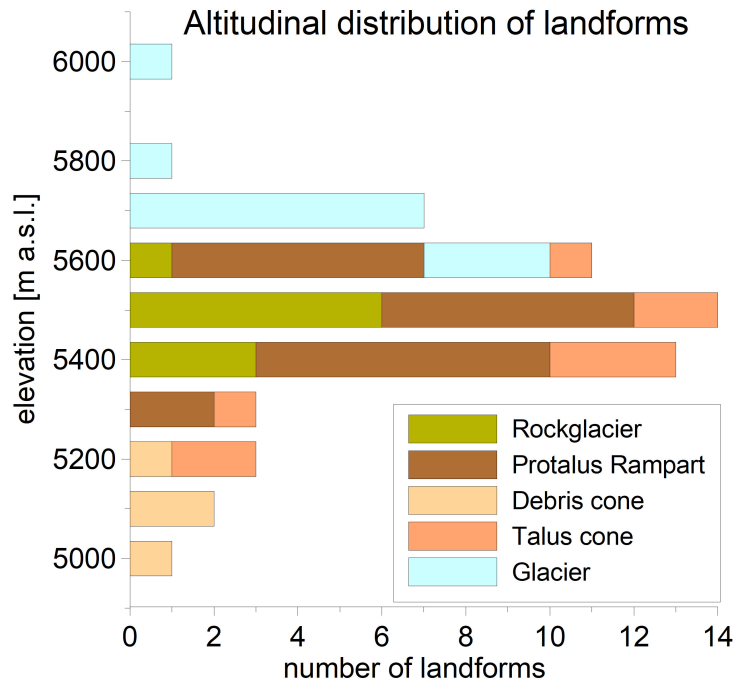


Figure 3.7: *Altitudinal (mean) landform distribution of the Qugaqie basin derived from the landform inventory.*

Most rock glaciers are located in cirques, and three are supplied by glacial meltwater resulting in greater extents compared to rock glaciers without a glacier in their catchment (Fig. 3.6, nos. 1, 2 and 3). Additionally, moraine deposits, talus slopes and protalus ramparts provide the sediment accumulation at the base required for the formation of a rock glacier besides water availability (Knight et al., 2019). The altitudinal distribution of the rock glaciers extends from 5363 to 5789 m a.s.l. with a mean elevation around 5500 m a.s.l. (Fig. 3.7, Table 3.2). Rock glacier surfaces display clear creep structures and rock-glacier-typical bulges, furrows and lobes (Fig. 3.4a). There is no pronounced lichen growth, and the uppermost material is extremely unstable. These field observations in combination with the observed creeping rates (Fig. 3.9b) allow the conclusion of an active status of the rock glaciers, which indicates ice occurrence and, thus, permafrost conditions (according to Barsch, 1996). The altitudinal distribution of protalus ramparts has a narrower range of min-max values, but they are located at a similar mean elevation. The mean area of the individual protalus ramparts is only half of the mean area of the individual rock glaciers, i.e., protalus ramparts are generally smaller than rock glaciers (Table 3.2, Fig. 3.6), but there are twice as many. Protalus ramparts are situated in front of rocky slopes and are characterized in contrast to rock glaciers by a shorter dimension downslope (Figs. 3.4 and 3.6). The mesoscale periglacial landforms (mean elevation) are situated between 5300 and 5600 m a.s.l. This altitudinal distribution serves as one component of the three methods for assessing the probable occurrence of permafrost in the catchment.

3.4.2 ERT-based ice detection

ERT is a common method to detect ground ice in the subsurface, inferring permafrost conditions (Lewkowicz et al., 2011), if ground ice is present for 2 consecutive years. With the help of ERT we were able to provide evidence for the existence of ground ice at specific test sites. Figure 3.6 displays the locations and indicates an altitudinal increase in the four ERT profiles (A to D). The measured resistivity values were compared with tables by Hauck and Kneisel (2008) and Mewes et al. (2017). These studies also address ice detection in high-altitude periglacial environments. Table 3.3 sums up our measured resistivity values and classifies the values in terms of material characteristics. Different studies show resistivity values of till in a range from 1 to 10 k Ω m(Reynolds, 2011), from 5 to 10 k Ω m(Thompson et al., 2017) and from 50 to 100 k Ω m(Vanhala et al., 2009). The diversity of resistivity ranges and the resulting non-uniqueness can be overcome by using additional methods to support the final conclusions.

Table 3.3: *Resistivity values for different materials derived by field measurement. The used terms of the interpreted material followed Hauck and Kneisel (2008) and Mewes et al. (2017).*

Material	Resistivity [k Ω m]
Sanstone (moist-dry)	0.5-5
Till	50-80
Unfrozen sediment (moist-dry)	1-20
Ice-poor permafrost (ice lenses, ice-interspersed till)	50-150
Ice-rich permafrost (massive ice body)	150-4000

Profile A (Fig. 3.8) ranges from 5090 to 5230 m and represents subsurface conditions in the lower altitudinal areas of the catchment, for example in a lateral moraine. At the surface the profile has a length of 348 m, but the length information in the following text refers to the x axis which corresponds to planar 2D view (the topographic effect is not displayed). From \sim 120 m on, we observe a slope-parallel, highly resistive layer (highlighted by the black line in Fig. 3.8a) with resistivity values ranging between 5 and 100 k Ω m and an average thickness of 10 m. We interpret this layer as compressed till without ice content, based on the resistivity range, the compressed glacial sediment accumulation and the absence of creeping structures indicating ice. According to Yu et al. (2019) the underlying bedrock consists of sandstone, which explains the low resistivity values below the resistive moraine deposits. Between 0 and 20 m along the profile, the electrodes were directly attached to the outcropping, weathered sandstone. The resistivity values around

5 kΩm correspond to dry sandstone bedrock, which is exposed to strong solar radiation. The hydraulically impermeable till cover is not present between 20 and 120 m, and moisture infiltrates as slope water saturating the sandstone bedrock underneath the moraine and decreasing electrical resistivity.

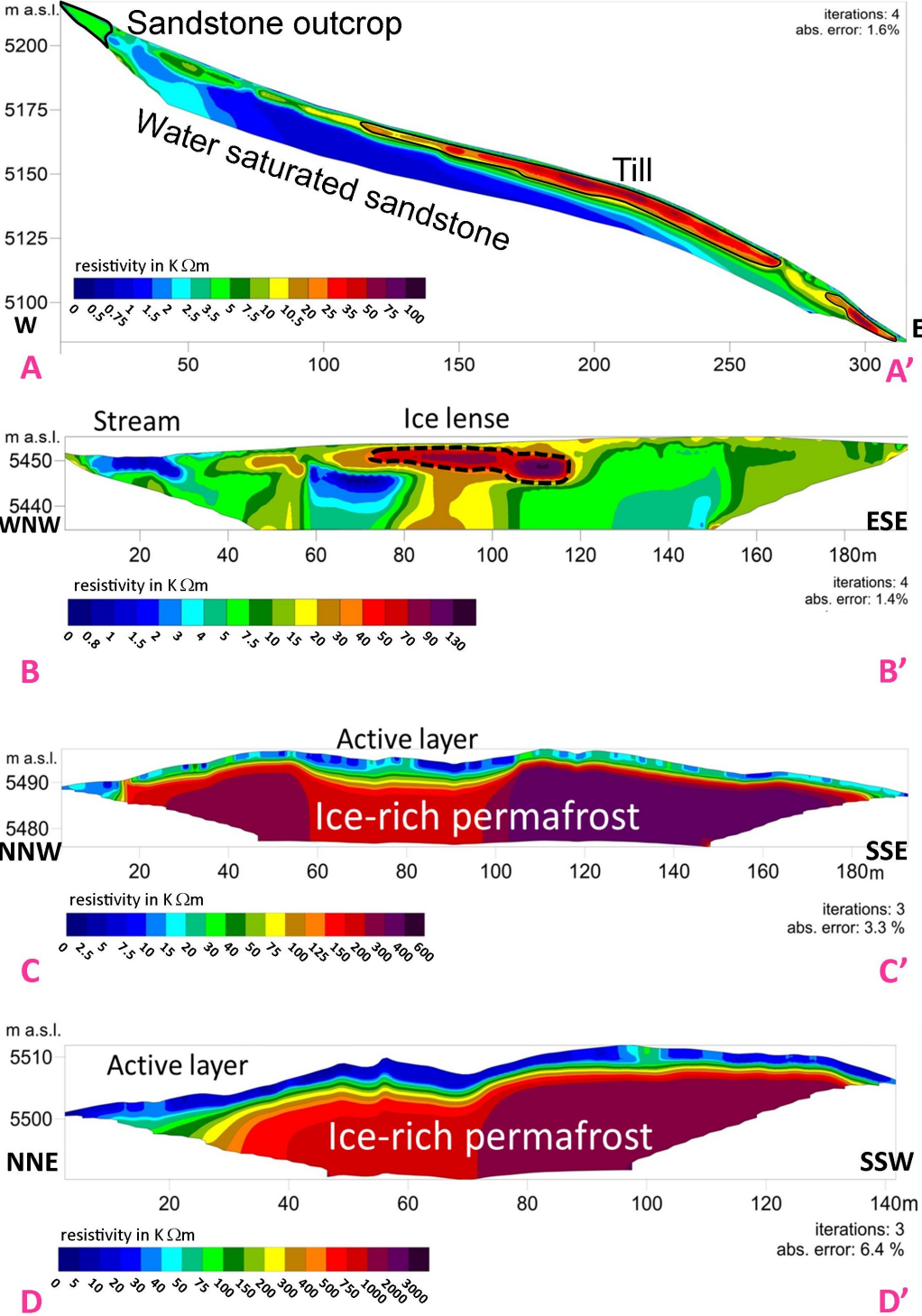


Figure 3.8: Electrical resistivity sections along the four ERT profiles recorded in July 2018 with a standard spacing of 2 m. Profiles C and D are located on rock glacier no. 1. Note the increasing elevation between profiles A and D.

Profile B (Fig. 3.8b) is located in hanging valley 3 on top of an old, terminal moraine crossing the stream, which drains the hanging valley (Fig. 3.6). Surrounding dead ice holes indicate former subsurface ice occurrence behind the former moraine terminus. Complete vegetation cover of *compresia pygmaea* interspersed with individual rockstones suggests an old and stable surface. From the high resistivity anomalies of up to 150 k Ω m, we conclude that ice-poor permafrost in contrast to ice-rich permafrost in profiles C and D is present as an ice lens at 5450 m a.s.l.

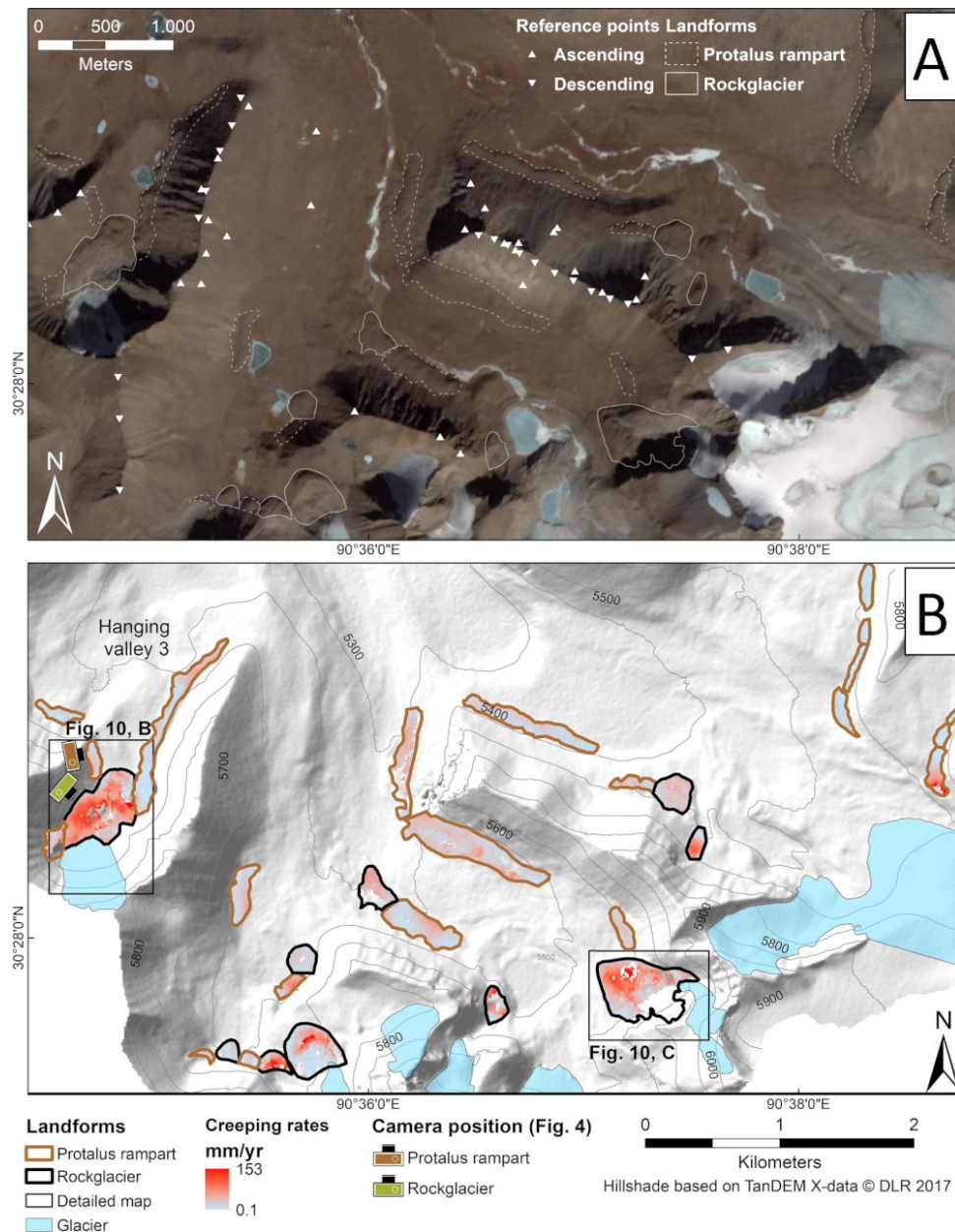


Figure 3.9: (A) Sentinel-2 satellite image, recorded 30 January 2018. Triangles indicate stable reference points. Dashed lines indicate the outlines of the periglacial landforms. (B) Creeping rates from periglacial landforms move in the slope direction over the observation period 2015-2018. The black rectangles mark the location of the two fastest rock glaciers in Fig. 3.10. The camera positions correspond to the photographs in Fig. 3.4.

Profiles C and D (possibly the highest-elevated ERT measurements worldwide) show the typical two-layer structure of rock glacier no. 1 with equally high resistivity values (Fig. 3.8c, d). The first layer is characterized by lower resistivity values (1-20 k Ω m), indicating the unfrozen active layer during the summer months. The active layer thickness varies between 2 and 5 m. The second layer shows high resistivity values of up to 3500 k Ω m and covers the complete section from below the active layer to the maximum depth of investigation. No internal heterogeneities are visible due to the lack of current flow within this highly resistive unit, which we interpret as a mixture of ice and sediment. According to Table 3.3, we interpret the second layer to be ice-rich permafrost. Similar resistivity values of ice-rich rock glacier material, reaching maximum values of 1000 k Ω m, have been reported in several studies from Haeberli and Vonder Mühll (1996), Vanhala et al. (2009), and Mewes et al. (2017). Profiles C and D confirm the presence of subsurface ice at an elevation around 5500 m a.s.l., which we use as evidence for the lower occurrence of probable permafrost.

The relatively large altitudinal steps between our four ERT profiles do not allow exclusion of the occurrence of subsurface ice in other, lower parts of the valley. Therefore, we use the following perennial creeping rates to exclude this case. The detection of subsurface ice is the second component of the three methods for estimating the probable occurrence of permafrost. Inferred by ERT data, subsurface ice can be expected at selected locations from an altitude of 5450 m and higher.

3.4.3 Creeping rates of periglacial landforms

The creeping rates for rock glaciers and protalus ramparts, including statistical information, are shown in Table 3.4. The fastest moving areas of landforms display lower coherence values and small spatial data gaps. The low coherence values in those areas are likely connected to the long temporal baselines of interferograms in summer of 2016 of up to 72 and 96 d for ascending and descending data respectively. Long temporal baselines on relatively fast moving landforms may lead to aliasing effects if the displacement exceeds a quarter of the wavelength of the satellite (Crosetto et al., 2016). This would correspond to a LOS displacement of ~ 14 mm for Sentinel-1, which emits a wavelength of 56 mm. A total of 14 mm in 72 d or 96 d corresponds to a LOS velocity of approximately 71 mmyr^{-1} for ascending and 53 mmyr^{-1} for descending data. Displacement values in areas with higher LOS velocities than these thresholds are likely to be underestimated with the InSAR technique and display poor coherence values near or below the coherence threshold of 0.3. Coherence values do not drop significantly in winter, which is likely due to the semiarid climate and therefore relatively thin snow cover.

Table 3.4: *Statistical description of cryotic landforms based on DEM analyses.*

Land-form	Creeping rate [mmyr ⁻¹]	Summer accel- eration [%]	Creeping rate precision [mmyr ⁻¹]	Coher- ence	Interpolated time period [%]	Data points
Protalus rampart	11.0 (6.8 to 16.7)	-2 (-36 to 36)	5.2 (3.9 to 7.8)	0.74 (0.70 to 0.80)	2.5 (0.7 to 6.2)	7984
Rock glaciers	21.1 (11.6 to 36.8)	-23 (-46 to 3)	5.1 (4.2 to 8.1)	0.66 (0.59 to 0.73)	7.9 (3.8 to 13.0)	5402

Protalus ramparts in the Qugaqie basin display lower average surface velocities than rock glaciers. The creeping rate of protalus ramparts (11.0 mmyr⁻¹ with an uncertainty from 6.8 to 16.7) is lower and shows more pronounced seasonal variations than on rock glaciers (21.1 mmyr⁻¹ with an uncertainty from 11.6 to 36.8). Rock glacier no. 1 of hanging valley 3, which we also studied with ERT measurement, displays creeping rates of up to 70 mmyr⁻¹ in most areas, with the fastest moving part reaching 153 mmyr⁻¹ (Fig. 3.10b), similar to rock glacier no. 2 (Fig. 3.10c). A time series of creeping rates of rock glacier no. 1 is shown in Fig. 3.10a (black line) and of rock glacier no. 2 in Fig. 3.10a (grey line). The spatial distribution of the creeping rates is relatively uniform in areas with good InSAR sensitivity, i.e. slopes with an east or west aspect, but displays significantly higher noise level in areas with poor InSAR sensitivity, i.e. slopes with a north or south aspect. We do not observe a clear correlation between variations in creeping rates and possible seasonal forcing mechanisms such as temperature or precipitation. Neither protalus ramparts nor rock glaciers display clear acceleration of creeping in summer compared to winter (Fig. 3.10a).

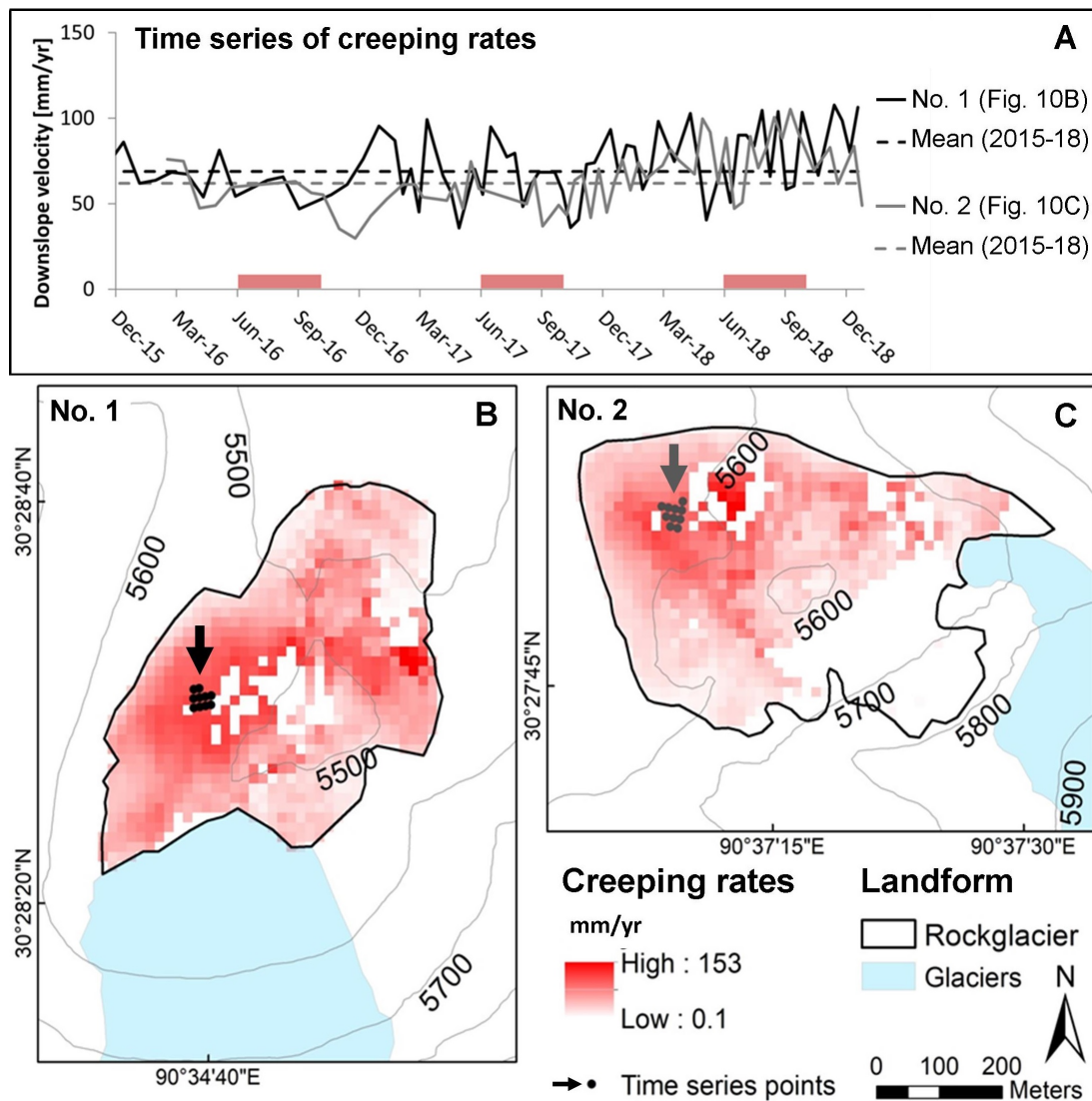


Figure 3.10: (A) Summer months with air temperatures $>0^{\circ}\text{C}$ Zhang et al. (according to 2013b) are shown in red. Time series represent the moving average of the 10 nearest values in time based on the median of time series points, located in (B) (black dots) and (C) (grey dots). The black time series (rock glacier no. 1 in b) is based on ascending data and the grey time series (rock glacier no. 2 in c) on descending data.

The third component for assessing the occurrence of permafrost is based on the movement rates of periglacial landforms. Based on the assumption that a measurable movement rate is determined by perennial ice in the subsurface, the observed active status of the periglacial landforms allows the conclusion of permafrost occurrence in the corresponding landform.

3.4.4 Assessment of the lower permafrost limit of the Qugaqie valley

The assessment of the lower permafrost limit consists of an integration of different results. The field-based mapping of periglacial landforms indicates the first precondition to find permafrost conditions. Field observations like furrows, ridges, coarse substrate and lichen coverage on the rock glaciers' surface corroborate the mapped landforms' classification and indicate activity of the landform. By integrating the ERT results of detected subsurface ice occurrence, a further component of the permafrost condition (subsurface below 0°) is validated. Completing the permafrost definition (of 2 or more consecutive years) the derived creeping rates by InSAR show a constant motion of more than 2 years, which is attributed to the deformation of the debris ice matrix of the periglacial landforms. So, the active status, the altitudinal distribution of the periglacial landforms and validated ice occurrence by ERT suggest a lower limit of probable permafrost between 5300-5450 m a.s.l. This range includes ice lenses detected by ERT data as well as all creeping landforms, indicating an active status and therefore an existence of ice.

3.5 Discussion

One critical issue for the estimation of the lower occurrence of probable permafrost by the used approach is the focus on periglacial landforms. These landforms are characterized by blocky material and a special thermal regime that lowers the internal temperature in comparison to the thermal regime outside of the blocky, rough surface (Gorbunov et al., 2004). This cooling effect of high-porosity, unconsolidated debris is especially observed in lower mountain regions by near-surface ground temperature measurements on rock glaciers (Onaca et al., 2020) and suggests a lowering of discontinuous and sporadic permafrost occurrence (Lambiel and Pieracci, 2008; Otto et al., 2012). By using the ERT method we found ice-poor permafrost in ice lenses in mineral soils next to the rock glacier that corroborates the idea of permafrost conditions outside of blocky material at an elevation of 5450 m a.s.l. The extreme cold mean annual air temperature of -6.8 °C at 5680 m a.s.l. (Zhang et al., 2013b) should minimize the effect of different regolith properties that favours permafrost conditions.

The next critical issue for the estimation of the lower occurrence of probable permafrost is the question of whether the huge resistivities observed on profile A (Fig. 3.8a, black lines) indicate ice or not. In general, subsurface material determination without additional cross-validating techniques by other geophysical methods or borehole data remains uncertain (Hauck and Kneisel, 2008; Guglielmin et al., 2018). Therefore, the geomorphological

knowledge of the study area is essential for an interpretation of the subsurface: in this case, the measured resistivity values of profile A (Fig. 3.8) of up to 100 k Ω m are consistent with both till and ice-poor permafrost (Schrott and Sass, 2008). From the resistivity values it is therefore not possible to determine whether the till contains ice or not. However, field observations allow the conclusion that no ice was measured because clear creep structures would have to be recognizable due to a significant slope. Furthermore, InSAR analysis of this location shows no clear perennial creep behaviour (Reinosch et al., 2020), making the presence of subsurface ice unlikely. In order to uniquely identify ice, it would have been desirable to apply additional geophysical methods, like ground-penetrating radar, refraction seismic tomography or capacitively coupled resistivity (Mudler et al., 2019). In particular, the combination of electrical and seismic methods allows the derivation of a petrophysical four-phase model (Hauck and Kneisel, 2008; Mewes et al., 2017) and the estimation of the sediment-to-ice ratios from electrical resistivity and seismic velocities. However, due to the extremely difficult logistical constraints in this remote location, these methods could not be applied, and we thus rely on combining evidence from field observations with geophysical results.

The approach by Kneisel and Kääb (2007) uses a similar combination of methods as used in this study to describe periglacial morphodynamics of a glacier forefield including a rock glacier. ERT profiles show the same range of layer thickness of 2-5 m as in our profiles in the summer months. They recommend the joint application of geoelectrical and surface-movement data to investigate periglacial landforms and to assess the permafrost distribution, because the combination of both tools allows a more comprehensive characterization of permafrost characteristics like ice-rich or ice-poor. Also, in our case, we believe the ground-based geophysical surveys are useful, as predicting subsurface ice content and deriving permafrost distribution maps only by modelling and/or using remote sensing includes various sources of error.

1. Low resolution (1 km gridded) of the permafrost-distribution models over the entire TP (Zou et al., 2017, Fig. 3.1c) prevents detailed analyses of permafrost occurrence at a mesoscale, especially in high-mountain relief.
2. Surface displacement patterns originate from different surface processes and take place in different time intervals, such as freeze-thaw cycles, seasonal creeping or constant, multiannual creep (Reinosch et al., 2020).
3. Remote sensing approaches can only guess the geomorphological process behind the surface displacement. Surrounding landscape features, underlying material and sediment source areas are essential factors that need to be considered during the interpretation of remote sensing imagery.

4. Without ground-based validation (e.g. ERT data) large-scaled permafrost distribution maps cannot accurately be used to predict permafrost occurrence in the remote, high-mountain areas.

Geomorphological field evidence allows a small-scaled interpretation and, in combination with remote sensing data, an extrapolation to larger scales. The periglacial landforms in this study show lower creeping rates than similar landforms of other regions. Other studies employing InSAR techniques observe creeping rates from centimetres to several metres per year for rock glaciers in the western Swiss Alps (Strozzi et al., 2020), in western Greenland (Strozzi et al., 2020) and in the Argentinian Andes (Villarroel et al., 2018; Strozzi et al., 2020). Furthermore, all of them clearly indicate seasonal variations in the rock glacier movement, with faster rates in summer and reduced creeping rates in winter months (Cicoira et al., 2019; Delaloye et al., 2008, 2010). In our study area neither rock glaciers nor protalus ramparts display significantly accelerated creep in summer (Fig. 3.10a). The lack of seasonality and the lower creeping rates compared to rock glaciers in the Alps (Cicoira et al., 2019; Kenner et al., 2017; Wirz et al., 2016) and the semiarid Andes (Strozzi et al., 2020) might be related to the semiarid climate conditions (lack of moisture) and the short time span of 3 months with positive air temperatures in the Qugaqie basin (Zhang et al., 2013b). Strozzi et al. (2020) figured out that their highest rock glacier “Dos Lenguas” (4300 m a.s.l.) in the Andes is characterized by “less amplitude variations of the annual cycle than observed for the Swiss Alps”. Hence, we hypothesize that the seasonality of rock glacier creeping behaviour is less pronounced the lower the mean annual air temperatures and the shorter the time spans of positive air temperature are. It seems that the magnitude of seasonal variations in the creeping rates also decreases with a lower availability of moisture, because the strongest seasonality is observed in moist regions such as the Alps. Additionally, catchments in the Qugaqie basin are quite small for sediment release, so the extent of our rock glaciers is limited by a small debris input. Probably for similar reasons, protalus ramparts investigated in this study creep with a median velocity of 11 mmyr^{-1} , while comparable creeping rates for protalus ramparts range from 40 up to 100 cmyr^{-1} in the Swiss Alps (e.g., Scapozza, 2015).

The optical image-based process of rock glacier mapping and outlining is subject to several uncertainties, like the quality of optical imagery and the rather subjective mapping style (Brardinoni et al., 2019). However, rock glacier inventories become increasingly important due to their function as indicators of stored water resources (Azócar and Brenning, 2010; Jones et al., 2018a,b) and their response to climate (Cicoira et al., 2019; Humlum, 1998). An IPA working group was installed to reduce the uncertainties of such inventories and to standardize mapping procedures (Delaloye et al., 2018). This year (2020) standardized guidelines were published on <https://www3.unifr.ch/geo/geomorphology/en/research/ipa-action-group-rock-glacier/> (last access: 4 November 2020), which we followed in our

mapping procedure (Delaloye and Echelard, 2020). Additionally with the opportunity to perform a field-based mapping, a decrease in these uncertainties is likely.

Using rock glaciers and their long-term ice content as indicators for permafrost occurrence must be critically evaluated because rock glaciers can overcome long distances and the terminus is far away from the routing zone (Bolch and Gorbunov, 2014). In this case rock glaciers are not suited for permafrost distribution assessment, because the ice-debris mass creeps out of the continuous permafrost zone, as the rock glacier distribution in combination with modelled permafrost occurrence demonstrate in the northern Tien Shan (Bolch and Gorbunov, 2014). In our study, periglacial landforms are characterized by a small extent and a low altitudinal range in extreme elevation. The rock glacier terminus is close to the rooting zone, and they do not span a significant elevation range. Temperature data (MAAT of -6.8°), elevated at Zhadang glacier (Zhang et al., 2013b), and different, large-scaled permafrost distribution maps (Zou et al., 2017; Obu et al., 2019) suggest a high permafrost probability at elevations greater than 5400 m a.s.l. in the study area. Nevertheless a detailed, small-scaled model of permafrost distribution would help to make a prognosis of permafrost occurrence by localizing probabilities, especially in lower areas of the catchment. “Permakart” considers topographic parameters and different slope characteristics by using a topo-climatic key to handle the heterogeneity of high-mountain areas (Schrott et al., 2012).

3.6 Conclusion and future work

In spite of the adverse logistical conditions in the study area, we were able to give insights into the cryosphere and to assess a lower permafrost occurrence in the Qugaqie basin on the TP using a multi-method approach. Thus, we add an important piece of information to the literature in a region where, due to its high altitude, ground truth data are usually difficult to obtain. Geomorphological mapping identifies the altitudinal distribution of periglacial landforms. ERT measurements validate ice occurrence of one periglacial landform, a rock glacier. The activity of the periglacial landforms is derived from surface displacement analysis of high-resolution InSAR data over 3 years. By combining the three findings we assess the lower occurrence of probable permafrost. The main outcomes are summarized as follows.

1. The altitudinal distribution of periglacial landforms ranges between 5300 and 5600 m a.s.l. and averages around 5500 m a.s.l. Protalus ramparts are more frequent, while rock glaciers have a larger extent and creep faster.
2. ERT measurements outside of blocky material of the periglacial landforms indicate ice-poor permafrost such as ice lenses (70-150 k Ω m) at 5450 m a.s.l.
3. ERT measurements on a rock glacier confirm perennial ice occurrence around 5500 m a.s.l. Resistivity values of more than 200 k Ω m indicate ice-rich permafrost.
4. Surface displacement analysis extrapolates the status of active creeping to other permafrost-related landforms. In particular rock glaciers show creeping rates up to a maximum of 150 mmyr⁻¹ (median 21 mmyr⁻¹). Protalus ramparts have much lower surface creeping rates (median 11 mmyr⁻¹).
5. Seasonality of rock glacier creep is lacking, probably due to low average temperatures and semiarid climate conditions.
6. The lower limit of probable occurrence of permafrost is higher than 5300-5450 m a.s.l.

Our results illustrate the benefit of combining field-based and remote sensing techniques and recommend interdisciplinary approaches to geomorphological and geocryological issues. Nevertheless, the current results should be compared with a permafrost model of the study area in order to make a prognosis and zonation of the permafrost distribution. We also follow the suggestion by Strozzi et al. (2020) to include rock glaciers and the monitoring of rock glacier velocities as an essential climate variable in the Global Climate Observing System (GCOS) of the World Meteorological Organization due to the essential contribution of the results as climate-sensitive parameters. As a next step, we plan to provide a rock glacier inventory for the western Nyainqêntanglha Range based on InSAR data as a status quo to understand the sensitivity and the vulnerability of the high-mountain cryosphere in reference to climate warming.

Data availability

The data sets can be obtained on request to the authors.

Author Contribution

JB designed the study, conducted fieldwork, processed and interpreted geomorphological and geophysical data, wrote the manuscript, and conceptualized figures. ER was in charge of InSAR analyses. AH participated in fieldwork, helped with the ERT data processing and revised the manuscript carefully several times. BR conducted field logistics and data acquisition. MG and BR participated in the interpretation of the remote sensing data. FZ provided substantial logistical support and contributed to the discussions on the data interpretation. AS, FZ and RM actively participated in the data interpretation and worked out the scientific concept underlying the research proposal leading to this work. All authors contributed to the revision of the text.

Competing interests

The authors declare that they have no conflict of interests.

Acknowledgements

We thank all colleagues who contributed to this study, especially Bernd Wünnemann for fruitful discussions and valuable comments during fieldwork, Jussi Baade for providing the TanDEM-X data (©DLR), Zhengliang Yu for support in the field, and Guoshuai Zhang and his team for logistical support at the Nam Co Station for Multisphere Observation and Research, Chinese Academy of Sciences. We thank Matthias Bücker and Felix Nieberding for the insightful and highly valuable suggestions during this manuscript's preparation and revision phase. We thank the editor Tobias Bolch and two anonymous reviewers for their comprehensive work on comments and suggestions to improve the manuscript. This research is a contribution to the International Research Training Group (GRK 2309/1) "Geo-ecosystems in transition on the Tibetan Plateau (TransTiP)" funded by the Deutsche Forschungsgemeinschaft (DFG).

Financial support

This research has been supported by the Deutsche Forschungsgemeinschaft (DFG) (grant no. GRK 2309/1). This open-access publication was funded by Technische Universität Braunschweig.

Review statement

This paper was edited by Tobias Bolch and reviewed by two anonymous referees.

Bibliography

- Angillieri, M. Y. E. (2017). Permafrost distribution map of San Juan Dry Andes (Argentina) based on rock glacier sites. *Journal of South American Earth Sciences*, 73:42–49.
- Azócar, G. and Brenning, A. (2010). Hydrological and geomorphological significance of rock glaciers in the dry Andes, Chile (27–33 S). *Permafrost and Periglacial Processes*, 21(1):42–53.
- Ballantyne, C. K. (2018). *Periglacial geomorphology*. John Wiley & Sons.
- Barsch, D. (1996). *Rockglaciers: indicators for the present and former geocology in high mountain environments*, volume 16. Springer Science & Business Media.
- Berardino, P., Fornaro, G., Lanari, R., and Sansosti, E. (2002). A new algorithm for surface deformation monitoring based on small baseline differential SAR interferograms. *IEEE Transactions on geoscience and remote sensing*, 40(11):2375–2383.
- Bibi, S., Wang, L., Li, X., Zhou, J., Chen, D., and Yao, T. (2018). Climatic and associated cryospheric, biospheric, and hydrological changes on the Tibetan Plateau: a review. *International Journal of Climatology*, 38:e1–e17.
- Bolch, T. and Gorbunov, A. P. (2014). Characteristics and origin of rock glaciers in northern Tien Shan (Kazakhstan/Kyrgyzstan). *Permafrost and Periglacial Processes*, 25(4):320–332.
- Bolch, T., Marchenko, S., Braun, L. N., Hagg, W., Severskiy, I. V., and Young, G. (2009). Significance of glaciers, rockglaciers and ice-rich permafrost in the Northern Tien Shan as water towers under climate change conditions. *IHP/HWRP-Berichte*, (8):132–144.
- Bolch, T., Rohrbach, N., Kutuzov, S., Robson, B., and Osmonov, A. (2019). Occurrence, evolution and ice content of ice-debris complexes in the Ak-Shiirak, Central Tien Shan revealed by geophysical and remotely-sensed investigations. *Earth Surface Processes and Landforms*, 44(1):129–143.

- Brardinoni, F., Scotti, R., Sailer, R., and Mair, V. (2019). Evaluating sources of uncertainty and variability in rock glacier inventories. *Earth Surface Processes and Landforms*, 44(12):2450–2466.
- Cao, B., Zhang, T., Wu, Q., Sheng, Y., Zhao, L., and Zou, D. (2019). Brief communication: Evaluation and inter-comparisons of Qinghai–Tibet Plateau permafrost maps based on a new inventory of field evidence. *Cryosphere*, 13(2).
- Chen, J., Zhao, L., Sheng, Y., Li, J., Wu, X.-d., Du, E.-j., Liu, G.-y., and Pang, Q.-q. (2016). Some characteristics of permafrost and its distribution in the Gaize area on the Qinghai–Tibet Plateau, China. *Arctic, Antarctic, and Alpine Research*, 48(2):395–409.
- Cheng, G. and Wu, T. (2007). Responses of permafrost to climate change and their environmental significance, Qinghai-Tibet Plateau. *Journal of Geophysical Research: Earth Surface*, 112(F2).
- Cicoira, A., Beutel, J., Faillettaz, J., and Vieli, A. (2019). Water controls the seasonal rhythm of rock glacier flow. *Earth and Planetary Science Letters*, 528:115844.
- Cogley, G., Gardner, A., Cogley, G., Earl, L., and Raup, B. (2015). Glims glacier database. *National Snow and Ice Data Center: Boulder, CO, USA*.
- Crosetto, M., Monserrat, O., Cuevas-González, M., Devanthéry, N., and Crippa, B. (2016). Persistent scatterer interferometry: A review. *ISPRS Journal of Photogrammetry and Remote Sensing*, 115:78–89.
- Delaloye, R., Barboux, C., Bodin, X., Brenning, A., Hartl, L., Hu, Y., Ikeda, A., Kaufmann, V., Kellerer-Pirklbauer, A., Lambiel, C., et al. (2018). Rock glacier inventories and kinematics: A new IPA Action Group. In *Proceedings of the 5th European Conference on Permafrost (EUCOP5-2018), Chamonix, France*, volume 23.
- Delaloye, R. and Echelard, T. (2020). Towards standard guidelines for inventorying rockglaciers – Baseline concepts (Version 4.1). <https://www3.unifr.ch/geo/geomorphology/en/research/ipa-action-group-rock-glacier/>. [Accessed November 13, 2020].
- Delaloye, R., Lambiel, C., and Gärtner-Roer, I. (2010). Overview of rock glacier kinematics research in the Swiss Alps. *Geographica Helvetica*, 65(2):135–145.
- Delaloye, R., Perruchoud, E., Avian, M., Kaufmann, V., Bodin, X., Hausmann, H., Ikeda, A., Kääh, A., Kellerer-Pirklbauer, A., Krainer, K., et al. (2008). Recent interannual variations of rock glacier creep in the European Alps.

- Deline, P., Gruber, S., Delaloye, R., Fischer, L., Geertsema, M., Giardino, M., Hasler, A., Kirkbride, M., Krautblatter, M., Magnin, F., et al. (2015). Ice loss and slope stability in high-mountain regions. In *Snow and Ice-related hazards, risks and disasters*, pages 521–561. Elsevier.
- Dong, G., Yi, C., and Caffee, M. (2014). ^{10}Be dating of boulders on moraines from the last glacial period in the Nyainqentanglha mountains, Tibet. *Science China Earth Sciences*, 57(2):221–231.
- Dusik, J.-M., Leopold, M., Heckmann, T., Haas, F., Hilger, L., Morche, D., Neugirg, F., and Becht, M. (2015). Influence of glacier advance on the development of the multipart Riffeltal rock glacier, Central Austrian Alps. *Earth Surface Processes and Landforms*, 40(7):965–980.
- Eckerstorfer, M., Eriksen, H. Ø., Rouyet, L., Christiansen, H. H., Lauknes, T. R., and Blikra, L. H. (2018). Comparison of geomorphological field mapping and 2D-InSAR mapping of periglacial landscape activity at Nordnesfjellet, northern Norway. *Earth Surface Processes and Landforms*, 43(10):2147–2156.
- El Sayed, A. N., Barseem, M. S., El Deen, H. M. E., and El Din, H. A. E. (2017). Using of Geo-electrical and Geochemical Techniques to Investigate the Change in Ground Water Quality-South West El Khatbah City-Cairo-Alexandria Desert Road, Egypt. *Advances in Applied Science Research*, 8(4):77–95.
- Emmert, A. and Kneisel, C. (2017). Internal structure of two alpine rock glaciers investigated by quasi-3-D electrical resistivity imaging. *The Cryosphere*, 11(2):841.
- Fort, F. and van Vliet-Lanoe, B. (2007). Permafrost and periglacial environment of Western Tibet. *Landform Analysis*, 5:25–29.
- Frauenfelder, R., Allgöwer, B., Haerberli, W., and Hoelzle, M. (1998). Permafrost investigations with GIS—a case study in the Fletschhorn area, Wallis, Swiss Alps. In *Proceedings of the 7th International Conference on Permafrost, Yellowknife, Canada, Collection Nordicana*, volume 57, pages 291–295.
- French, H. (2012). Periglacial Landform. <https://www.thecanadianencyclopedia.ca/en/article/periglacial-landform>. [Accessed November 18, 2020].
- French, H. M. (2017). *The periglacial environment*. John Wiley & Sons.
- Gorbunov, A. P., Marchenko, S. S., and Seversky, E. V. (2004). The thermal environment of blocky materials in the mountains of Central Asia. *Permafrost and Periglacial Processes*, 15(1):95–98.

- Gruber, S., Fleiner, R., Guegan, E., Panday, P., Schmid, M.-O., Stumm, D., Wester, P., Zhang, Y., and Zhao, L. (2017). Inferring permafrost and permafrost thaw in the mountains of the Hindu Kush Himalaya region.
- Guglielmin, M., Ponti, S., and Forte, E. (2018). The origins of Antarctic rock glaciers: periglacial or glacial features? *Earth Surface Processes and Landforms*, 43(7):1390–1402.
- Guo, W., Liu, S., Xu, J., Wu, L., Shangguan, D., Yao, X., Wei, J., Bao, W., Yu, P., Liu, Q., et al. (2015). The second Chinese glacier inventory: data, methods and results. *Journal of Glaciology*, 61(226):357–372.
- Haerberli, W., Hallet, B., Arenson, L., Elconin, R., Humlum, O., Käab, A., Kaufmann, V., Ladanyi, B., Matsuoka, N., Springman, S., et al. (2006). Permafrost creep and rock glacier dynamics. *Permafrost and periglacial processes*, 17(3):189–214.
- Haerberli, W. and Vonder Mühl, D. (1996). On the characteristics and possible origins of ice in rock glacier permafrost. *Zeitschrift für Geomorphologie. Supplementband*, (104):43–57.
- Hartmeyer, I., Keuschnig, M., and Schrott, L. (2012). A scale-oriented approach for the long-term monitoring of ground thermal conditions in permafrost-affected rock faces, Kitzsteinhorn, Hohe Tauern Range, Austria. *Austrian Journal of Earth Sciences*, 105(2).
- Hauck, C. and Kneisel, C. (2008). *Applied geophysics in periglacial environments*. Cambridge University Press.
- Hauck, C. and Vonder Mühl, D. (2003). Evaluation of geophysical techniques for application in mountain permafrost studies. *Zeitschrift für Geomorphologie, NF Suppl., Bd*, 132:161–190.
- Hedding, D. W. (2016). Pronival ramparts: A review. *Progress in Physical Geography*, 40(6):835–855.
- Hock, R., Rasul, G., Adler, C., Cáceres, B., Gruber, S., Hirabayashi, Y., Jackson, M., Käab, A., Kang, S., Kutuzov, S., et al. (2019). High mountain areas.
- Höllermann, P. (1983). *Blockgletscher als Mesformen der Periglazialstufe: Studien aus europäischen und nordamerikanischen Hochgebirgen*. Dümmler.
- Hu, G., Zhao, L., Li, R., Wu, X., Wu, T., Xie, C., Zhu, X., and Hao, J. (2020). Estimation of ground temperatures in permafrost regions of the Qinghai-Tibetan Plateau from climatic variables. *Theoretical and Applied Climatology*, pages 1–11.

- Hu, J., Li, Z.-W., Li, J., Zhang, L., Ding, X.-L., Zhu, J.-J., and Sun, Q. (2014). 3-D movement mapping of the alpine glacier in Qinghai-Tibetan Plateau by integrating D-InSAR, MAI and Offset-Tracking: Case study of the Dongkemadi Glacier. *Global and Planetary Change*, 118:62–68.
- Humlum, O. (1998). The climatic significance of rock glaciers. *Permafrost and periglacial processes*, 9(4):375–395.
- Immerzeel, W. W., Lutz, A., Andrade, M., Bahl, A., Biemans, H., Bolch, T., Hyde, S., Brumby, S., Davies, B., Elmore, A., et al. (2020). Importance and vulnerability of the world’s water towers. *Nature*, 577(7790):364–369.
- Jarvis, A., Reuter, H. I., Nelson, A., Guevara, E., et al. (2008). Hole-filled SRTM for the globe Version 4. *available from the CGIAR-CSI SRTM 90m Database (<http://srtm.csi.cgiar.org>)*, 15:25–54.
- Jones, D., Harrison, S., Anderson, K., and Betts, R. (2018a). Mountain rock glaciers contain globally significant water stores. *Scientific reports*, 8(1):2834.
- Jones, D., Harrison, S., Anderson, K., Selley, H., Wood, J., and Betts, R. (2018b). The distribution and hydrological significance of rock glaciers in the Nepalese Himalaya. *Global and Planetary Change*, 160:123–142.
- Jones, D. B., Harrison, S., Anderson, K., and Whalley, W. B. (2019). Rock glaciers and mountain hydrology: A review. *Earth-science reviews*, 193:66–90.
- Kääb, A. (2013). Permafrost and Periglacial Features: Rock Glaciers and Protalus Forms. *Encyclopedia of Quaternary Science, 2nd ed.; Mock, CJ, Elias, SA, Eds*, pages 535–541.
- Kang, S., Chen, F., Gao, T., Zhang, Y., Yang, W., Yu, W., and Yao, T. (2009). Early onset of rainy season suppresses glacier melt: a case study on Zhadang glacier, Tibetan Plateau. *Journal of glaciology*, 55(192):755–758.
- Kapp, J. L. D., Harrison, T. M., Kapp, P., Grove, M., Lovera, O. M., and Lin, D. (2005). Nyainqentanglha Shan: a window into the tectonic, thermal, and geochemical evolution of the Lhasa block, southern Tibet. *Journal of Geophysical Research: Solid Earth*, 110(B8).
- Keil, A., Berking, J., Mügler, I., Schütt, B., Schwalb, A., and Steeb, P. (2010). Hydrological and geomorphological basin and catchment characteristics of Lake Nam Co, South-Central Tibet. *Quaternary International*, 218(1-2):118–130.
- Kenner, R., Phillips, M., Beutel, J., Hiller, M., Limpach, P., Pointner, E., and Volken, M. (2017). Factors controlling velocity variations at short-term, seasonal and multiyear

- time scales, Ritigraben rock glacier, Western Swiss Alps. *Permafrost and Periglacial Processes*, 28(4):675–684.
- Kidd, W., Yusheng, P., Chengfa, C., Coward, M. P., Dewey, J. F., Gansser, A., Molnar, P., Shackleton, R. M., and Yiyin, S. (1988). Geological mapping of the 1985 Chinese—British Tibetan (Xizang—Qinghai) Plateau Geotraverse route. *Philosophical Transactions of the Royal Society of London. Series A, Mathematical and Physical Sciences*, 327(1594):287–305.
- Kneisel, C., Hauck, C., Fortier, R., and Moorman, B. (2008). Advances in geophysical methods for permafrost investigations. *Permafrost and periglacial processes*, 19(2):157–178.
- Kneisel, C. and Kääh, A. (2007). Mountain permafrost dynamics within a recently exposed glacier forefield inferred by a combined geomorphological, geophysical and photogrammetrical approach. *Earth Surface Processes and Landforms: The Journal of the British Geomorphological Research Group*, 32(12):1797–1810.
- Kneisel, C., Lehmkuhl, F., Winkler, S., Tressel, E., and Schröder, H. (1998). *Legende für geomorphologische Kartierungen in Hochgebirgen (GMK Hochgebirge)*. Geographische Ges.
- Knight, J., Harrison, S., and Jones, D. B. (2019). Rock glaciers and the geomorphological evolution of deglaciating mountains. *Geomorphology*, 324:14–24.
- Knight, J., Mitchell, W., and Rose, J. (2011). Geomorphological Field Mapping. In *Geomorphological Mapping: methods and applications*. Smith MJ, Paron P, Griffiths J.
- Krautblatter, M., Verleysdonk, S., Flores-Orozco, A., and Kemna, A. (2010). Temperature-calibrated imaging of seasonal changes in permafrost rock walls by quantitative electrical resistivity tomography (Zugspitze, German/Austrian Alps). *Journal of Geophysical Research: Earth Surface*, 115(F2).
- Lambiel, C. and Pieracci, K. (2008). Permafrost distribution in talus slopes located within the alpine periglacial belt, Swiss Alps. *Permafrost and Periglacial Processes*, 19(3):293–304.
- Lewkowicz, A. G., Etzelmüller, B., and Smith, S. L. (2011). Characteristics of discontinuous permafrost based on ground temperature measurements and electrical resistivity tomography, southern Yukon, Canada. *Permafrost and Periglacial Processes*, 22(4):320–342.

- Li, J., Sheng, Y., Wu, J., Chen, J., and Zhang, X. (2009a). Probability distribution of permafrost along a transportation corridor in the northeastern Qinghai province of China. *Cold Regions Science and Technology*, 59(1):12–18.
- Li, M., Ma, Y., Hu, Z., Ishikawa, H., and Oku, Y. (2009b). Snow distribution over the Namco lake area of the Tibetan Plateau. *Hydrology and Earth System Sciences*, 13(11):2023.
- Liu, S. and Guo, W. (2014). Glims glacier database. *National Snow and Ice Data Center: Boulder, CO, USA*.
- Loke, M. and Barker, R. (1995). Least-squares deconvolution of apparent resistivity pseudosections. *Geophysics*, 60(6):1682–1690.
- López-Martínez, J., Serrano, E., Schmid, T., Mink, S., and Linés, C. (2012). Periglacial processes and landforms in the South Shetland Islands (northern Antarctic Peninsula region). *Geomorphology*, 155:62–79.
- Lu, Q., Zhao, D., and Wu, S. (2017). Simulated responses of permafrost distribution to climate change on the Qinghai–Tibet Plateau. *Scientific Reports*, 7(1):1–13.
- Ma, W., Shi, C.-h., Wu, Q.-b., Zhang, L.-x., and Wu, Z.-j. (2006). Monitoring study on technology of the cooling roadbed in permafrost region of Qinghai–Tibet plateau. *Cold Regions Science and Technology*, 44(1):1–11.
- Mewes, B., Hilbich, C., Delaloye, R., and Hauck, C. (2017). Resolution capacity of geophysical monitoring regarding permafrost degradation induced by hydrological processes. *The Cryosphere*, 11(6):2957–2974.
- Mollaret, C., Hilbich, C., Pellet, C., Flores-Orozco, A., Delaloye, R., and Hauck, C. (2019). Mountain permafrost degradation documented through a network of permanent electrical resistivity tomography sites. *The Cryosphere*, 13(10):2557–2578.
- Monnier, S., Kinnard, C., Surazakov, A., and Bossy, W. (2014). Geomorphology, internal structure, and successive development of a glacier foreland in the semiarid Chilean Andes (Cerro Tapado, upper Elqui Valley, 30° 08' S., 69° 55' W.). *Geomorphology*, 207:126–140.
- Mudler, J., Hördt, A., Przyklenk, A., Fiandaca, G., Maurya, P. K., and Hauck, C. (2019). Two-dimensional inversion of wideband spectral data from the capacitively coupled resistivity method—first applications in periglacial environments. *The Cryosphere*, 13(9):2439–2456.

- Mügler, I., Gleixner, G., Günther, F., Mäusbacher, R., Daut, G., Schütt, B., Berking, J., Schwab, A., Schwark, L., Xu, B., et al. (2010). A multi-proxy approach to reconstruct hydrological changes and Holocene climate development of Nam Co, Central Tibet. *Journal of Paleolimnology*, 43(4):625–648.
- Notti, D., Herrera, G., Bianchini, S., Meisina, C., García-Davalillo, J. C., and Zucca, F. (2014). A methodology for improving landslide PSI data analysis. *International journal of remote sensing*, 35(6):2186–2214.
- Obu, J., Westermann, S., Bartsch, A., Berdnikov, N., Christiansen, H. H., Dashtseren, A., Delaloye, R., Elberling, B., Etzelmüller, B., Kholodov, A., et al. (2019). Northern Hemisphere permafrost map based on TTOP modelling for 2000–2016 at 1 km² scale. *Earth-Science Reviews*, 193:299–316.
- Onaca, A., Ardelean, F., Ardelean, A., Magori, B., Sirbu, F., Voiculescu, M., and Gachev, E. (2020). Assessment of permafrost conditions in the highest mountains of the Balkan Peninsula. *Catena*, 185:104288.
- Osmanoğlu, B., Sunar, F., Wdowinski, S., and Cabral-Cano, E. (2016). Time series analysis of InSAR data: Methods and trends. *ISPRS Journal of Photogrammetry and Remote Sensing*, 115:90–102.
- Otto, J. C. and Dikau, R. (2008). Symbols for geomorphologic mapping in high mountains for ArcGIS; Geomorphologic System Analysis of a High Mountain Valley in the Swiss Alps. *Geomorphology*, 48:323–341.
- Otto, J.-c., Keuschnig, M., Götz, J., Marbach, M., and Schrott, L. (2012). Detection of mountain permafrost by combining high resolution surface and subsurface information— an example from the Glatzbach catchment, Austrian Alps. *Geografiska Annaler: Series A, Physical Geography*, 94(1):43–57.
- Otto, J. C. and Smith, M. J. (2013). *Geomorphological mapping, in: Geomorphological Techniques*.
- Ran, Y., Li, X., Cheng, G., Zhang, T., Wu, Q., Jin, H., and Jin, R. (2012). Distribution of permafrost in China: an overview of existing permafrost maps. *Permafrost and Periglacial Processes*, 23(4):322–333.
- Ran, Z. and Liu, G. (2018). Rock glaciers in Daxue Shan, south-eastern Tibetan Plateau: an inventory, their distribution, and their environmental controls. *Cryosphere*, 12(7).
- Rangecroft, S., Harrison, S., and Anderson, K. (2015). Rock glaciers as water stores in the Bolivian Andes: an assessment of their hydrological importance. *Arctic, Antarctic, and Alpine Research*, 47(1):89–98.

- Reinosch, E., Buckel, J., Dong, J., Gerke, M., Baade, J., and Riedel, B. (2020). InSAR time series analysis of seasonal surface displacement dynamics on the Tibetan Plateau. *The Cryosphere*, 14(5):1633–1633.
- Reynolds, J. M. (2011). *An introduction to applied and environmental geophysics*. John Wiley & Sons.
- Rosset, E., Hilbich, C., Schneider, S., and Hauck, C. (2013). Automatic filtering of ERT monitoring data in mountain permafrost. *Near Surface Geophysics*, 11(4):423–434.
- Scapozza, C. (2015). Investigation on protalus ramparts in the Swiss Alps. *Geographica Helvetica*, 70:135–139.
- Schmid, M.-O., Baral, P., Gruber, S., Shahi, S., Shrestha, T., Stumm, D., and Wester, P. (2015). Assessment of permafrost distribution maps in the Hindu Kush Himalayan region using rock glaciers mapped in Google Earth. *Cryosphere*, 9(6).
- Schrott, L. (1996). Some geomorphological-hydrological aspects of rock glaciers in the Andes (San Juan, Argentina). *Zeitschrift für Geomorphologie. Supplementband*, (104):161–173.
- Schrott, L., Otto, J.-C., and Keller, F. (2012). Modelling alpine permafrost distribution in the hohe tauern region, Austria. *Austrian Journal of Earth Sciences*, 105(2).
- Schrott, L. and Sass, O. (2008). Application of field geophysics in geomorphology: advances and limitations exemplified by case studies. *Geomorphology*, 93(1-2):55–73.
- Schütt, B., Berking, J., Frechen, M., Frenzel, P., Schwalb, A., and Wrozyna, C. (2010). Late Quaternary transition from lacustrine to a fluvio-lacustrine environment in the north-western Nam Co, Tibetan Plateau, China. *Quaternary International*, 218(1-2):104–117.
- Song, C., Wang, G., Mao, T., Dai, J., and Yang, D. (2020). Linkage between permafrost distribution and river runoff changes across the Arctic and the Tibetan Plateau. *Science China Earth Sciences*, 63(2):292–302.
- Sowter, A., Bateson, L., Strange, P., Ambrose, K., and Syafiudin, M. F. (2013). DInSAR estimation of land motion using intermittent coherence with application to the South Derbyshire and Leicestershire coalfields. *Remote Sensing Letters*, 4(10):979–987.
- Strozzi, T., Caduff, R., Jones, N., Barboux, C., Delaloye, R., Bodin, X., Käab, A., Mätzler, E., and Schrott, L. (2020). Monitoring Rock Glacier Kinematics with Satellite Synthetic Aperture Radar. *Remote Sensing*, 12(3):559.

- Sun, Z., Zhao, L., Hu, G., Qiao, Y., Du, E., Zou, D., and Xie, C. (2020). Modeling permafrost changes on the Qinghai–Tibetan plateau from 1966 to 2100: A case study from two boreholes along the Qinghai–Tibet engineering corridor. *Permafrost and Periglacial Processes*, 31(1):156–171.
- Thompson, S. S., Kulesa, B., Benn, D. I., and Mertes, J. R. (2017). Anatomy of terminal moraine segments and implied lake stability on Ngozumpa Glacier, Nepal, from electrical resistivity tomography (ERT). *Scientific Reports*, 7:46766.
- Tian, K., Liu, J., Kang, S., and Li, C. (2006). A Primary Study on the Environment of Frozen Ground in the Nam Co Basin, Tibet. *Advances in Earth Science*, 21(12):1324–1332.
- Vanhala, H., Lintinen, P., and Ojala, A. (2009). Electrical resistivity study of permafrost on Ridnitsöhkka fell in northwest Lapland, Finland. *Geophysica*, 45(1-2):103–118.
- Villarroel, C. D., Tamburini Beliveau, G., Forte, A. P., Monserrat, O., and Morvillo, M. (2018). DInSAR for a Regional Inventory of Active Rock Glaciers in the Dry Andes Mountains of Argentina and Chile with Sentinel-1 Data. *Remote Sensing*, 10(10):1588.
- Vonder Mühl, D., Hauck, C., and Gubler, H. (2002). Mapping of mountain permafrost using geophysical methods. *Progress in Physical Geography*, 26(4):643–660.
- Wang, B. and French, H. M. (1995). Permafrost on the Tibet plateau, China. *Quaternary Science Reviews*, 14(3):255–274.
- Wang, J., Zhu, L., Daut, G., Ju, J., Lin, X., Wang, Y., and Zhen, X. (2009). Investigation of bathymetry and water quality of Lake Nam Co, the largest lake on the central Tibetan Plateau, China. *Limnology*, 10(2):149–158.
- Wang, T., Yang, D., Fang, B., Yang, W., Qin, Y., and Wang, Y. (2019). Data-driven mapping of the spatial distribution and potential changes of frozen ground over the Tibetan Plateau. *Science of The Total Environment*, 649:515–525.
- Wang, Y., Fu, Z., Lu, X., Qin, S., Wang, H., and Wang, X. (2020). Imaging of the Internal Structure of Permafrost in the Tibetan Plateau Using Ground Penetrating Radar. *Electronics*, 9(1):56.
- Washburn, A. L. (1980). *Geocryology: a survey of periglacial processes and environments*. Wiley.
- Wei, D., Wang, Y., Wang, Y., Liu, Y., Yao, T., et al. (2012). Responses of CO₂, CH₄ and N₂O fluxes to livestock enclosure in an alpine steppe on the Tibetan Plateau, China. *Plant and Soil*, 359(1-2):45–55.

- Wirz, V., Gruber, S., Purves, R. S., Beutel, J., Gärtner-Roer, I., Gubler, S., and Vieli, A. (2016). Short-term velocity variations at three rock glaciers and their relationship with meteorological conditions. *Earth Surface Dynamics*, 4(1):103–123.
- Wu, T., Li, S., Cheng, G., and Nan, Z. (2005). Using ground-penetrating radar to detect permafrost degradation in the northern limit of permafrost on the Tibetan Plateau. *Cold Regions Science and Technology*, 41(3):211–219.
- Yagüe-Martínez, N., Prats-Iraola, P., Gonzalez, F. R., Brcic, R., Shau, R., Geudtner, D., Eineder, M., and Bamler, R. (2016). Interferometric processing of Sentinel-1 TOPS data. *IEEE Transactions on Geoscience and Remote Sensing*, 54(4):2220–2234.
- Yang, M., Nelson, F. E., Shiklomanov, N. I., Guo, D., and Wan, G. (2010). Permafrost degradation and its environmental effects on the Tibetan Plateau: A review of recent research. *Earth-Science Reviews*, 103(1-2):31–44.
- Yao, T., Guo, X., Thompson, L., Duan, K., Wang, N., Pu, J., Xu, B., Yang, X., and Sun, W. (2006). δ 18 O record and temperature change over the past 100 years in ice cores on the Tibetan Plateau. *Science in China Series D*, 49(1):1–9.
- Yao, T., Masson-Delmotte, V., Gao, J., Yu, W., Yang, X., Risi, C., Sturm, C., Werner, M., Zhao, H., He, Y., et al. (2013). A review of climatic controls on δ 18O in precipitation over the Tibetan Plateau: Observations and simulations. *Reviews of Geophysics*, 51(4):525–548.
- Yao, T., Thompson, L., Yang, W., Yu, W., Gao, Y., Guo, X., Yang, X., Duan, K., Zhao, H., Xu, B., et al. (2012). Different glacier status with atmospheric circulations in Tibetan Plateau and surroundings. *Nature climate change*, 2(9):663–667.
- You, Y., Yu, Q., Pan, X., Wang, X., and Guo, L. (2013). Application of electrical resistivity tomography in investigating depth of permafrost base and permafrost structure in Tibetan Plateau. *Cold Regions Science and Technology*, 87:19–26.
- You, Y., Yu, Q., Pan, X., Wang, X., and Guo, L. (2017). Geophysical imaging of permafrost and talik configuration beneath a thermokarst lake. *Permafrost and Periglacial Processes*, 28(2):470–476.
- Yu, W., Han, F., Liu, W., and Harris, S. A. (2016). Geohazards and thermal regime analysis of oil pipeline along the Qinghai–Tibet Plateau Engineering Corridor. *Natural Hazards*, 83(1):193–209.
- Yu, Z., Wu, G., Keys, L., Li, F., Yan, N., Qu, D., and Liu, X. (2019). Seasonal variation of chemical weathering and its controlling factors in two alpine catchments, Nam Co basin, central Tibetan Plateau. *Journal of Hydrology*, 576:381–395.

- Zhang, G., Kang, S., Fujita, K., Huintjes, E., Xu, J., Yamazaki, T., Haginoya, S., Wei, Y., Scherer, D., Schneider, C., et al. (2013a). Energy and mass balance of Zhadang glacier surface, central Tibetan Plateau. *Journal of Glaciology*, 59(213):137–148.
- Zhang, G., Kang, S., Fujita, K., Huintjes, E., Xu, J., Yamazaki, T., Haginoya, S., Wei, Y., Scherer, D., Schneider, C., et al. (2013b). Energy and mass balance of Zhadang glacier surface, central Tibetan Plateau. *Journal of Glaciology*, 59(213):137–148.
- Zhang, Q. and Zhang, G. (2017). Glacier elevation changes in the western Nyainqentanglha Range of the Tibetan Plateau as observed by TerraSAR-X/TanDEM-X images. *Remote Sensing Letters*, 8(12):1142–1151.
- Zhang, Z. and Wu, Q. (2012). Thermal hazards zonation and permafrost change over the Qinghai–Tibet Plateau. *Natural hazards*, 61(2):403–423.
- Zou, D., Zhao, L., Yu, S., Chen, J., Hu, G., Wu, T., Wu, J., Xie, C., Wu, X., Pang, Q., et al. (2017). A new map of permafrost distribution on the Tibetan Plateau. *The Cryosphere*, 11(6):2527.

Chapter 4

InSAR time series analysis of seasonal surface displacement dynamics on the Tibetan Plateau

Eike Reinosch¹, Johannes Buckel², Jie Dong³, Markus Gerke¹, Jussi Baade⁴,
Björn Riedel¹

¹ Institute of Geodesy and Photogrammetry, Technische Universität Braunschweig, Braunschweig, Germany

² Institute of Geophysics and extraterrestrial Physics, Technische Universität Braunschweig, Braunschweig, Germany

³ School of Remote Sensing and Information Engineering, Wuhan University, Wuhan, China

⁴ Department of Geography, Friedrich-Schiller-Universität Jena, Jena, Germany

Corresponding author: Eike Reinosch (e.reinosch@tu-braunschweig.de)

Abstract

Climate change and the associated rise in air temperature have affected the Tibetan Plateau to a significantly stronger degree than the global average over the past decades. This has caused deglaciation, increased precipitation and permafrost degradation. The latter in particular is associated with increased slope instability and an increase in mass-wasting processes, which pose a danger to infrastructure in the vicinity. Interferometric synthetic aperture radar (InSAR) analysis is well suited to study the displacement patterns driven by permafrost processes, as they are on the order of millimeters to decimeters. The Nyainqêntanglha range on the Tibetan Plateau lacks high vegetation and features relatively thin snow cover in winter, allowing for continuous monitoring of those displacements throughout the year. The short revisit time of the Sentinel-1 constellation further reduces the risk of temporal decorrelation, making it possible to produce surface displacement models with good spatial coverage. We created three different surface displacement

models to study heave and subsidence in the valleys, seasonally accelerated sliding and linear creep on the slopes. Flat regions at Nam Co are mostly stable on a multiannual scale but some experience subsidence. We observe a clear cycle of heave and subsidence in the valleys, where freezing of the active layer followed by subsequent thawing cause a vertical oscillation of the ground of up to a few centimeters, especially near streams and other water bodies. Most slopes of the area are unstable, with velocities of 8 to 17 mmyr^{-1} . During the summer months surface displacement velocities more than double on most unstable slopes due to freeze–thaw processes driven by higher temperatures and increased precipitation. Specific landforms, most of which have been identified as rock glaciers, protalus ramparts or frozen moraines, reach velocities of up to 18 cmyr^{-1} . Their movement shows little seasonal variation but a linear pattern indicating that their displacement is predominantly gravity-driven.

4.1 Introduction

Permafrost describes subsurface material with a temperature of 0 °C or lower for at least 2 consecutive years (French and Williams, 1976). Permafrost is covered by the active layer, which freezes and thaws seasonally (Shur et al., 2005). This causes frost heave and subsidence of wet ground on the order of centimeters due to the volume change associated with the ice–water phase transition. The amplitude of this heave-andsubsidence cycle is dependent on the water content of the active layer and the material of the ground (Matsuoka et al., 2003). On permafrost slopes the freezing and thawing of the active layer reduces slope stability (Zhang and Michalowski, 2015) and might create solifluction lobes (Matsuoka, 2001). Further examples of creeping landforms associated with permafrost are rock glaciers (Haeberli et al., 2006) and protalus ramparts (Whalley and Azizi, 2003).

The Tibetan Plateau (TP) has been the object of many studies focusing on climate change over the past decades, especially since it has become known that its temperature has risen significantly faster than the global average with a rate of 0.25 °C per decade (Yao et al., 2000). This issue is exacerbated by the importance of the TP as a source of fresh water for large parts of greater Asia (Messerli et al., 2004). The TP is often referred to as the “Third Pole”, as it carries the largest volume of frozen fresh water after the North Pole and South Pole. The rising temperature has led to deglaciation at rates of over 0.2 $\% \text{yr}^{-1}$ (Ye et al., 2017) and permafrost degradation (Wu et al., 2010) throughout the plateau, increasing the river runoff by 5.5 % (Yao et al., 2007). Approximately 40 % of the TP is considered permafrost and 56 % seasonally frozen ground (Zou et al., 2017). Permafrost is vulnerable to climate change (Schuur et al., 2015), and it has been shown that climate warming may accelerate permafrost-related creeping and

sliding (Daanen et al., 2012). Glaciers and their retreat are very well documented on the TP, as they can be assessed using optical satellite data with high accuracy (e.g., Zhang et al., 2013a). Permafrost features, such as rock glaciers or buried ice lenses, are harder to quantify using optical remote sensing due to their relatively slow motion and often smaller size than glaciers (Kääb, 2008). This has led to a severe lack of inventories documenting these permafrost features, despite their importance in water storage (Jones et al., 2019) and the vulnerability of rock glaciers to climate warming (Müller et al., 2016).

Permafrost-related displacement processes, such as rockslides and the creeping of rock glaciers, can be monitored through the collection of in situ surface (e.g., Böhme et al., 2016) and subsurface data (e.g., Kneisel et al., 2014) or with terrestrial remote sensing techniques like laser scanners (e.g., Bauer et al., 2003). These techniques are generally labor intensive, require access to the often remote study sites and provide only sparse spatial coverage. Satellite-based remote sensing does not require access to the study sites and provides large spatial coverage, making it a valuable tool for the study of permafrost-related displacements. The displacements vary from a few centimeters (heave and subsidence of the active layer) to decimeters or meters per year (creep of rock glaciers) and are therefore often too small to be studied with optical satellite techniques (Kääb, 2008). Cloud cover may inhibit the collection of continuous optical time series data (Joshi et al., 2016). However, satellites emitting microwaves, like the Sentinel-1 constellation launched by the ESA in 2014, make the continuous detection of these displacements possible through Interferometric Synthetic Aperture Radar (InSAR) techniques. InSAR analysis is an active remote sensing technique, which exploits phase changes of backscattered microwaves to determine relative surface displacements taking place between two or more acquisition dates (Osmanoglu et al., 2016). Other studies have employed InSAR techniques to study permafrost-related processes on the TP (Li et al., 2015; Daout et al., 2017), in northwestern Bhutan (Dini et al., 2019), Norway (Eriksen et al., 2017), in Svalbard (Rouyet et al., 2019) and in Siberia (Antonova et al., 2018). Both seasonal processes, such as the heave and subsidence of freezing and thawing ground, and multiannual processes, like creep of periglacial landforms, have been studied. However, interpreting InSAR data can be challenging and often a number of assumptions have to be made. InSAR results provide only motion towards the satellite or away from it, not absolute ground displacement. It is therefore very difficult to accurately assess ground motion, without making assumptions about its actual direction. Unlike optical satellites, which observe the Earth from a vertical line of sight (LOS), SAR satellites are side-looking and observe the Earth obliquely.

This paper presents the results of an analysis of ground movement in the permafrost-prone area of the eastern and southern shores of Nam Co based on 3- to 4-year time series of Sentinel-1 acquisitions. We identify the various surface processes driving surface

displacement around Nam Co on the southern TP and evaluate their potential causes. It is vital to understand these displacement patterns and to compare our results to similar studies, as the TP has been shown to react heterogeneously to climate change (Song et al., 2014). To that end we developed multiple surface displacement models, analyzing geomorphological processes in the valleys and on the mountain slopes on both seasonal and multiannual scales.

4.2 Study area

Nam Co is the second largest lake of the TP (Zhou et al., 2013), with a catchment covering an area of 10,789 km², 2018 km² of which is the lake’s own surface area (Zhang et al., 2017). The proximity to Lhasa, its accessibility and the presence of the Nam Co Monitoring and Research Station for Multisphere Interactions CAS (NAMORS, Fig. 4.1) have made it a prime location to study the effects of climate change on the TP. The current lake level lies at 4726 m a.s.l. (Jiang et al., 2017), but it has featured a rising trend of approximately 0.3 myr⁻¹ over the past decades (Kropáček et al., 2012; Lei et al., 2013). The eastern and southern borders of the catchment are defined by the Nyainqêntanglha mountain range with elevations of up to 7162 m a.s.l. The highest parts are glaciated (Zhang et al., 2013a), while most other areas are considered to be in the periglacial zone (Keil et al., 2010; Li et al., 2014).

The climate at Nam Co is dominated by the Indian Monsoon in summer and the westerlies in winter (Yao et al., 2013). The former brings warm moist air from the south, providing 250 to 450 mm of rainfall from June to September and accounting for approximately 80 % of the annual precipitation (NAMORS, 2017, location in Fig. 4.1a). The westerlies maintain semiarid to arid conditions during the rest of the year. The snow cover is relatively sparse in winter, due to low precipitation outside of the monsoon season. The vegetation consists primarily of alpine steppe (Li, 2018), with high vegetation, such as shrubs and trees, being almost completely absent. The sparse snow cover and the lack of high vegetation make this region a prime study site for surface displacement related to periglacial processes using InSAR technology. Wang et al. (2017) used a combination of InSAR and optical satellite data to map rock glaciers in the northern Tien Shan of China, where the winters are similarly dry. The risk of temporal decorrelation, i.e., the loss of data coverage due to considerable change of physical surface characteristics, is lower than in other regions where such processes may be studied, such as Norway (Eriksen et al., 2017) or the Sierra Nevada in the USA (Liu et al., 2013). These regions feature considerable snow cover during long periods of the year, making continuous temporal coverage of fast-moving structures, like rock glaciers, difficult. This is especially a problem for satel-

lites with the shorter X-band (2–4 cm) or C-band (4–8 cm) wavelengths, like TerraSAR-X (3.1 cm) and Sentinel-1 (5.6 cm), as they are more susceptible to temporal decorrelation (Crosetto et al., 2016) compared to systems with a longer wavelength such as the L-band (15–30 cm).

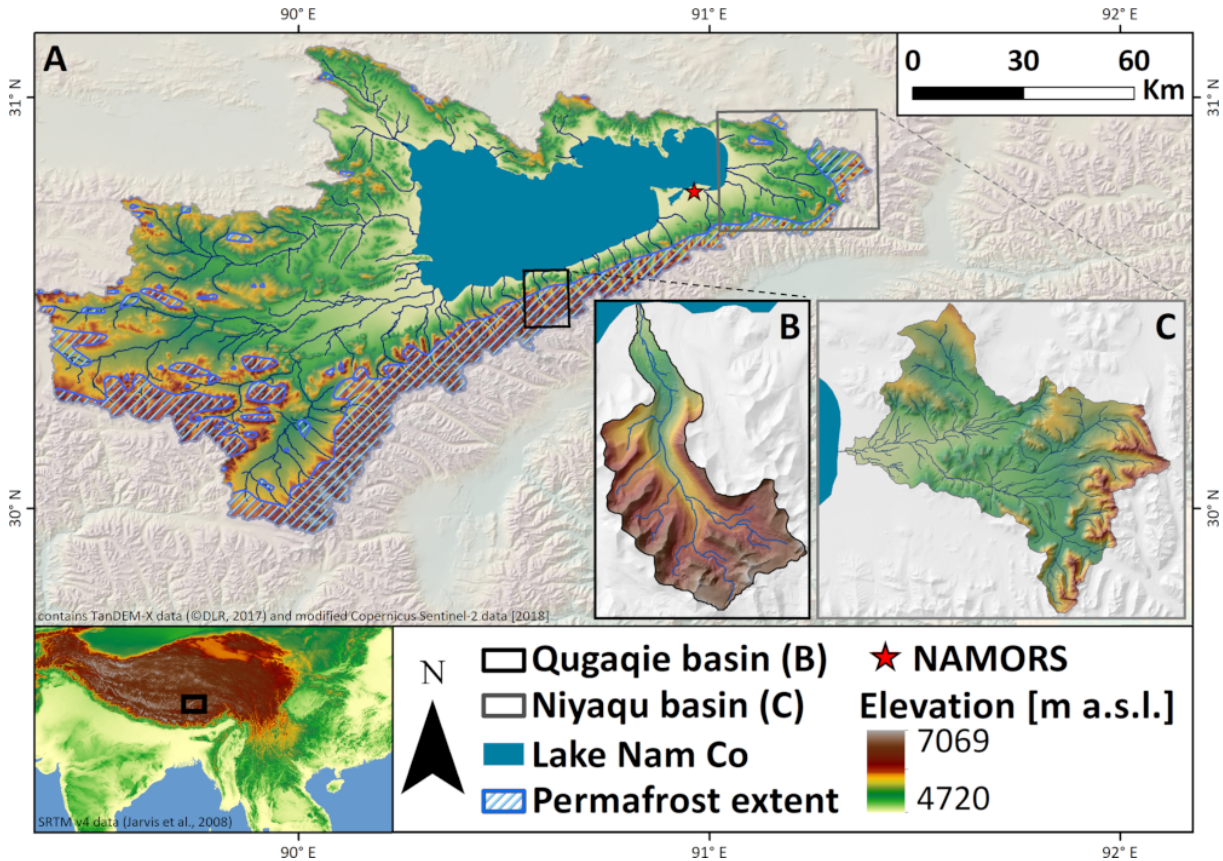


Figure 4.1: Overview map of the Nam Co catchment (A) including the locations of the NAMORS research station and the two main study areas: Qugaqie basin (B) and Niyaqu basin (C). Elevation data is based on SRTM v4 (Jarvis et al., 2008) and TanDEM-X 0.4" DEM (©DLR, 2017). Permafrost extent according to Zou et al. (2017) and lake extent based on the Normalized Difference Water Index (NDWI) of Sentinel-2 optical imagery (©Copernicus Sentinel data 2018, processed by ESA).

The two areas of interest for this study are the Qugaqie basin (58 km²) within the western Nyainqêntanglha mountain range, south of Nam Co and the Niyaqu basin (409 km²) in the eastern Nyainqêntanglha mountain range, on the eastern shore of the lake (Fig. 4.1). These sub-catchments were chosen as they feature different levels of glacial impact and represent the predominant landscapes and their related surface processes at Nam Co. The Niyaqu basin represents the majority of Nam Co's catchment with extensive alpine steppe vegetation and wetlands surrounded by hills with little exposed bedrock in the lower regions. The global permafrost map of Zou et al. (2017) shows that permafrost is limited to the higher parts of the sub-catchment, in the eastern Nyainqêntanglha mountain range. The Qugaqie basin represents the periglacial landscape of the western Nyainqêntanglha

mountain range. A total of 60 % of its area is considered periglacial landforms (Li et al., 2014), some of which are still active in the higher parts of the catchment due to their potential ice content, such as rock glaciers. Rock glaciers are steadily creeping ice-rich debris on mountainous slopes associated with permafrost (Haeberli et al., 2006). Other landforms were shaped by fluvial, glaciofluvial, glacial and aeolian processes (Keil et al., 2010). The vegetation cover is similar to that of the Niyaqu basin but with more areas of exposed glacial valley fill and bedrock interspersed in between the vegetated areas. Both the valleys and the slopes are covered by unconsolidated debris, mostly coarse gravel and boulders, and some slopes in the higher parts are free of soil and vegetation. Steep topography and the presence of warming permafrost can be associated with rock slope instabilities, such as rockfalls and rockslides (Fischer et al., 2006), making them a likely occurrence throughout the Qugaqie basin and in the higher zones of the Niyaqu basin. The bedrock consists of sandstone and carbonates in the lower areas of the basins and granodiorite and metasedimentary rocks in the higher parts (Kapp et al., 2005; Yu et al., 2019). The main river is fed by hanging valleys, some containing glaciers, as well as the two main glaciers Zhadang and Genpu to the south. The glaciers cover 8.4 % of the basin’s surface area and account for 15 % of its runoff in summer (Li et al., 2014). Two automated weather stations and a rain gauge were operated near the ablation zone of Zhadang Glacier between 2005 and 2010. Daily temperature averages range from approximately -15 °C in winter to 3 °C in summer in the Qugaqie basin and -10 °C to 10 °C in the Niyaqu basin (NAMORS, 2017; Zhang et al., 2013b).

4.3 Data

We use Sentinel-1 Level-1 single-look complex data for all InSAR analysis, from both ascending and descending orbits from the interferometric wide-swath mode with a ground resolution of 20 m azimuth and 5 m in the range direction (Fletcher, 2012). We used a multi-looking factor of 4 in the range direction and 1 in the azimuth direction to achieve a ground resolution of 20 m. Sentinel-1 observes the Earth’s surface at an angle of 33 to 43° from the vertical (Yagüe-Martínez et al., 2016). SAR satellites are generally right-looking, meaning the microwaves are emitted to the right of the satellite. Due to the polar orbit, this causes the microwaves to be emitted in a near-east direction while the satellite is ascending and in a near-west direction during descending data acquisitions. The high elevation of the TP brings both advantages and disadvantages to InSAR applications. Large altitude variations can be problematic due to artifacts caused by atmospheric delay (Li et al., 2012), while the lack of high and dense vegetation reduces the risk of decorrelation, which would otherwise lead to poor phase stability, so-called coherence.

Table 4.1: *Sentinel-1 data used for the time series analysis of both study areas.*

Area of interest	Orbit	Acquisition period	Acquisitions/interferograms	Temporal baselines	Incidence angle
Niyaqu	ascending	2014-12-31- 2018-12-22	79/244	12-60 d	40-42°
Niyaqu	descending	2014-12-14- 2018-11-11	72/227	12-60 d	39-41°
Qugaqie	ascending	2015-06-05- 2018-12-22	74/278	12-72 d	36-37°
Qugaqie	descending	2015-11-15- 2018-12-29	63/257	12-96 d	43°

Sentinel-1a has been acquiring data since October 2014 and Sentinel-1b since September 2016. We started our time series analysis of the Qugaqie basin in May and November 2015 for ascending and descending acquisitions, respectively, due to low coherence in earlier acquisitions. Early data over the Niyaqu basin produce better interferograms; here we start our time series analysis in December 2014 already for both ascending and descending acquisitions. The latest acquisitions included in the analysis are from November and December 2018. Sentinel-1b data are not available for this region, except for a 3-month period at the end of 2016 in descending orbit. More detailed information about the number of acquisitions and interferograms is shown in Table 4.1. The temporal baselines of interferograms are 12 to 60 d for the Niyaqu basin and 12 to 96 d for the Qugaqie basin. We increased the temporal baseline for the Qugaqie basin to avoid a temporal data gap during the summer months of 2016 and 2017 caused by interferograms with low overall coherence. Decorrelation can occur where the surface displacement is greater than half the wavelength between two acquisitions (Crosetto et al., 2016). This applies to areas with LOS velocities >17.0 cm yr^{-1} in the Niyaqu basin and 10.6 cm yr^{-1} in the Qugaqie basin. All topographic analysis and processing, including the removal of the topographic phase from the In-SAR data, were conducted using the 0.4 arcsec, equal to 12 m at the Equator, resolution TanDEM-X DEM (©DLR, 2017). This new and truly global DEM was acquired in 2010 to 2015 using single-pass X-band SAR interferometry (Zink et al., 2014) and finally released by German Aerospace Agency in 2017. On the global scale the DEM features an absolute error at the 90 % confidence level of <2 m (Wessel et al., 2018). In steep terrain accuracy is ensured by multiple data takes in ascending and descending orbits with varying incidence angles to prevent radar shadows and overlay. In the Niyaqu basin, the number of acquisitions per pixel ranges from five to eight, with the majority

representing average height estimates based on six acquisitions. Here, the mean 1σ height error is 0.30 m. In the steeper Qugaqie basin the number of acquisitions ranges from 8 to 12, with the majority at nine acquisitions. Here, the mean of the 1σ height error is 0.35 m.

4.4 Methods

4.4.1 ISBAS Processing

There are many different InSAR techniques capable of time series analysis to determine surface displacement over time. We chose a modified version of the small baseline subset (SBAS) method (Berardino et al., 2002), which we performed with the ENVI SARscape software (©Sarmap SA, 2001-2019). The SBAS method generates interferograms between SAR acquisitions with a temporal baseline under a chosen threshold and stacks them to estimate displacement and velocity over a longer time period. Interferograms are a spatial representation of the phase difference of two SAR acquisitions and can be used to determine the relative surface displacement between them. The phase stability, so-called coherence, is often used to represent the quality of an interferogram and to determine which pixels will be processed further (Crosetto et al., 2016). The modified SBAS approach we employ, referred to as intermittent SBAS (ISBAS), produces an improved spatial coverage by allowing limited interpolation of temporal gaps for areas where the coherence is intermittently below the chosen threshold (Sowter et al., 2013; Bateson et al., 2015). This reduces one of the downsides of the original SBAS algorithm, where partially vegetated areas can often not be processed, due to the poor coherence induced by vegetation. We chose a coherence threshold of 0.3 for our velocity models with an intermittent value of 0.75, and therefore 75 % of the interferograms need to produce a coherence of at least 0.3 to be considered during unwrapping. These parameters are similar to those used by Sowter et al. (2013) and Bateson et al. (2015) and produce an acceptable compromise of good spatial coverage, while excluding most unreliable data from the unwrapping process. We carefully analyzed all individual interferograms and excluded those with unwrapping errors and overall low coherence and therefore poor spatial coverage.

The topographic phase was removed from the interferograms with the TanDEM-X 0.4 arcsec resolution DEM (Wessel et al., 2018), and the orbital phase was removed by subtracting a constant simulated phase from our interferograms. We then estimated and subsequently subtracted a third-order polynomial function over flat stable areas to remove any remaining large-scale phase ramps. To reduce spatial trends connected to the small size of the Qugaqie basin, we processed a larger area which also includes the two neighboring catchments during the ISBAS workflow. Zhao et al. (2016) demonstrated

that using a linear model to process regions with cyclical heave–subsidence mechanisms leads to an overestimation of the displacement signal. We could not confirm their findings in our study areas. We therefore decided to use a linear model for all processing, as the quadratic model produced almost identical results and the cubic model produced unreliable results with poor spatial coverage. We applied a short atmospheric high-pass filter of only 100 d, to preserve the seasonal signal for our time series analysis, and a lowpass filter of 1200 m.

After performing the ISBAS processing chain, flat areas within the Qugaqie basin retained a relatively strong spatial trend of up to 9 and 13 mmyr^{-1} in ascending and descending datasets, respectively. This signal is likely connected to an atmospheric phase delay rather than actual surface displacement. We therefore performed a linear trend correction to remove this spatial trend from both ascending and descending datasets. The linear spatial trend was estimated through likely unmoving areas with a very low slope of $<5^\circ$ with at least 200m distance to water bodies (based on NDWI of Sentinel-2 optical imagery, ©Copernicus Sentinel data 2018, processed by ESA). After these corrections we performed a decomposition of ascending and descending datasets where we assume displacement in the north–south direction to be insignificant, to determine vertical and east–west displacements. We observe insignificant mean east–west velocities of -0.2 and -0.9 mmyr^{-1} with standard deviations of 2.2 and 2.4 mmyr^{-1} in likely stable areas in the Niyaqu and Qugaqie basins, respectively.

4.4.2 Selection of reference areas

InSAR displacement products are spatially relative to the chosen reference areas. It is necessary to select at least one reference to perform the unwrapping process during the In-SAR processing chain. Stable GNSS stations are preferred reference points but there are no permanent GNSS stations installed near the study areas. Therefore it is necessary to select the stable reference areas carefully to avoid introducing an erroneous trend signal into the surface displacement models. The parameters by which those stable reference areas were chosen are as follows.

1. The reference points must be at locations which are represented clearly in 100 % of all interferograms generated during the SBAS processing chain, to ensure that the displacement of all interferograms can be correctly determined relative to those points.
2. Whenever possible we selected bedrock at high elevations far away from the valley floor. The annual heave–subsidence cycle, and the corresponding uplift and subsi-

dence of the ground, is very strongly represented in the highly moisturized ground of the valley floor. Choosing reference points in this environment would remove this annual ground oscillation from the dataset in the valley floor and create an artificial and opposite oscillation pattern in other areas. Bedrock has a much smaller porosity than loose sediment or soil and is therefore less prone to oscillations forced by freezing and thawing of pore fluid. Stable bedrock is associated with a high coherence throughout the year, due to its relatively stable backscatter characteristics.

3. The chosen reference points must be stable during the entire period of observation, as moving reference points would shift the entire velocity model. We compared the results of different reference points in areas where we expect little motion and discarded those that caused a shift. As reference areas we chose regions with a low slope, good coherence and no obvious deformation structures, and we assume them to be stable in time.

Despite our careful selection of reference points, we cannot be certain that those areas are in fact stable throughout the entire data acquisition period. We therefore chose to use multiple reference points instead of a single point to produce the surface velocity models. This prevents a single, potentially poorly selected, reference point from invalidating the entire dataset by introducing either a multiannual velocity shift or seasonal displacement signal. The areas of partially exposed bedrock and the mountainous terrain of the Qugaqie basin made the selection of reference points easier compared to the Niyaqu basin, where exposed bedrock is rare. Selecting only points positioned at these optimal locations left us with none near the center of the basins or the lakeshore. This caused velocity shifts along the LOS on a millimeter scale in presumably stable flat areas, if they were far away from the reference points. We therefore increased the number of reference points to 90 and 51 in the Qugaqie basin and 92 and 61 in the Niyaqu basin for ascending and descending acquisitions, respectively. Maps showing their locations are included in the Supplement. The number of reference areas varies between ascending and descending acquisitions, due to differences in coherence, but we chose the same reference areas whenever possible.

4.4.3 Surface displacement models

In total we produced three different types of surface displacement models (Table 2) for the Niyaqu and Qugaqie basins: the linear velocity model (LVM), the heave–subsidence model (HSM) and the seasonal slope process model (SSM). The LVM portrays the mean surface velocity from 2015 to 2018 and does not portray seasonal variations. It describes both valleys and slopes, but we make the assumption that displacements are predominantly vertical in areas with slopes $<10^\circ$ and orientated in a downslope direction in steeper areas. The HSM models the heave–subsidence cycle caused by freezing of the active layer in

autumn followed by subsequent thawing of the active layer in spring. It covers only areas with slopes $<10^\circ$, shows only seasonal displacement and assumes that all displacement is vertical. The SSM focuses on slopes where sliding is accelerated from spring to autumn, to be differentiated from slopes in the LVM where sliding takes place throughout the year at a near-linear rate. It only covers slopes $>10^\circ$ and assumes that all displacement is orientated in a downslope direction.

Table 4.2: *Overview of the 3 surface displacement models with information regarding their purpose, displacement patterns and their connections to geomorphological und geological parameters.*

Model type	LVM (linear velocity model)	HSM (heave-subsidence model)	SSM (seasonal slope process model)
Purpose	Multiannual subsidence, sediment accumulation and permafrost creep	Seasonal heave-subsidence cycle due to freezing and thawing of the active layer	Seasonally accelerating slope processes
Displacement type	Multiannual linear velocity along the slope or vertical	Seasonal vertical displacement	Seasonal displacement along the slope
Slope	$<10^\circ$: vertical velocity $>10^\circ$: along slope velocity	$<10^\circ$	$>10^\circ$
Material	Soil, regolith, till, debris and ice	Mainly soil	Regolith, debris and ice
Related geomorphological processes	Long-term subsidence, sediment accumulation and permafrost creep	Heave-subsidence cycles connected to cryoturbation	Solifluction, gelifluction and rock slope instability on seasonally frozen slopes
Associated landform	Rock glaciers, protalus ramparts and moraines	Valley bottom terrain	Debris mantle slopes, solifluction lobes and rockslides

4.4.4 Linear velocity model (LVM)

This model portrays the mean annual surface velocity, with different methods applied to regions with a slope $>10^\circ$ and with a slope $<10^\circ$. Seasonal displacement trends are not present in this model, as we address those in the separate models HSM and SSM. The original ISBAS processing chain (Section 4.4.1) is the same but we applied different methods to project the LOS results into a more meaningful direction. For areas with a slope $<10^\circ$, we assumed that displacement would occur mainly in the vertical direction, as the slope would be too small to facilitate significant sliding or creep in most cases. Matsuoka (2001) shows that while solifluction has been documented on slopes as low as 2° , most affected areas in midlatitude to tropical mountains (including the TP) feature slopes $>10^\circ$. To determine the vertical velocity, we performed a decomposition of ascending and descending time series data. For this process we assume the north–south component of the surface displacement to be zero, which allows us to determine the vertical and east–west components (Eriksen et al., 2017). The vertical component represents our expected surface velocity for flat areas, while the east–west component can be used to assess the error range of the velocity model.

The decomposition method works well for flat regions and slopes with an east or west aspect but does not produce useful data for slopes with a north or south aspect. The Sentinel-1 SAR satellite constellation is quite sensitive to both east–west and vertical surface displacement, but very insensitive to displacement with a strong north or south component. This is problematic when studying displacements with a large horizontal component, as the velocity of surfaces moving in a northern or southern direction will be either severely underestimated or completely overlooked. We therefore employed a different method for slopes. Areas with a slope $>10^\circ$ were projected in the direction of the steepest slope, as most surface displacement is assumed to be caused by sliding processes transporting material parallel to the slope. We made an exception for areas with an east–west velocity $>10 \text{ mmyr}^{-1}$, as our study areas feature a periglacial setting with landforms such as rock glaciers, which move in a downslope direction and may extend into flatter areas. Those areas were projected in a downslope direction, even on slopes $<10^\circ$. This approach (Notti et al., 2014) originated from landslide studies to produce a more accurate result for a process where the direction of the moving structure is either known or can be assumed with reasonable certainty.

To estimate the downslope velocity, we calculate a downslope coefficient, with values between 0.2 and 1, and divide the LOS velocity by this coefficient to determine the downslope velocity. Maps of the spatial distribution of this coefficient are included in the Supplement. We used a smoothed version ($90 \text{ m} \times 90 \text{ m}$ moving mean) of the TanDEM-

X DEM to determine the motion direction, as we assume that structures such as rock glaciers and landslides move a larger amount of sediment in a similar direction. Small-scale variations in the aspect or slope have a strong impact on the downslope coefficient and would create outliers in the slope projection in areas with high surface roughness. It is important to note that by projecting LOS velocities along the steepest slope, we not only assume the direction vector, but we also simplify the mechanics to that of a planar slide. In doing so we assume that neither rotational nor compressing processes are involved. This is an obviously unrealistic but necessary simplification, which leads to an overestimation of the downslope velocity. The error range of the slope projection can be up to 5 times higher for areas with a very strong downslope coefficient than the range of ± 2.4 mm we determined over flat ground.

4.4.5 Heave-subsidence model (HSM)

Prior to analyzing the heave-subsidence amplitude, we projected the LOS displacements from both ascending and descending datasets to vertical displacements. We then removed the linear multiannual trend from the datasets to isolate the seasonal signal. Sum-of-sine functions were estimated for each individual time series. For the amplitude estimation in the Qugaqie basin we used a function with two sine terms and for the Niyaqu basin a function with three terms. We identified the sine term representing the seasonal signal and discarded the other terms. We calculated the mean values and the standard deviation of the amplitude, shift and period of the sine curve during the three to four seasonal cycles. We use the standard deviation of the amplitude and the shift as a measure of their error ranges. We also calculated the explained variation (R^2), which represents the proportion of variation in the time series explained by the sine curve regression. To qualify for further analysis, a time series must display a heave-subsidence amplitude larger than 3 mm, with an $R^2 > 0.5$ and a period of 350 to 380 d. The main results of the HSM are the mean amplitude of the heave-subsidence cycle and the day of maximum subsidence (DMS). The DMS describes the mean day on which the sine function reaches its minimum. This represents the day on which the soil has subsided to its minimum level due to thawing before beginning to heave again due to freezing. The final HSM contains both ascending and descending data. In areas where they overlap we show the mean value of the two. Slopes $> 10^\circ$ were excluded from the HSM as these areas are likely to display mainly gravity-driven displacement with a downslope direction and not only vertical heave-subsidence cycles. The seasonal displacement of slopes is covered by the SSM, and their multiannual velocity is shown in the LVM instead.

4.4.6 Seasonal slope process model (SSM)

The average seasonal velocities represent the median summer and median winter velocities over the entire time series. We divided the median summer velocity by the median winter velocity to produce the seasonal sliding coefficient, which represents how fast a surface is moving in summer compared to winter. Our SSM features a precision (1 sigma) of around 2.4 mmyr^{-1} . Time series with median seasonal velocities $<2 \text{ mmyr}^{-1}$ were set to 2 mmyr^{-1} , to avoid artificially large values when calculating the seasonal sliding coefficient with median seasonal velocities close to 0. This affects 18.1 % of slopes in the Niyaqu basin and 4.3 % of slopes in the Qugaqie basin. The higher value in the Niyaqu basin is due to the lower overall velocity of slopes in that region and the reduced spatial coverage due to lower coherence in the higher zone where larger velocities occur. A seasonal sliding coefficient of 1.5 represents a 50 % increased summer velocity compared to the winter velocity. We chose this threshold of 1.5 to differentiate between seasonally accelerated slopes and slopes with relatively linear velocity.

4.5 Results

4.5.1 Linear surface velocity derived from LVM

Solifluction may occur on slopes as low as 2° but mostly affects areas with a slope $>10^\circ$ in midlatitude to tropical mountain areas (Matsuoka, 2001). This is corroborated by the east–west velocity produced by our decomposition of ascending and descending data. For the slopes of $0\text{--}5^\circ$, $5\text{--}10^\circ$ and $10\text{--}15^\circ$ we observe mean east–west velocities of -0.1 , -0.6 and -0.6 mmyr^{-1} at standard deviations of 3.0 , 2.9 and 5.0 mmyr^{-1} , respectively. The jump in standard deviation from $5\text{--}10^\circ$ to $10\text{--}15^\circ$ from 2.9 to 5.0 mmyr^{-1} , suggests that we observe considerably more horizontal displacement in the latter group. This makes the 10° mark a good threshold between the vertical and the downslope projections. For areas with a slope $>10^\circ$ we assumed that the displacement would occur along the steepest slope, driven by gravitational pull (Haeberli et al., 2006). Unconsolidated material and the lack of deep-rooted vegetation in the area (Li et al., 2014) facilitate downslope motion.

Spatial data gaps in our InSAR models are caused by layover and shadow effects in mountainous regions or where the coherence was lost due to streams, vegetation, rockfalls and glaciers. These data gaps make up 34.7 % in flat and 31.4 % in steep terrain within the Qugaqie basin and 30.5 % and 36.0 % in the Niyaqu basin. The decomposition of ascending and descending datasets of areas with flat terrain (slope $<10^\circ$) shows that both basins have relatively stable flat terrain on a multiannual scale. A total of 53.3 % of flat

areas in the Qugaqie basin and 64.4 % in the Niyaqu basin fall within the $\pm 5 \text{ mmyr}^{-1}$ velocity group in both vertical and east–west directions. We consider these areas to be stable. In the Qugaqie basin, 3.3 % of flat areas experience uplift, most of which are near the main stream, while 2.8 % of flat areas are subsiding. In the Niyaqu basin, 0.2 % of flat areas experience uplift and 2.7 % experience subsidence (Fig. 4.2). The remaining flat areas, 5.8 % in the Qugaqie basin and 2.1 % in the Niyaqu basin, experience minor horizontal motion. Steep terrain is considerably more unstable in both study areas. In the Qugaqie basin only 20.9% of areas in steep terrain are stable, with 2.8 % being very unstable with velocities $>30 \text{ mmyr}^{-1}$. In the Niyaqu basin 21.1 % of areas in steep terrain are stable and 3.1 % are very unstable. A summary of the spatial data coverage is shown in Table 4.3. A distribution of the absolute surface velocity results in different regions is shown in Fig. 4.3.

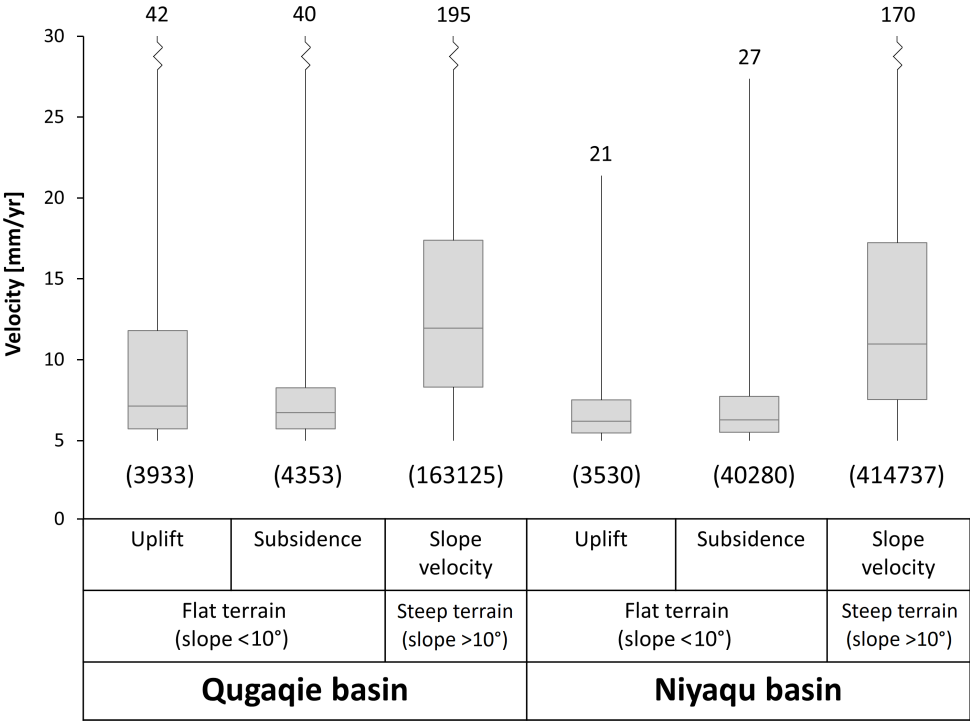


Figure 4.2: Distribution of the mean velocity results of the LVM for unstable flat and steep terrain in both study areas. All surface motion in flat areas (slope $<10^\circ$) was projected into the vertical direction (uplift and subsidence), and motion in steeper areas was projected along the direction of the slope. The maximum values are shown above the respective boxplots and the number of data points included in each plot is shown in parentheses below them. Areas with velocities $<5 \text{ mmyr}^{-1}$ are considered stable and are not shown here.

Table 4.3: Summary of the spatial data coverage of the LVM in the study areas. The values represent the percentages compared to all flat or steep terrain in the respective study area. Incoherent areas display a mean coherence of <0.3 . Stable areas are characterized by multiannual velocities $<5 \text{ mmyr}^{-1}$ in all directions. Unstable flat areas move at $>5 \text{ mmyr}^{-1}$ and are divided into uplift, subsidence and horizontal motion (uplift/subsidence/horizontal). Steep unstable areas move at $>5 \text{ mmyr}^{-1}$ downslope and very unstable terrain moves at $>30 \text{ mmyr}^{-1}$.

	Terrain	Incoherent	Stable	Unstable	Very unstable
Qugaqie basin	flat ($<10^\circ$)	34.7	53.3	3.3/2.8/5.8	0.1
	steep ($>10^\circ$)	31.4	20.9	44.9	2.8
Niyaqu basin	flat ($<10^\circ$)	30.5	64.4	0.2/2.7/2.1	0.0
	steep ($>10^\circ$)	36.0	21.1	39.7	3.1

The coherence in both basins is much reduced in valley bottoms. Streams and other water bodies also affecting the soil moisture status of the neighboring land surfaces cause large changes in microwave backscatter properties depending on the season. More extensive vegetation near the valley bottom further reduces the coherence. The coherence is especially low in valley bottoms during the spring and the summer monsoon period, when the ground thaws, the surface is inundated by rainwater or runoff, and biomass production increases. This causes an overall drop in spatial data coverage in valley bottoms, as many resolution cells exhibit coherence values below the threshold. Coherence maps of ascending and descending orbit of both study sites are included in the Supplement.

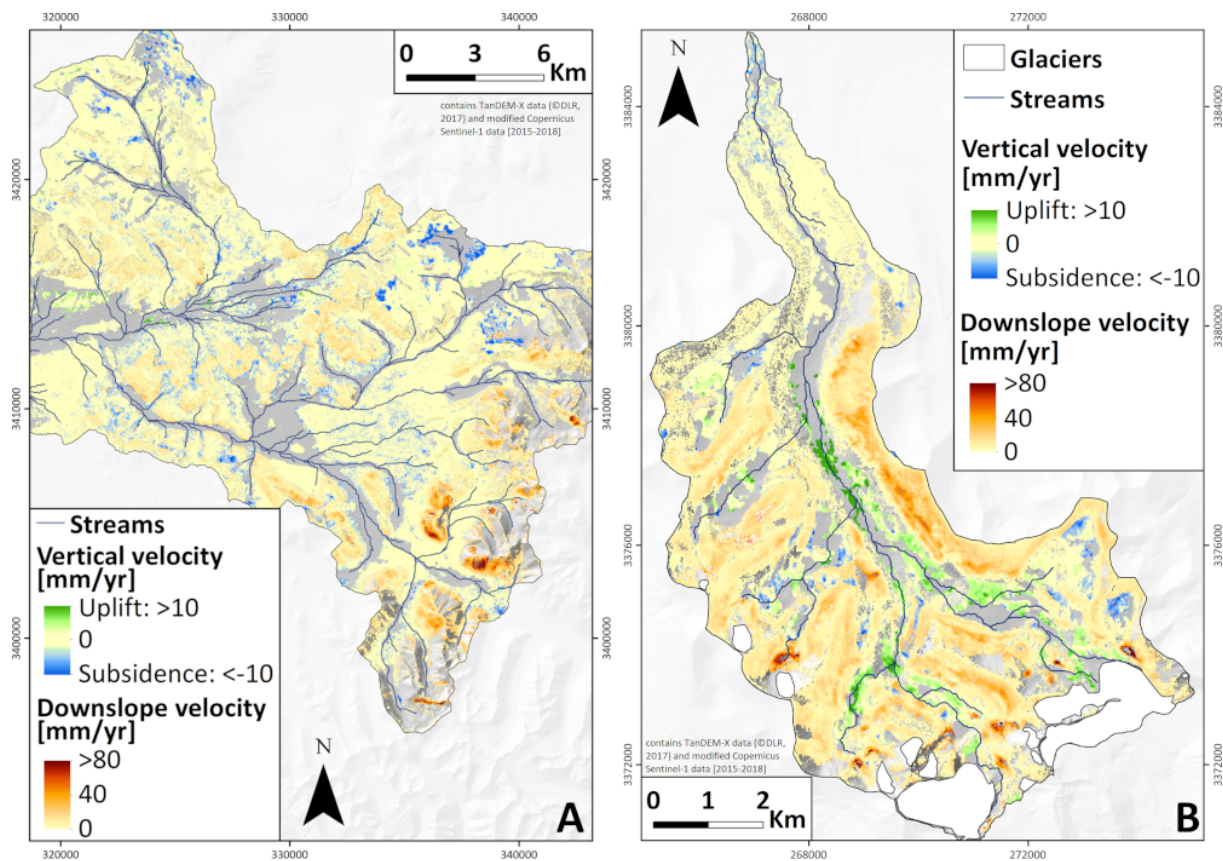


Figure 4.3: LVM of the Niyaqu (A) and Qugaqie (B) basins based on Sentinel-1 data (@Copernicus 2015–2018) over TanDEM-X DEM (@DLR, 2017). Flat terrain with a slope $<10^\circ$ shows vertical velocity, and steeper terrain shows the surface velocity projected along the steepest slope. Maps showing the spatial distribution of flat and steep terrain are included in the Supplement.

4.5.2 Heave-subsidence cycle derived from HSM

The seasonal vertical oscillation of the ground due to freezing and thawing of the soil is strongest in the valley bottom, especially near streams, lakes, ponds and, in the case of the Qugaqie basin, glaciers (Fig. 4.5a, b). In these areas the amplitude of this oscillation can reach up to 19 mm in the Qugaqie basin or even 27 mm in the Niyaqu basin. The median amplitude error is 1.3 mm in the Niyaqu basin and 1.1 mm in the Qugaqie basin. The day of maximum subsidence (DMS) is the day in summer during which the soil has subsided to its minimum level before beginning to heave again in autumn (Fig. 4.5c, d). In the Qugaqie basin the median DMS is on 19 July and in the Niyaqu basin it is on 23 August (Fig. 4.4). Most data points with heave–subsidence amplitudes of <7 mm reach their DMS in July to August in the Niyaqu basin and May to July in the Qugaqie basin, while areas with larger amplitudes tend to reach theirs in September to October (Fig. 4.5e, f). The median shift error of the sine function modeling the heave–subsidence cycle is 33 d in the Niyaqu basin and 27 d in the Qugaqie basin. We compared the DMS results of ascending and descending datasets and noticed that in both basins the mean

DMS of the descending dataset occurs earlier. In the Niyaqu basin the difference between ascending and descending DMS is 27 d and in the Qugaqie basin it is 10 d. Maps showing the spatial distribution of this disparity are included in the Supplement.

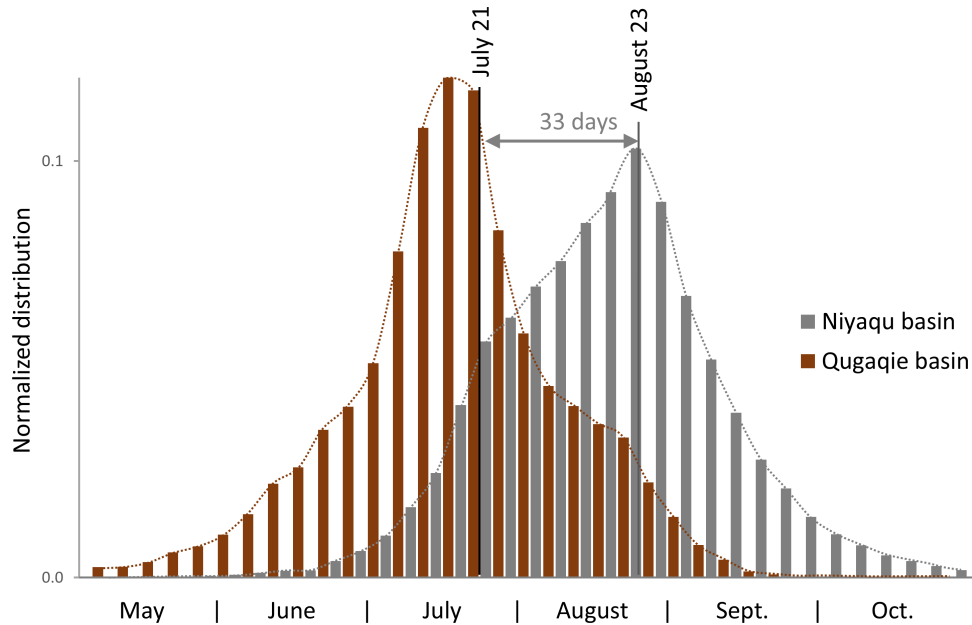


Figure 4.4: Normalized distribution of the thaw-induced day of maximum subsidence (DMS) in the Niyaqu basin (grey) with a median value on 24 August and the Qugaqie basin (brown) with a median value on 21 July. The lag time of 33 d between the median value of the Niyaqu basin and the day of the mean maximum air temperature on 21 July (NAMORS, 2017) is also shown. The median DMS of the Qugaqie basin occurs on 19 July, resulting in no clear lag time.

The freezing and thawing of soil follows the Stefan equation (Riseborough et al., 2008), and there is a significant lag time between the day of maximum air temperature and the DMS. This lag time has been studied with InSAR remote sensing techniques on both the northern and the southern TP (Li et al., 2015; Daout et al., 2017). According to the weather data from the NAMORS research station, the air temperature has a mean peak on 21 July from 2010 to 2017. Data from the weather station at the Zhadang glacier (Zhang et al., 2013b) show this mean peak on 27 July for 2010 to 2011 (19 July for the same period at NAMORS). NAMORS research station is close to the Niyaqu basin but about 50 km distant from the Qugaqie basin and at lower altitude. The Zhadang glacier and its weather station are located within the Qugaqie basin. Due to the very short acquisition period of only 2 years for the Zhadang weather station, we chose the 8-year dataset of NAMORS for both study areas. This produces a lag time of approximately 33 d for the Niyaqu basin (Fig. 4.4, grey), while in the Qugaqie basin the median DMS occurs on 19 July, 2 d before the maximum air temperature on 21 July, resulting in no clear lag time (Fig. 4.4, brown).

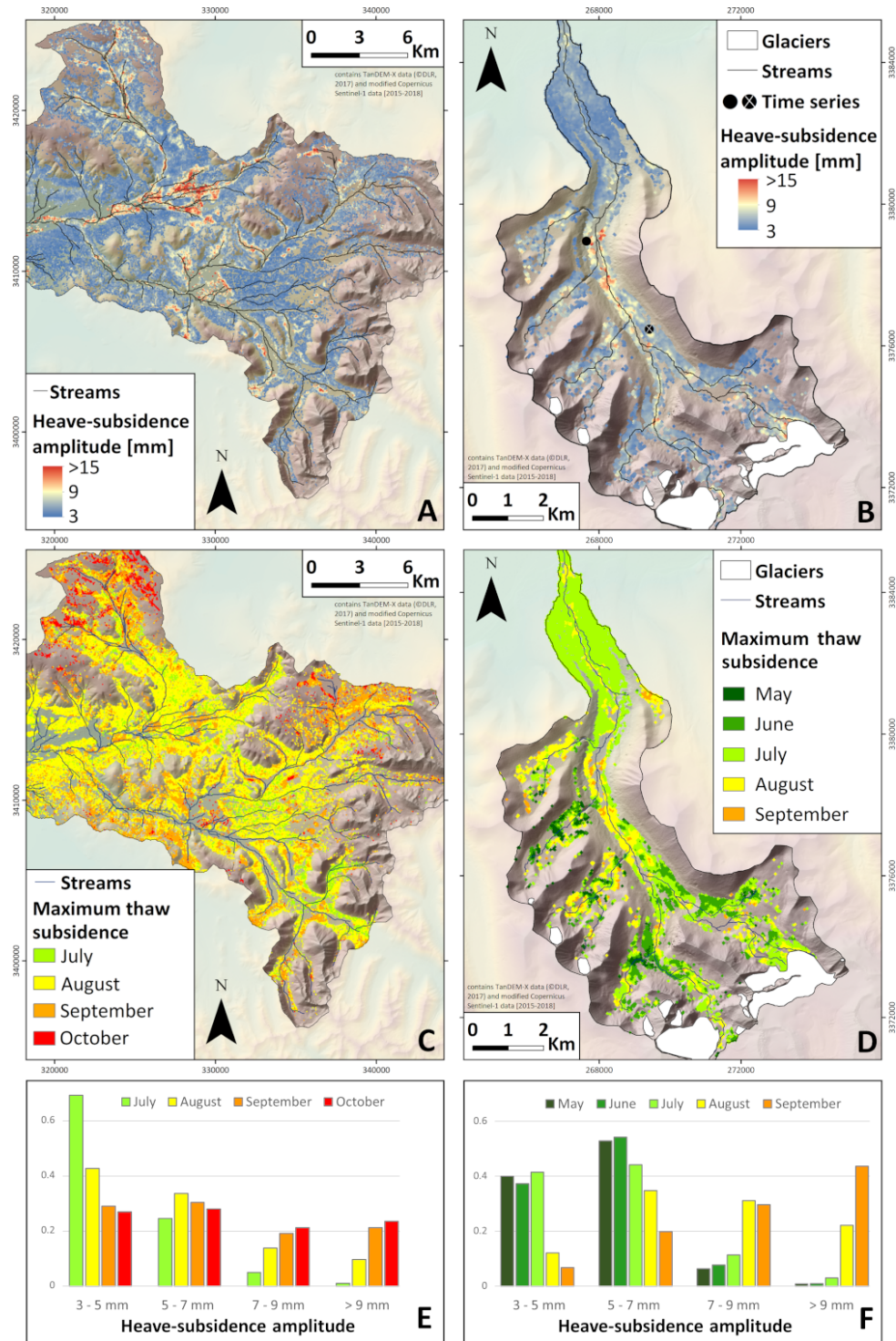


Figure 4.5: Parameters of the HSM (modified Copernicus Sentinel-1 data, 2015–2018) over TanDEM-X DEM (@DLR, 2017). Spatial variations in the mean amplitude (A, B) and the day of maximum subsidence (C, D) of the HSM within the Niyaqu and Qugaqie basins. The locations of the time series of Fig. 4.6a are displayed as black dots. (E, F) Normalized distribution of the months in which the heave–subsidence cycle reaches its maximum subsidence split up into four groups according to their amplitude for the Niyaqu and Qugaqie basins.

4.5.3 Seasonally accelerating slopes derived from SSM

We identified two distinct seasons, the wet monsoon season in summer and the dry winter season, which have a clear impact on the displacement data. The former season causes accelerated ground sliding on many slopes, while the latter slows most sliding processes (Fig. 4.6c). We refer to this seasonally accelerated sliding as freeze–thaw-driven but it is possible that the water input during the monsoon period, which coincides with the highest annual air temperatures, amplifies this process. In the Niyaqu basin the accelerated displacement pattern of the summer period lasts from May to September and in the Qugaqie basin from June to October. The slower winter displacement patterns last from November to March and from December to April. We compared the median summer velocities to the median winter velocities of each time series over the entire study period. Most soil- or debris-covered slopes in both basins display accelerated sliding rates of 100 % to 300 % towards the end of the summer monsoon. They reach downslope velocities of mostly 50 to 150 mmyr^{-1} during that time. The lower areas of most slopes appear to move at a linear rate. This marks the interface between the heave–subsidence cycle of the valley bottoms and the seasonally accelerated sliding on the slopes. These two seasonal displacement processes (Fig. 4.6a, c) are both present in those interface areas and often interfere with each other in such a manner that they appear to move linearly in the SSM.

In the Qugaqie basin and to a lesser extent in the Niyaqu basin, we observe that some of the fastest-moving structures creep at a linear rate, as opposed to the strong seasonality of most slopes. They do not display a clear acceleration in summer, and their multiannual velocity is generally between 30 and 180 mmyr^{-1} (Fig. 4.6b). We identified some of these landforms as rock glaciers or protalus ramparts from optical satellite imagery, field observations and topographic analysis. The motion of these permafrost-related landforms is driven by an ice matrix in between unconsolidated debris material (Haeberli et al., 2006). Rock glaciers and protalus ramparts represent 36 % of the linearly fast-moving landforms in the Qugaqie basin and include the largest and the fastest landforms with this displacement pattern. Other landforms with this displacement pattern are rock slope instabilities (24 %) and frozen moraines (39 %). Example pictures of those three landform types are included in the Supplement. We focus our analysis of slope displacements on the Qugaqie basin, due to the considerably better overall coherence and therefore spatial coverage of slopes in the periglacial zone. The maps equivalent to Fig. 4.7 for the Niyaqu basin characterized by poor coherence in the periglacial zone can be found in the Supplement.

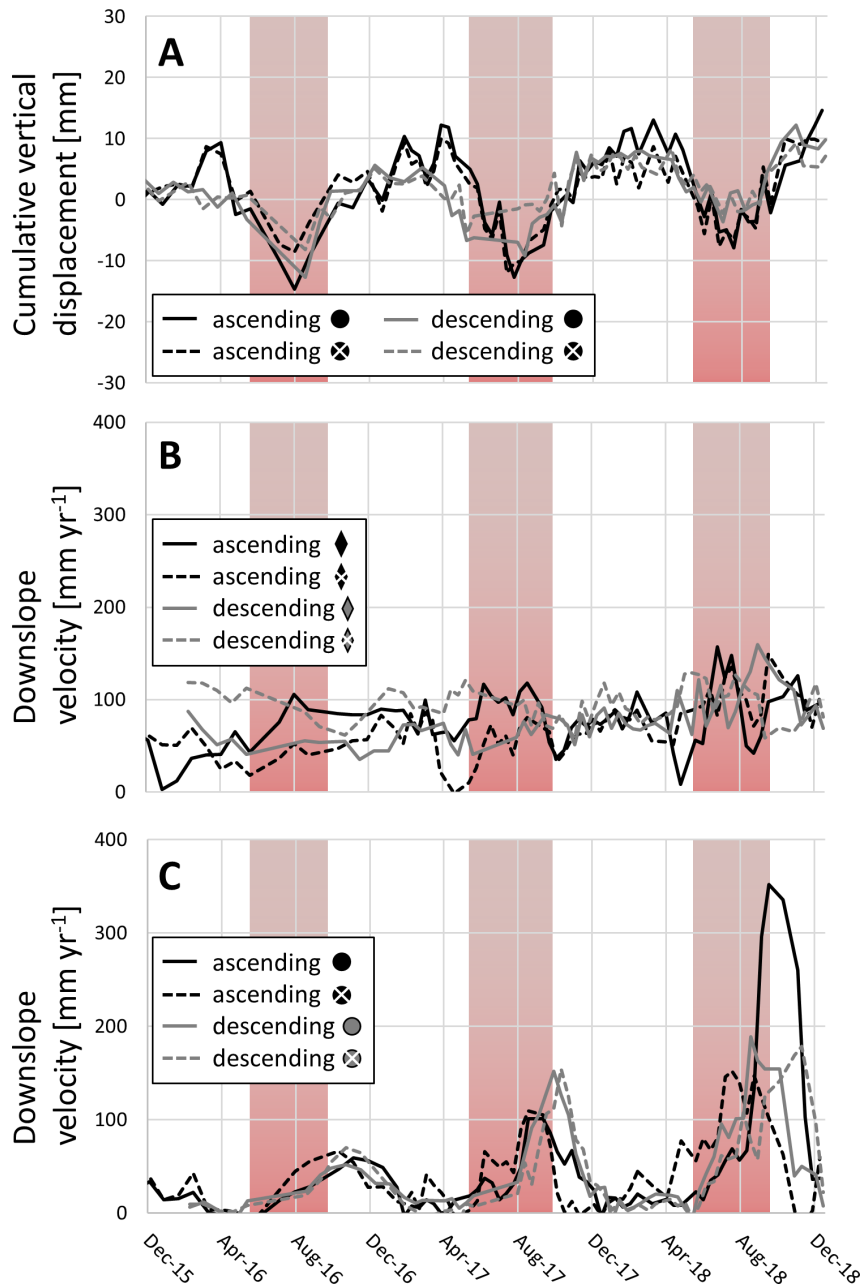


Figure 4.6: Surface displacement time series of both ascending (black, dashed black) and descending (grey, dashed grey) data of various areas throughout the Qugaqie basin highlighting the three seasonal patterns. June to September are shown with a red background as they display the strongest monsoon activity and air temperatures $>0^{\circ}\text{C}$ (Zhang et al., 2013b). (A) Cumulative vertical displacement showing the seasonal heave–subsidence cycle of the HSM at two locations near the stream of the main valley (black dots in Fig. 4.5b). (B) Downslope velocity time series of the four gravitydriven landforms (rhombi in Fig. 4.7a) with relatively constant velocities (blue areas in Fig. 4.7a). (C) Freeze–thaw–driven displacement patterns on four slopes (dots in Fig. 4.7a) with accelerated displacements in summer and comparatively minor displacements in winter (red areas in Fig. 4.7a). Panels (B) and (C) display moving average values of the closest four values in time.

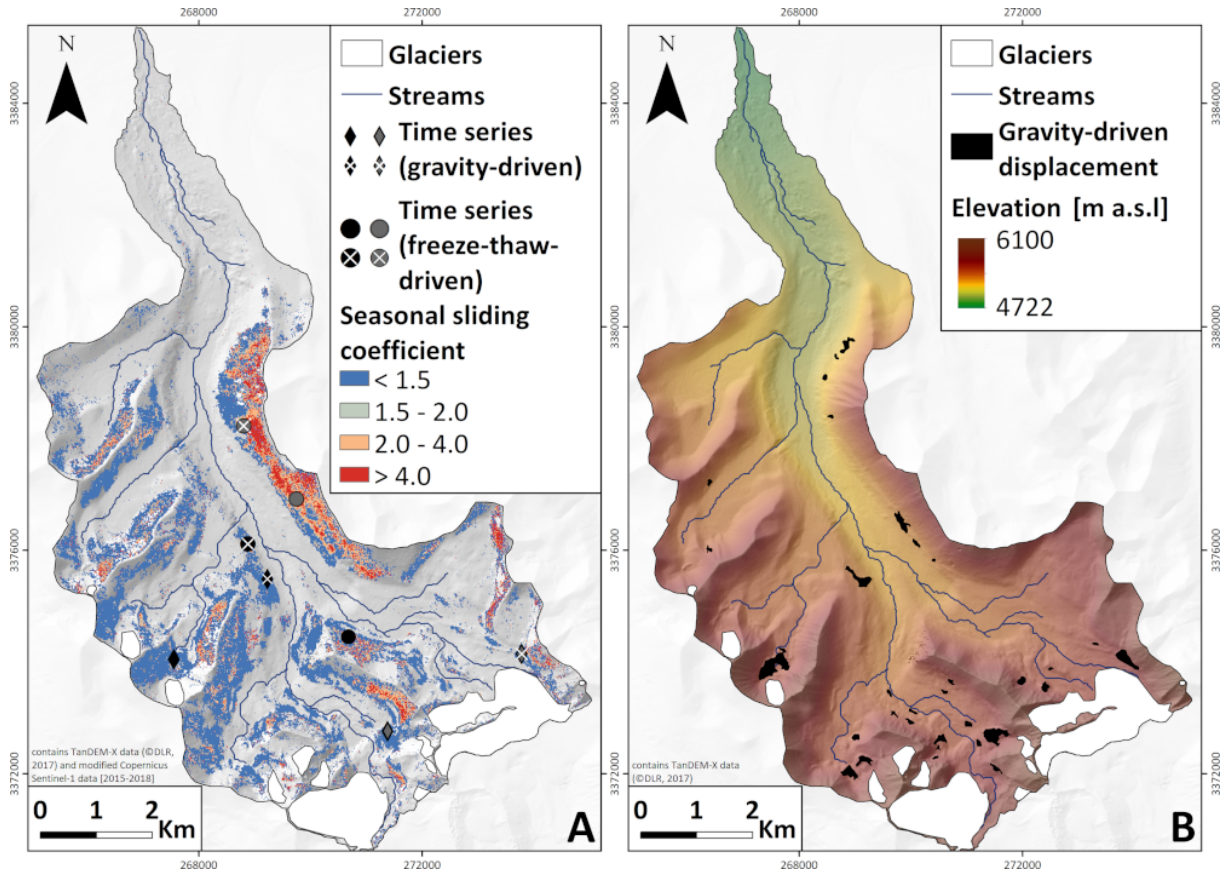


Figure 4.7: (A) SSM of the Qugaqie basin displaying the spatial distribution of slopes with accelerated surface velocity in summer compared to winter. A seasonal sliding coefficient of 1.5 represents a 50% increase in the velocity in summer. Only areas with a slope $>10^\circ$ and a slope velocity $>10 \text{ mmyr}^{-1}$ are shown. The locations of the time series in Fig. 4.6b, c are shown as rhombi/dots. (B) Spatial distribution of clusters where we assume displacement to be gravity-driven. These clusters display slope velocities $>50 \text{ mmyr}^{-1}$ and a seasonal sliding coefficient <1.5 .

4.6 Discussion

We created three different models to study both seasonal and multiannual surface displacements and their driving processes in steep and flat terrain at Nam Co. We discuss the multiannual displacements of the LVM and the seasonal displacements of the HSM in flat terrain in Sect. 4.6.1 and 4.6.2, respectively. Multiannual displacements of the LVM and seasonal displacements of the SSM in steep terrain are discussed in Sect. 4.6.3 and 4.6.4, respectively.

For both our seasonal and our multiannual surface displacement models we distinguish between flat terrain with slopes $<10^\circ$ where we assume all displacement to be mainly vertical and steep terrain with slopes $>10^\circ$ where we assume displacement to occur in a downslope direction. We chose this threshold based on the decomposition of ascending and descending results, which shows a considerable increase in horizontal velocities on

slopes $>10^\circ$ compared to flatter areas. While this simplification is necessary and mostly accurate for our study areas, it leads to inaccuracies in particular in areas with slopes of 5 to 15° where displacements can occur in both vertical and downslope directions.

4.6.1 Multiannual displacements in flat terrain

Flat terrain throughout both basins can be considered relatively stable with mean vertical and east–west velocities within $\pm 5 \text{ mmyr}^{-1}$. Some areas in valley bottoms show uplift rates of up to 40 mmyr^{-1} (Qugaqie basin, Fig. 4.3b) and 21 mmyr^{-1} (Niyaqu basin, Fig. 4.3a). A possible explanation is that seasonal variations in the soil moisture content were misidentified as surface displacement. The meltwater and high monsoon precipitation increases the soil moisture in summer, which can lead to a false interpretation of surface displacement of 10 % to 20 % (Zwieback et al., 2017). In our case this would represent 5 to 10mm per monsoon season for a total of 15 to 30 mm. This is corroborated by the large amplitude of the heave–subsidence model in the same areas, which is associated with more water during the freezing process (Fort and van Vliet-Lanoe, 2007).

We also observe subsidence rates of up to -12 mmyr^{-1} in the Qugaqie basin and -25 mmyr^{-1} in the Niyaqu basin. Many of those pixels are close to streams and water bodies. Approximately 30 % in the Niyaqu basin and 60 % in the Qugaqie basin fall into permafrost regions (Zou et al., 2017; Tian et al., 2009). This makes permafrost degradation a potential driver of this subsidence, as a thinning permafrost layer would result in meltwater escaping from the thawing soil. However, longer periods of observation are needed to come up with reliable conclusions.

4.6.2 Seasonal displacements in flat terrain

Both the Niyaqu and the Qugaqie basins have relatively stable flat terrain on a multiannual scale but show a strong seasonal signal in the same areas (Fig. 4.6a). It is unlikely that this signal is induced by seasonal atmospheric effects, as the amplitude would likely correlate to some degree with relative elevation to the reference points (Dong et al., 2019), which is not the case for our data. The most likely explanation is that this signal represents the heave–subsidence cycle of freezing and thawing of moist soil. Others observed very similar signals over permafrost areas on the northern TP (Daout et al., 2017) and over seasonally frozen ground in Dangxiong county on the southern side of the Nyainqêntanglha range (Li et al., 2015). The heave–subsidence amplitude of these studies agrees well with our results of mostly 3 to 15 mm in both basins. In similar areas they observe amplitudes of 2.5 to 12 mm and 10 to 25 mm, respectively. Comparable studies

of permafrost landscapes measured thaw subsidence of predominantly 10 to 70 mm and 2 to 68 mm per thawing season on Spitsbergen (Rouyet et al., 2019) and in northern Siberia (Antonova et al., 2018), respectively.

In both of our study sites we observe a relation between the amplitude of the heave–subsidence cycle and the DMS (Fig. 4.5e, f). Areas with high amplitudes tend to reach the DMS later in the year (September to October) and areas with small amplitudes tend to reach their DMS earlier (July to August). The lag time between maximum air temperature and DMS is therefore greater for areas with a large heave–subsidence amplitude. Longer lag times have been associated with a deeper active layer when assuming a one-dimensional heat transfer in soils (Li et al., 2015). For our study areas this would imply that the active layer tends to be deeper near streams and water bodies, as both the heave–subsidence amplitude and the lag time are highest there. This agrees with other studies on active layer thickness, which also observe a deeper active layer in those areas, especially where water bodies remain partially unfrozen in winter (e.g., McKenzie and Voss, 2013).

Other studies observed considerably higher lag times between the highest air temperature and the DMS. They observe lag times of 97 and 65 d in flat areas (Daout et al., 2017; Li et al., 2015) with longer lag times in mountainous areas, which they attributed to thicker permafrost, colder surroundings and less soil moisture. A small number of the data points of Li et al. (2015) fall within the Qugaqie basin, showing lag times of 50 to 90 d. In the Qugaqie basin we observe no clear median lag time (Fig. 4.4). It is possible that the difference between their results and ours reflects actual changes to the lag time between their dataset of 2007 to 2011 and ours of 2015 to 2018, but the point density of their data within the Qugaqie basin is too low to draw reliable conclusions. We determined the lag time by comparing the DMS to the average maximum air temperature at NAMORS from 2010 to 2017. NAMORS is located at an elevation of 4730 m, which is considerably lower than most valley areas of the Qugaqie basin at up to 5600 m. The temperature data acquired by Zhang et al. (2013b) within the Qugaqie basin show a maximum air temperature on 27 July, 6 d later than at NAMORS. Their dataset covers a period of less than 2 years and is therefore likely too short for an accurate comparison but it indicates that the maximum air temperature is similar to that of NAMORS. The Qugaqie basin has a short thaw period, with only 80 to 100 d in summer reaching daily air temperatures >0 °C (Zhang et al., 2013b). Together with the presence of permafrost this may explain the short lag time between the maximum air temperature and the DMS. A short thaw period is associated with a thinner active layer (Åkerman and Johansson, 2008), and the cold mountain climate and the permafrost would accelerate the freezing process of the active layer. While this may help to explain the short lag time, it also highlights

a major limitation of the model. For the HSM we estimated a sine function for every individual time series to determine the spatial distribution of the heave–subsidence cycle. Areas where this cycle does not follow a sinusoidal pattern are therefore not represented accurately by the HSM. The short thaw period of the Qugaqie basin also shortens the periods of maximum subsidence compared to the periods of maximum heave (Fig. 4.6a), hence making the heave–subsidence cycle less sinusoidal. Together with the short time series of only 3 to 4 years, this leads to a high shift error of the sine function of 27 d in the Qugaqie basin and 33 d in the Niyaqu basin.

The difference of the DMS between ascending and descending datasets is 10 d in the Qugaqie basin and 27 d in the Niyaqu basin and not distributed randomly. This is a very high disparity for a displacement with a predominantly vertical direction, which should be represented equally in ascending and descending datasets if the incidence angles are comparable. The difference in incidence angles between the two orbits is 6° over the Qugaqie basin and 1° over the Niyaqu basin. Over the Qugaqie basin the resulting difference in sensitivity to vertical displacement and the different number of summer seasons during the observation period (four for ascending and three for descending) may help to explain the 10 d disparity between ascending and descending datasets. This does not explain the large disparity of 27 d in the Niyaqu basin, as the difference in incidence angle is very small and the same time period is covered by ascending and descending datasets. For the Niyaqu basin in particular it was necessary to select different reference areas during interferogram generation, as the same areas often did not feature a high coherence in both orbits. Minor displacement signals of reference areas which were used in only one of the orbits may explain the widespread disparity of the DMS in the Niyaqu basin. The imperfect manner in which the sine curve of the HSM estimates the heave and subsidence of the ground also introduces uncertainties, as this disparity drops to 21 d in areas of the Niyaqu basin where the explained variation $R^2 > 0.9$ and rises to 29 where $R^2 > 0.6$. The high disparity between the DMS results of ascending and descending datasets and the high shift error of the sine function suggest that the sinusoidal HSM does not produce reliable results of the DMS for such a short time series with only three to four seasons.

4.6.3 Multiannual displacements in steep terrain

Most data points on slopes in both basins show downslope velocities of 8 to 17 mmyr^{-1} with a small number of landforms moving faster than 30 mmyr^{-1} . The instability of most steep terrain is to be expected, as there is very little deep-rooted vegetation to prevent the unconsolidated material from sliding. In our field campaigns we observed that soil-covered slopes, especially in the Niyaqu basin, feature *Kobresia pygmaea* pastures, which forms

a grass mat with a thick root system of up to 30 cm. This may provide some stability in the absence of larger vegetation; however, both climate change and overgrazing are degrading this grass mat (Miehe et al., 2008), which could lead to larger sliding velocities in the future.

When studying relatively fast land surface changes with InSAR, it is important to consider the maximum LOS displacement that can be calculated reliably between two SAR acquisitions. Among other factors this is dependent on the wavelength of the satellite (5.6 cm for Sentinel-1) and the temporal baseline of the interferogram. Measurements of displacement exceeding a quarter of the wavelength between two acquisitions are unreliable (Crosetto et al., 2016) and are likely to lead to an underestimation of the displacement signal and low coherence values. This is the case for some of our fast-moving landforms during the summer of 2016, when the temporal baseline is up to 96 d for the Qugaqie basin in descending orbit. It is therefore likely that we underestimate velocities during that time period. Most interferograms feature much shorter baselines of 12 to 36 d and are therefore not affected by this issue. It is unlikely that this is the cause of the linear pattern of the fastest landforms, as the temporal baselines of the summer of 2018 are short and also do not show a clear acceleration of the velocity (Fig. 4.6b). Our data for the Niyaqu basin are less affected by this underestimation of surface velocity, as the maximum temporal baseline is 60 d, and therefore only areas with a LOS velocity greater than 8.5 cm yr^{-1} are affected. High velocity reduces coherence values in the center of the fastest landforms and leads to decorrelation in some cases.

We do not observe a clear seasonally accelerated pattern for most of the fastest-moving landforms like rock glaciers. These landforms are creeping at comparatively linear rates, without distinct differences between summer and winter (Fig. 4.6b), often with multianual downslope velocities $>50 \text{ m yr}^{-1}$. We were able to identify 19 of these landforms in the Niyaqu basin and 33 in the Qugaqie basin by forming clusters of data points with a linear velocity pattern (less than 50 % acceleration of the velocity in summer) and slope velocities $>50 \text{ m yr}^{-1}$. Our spatial data coverage of steep slopes is better in the Qugaqie basin compared to the Niyaqu basin. It is therefore unlikely that this 19 to 33 comparison is an accurate reflection of the difference in frequency of these landforms between both study areas. It is likely that some of these clusters have been misidentified as linearly moving, while actually featuring both the seasonal heave–subsidence cycle prevalent in the valleys and the seasonal sliding pattern of the slopes. In some cases those two cycles may cancel each other out to such a degree that the resulting velocity appears linear. This can be observed at the interface between slopes and the valley (Fig. 4.7a, b).

We determined from optical satellite data, DEM analysis and field observations that

36 % of these linearly creeping clusters are associated with rock glaciers or protalus ramparts, where motion is generally driven by massive ice within the landforms (Whalley and Azizi, 2003). Other studies observe strong seasonal variations in the velocities of rock glaciers (e.g., Kääb and Vollmer, 2000). Rock glacier kinematics are highly dependent on the climatic setting, ice content, ground lithology and slope (Haeberli et al., 2006), making comparison between rock glaciers of different regions difficult. Rock glaciers studied in northwestern Bhutan show velocities of up to 300 mmyr⁻¹ and in rare cases up to 700 mmyr⁻¹ (Dini et al., 2019). However, neither study could analyze the seasonal displacement patterns of rock glaciers due to large temporal baselines of their interferograms. Strozzi et al. (2020) observe rock glacier velocities of approximately 1.5 to 2 myr⁻¹ in the Argentinian Andes, 2 to 4 myr⁻¹ in western Greenland and 1 to 2 myr⁻¹ in the Swiss Alps. The former two show a velocity increase of 30 % to 50 % and the latter around 100 % between winter and late summer.

Not all fast and linearly moving areas are associated with landforms containing massive ice. Rock slope instabilities such as rockslides are common on the debris-covered slopes, and while most of them follow a seasonally accelerated displacement pattern, around 24 % of fast and linearly moving areas are likely associated with rock slope instabilities. We can therefore not be certain if fast linear motion is indeed an indicator of displacement driven by massive ice. Their relatively low dependency on seasonality indicates, however, that their displacement is mainly gravity-driven as opposed to slopes with strong seasonal variations, where the displacement is driven by both gravity and freeze–thaw-related processes.

4.6.4 Seasonal displacements in steep terrain

Most slopes moving at least 10 mmyr⁻¹ experience a clear seasonal displacement signal, with velocities increasing considerably towards the end of the summer monsoon period (Fig. 4.6c). Monsoon season is associated with both the highest temperatures and approximately 80 % of the annual precipitation over a period of 4 months from June to September (NAMORS, 2017). For the Qugaqie basin it is also the only time when the average daily air temperature exceeds 0 °C (Zhang et al., 2013b). The clear connection between accelerated surface displacement and the increased air temperature in summer makes freeze–thaw-related processes like solifluction a likely driver of displacements on soil-covered slopes. Solifluction describes a process where seasonal freezing and thawing of the ground induces downslope displacement of up to 1 myr⁻¹ (Matsuoka, 2001). Affected slopes in the Qugaqie basin display downslope velocities of mostly 50 to 150 mmyr⁻¹ and up to 400 mmyr⁻¹ in some cases towards the end of the summer season.

4.7 Conclusion

Our InSAR time series analysis of Sentinel-1 data clearly shows both multiannual and seasonal surface displacement patterns in the Nam Co area. Most flat areas are relatively stable on a multiannual scale but show a strong seasonal pattern induced by freezing of the active layer in late autumn and winter and its subsequent thawing in spring and summer. This induces a vertical oscillation with an amplitude of 5 to 10 mm in most regions, with areas near water bodies showing a more pronounced pattern with an amplitude of up to 24 mm. Most steep terrain in both study areas is unstable, due to the unconsolidated material and the lack of deep-rooted vegetation. The terrain moves downslope with velocities of 8 to 17 mmyr^{-1} . Most steep terrain also shows a seasonal displacement pattern driven by freeze–thaw processes, such as solifluction, on soil-covered slopes and associated with rock slope instabilities, such as rockslides, on debris-covered slopes. Downslope velocities on these slopes accelerate from around 20 mmyr^{-1} in winter to 50 to 150 mmyr^{-1} in late summer for mean velocities of 30 to 70 mmyr^{-1} . The fastest landforms can reach mean velocities of 100 to 180 mmyr^{-1} . These landforms do not follow the seasonally accelerated sliding pattern of most slopes but creep linearly with little difference between summer and winter velocity, indicating that they are gravity-driven. While we have identified some of those landforms as rock glaciers and protalus ramparts, we cannot be certain to which extent fast linear velocity is an indicator for motion driven by massive ice in this area.

Data availability

The data of the surface displacement models presented in this study can be found at <https://doi.org/10.1594/PANGAEA.907743>.

Supplement

The supplement related to this article is available online at: <https://doi.org/10.5194/tc-14-1633-2020-supplement>.

Team List

1. M. Sc. Eike Reinosch, Institute of Geodesy and Photogrammetry, Technische Universität Braunschweig, 38106, Braunschweig, Germany, e.reinosch@tu-braunschweig.de, phone: +49 531 391 94587
2. M. Sc. Johannes Buckel, Institute of Geophysics and extraterrestrial Physics, Technische Universität Braunschweig, 38106, Braunschweig, Germany, j.buckel@tu-bs.de, phone: +49 531 391 8506
3. Dr. Jie Dong, School of Remote Sensing and Information Engineering, Wuhan University, 430079, Wuhan, China, dongjie@whu.edu.cn, phone: +86 15072317889
4. Prof. Markus Gerke, Institute of Geodesy and Photogrammetry, Technische Universität Braunschweig, 38106, Braunschweig, Germany, m.gerke@tu-bs.de, phone: +49 531 391 94570
5. Dr. Jussi Baade, Department of Geography, Friedrich-Schiller- Universität Jena, 07743, Jena, Germany, jussi.baade@uni-jena.de, phone: +49 3641 9-48803
6. Dr. Björn Riedel, Institute of Geodesy and Photogrammetry, Technische Universität Braunschweig, 38106, Braunschweig, Germany, b.riedel@tu-bs.de, phone: +49 531 391 94593

Author Contribution

The majority of the scientific writing and the figures were produced by ER. He also performed most of the literature research and data processing. JB performed literature research of the study areas, especially about their geomorphology, and wrote parts of the respective section. Furthermore he proofread the entire document regarding geomorphological and geological data and established connections between the results of the satellite analysis and relevant geomorphological landforms and processes in the field. BR provided guidance regarding InSAR processing and proofreading of the manuscript, with a focus on the technical aspects of InSAR time series analysis. He also secured the funding for this research as part of the TransTiP project. MG proofread a previous version of the manuscript; provided guidance about the relevant research questions, research direction and the manuscript structure; and aided in establishing connections to other remote sensing institutions to discuss the content of this research with fellow researchers. JB secured funding for the project, evaluated potential study areas and provided us with additional data through additional proposals to the DLR. JD performed a review of the methods

used with a focus on the seasonal displacement signal present in our data and the potential causes thereof.

Competing interests

The authors declare that they have no conflict of interests.

Acknowledgements

We would like to thank the DLR for providing us with the high-resolution TanDEM-X DEM for our data processing (Proposal ID DEM_HYDR1727) and the ESA and Copernicus for making Sentinel-1 and Sentinel-2 data freely available to the public. We are especially grateful to the ‘Deutsche Forschungsgemeinschaft’ (DFG) for funding our work as part of the Sino-German project ‘Geo-ecosystems in transition on the Tibetan Plateau’ (TransTiP; GRK 2309/1) and to the Open Access Publication Funds of the Technische Universität Braunschweig. We thank our Chinese colleagues, who have worked tirelessly to support us before and during our field work.

Financial support

This research has been supported by the Deutsche Forschungsgemeinschaft (grant no. GRK 2309/1). This open-access publication was funded by Technische Universität Braunschweig.

Review statement

This paper was edited by Christian Hauck and reviewed by two anonymous referees.

Bibliography

- Åkerman, H. J. and Johansson, M. (2008). Thawing permafrost and thicker active layers in sub-arctic Sweden. *Permafrost and periglacial processes*, 19(3):279–292.
- Antonova, S., Sudhaus, H., Strozzi, T., Zwieback, S., Käab, A., Heim, B., Langer, M., Bornemann, N., and Boike, J. (2018). Thaw subsidence of a yedoma landscape in northern Siberia, measured in situ and estimated from TerraSAR-X interferometry. *Remote Sensing*, 10(4):494.
- Bateson, L., Cigna, F., Boon, D., and Sowter, A. (2015). The application of the Intermittent SBAS (ISBAS) InSAR method to the South Wales Coalfield, UK. *International Journal of Applied Earth Observation and Geoinformation*, 34:249–257.
- Bauer, A., Paar, G., and Kaufmann, V. (2003). Terrestrial laser scanning for rock glacier monitoring. In *8th International Conference on Permafrost, Proceedings*, volume 1, pages 55–60.
- Berardino, P., Fornaro, G., Lanari, R., and Sansosti, E. (2002). A new algorithm for surface deformation monitoring based on small baseline differential SAR interferograms. *IEEE Transactions on geoscience and remote sensing*, 40(11):2375–2383.
- Böhme, M., Bunkholt, H., Oppikofer, T., Dehls, J., Hermanns, R., Eriksen, H., Lauknes, T., and Eiken, T. (2016). *Using 2D InSAR, dGNSS and structural field data to understand the deformation mechanism of the unstable rock slope Gamanjunki 3, northern Norway*. CRC Press.
- Crosetto, M., Monserrat, O., Cuevas-González, M., Devanthéry, N., and Crippa, B. (2016). Persistent scatterer interferometry: A review. *ISPRS Journal of Photogrammetry and Remote Sensing*, 115:78–89.
- Daanen, R., Grosse, G., Darrow, M., Hamilton, T., Jones, B. M., et al. (2012). Rapid movement of frozen debris-lobes: implications for permafrost degradation and slope instability in the south-central Brooks Range, Alaska. *Natural Hazards and Earth System Sciences*, 12(5):1521–1537.
- Daout, S., Doin, M.-P., Peltzer, G., Socquet, A., and Lasserre, C. (2017). Large-scale InSAR monitoring of permafrost freeze-thaw cycles on the Tibetan Plateau. *Geophysical Research Letters*, 44(2):901–909.
- Dini, B., Daout, S., Manconi, A., and Loew, S. (2019). Classification of slope processes based on multitemporal DInSAR analyses in the Himalaya of NW Bhutan. *Remote Sensing of Environment*, 233:111408.

- Dong, J., Zhang, L., Liao, M., and Gong, J. (2019). Improved correction of seasonal tropospheric delay in InSAR observations for landslide deformation monitoring. *Remote Sensing of Environment*, 233:111370.
- Eriksen, H. Ø., Lauknes, T. R., Larsen, Y., Corner, G. D., Bergh, S. G., Dehls, J., and Kierulf, H. P. (2017). Visualizing and interpreting surface displacement patterns on unstable slopes using multi-geometry satellite SAR interferometry (2D InSAR). *Remote Sensing of Environment*, 191:297–312.
- Fischer, L., Kääh, A., Huggel, C., and Noetzli, J. (2006). Geology, glacier retreat and permafrost degradation as controlling factors of slope instabilities in a high-mountain rock wall: the Monte Rosa east face. *Natural Hazards and Earth System Sciences*, 6(5):761–772.
- Fletcher, K. (2012). *SENTINEL 1: ESA’s Radar Observatory Mission for GMES Operational Services*. European Space Agency.
- Fort, F. and van Vliet-Lanoe, B. (2007). Permafrost and periglacial environment of Western Tibet. *Landform Analysis*, 5:25–29.
- French, H. M. and Williams, P. (1976). *The periglacial environment*, volume 341. Wiley Online Library.
- Haerberli, W., Hallet, B., Arenson, L., Elconin, R., Humlum, O., Kääh, A., Kaufmann, V., Ladanyi, B., Matsuoka, N., Springman, S., et al. (2006). Permafrost creep and rock glacier dynamics. *Permafrost and periglacial processes*, 17(3):189–214.
- Jarvis, A., Reuter, H. I., Nelson, A., Guevara, E., et al. (2008). Hole-filled SRTM for the globe Version 4. available from the CGIAR-CSI SRTM 90m Database (<http://srtm.csi.cgiar.org>), 15:25–54.
- Jiang, L., Nielsen, K., Andersen, O. B., and Bauer-Gottwein, P. (2017). Monitoring recent lake level variations on the Tibetan Plateau using CryoSat-2 SARIn mode data. *Journal of Hydrology*, 544:109–124.
- Jones, D. B., Harrison, S., Anderson, K., and Whalley, W. B. (2019). Rock glaciers and mountain hydrology: A review. *Earth-science reviews*, 193:66–90.
- Joshi, N., Baumann, M., Ehammer, A., Fensholt, R., Grogan, K., Hostert, P., Jepsen, M. R., Kuemmerle, T., Meyfroidt, P., Mitchard, E. T., et al. (2016). A review of the application of optical and radar remote sensing data fusion to land use mapping and monitoring. *Remote Sensing*, 8(1):70.
- Kääh, A. (2008). Remote sensing of permafrost-related problems and hazards. *Permafrost and periglacial processes*, 19(2):107–136.

- Kääb, A. and Vollmer, M. (2000). Surface geometry, thickness changes and flow fields on creeping mountain permafrost: automatic extraction by digital image analysis. *Permafrost and Periglacial Processes*, 11(4):315–326.
- Kapp, J. L. D., Harrison, T. M., Kapp, P., Grove, M., Lovera, O. M., and Lin, D. (2005). Nyainqentanglha Shan: a window into the tectonic, thermal, and geochemical evolution of the Lhasa block, southern Tibet. *Journal of Geophysical Research: Solid Earth*, 110(B8).
- Keil, A., Berking, J., Mügler, I., Schütt, B., Schwalb, A., and Steeb, P. (2010). Hydrological and geomorphological basin and catchment characteristics of Lake Nam Co, South-Central Tibet. *Quaternary International*, 218(1-2):118–130.
- Kneisel, C., Rödder, T., and Schwindt, D. (2014). Frozen ground dynamics resolved by multi-year and year-round electrical resistivity monitoring at three alpine sites in the Swiss Alps. *Near Surface Geophysics*, 12(1):117–132.
- Kropáček, J., Braun, A., Kang, S., Feng, C., Ye, Q., and Hochschild, V. (2012). Analysis of lake level changes in Nam Co in central Tibet utilizing synergistic satellite altimetry and optical imagery. *International Journal of Applied Earth Observation and Geoinformation*, 17:3–11.
- Lei, Y., Yao, T., Bird, B. W., Yang, K., Zhai, J., and Sheng, Y. (2013). Coherent lake growth on the central Tibetan Plateau since the 1970s: Characterization and attribution. *Journal of Hydrology*, 483:61–67.
- Li, B., Yu, Z., Liang, Z., and Acharya, K. (2014). Hydrologic response of a high altitude glacierized basin in the central Tibetan Plateau. *Global and Planetary Change*, 118:69–84.
- Li, Q. (2018). Spatial variability and long-term change in pollen diversity in Nam Co catchment (central Tibetan Plateau): Implications for alpine vegetation restoration from a paleoecological perspective. *Science China Earth Sciences*, 61(3):270–284.
- Li, Z., Xu, W., Feng, G., Hu, J., Wang, C., Ding, X., and Zhu, J. (2012). Correcting atmospheric effects on InSAR with MERIS water vapour data and elevation-dependent interpolation model. *Geophysical journal international*, 189(2):898–910.
- Li, Z., Zhao, R., Hu, J., Wen, L., Feng, G., Zhang, Z., and Wang, Q. (2015). InSAR analysis of surface deformation over permafrost to estimate active layer thickness based on one-dimensional heat transfer model of soils. *Scientific reports*, 5:15542.

- Liu, L., Millar, C. I., Westfall, R. D., and Zebker, H. A. (2013). Surface motion of active rock glaciers in the Sierra Nevada, California, USA: inventory and a case study using InSAR. *The Cryosphere*, 7: 1109-1119, 7:1109–1119.
- Matsuoka, N. (2001). Solifluction rates, processes and landforms: a global review. *Earth-Science Reviews*, 55(1-2):107–134.
- Matsuoka, N., Abe, M., and Ijiri, M. (2003). Differential frost heave and sorted patterned ground: field measurements and a laboratory experiment. *Geomorphology*, 52(1-2):73–85.
- McKenzie, J. M. and Voss, C. I. (2013). Permafrost thaw in a nested groundwater-flow system. *Hydrogeology Journal*, 21(1):299–316.
- Messerli, B., Viviroli, D., and Weingartner, R. (2004). Mountains of the world: vulnerable water towers for the 21st century. *AMBIO: A Journal of the Human Environment*, 33(sp13):29–34.
- Miehe, G., Miehe, S., Kaiser, K., Jianquan, L., and Zhao, X. (2008). Status and dynamics of the Kobresia pygmaea ecosystem on the Tibetan Plateau. *AMBIO: A Journal of the Human Environment*, 37(4):272–279.
- Müller, J., Vieli, A., and Gärtner-Roer, I. (2016). Rock glaciers on the run—understanding rock glacier landform evolution and recent changes from numerical flow modeling. *The Cryosphere*, 10(6):2865–2886.
- NAMORS (2017). Meteorological Data for the NAMORS research station. ITP – CAS Lhasa.
- Notti, D., Herrera, G., Bianchini, S., Meisina, C., García-Davalillo, J. C., and Zucca, F. (2014). A methodology for improving landslide PSI data analysis. *International journal of remote sensing*, 35(6):2186–2214.
- Osmanoğlu, B., Sunar, F., Wdowinski, S., and Cabral-Cano, E. (2016). Time series analysis of InSAR data: Methods and trends. *ISPRS Journal of Photogrammetry and Remote Sensing*, 115:90–102.
- Riseborough, D., Shiklomanov, N., Etzelmüller, B., Gruber, S., and Marchenko, S. (2008). Recent advances in permafrost modelling. *Permafrost and Periglacial Processes*, 19(2):137–156.
- Rouyet, L., Lauknes, T. R., Christiansen, H. H., Strand, S. M., and Larsen, Y. (2019). Seasonal dynamics of a permafrost landscape, Adventdalen, Svalbard, investigated by InSAR. *Remote Sensing of Environment*, 231:111236.

- Schuur, E. A., McGuire, A. D., Schädel, C., Grosse, G., Harden, J., Hayes, D. J., Hugelius, G., Koven, C. D., Kuhry, P., Lawrence, D. M., et al. (2015). Climate change and the permafrost carbon feedback. *Nature*, 520(7546):171–179.
- Shur, Y., Hinkel, K. M., and Nelson, F. E. (2005). The transient layer: implications for geocryology and climate-change science. *Permafrost and Periglacial Processes*, 16(1):5–17.
- Song, C., Huang, B., Ke, L., and Richards, K. S. (2014). Seasonal and abrupt changes in the water level of closed lakes on the Tibetan Plateau and implications for climate impacts. *Journal of Hydrology*, 514:131–144.
- Sowter, A., Bateson, L., Strange, P., Ambrose, K., and Syafiudin, M. F. (2013). DInSAR estimation of land motion using intermittent coherence with application to the South Derbyshire and Leicestershire coalfields. *Remote Sensing Letters*, 4(10):979–987.
- Strozzi, T., Caduff, R., Jones, N., Barboux, C., Delaloye, R., Bodin, X., Käab, A., Mätzler, E., and Schrott, L. (2020). Monitoring Rock Glacier Kinematics with Satellite Synthetic Aperture Radar. *Remote Sensing*, 12(3):559.
- Tian, K., Liu, J., Kang, S., Campbell, I. B., Zhang, F., Zhang, Q., and Lu, W. (2009). Hydrothermal pattern of frozen soil in Nam Co lake basin, the Tibetan Plateau. *Environmental geology*, 57(8):1775–1784.
- Wang, X., Liu, L., Zhao, L., Wu, T., Li, Z., and Liu, G. (2017). Mapping and inventorying active rock glaciers in the northern Tien Shan of China using satellite SAR interferometry. *Cryosphere*, 11(2).
- Wessel, B., Huber, M., Wohlfart, C., Marschalk, U., Kosmann, D., and Roth, A. (2018). Accuracy assessment of the global TanDEM-X Digital Elevation Model with GPS data. *ISPRS Journal of Photogrammetry and Remote Sensing*, 139:171–182.
- Whalley, W. B. and Azizi, F. (2003). Rock glaciers and protalus landforms: Analogous forms and ice sources on Earth and Mars. *Journal of Geophysical Research: Planets*, 108(E4).
- Wu, Q., Zhang, T., and Liu, Y. (2010). Permafrost temperatures and thickness on the Qinghai-Tibet Plateau. *Global and Planetary Change*, 72(1-2):32–38.
- Yagüe-Martínez, N., Prats-Iraola, P., Gonzalez, F. R., Brcic, R., Shau, R., Geudtner, D., Eineder, M., and Bamler, R. (2016). Interferometric processing of Sentinel-1 TOPS data. *IEEE Transactions on Geoscience and Remote Sensing*, 54(4):2220–2234.
- Yao, T., Liu, X., Wang, N., and Shi, Y. (2000). Amplitude of climatic changes in Qinghai-Tibetan Plateau. *Chinese Science Bulletin*, 45(13):1236–1243.

- Yao, T., Masson-Delmotte, V., Gao, J., Yu, W., Yang, X., Risi, C., Sturm, C., Werner, M., Zhao, H., He, Y., et al. (2013). A review of climatic controls on $\delta^{18}\text{O}$ in precipitation over the Tibetan Plateau: Observations and simulations. *Reviews of Geophysics*, 51(4):525–548.
- Yao, T., Pu, J., Lu, A., Wang, Y., and Yu, W. (2007). Recent glacial retreat and its impact on hydrological processes on the Tibetan Plateau, China, and surrounding regions. *Arctic, Antarctic, and Alpine Research*, 39(4):642–650.
- Ye, Q., Zong, J., Tian, L., Cogley, J. G., Song, C., and Guo, W. (2017). Glacier changes on the Tibetan Plateau derived from Landsat imagery: mid-1970s–2000–13. *Journal of Glaciology*, 63(238):273–287.
- Yu, Z., Wu, G., Keys, L., Li, F., Yan, N., Qu, D., and Liu, X. (2019). Seasonal variation of chemical weathering and its controlling factors in two alpine catchments, Nam Co basin, central Tibetan Plateau. *Journal of Hydrology*, 576:381–395.
- Zhang, G., Kang, S., Fujita, K., Huintjes, E., Xu, J., Yamazaki, T., Haginoya, S., Wei, Y., Scherer, D., Schneider, C., et al. (2013a). Energy and mass balance of Zhadang glacier surface, central Tibetan Plateau. *Journal of Glaciology*, 59(213):137–148.
- Zhang, G., Kang, S., Fujita, K., Huintjes, E., Xu, J., Yamazaki, T., Haginoya, S., Wei, Y., Scherer, D., Schneider, C., et al. (2013b). Energy and mass balance of Zhadang glacier surface, central Tibetan Plateau. *Journal of Glaciology*, 59(213):137–148.
- Zhang, G., Li, J., and Zheng, G. (2017). Lake-area mapping in the Tibetan Plateau: an evaluation of data and methods. *International journal of remote sensing*, 38(3):742–772.
- Zhang, Y. and Michalowski, R. L. (2015). Thermal-hydro-mechanical analysis of frost heave and thaw settlement. *Journal of geotechnical and geoenvironmental engineering*, 141(7):04015027.
- Zhao, R., Li, Z.-w., Feng, G.-c., Wang, Q.-j., and Hu, J. (2016). Monitoring surface deformation over permafrost with an improved SBAS-InSAR algorithm: With emphasis on climatic factors modeling. *Remote Sensing of Environment*, 184:276–287.
- Zhou, S., Kang, S., Chen, F., and Joswiak, D. R. (2013). Water balance observations reveal significant subsurface water seepage from Lake Nam Co, south-central Tibetan Plateau. *Journal of Hydrology*, 491:89–99.
- Zink, M., Bachmann, M., Brautigam, B., Fritz, T., Hajnsek, I., Moreira, A., Wessel, B., and Krieger, G. (2014). TanDEM-X: The new global DEM takes shape. *IEEE Geoscience and Remote Sensing Magazine*, 2(2):8–23.

- Zou, D., Zhao, L., Yu, S., Chen, J., Hu, G., Wu, T., Wu, J., Xie, C., Wu, X., Pang, Q., et al. (2017). A new map of permafrost distribution on the Tibetan Plateau. *The Cryosphere*, 11(6):2527.
- Zwieback, S., Hensley, S., and Hajnsek, I. (2017). Soil moisture estimation using differential radar interferometry: Toward separating soil moisture and displacements. *IEEE Transactions on Geoscience and Remote Sensing*, 55(9):5069–5083.

Chapter 5

Rock glacier inventory of the western Nyainqêntanglha Range, Tibetan Plateau, supported by InSAR time series and automated classification

Eike Reinosch¹, Markus Gerke¹, Björn Riedel¹, Antje Schwalb², Qinghua Ye³, Johannes Buckel⁴

¹ Institute of Geodesy and Photogrammetry, Technische Universität Braunschweig, Braunschweig, Germany

² Institute of Geosystems and Bioindication, Technische Universität Braunschweig, Langer Kamp 19C, 38106 Braunschweig, Germany

³ Institute of Tibetan Plateau Research (ITP), Chinese Academy of Sciences (CAS), Building 3 Yard 16, Lincui Road, 100101 Beijing, China

⁴ Institute of Geophysics and extraterrestrial Physics, Technische Universität Braunschweig, Braunschweig, Germany

Corresponding author: Eike Reinosch (e.reinosch@tu-braunschweig.de)

Abstract

The western Nyainqêntanglha Range on the Tibetan Plateau reaches an elevation of 7162 m and is characterized by an extensive periglacial environment under semi-arid climatic conditions. Rock glaciers play an important part of the water budget in high mountain areas and recent studies suggest that they may even act as climate resistant water storages. In this study we present the first rock glacier inventory of this region containing 1433 rock glaciers over an area of 4622 km. To create the most reliable inventory we combine manually created rock glacier outlines with an automated classification approach. The manual outlines were generated based on surface elevation data, optical satellite imagery and a surface velocity estimation. This estimation was generated via InSAR time series

analysis with Sentinel-1 data from 2016 to 2019. Our pixel-based automated classification was able to correctly identify 87.8 % of all rock glaciers in the study area at a true positive rate of 69.5 %. 65.9 % of rock glaciers are classified as transitional with surface velocities of 1 to 10 cm yr⁻¹. 18.5 % are classified as active with higher velocities of up to 87 cm yr⁻¹. The southern windward side of the mountain range contains more numerous and more active rock glaciers. We attribute this to higher moisture availability supplied by the Indian Monsoon.

5.1 Introduction

5.1.1 Importance of rock glacier inventories

Rock glaciers are lobate or tongue-shaped landforms developing through gravity-driven creep of frozen debris and interstitial ice (Barsch, 1996; French, 2017; Haeberli et al., 2006). Rock glaciers play an important part in the water budget of high mountain areas (Jones et al., 2018). Their capacity to store fresh water in winter makes them important sources of fresh water in summer for semi-arid and arid regions such as the central Andes and the Sierra Nevada (Azócar and Brenning, 2010; Rangescroft et al., 2015; Villarroel et al., 2018; Halla et al., 2021; Millar et al., 2013). Recent studies have highlighted the importance of rock glaciers to act as temperature and climate resistant water storages and buffers to hydrological seasonality due to the insulating effect of the debris (Jones et al., 2018; Anderson et al., 2018; Brighenti et al., 2019). Their importance to mountain hydrology is likely to increase over the coming decades due to global glacial retreat (Jones et al., 2019). Rock glacier inventories have been used to estimate the regional lower permafrost limit (Ran and Liu, 2018; Scotti et al., 2013), though subsurface ice may still be found in favorable conditions at much lower elevations (Colucci et al., 2019). Rock glaciers have displayed accelerated motion rates over the past decades in the European Alps, northern Norway, the Carpathian Mountains and the Tien Shan (Eriksen et al., 2018; Necsoiu et al., 2016; Kääh et al., 2021). This can potentially lead to hazardous mass wasting processes due to destabilizing rock glaciers (Scotti et al., 2017; Marcer et al., 2019). The potential of rock glaciers to act as climate resistant water storages combined with the importance of the Tibetan Plateau (TP) as a source of fresh water to ~1.65 billion people in Asia (Cuo and Zhang, 2017) and the amplified warming effect of climate change on the TP (Kang et al., 2010), emphasize the necessity to study rock glacier distribution on the TP.

5.1.2 Rock glacier morphology

The precise definition of what constitutes a rock glacier and its potential origins have been discussed but remain contested still. Rock glaciers are described as the visible expression of cumulative deformation by long-term creep of ice/debris mixtures under permafrost conditions (Berthling, 2011). Rock glaciers may develop in periglacial, paraglacial or glacial environments (Knight et al., 2019). They may exist in areas where permafrost is unlikely outside the rock glaciers themselves when gravity-driven creep extends the landform beyond the expected periglacial zone (Bolch and Gorbunov, 2014). They are typical landforms of high mountain environments and can extend up to multiple kilometers in length and several hundred meters to a kilometer in width. Rock glacier debris often originates from avalanche processes and rock falls, which can be triggered by continuous headwall weathering, sudden heavy precipitation or earthquakes (Haeberli et al., 2006). Rock glaciers may also develop from frozen moraines or debris-covered glaciers (Anderson et al., 2018; Lilleøren and Etzelmüller, 2011; Monnier and Kinnard, 2015). The latter often include glacial ice within the rock glacier body. Rock glaciers developing without a connection to a glacier form ice within the debris by freezing rain or melt water and/or by burying accumulations of snow and ice (Burger et al., 1999).

5.1.3 Rock glacier activity

Rock glaciers that contain ice are categorized as active if they display motion and as inactive if they are unmoving. Unmoving rock glaciers without ice in their bodies are referred to as fossil or relict rock glaciers (Barsch, 1996). Active rock glaciers often display horizontal velocities of centimeters to decimeters per year but may reach velocities of several meters per year (Eriksen et al., 2018; Kääb et al., 2021). Velocities are influenced by changes of ground temperature as well as moisture availability, which may accelerate or decelerate a rock glacier on a decadal scale (Kääb et al., 2007; Kellerer-Pirklbauer and Kaufmann, 2012; Kenner et al., 2020; Cicoira et al., 2019). Rock glaciers also display strong seasonal variations in their surface motion in many cases, with higher velocities in summer and autumn compared to winter and spring (Sorg, Annina and Kääb, Andrea and Roesch, Andrea and Bigler, Christof and Stoffel, Markus, 2015; Wirz et al., 2016; Strozzi et al., 2020).

5.1.4 Creating rock glacier inventories

The spatial coverage and comparability of rock glacier inventories are lagging behind inventories of glaciers on a global scale (Jones et al., 2019). This is due to a number of rea-

sons including: (1) The necessity of high-resolution satellite data to identify rock glaciers and to distinguish them from surrounding landforms. (2) The difficulty in judging their status of activity and their ice content. (3) The subjectivity of identifying and outlining rock glaciers and the dependency on the analyst's experience to distinguish them from similar landforms such as debris-covered glaciers and ice-cored glacial moraines (Lilleøren and Etzelmüller, 2011; Brardinoni et al., 2019). The availability of freely accessible global map providers like Bing Map, Google Maps or Zoom Earth are alleviating issue (1). However, remote areas often display lower temporal and spatial data coverage compared to urban centers and the positional accuracy may vary. Microwave remote sensing data and Interferometric Synthetic Aperture Radar (InSAR) techniques have been applied successfully to determine rock glacier activity in some large-scale inventories in recent years (Table 5.1). This addresses issue (2). InSAR techniques allow monitoring surface motion on the order of a few millimeters to decimeters per year depending on the technique used, the wavelength and the revisit time of the satellite constellation (Crosetto et al., 2016). Issue (3) has led to problems in the comparability of rock glacier inventories of different regions due to varying inventorying methodologies. Identifying a landform as a rock glacier and subsequently manually creating its outline is subjective. This leads to large variabilities in both the number of rock glaciers and their surface areas when comparing the rock glacier inventories created by different analysts (Brardinoni et al., 2019). The recently formed action group on 'Rock glacier inventories and kinematics' of the International Permafrost Association (IPA) aims to address these issues. They explore the feasibility of developing widely accepted standard guidelines for inventorying rock glaciers on a global scale, including information on their kinematics (Delaloye et al., 2018; Delaloye and Echelard, 2020). Furthermore, varying techniques to detect rock glaciers automatically based on remote sensing data have achieved promising results (Brenning, 2009; Brenning et al., 2012; Robson et al., 2020; Marcer, 2020; Kofler et al., 2020). In this study we follow the practical guidelines of the IPA action group to generate a manual inventory and compare it to automated classification results to work towards a global rock glacier inventory.

5.1.5 Purpose of this study

We present an inventory of actively moving rock glaciers within the western Nyainqêntanglha Range on the south-eastern TP (Fig. 5.1). We combine a manual approach with an automated classification algorithm to generate an exhaustive rock glacier inventory. Following the IPA guidelines ensures the comparability with future rock glacier inventories following these guidelines. Combining the manual approach with a semi-automated classification increases the reliability of the inventory. This inventory is the first of its kind in this mountain range and will help to fill the gaps in a global rock glacier inventory. We use

Sentinel-1 satellite data of 2016 to 2019 processed with InSAR time series techniques to estimate the inter-annual surface velocity and infer rock glacier activity. In the following we introduce our study area and related work of previous studies. We then explain the data and methods we used to generate the inventory. Finally we present the inventory followed by a discussion on the limitations of our methods, potential implications regarding the regional climate and finally our conclusions.

Table 5.1: *Rock glacier inventories with velocity information based on Differential Interferometric Synthetic Aperture Radar (DInSAR) techniques.*

Region	Number of rock glaciers	Period of InSAR velocity data	InSAR technique
Tien Shan Kääb et al. (2021)	551	1998 to 2018	DInSAR
Dry Andes Villarroel et al. (2018)	2116	2014 to 2017	DInSAR
Tien Shan Wang et al. (2017)	261	2007 to 2009	DInSAR
Swiss Alps Barboux et al. (2014)	908	1991 to 2012	DInSAR
Sierra Nevada Liu et al. (2013)	59	2007 to 2008	DInSAR
Swiss Alps Strozzi et al. (2004)	not specified (~30)	1995 to 1999	DInSAR

5.2 Study area: The western Nyainqêntanglha Range

5.2.1 Climate

The western Nyainqêntanglha Range is located in the south-eastern center of the TP (Fig. 5.1) with an elevation of approximately 4500 to 7162 m. The median elevation of the study area is 5369 m with an interquartile range of 5109 to 5632 m. The study area is about 230 km in length and covers an area of 4622 km². The mountain range strikes from the south-west to the north-east, forming a climatic divide as a topographic barrier. Glaciers cover the highest parts and most other areas are considered to be in

the periglacial zone (Keil et al., 2010). The northern side of the mountain range drains mainly into the endorheic Nam Co, currently the second largest lake on the central TP with a surface area of 2018 km² (Zhang et al., 2017). Catchments on the south-eastern side drain into the Yangbajain-Damxung Valley as part of the Tsangpo-Brahmaputra River system. The climate is controlled by the Indian Monsoon system in the south and the dry continental climate of Central Asia from the north-west (Fig. 5.1B, Wünnemann et al., 2018). The Indian Monsoon delivers the majority of the annual precipitation within the summer period from June to September, while the Westerlies bring dry continental air and semi-arid conditions during the winter months (Yao et al., 2013). Annual precipitation is higher on the southern side of the mountain range with 460 mm in Damxung from 1971 to 2000 compared to 406 mm at Nam Co Monitoring and Research Station for Multisphere Interactions (NAMORS) from 2006 to 2017 (Fig. 5.2, Zhang et al., 2013b; Anslan et al., 2020). A meteorological station at Zhadang Glacier recorded an annual precipitation between 487 mm and 568 mm from 2009 to 2011 (Zhang et al., 2013c). The mean annual air temperatures at those meteorological stations during the same time periods were 1.6 °C, -0.6 °C and -5.9 °C respectively.

5.2.2 Glaciers and lakes

The effects of climate change on glaciers and glacial lakes in the western Nyainqêntanglha Range and the TP as a whole are well documented. Large-scale remote sensing studies show, that glaciers lost 22 % of their surface area from 1977 to 2010 (Wang et al., 2013) with a glacier mass balance of -0.3 m yr⁻¹ from 2000 to 2017 (Ren et al., 2020). Most other regions on the TP show similar negative glacier mass balances with the exception of the northern TP, where positive mass balances are documented for some regions (Neckel et al., 2014). Multiple studies have investigated the changes to the extent of the Nam Co over the past decades, reporting an average increase of lake surface area of 0.1 % per year since the 1970s (Zhang et al., 2017; Li et al., 2017). The contribution of increased glacial melt water to the increase in lake level was estimated to be 10 % from 1971 to 2004 and 30 % from 1990 to 2010 for different parts of the mountain range (Zhu et al., 2010; Lei et al., 2013). Glacial lakes have also been expanding greatly both in number and surface area. Increases in the surface area of glacial lakes from 2.69 to 7.15 km² between 1972 and 2009 and 6.75 to 9.12 km² between 1976 and 2018 have been reported for different parts of our study area (Wang et al., 2013; Luo et al., 2020).

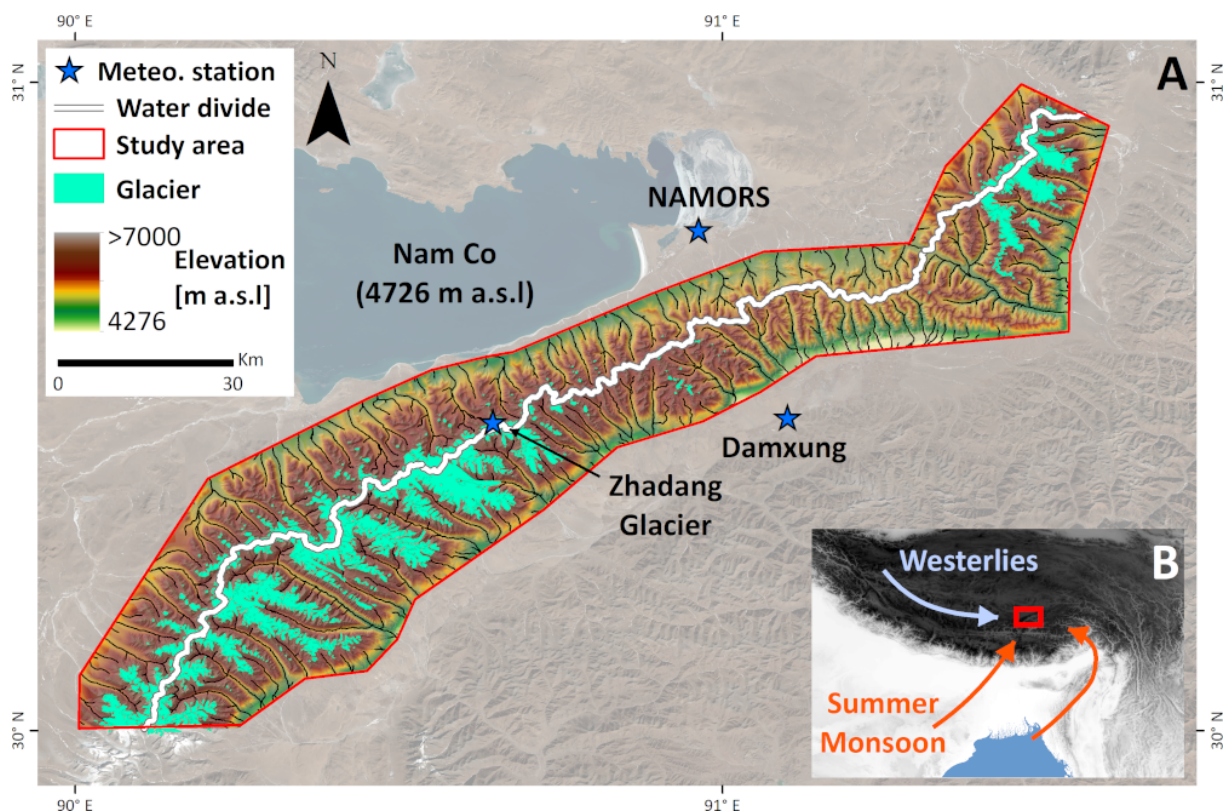


Figure 5.1: (A) Overview of the study area within the western Nyainqentanglha Range and the location on the Tibetan Plateau. We display glacier outlines and background optical imagery based on Sentinel-2 data of 30 January 2018 (©Copernicus Sentinel data 2018, processed by ESA) and the geoid elevation of the TanDEM-X (©DLR, 2017; geoid heights of EGM96). (B) Major atmospheric systems affecting the study area in summer (Indian Monsoon) and winter (Westerlies) above the SRTM v4 elevation of the Tibetan Plateau (Wünnemann et al., 2018; Jarvis et al., 2008).

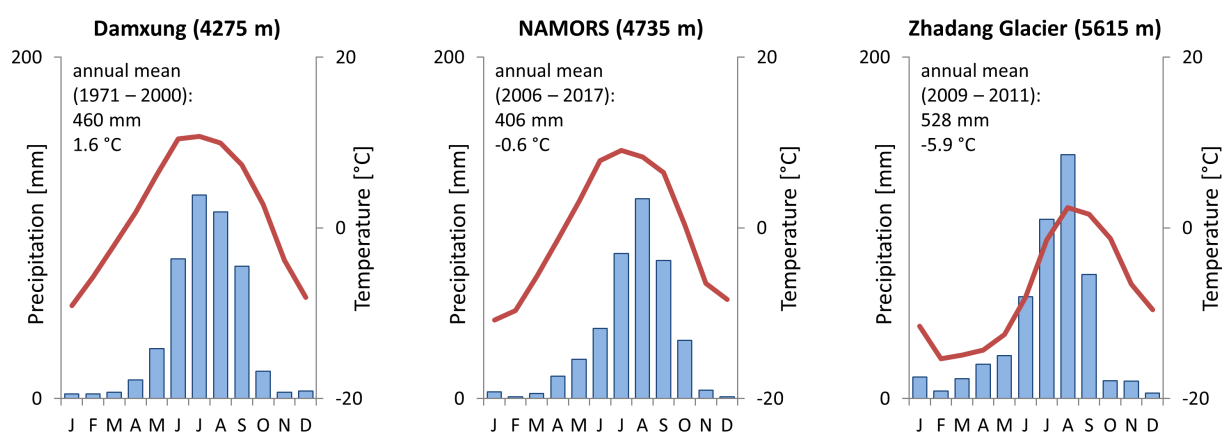


Figure 5.2: Meteorological data of three stations at the study area. Their locations are shown in Fig. 5.1 (Zhang et al., 2013b; Anslan et al., 2020; Zhang et al., 2013c).

5.2.3 Permafrost and periglacial landforms

The study of permafrost and associated periglacial landforms in the western Nyainqentanglha Range has received much less attention compared to glaciers and lakes (Anslan

et al., 2020). InSAR time series analysis display seasonal heave-thaw cycles with an amplitude of up to 2.5 cm near water bodies (Li et al., 2015; Reinosch et al., 2020). Large-scale permafrost maps of the TP predict permafrost for most non-glaciated parts of the mountain range (Zou et al., 2017; Obu et al., 2019). Field studies estimate a lower permafrost limit of 5300 m to 5450 m in two north-orientated catchments (Tian et al., 2006; Buckel et al., 2021). They identified a small number of rock glaciers displaying moderate velocities of 5 – 10 cm yr⁻¹ (Buckel et al., 2021). Rock glacier inventories on the TP are rare, though one recently identified 295 rock glaciers in Daxue Shan, south-eastern TP (Ran and Liu, 2018). Our study is the first to provide a rock glacier inventory of the western Nyainqêntanglha Range.

5.3 Data and Methods

Our general workflow to create the rock glacier inventory contains the following steps (Fig. 5.3): First we generate the line-of-sight (LOS) surface velocity estimation from Sentinel-1 InSAR data and project it along the direction of the steepest slope (Sections 5.3.1 to 5.3.3). Then we create the manual rock glacier outlines based on optical satellite imagery, surface elevation data and surface velocity (Section 5.3.5). A subset of the manually created rock glacier outlines is used to train the maximum likelihood algorithm. A different subset acts as validation to identify the best feature selection for the automated classification. Finally we create the automated classification results based on the resulting optimal feature selection and validate it against the entire manually created inventory (Section 5.3.6).

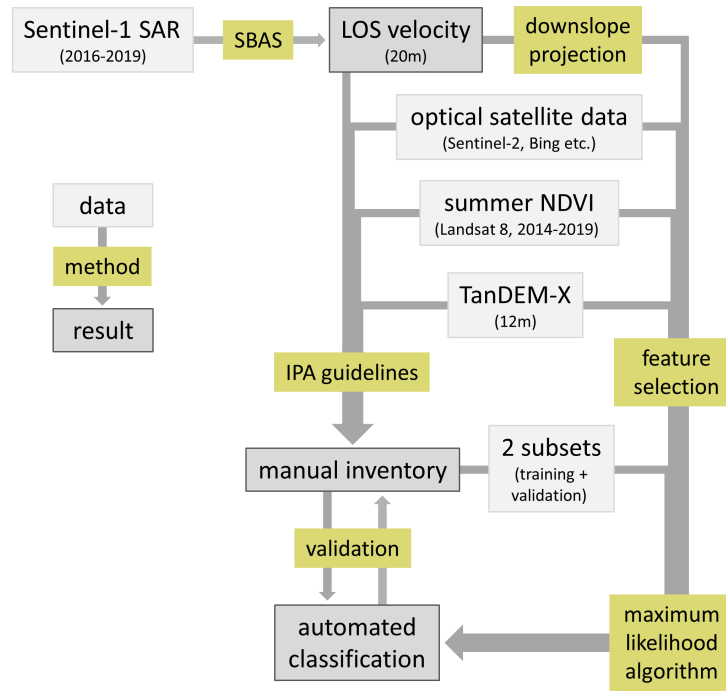


Figure 5.3: *The workflow we followed to generate the manual rock glacier inventory and the automated classification results.*

5.3.1 InSAR processing

Interferograms are a spatial representation of the phase difference between two SAR acquisitions and can be used to determine LOS surface displacement (Crosetto et al., 2016). The phase stability, so-called coherence, is often used to represent the quality of an interferogram. A variety of different InSAR algorithms are available to process consecutive interferograms to study surface displacement over several years, often referred to as InSAR time series analysis. InSAR time series analysis generally increases the accuracy of surface displacement estimations, as temporally uncorrelated atmospheric effects can be removed with filters (Osmanoğlu et al., 2016). Most studies employing InSAR techniques to investigate rock glacier velocity use individual SAR pairs (DInSAR) or relatively short time series analysis during the snow-free months (Villarroel et al., 2018; Strozzi et al., 2020; Wang et al., 2017; Liu et al., 2013). Other related approaches include pixel tracking of optical or SAR images, though these are generally only used for fast-moving rock glaciers or for long temporal gaps between data acquisitions (Eriksen et al., 2018; Käab et al., 2021). The winters in our study area are semi-arid, due to the dominance of the mid-latitude-westerlies during those months (Wünnemann et al., 2018). Our field work has shown that snow storms may occur in autumn, which causes decorrelation of InSAR data. The dry winter climate leads to stable backscatter properties of the frozen ground, which is reflected by good coherence values. We therefore opted to use a modified version of the Small Baseline Subset (SBAS) method (Berardino et al., 2002), which we performed with the ENVI SARscape software (©Sarmap SA, 2001-2020). The original

SBAS method requires a pixel to be coherent in all interferograms during the observation period. The results often show large data gaps in seasonally variable areas where the coherence may not be high enough all the time due to changing backscatter properties. The SBAS algorithm we employ was originally described as ‘intermittent SBAS’ (Sowter et al., 2013) and is included in SARscape as an option of the SBAS processing chain labelled ‘disconnected blocks’. Intermittent SBAS interpolates time periods where the coherence of a pixel drops below the chosen coherence threshold in some interferograms. This may occur due to heavy rainfall, snow cover or large displacement. Intermittent SBAS results in a greatly improved spatial coverage compared to the original SBAS algorithm for partially vegetated study areas (Sowter et al., 2013; Bateson et al., 2015). In our study area it helps to interpolate time periods in spring and autumn when the transition between snow-free summers and frozen ground in winter causes decorrelation. For our analysis we chose a coherence threshold of 0.2, which is lower than the threshold of 0.3 used by others for intermittent SBAS methods (Sowter et al., 2013; Bateson et al., 2015). The lower threshold is justified in our opinion, as good spatial coverage is most important for this study. Pixels need to exceed the coherence threshold in at least 60 % of all interferograms during our three-year observation period. A pixel may therefore contain up to 40 % interpolated information, though the median value of all pixels on rock glaciers is only 2 %.

We use Sentinel-1 Level-1 single look complex data from the interferometric wide swath mode to perform our InSAR time series analysis. The wide swath mode has a ground resolution of 20 m in azimuth and 5 m in range (Yagüe-Martínez et al., 2016). We used a multi-looking factor of 4 in range and 1 in azimuth to achieve a ground resolution of 20 m. Sentinel-1 has been acquiring data since October 2014 but we only use data acquisitions from September 2016 to October 2019 due to temporal data gaps. Long temporal baselines of 48 to 96 days lead to strong underestimation of rock glacier velocity and poor coherence with earlier acquisitions. Sentinel-1 emits at a wavelength of ~ 5.6 cm (Notti et al., 2014). Displacements larger than half the emitted wavelength between two acquisitions are likely to be underestimated during interferogram generation (Crosetto et al., 2016). A temporal baseline of 96 days would result in a maximum detectable velocity of 10.6 cm yr^{-1} in LOS. It would therefore make the distinction between active and transitional rock glaciers very difficult. Sentinel-1 acquisitions of 2016 are available at 24-day intervals and at 12-day intervals from 2017 onwards. We use 80 acquisitions in ascending and 74 in descending geometry. The longest temporal data gap occurs in the summer of 2017. For the descending data set this causes a maximum temporal baseline of 72 days between two acquisitions during that time. There is no data gap in the ascending data set from September 2016 onwards. We chose a maximum temporal baseline of 60 days for ascending acquisitions. This results in a maximum detectable velocity of 17.0

cm yr⁻¹ in ascending geometry and 14.2 cm yr⁻¹ in descending geometry. The velocity of faster landforms can therefore not be determined reliably though it can still be detected very well. We generated a total of 181 interferograms in ascending geometry and 163 in descending geometry for the three-year observation period. The time-position plots for both the ascending and descending time series are included in the supplement. Some parts of the study area show coherence values below our chosen threshold of 0.2, especially in the north-eastern part in the descending geometry. We therefore selected a temporal subset of 14 interferograms for ascending and 13 interferograms for descending geometry from October 2017 to February 2018. This time period displays good coherence values throughout the study area and we used the SBAS results of this shorter period to fill in spatial data gaps in our three-year time series results.

5.3.2 Removal of large-scale phase delay

It is necessary to carefully select stable reference points in the study area to achieve InSAR results with a high accuracy (Crosetto et al., 2016). Poorly selected reference points can introduce seasonal artefacts and inter-annual shifts leading to misinterpretation of displacement patterns. No long-term data from the global navigation satellite system is available for this area to act as reference points. We therefore selected likely stable areas on the outskirts of the mountain range for our reference points. These 385 reference points were placed both along the northern and the southern side of the mountain range. We only selected points without visible signs of displacement and with high coherence throughout all interferograms. We avoided areas near the valley bottom during the selection of our reference points, as they likely experience heaving and thawing related to freezing and thawing of the ground (Li et al., 2015; Reinosch et al., 2020). We applied an atmospheric high pass filter of 100 days and a low pass filter of 1200 m to reduce atmospheric artefacts.

5.3.3 Downslope projection

We projected the LOS surface velocity of both geometries in the direction of the steepest slope (Notti et al., 2014). The following areas were masked prior to the projection:

1. Areas of glaciers where free ice is visible.
2. Areas with a slope $< 2^\circ$, as these areas are generally too flat to support downslope motion (Matsuoka, 2001).
3. Areas with a low slope and strong vertical displacement signal (based on a decomposition of ascending and descending time series results). This displacement is likely not gravity-driven and therefore not directed along the steepest slope.

4. We masked wetlands and the immediate surrounding of rivers and lakes. Changing soil moisture in these areas may lead to a false identification of displacement (Zwieback et al., 2017).

To perform the downslope projection, we calculated a sensitivity coefficient with a value between 0.2 and 1 and divided the LOS velocity by this coefficient to receive the downslope velocity. A sensitivity coefficient of 1 represents slopes where the angle between the LOS vector and the downslope direction is zero. The sensitivity of the satellite to displacement in that direction is therefore very high. A sensitivity coefficient of 0.2 represents areas where the angle between the LOS vector and the downslope direction is large. The sensitivity of the satellite to displacement in that direction is therefore very small. Ascending and descending data sets have different LOS and their respective sensitivity coefficients are therefore also different when observing the same area. We included the spatial distribution of this sensitivity coefficient in the supplementary material. After projecting both ascending and descending data sets into the downslope direction, we combined both data sets according to the following criteria:

1. We only use the downslope projection of the more sensitive geometry in areas where the sensitivity coefficient of the more sensitive geometry is at least 50 % larger than the sensitivity coefficient of the other geometry and is larger than 0.2.
2. We calculate the mean value of the downslope projections of both geometries in all other areas, as the sensitivity of neither geometry is clearly superior.

When we refer to the velocity in the text hereafter, we are referring to the combined downslope velocity of both ascending and descending geometries. The only exception is where we specifically refer to the LOS velocity.

5.3.4 Optical satellite and DEM products

We use seven optical Landsat 8 acquisitions with a 30 m resolution to calculate the summer Normalized Difference Vegetation Index (NDVI) in our study area. The NDVI is calculated from the red and near infrared bands (bands 3 and 4 for Landsat 8) and is a measure of vegetation density and productivity. Moving rock glaciers are generally sparsely vegetated and have lower NDVI values than their immediate surrounding, potentially making NDVI a valuable indicator to identify rock glaciers (Brenning, 2009; Cannone and Gerdol, 2003). Combining multiple acquisitions is necessary due to the partial or full cloud cover associated with the summer monsoon climate in the study area. The Landsat 8 datasets

were acquired on the following dates: 12 August 2014, 30 July 2015, 16 May 2017, 1 June 2017, 20 June 2018, 25 July 2019 and 26 August 2019. We chose these dates, as they represent the Landsat 8 acquisitions with the lowest cloud cover during the growing season of May to September (Zhang et al., 2013a). The irregularity of these dates may introduce a bias but they were necessary to produce a NDVI map with near total coverage of the study area. We masked snow covered areas as well as clouds and their shadows prior to the calculation of the NDVI. The NDVI data sets were then merged into one raster with pixels present in multiple NDVI data sets receiving their mean value. The free ice glacier outlines were derived from a cloud-free Sentinel-2 acquisition of 30 January 2018 with a supervised maximum likelihood classification and checked manually.

We use the 12 m resolution TanDEM-X (©DLR, 2017) Digital Elevation Model (DEM) to perform all topographic analysis and to remove the topographic phase from the InSAR data. This global DEM was acquired between 2010 and 2015 using single-pass X-Band SAR interferometry and released by the German Aerospace Agency in 2017 (Zink et al., 2014). In our study area it has a vertical accuracy with an interquartile range of 0.26 to 0.40 m in areas with a slope $<40^\circ$ and 0.77 to 1.83 m in steeper areas.

5.3.5 Manually generating the rock glacier inventory

We followed the guidelines of the IPA Action Group on ‘Rock glacier inventories and kinematics’ to identify, outline and classify all actively moving rock glaciers in the study area (Delaloye et al., 2018). These guidelines consist of two detailed documents describing the baseline concepts and practical guidelines of which we used the versions 4.1 and 3.0.1 respectively (Delaloye and Echelard, 2020). The guidelines propose a general methodological framework for inventorying rock glaciers using InSAR. They recommend generating point information to identify individual rock glacier units and outlines to locate the moving part of the rock glacier. Our first step was therefore to identify rock glacier units based on the interpretation of surface velocity, optical satellite imagery and DEM data. The initial point identification was performed by one analyst and then checked and adjusted by two other experts. After this initial step the outlines were generated manually and checked and adjusted again by two experts.

The following data sets were used for the identification and outlining process: (1) Optical imagery from Bing Maps, Google Earth, Zoom Earth and a cloudless and largely snow-free 10 m resolution Sentinel-2 acquisition of 30 January 2018. (2) Hillshade and slope maps derived from the 12 m resolution TanDEM-X DEM and (3) NDVI derived from seven Landsat 8 summer acquisitions. (4) Median surface velocity from 2016 to 2019

based on Sentinel-1 data. Mandatory criteria of a rock glacier in our study are clearly discernible frontal and lateral margins overriding the surrounding terrain. In some instances, optical and DEM data may suggest different outlines due to georeferencing errors. The rock glacier outlines were drawn to match the DEM data in those cases, as we consider it to be more reliable. Optional criteria are a ridge-and-furrow topography associated with compressive flow and a reduced NDVI compared to the surrounding indicating a lack of vegetation due to active creeping. Rock glaciers are classified as transitional or active according to their surface velocity. Rock glaciers without a clear surface velocity are only included if the sensitivity of InSAR is low in this area, in which case they are included with an undefined activity. Debris-covered glaciers and rock glaciers represent two ends of a continuum (Haerberli et al., 2006; Anderson et al., 2018). Debris-covered glaciers with visible bodies of ice upslope are not included in the rock glacier inventory.

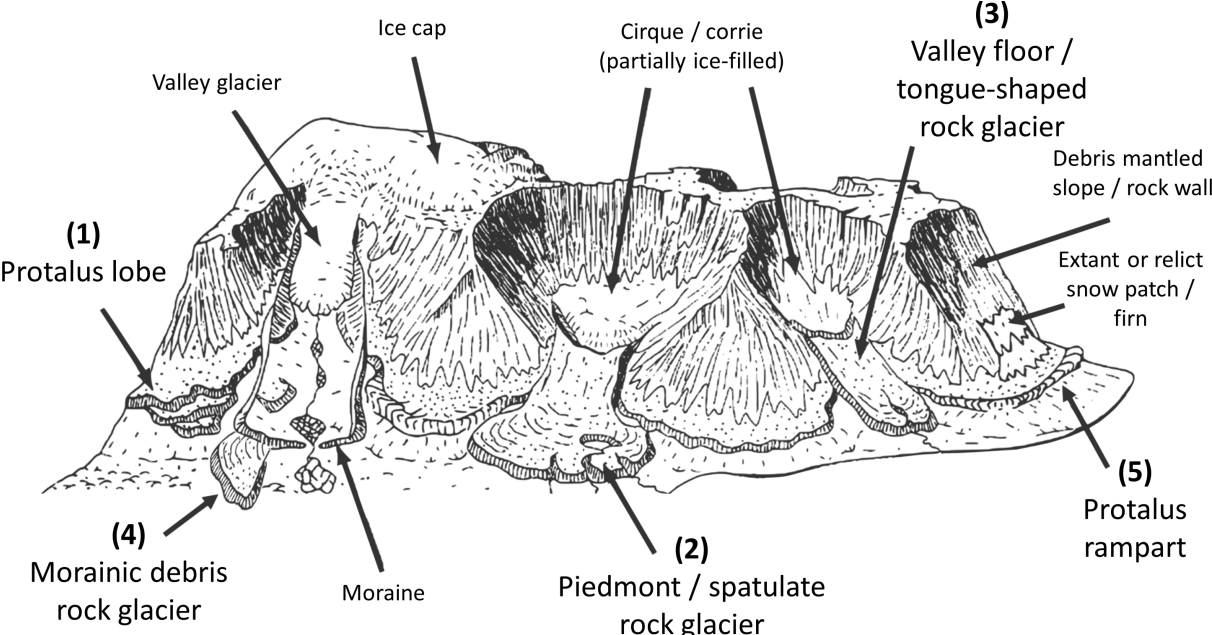


Figure 5.4: Schematic view on rock glacier morphology and protalus ramparts of the western Nyainqêntanglha Range. Numbers in parenthesis refer to the different morphological classes of rock glaciers (found in the inventory as the attribute ‘morph_clas’; changed after Hamilton and Whalley, 1995; Humlum, 1982). Examples of the different morphological classes in the study area are included in the supplementary material.

We decided to add an additional attribute not included in the IPA guidelines to the rock glacier outlines, to describe the morphology of the rock glacier in greater detail (Fig. 5.4). This attribute is important for further investigations regarding the evolution of rock glaciers in the mountain range. Here, we differentiate between debris rock glaciers (morainic origin) and talus rock glaciers (rock wall origin) (Barsch, 1996). For talus rock glaciers we adopted the definitions of detailed studies (Hamilton and Whalley, 1995; Humlum, 1982), as these fit well to the morphology of rock glaciers we observe in the western

Nyainqêntanglha Range. Protalus lobes and protalus ramparts are underlying landforms of debris mantles, scree slopes or rock walls.

5.3.6 Supervised maximum likelihood classification

Manually outlining rock glaciers is inherently subjective and dependent on the experience of the analyst. Multiple studies in recent years have therefore evaluated different classification algorithms and varying input parameters to automatically identify and classify rock glaciers (Brenning, 2009; Brenning et al., 2012; Robson et al., 2020; Marcer, 2020; Kofler et al., 2020). In addition to the manual approach described above, we also performed a pixel-based supervised maximum likelihood classification. We masked glaciers, flat areas, wetlands and the immediate surrounding of rivers and lakes (see Section 5.3.3). We used the ENVI software to perform the automated classification based on the surface features described in Table 5.2. The input parameters (such as elevation, slope or NDVI) which the classification algorithm uses to identify rock glaciers, are referred to as features hereafter. Our initial feature selection is comprised of features which were successfully used by similar studies to identify rock glaciers (Brenning, 2009; Brenning et al., 2012; Robson et al., 2020).

Firstly we identified the most suitable feature combination to automatically classify rock glaciers in the study area. We selected 40 rock glaciers with clear outlines spread throughout the study area to validate and adjust the performance of different feature combinations. Of those rock glaciers, 25 were randomly chosen as training areas, while the remaining 15 rock glaciers were used to validate the performance. We also selected 20 non rock glacier areas, to assess the number of pixels falsely classified as rock glacier. We evaluated different feature combinations to determine the most suitable selection to automatically classify rock glaciers in our study area. All features were resampled to the 12 x 12 m resolution of the TanDEM-X DEM. For the initial evaluation we performed the classification with the following five features: Elevation, slope, NDVI, slope variability and height error. Elevation, slope and NDVI scored highly in a similar study by (Brenning, 2009). Slope variability was to represent surface roughness. Height error was included to avoid false classifications of slopes with high noise levels due to the associated high surface roughness. To validate the importance of each of the five initial features, we then repeated the classification with just four of the initial five features (leaving out a different feature every time). All classifications with only four of the five initial features performed worse. This confirmed the importance of all five initial features. We then performed the classification again with the five initial features and different combinations of the remaining features to determine the optimal feature combination.

Table 5.2: *Description of all surface features evaluated for automated rock glacier classification.*

Feature	Description	Resolution
Elevation	The elevation displayed by the TanDEM-X DEM.	12 m
Slope	The slope derived from the TanDEM-X DEM.	12 m
Surface velocity	The downslope velocity is based on Sentinel-1 SAR data of 2016 to 2019.	20 m
Sentinel-2	Bands 2 and 3 of Sentinel-2 from 30 January 2018. These correspond to central wavelengths of 490 nm (blue light) and 560 nm (green light), respectively. (Drusch et al., 2012)	10 m
Height error	Auxiliary data set displaying the vertical accuracy of the TanDEM-X DEM.	12 m
North exposure / east exposure	These features are derived from a pixel's aspect, describing how close a pixel's aspect is to north exposure or east exposure.	12 m
Slope variability	Slope variability is a measure of surface roughness and represents the variation in slope within the 8 surrounding pixels (Otto et al., 2018)	12 m
NDVI	Summer NDVI of seven Landsat 8 acquisitions of 2014 to 2019.	30 m
Topographic position index (TPI)	The TPI displays the elevation of a pixel relative to the mean elevation of its surrounding (Weiss, 2001). Different landforms can be highlighted by choosing different search radii around the pixel to calculate the mean elevation. We evaluate the impact of the TPI with a radius of 200 m and with a radius of 800 m.	12 m

5.4 Results

5.4.1 Accuracy of surface velocity

It was not possible to validate the results of our time series analysis with other datasets such as terrestrial measurements as no such data was available to this study. In order to evaluate the reliability of our data, we therefore analyzed the surface displacement calculated by the time series analysis in areas that were likely stable during the observation period. We analyzed all areas with a slope $<5^\circ$ that are not part of a clearly subsiding structure or are in the vicinity (<200 m) of a stream, lake or wetland. The interquartile range of all pixels ($n = 194,114$) in likely stable areas in LOS is -0.3 to 0.6 cm yr^{-1} on the northern side of the mountain range in ascending -0.6 to 0.2 in cm yr^{-1} descending geometry. On the southern side ($n=67,230$) the interquartile range is -0.8 to -0.1 cm yr^{-1} in both geometries. The median coherence on rock glaciers is 0.33 with an interquartile range of 0.27 to 0.41 .

5.4.2 Manual Rock glacier inventory

The rock glacier inventory contains a total of 1433 rock glaciers (Table 5.3; Fig. 5.5). The IPA guidelines classify rock glaciers with a maximum velocity of 1 to 10 cm yr^{-1} as transitional, and faster rock glaciers as active. If the velocity of a rock glacier was very close to the higher activity class we assigned it the higher class. Relict rock glaciers with velocities below 1 cm yr^{-1} are not part of this inventory. We included rock glaciers without clear surface velocity signal, if their likely motion direction is one that InSAR is not sensitive to (i.e. north or south). These rock glaciers and other rock glaciers in areas with poor InSAR sensitivity are classified as ‘undefined’ regarding their activity. Undefined rock glaciers represent 15.6 % of the inventory, 65.9 % are transitional and 18.5 % are active. Rock glaciers cover a combined area of 124.9 km^2 equivalent to 2.7 % of the study area. Free ice glaciers cover a combined area of 575.7 km^2 . The water divide splits the study area into a northern and a southern side. The northern side has a median elevation of 5319 m, represents 41 % of the study area, 26.0 % of the free ice glacial area and contains 20.9 % of all rock glaciers. The southern side has a median elevation of 5411 m, represents 59 % of the study area, 74.0 % of the free ice glacial area and 79.1 % of all rock glaciers. 91.3 % of all active rock glaciers are located south of the water divide. Rock glaciers on the southern side are located at lower elevations (median = 5321 m) compared to the northern side (median = 5408 m). The lowest rock glacier reaches an elevation of 4498 m, while the highest reaches 5899 m. A summary of this data can be found in Table 5.3.

Table 5.3: Summary of spatial information of the rock glacier inventory. Elevation takes into account all pixels within rock glaciers of either the northern or southern side. Range refers to the difference in elevation between the highest and lowest pixel in a rock glacier.

	North (300 rock glaciers)			South (1133 rock glaciers)		
	Median	Interquartile range	Range	Median	Interquartile range	Range
Elevation [m]	5408	5319-5505	4943-5827	5321	5200-5442	4498-5899
Range [m]	81	59-117	19-311	104	72-156	14-584
Surface area[ha]	5.0	3.0-9.2	0.5-102.9	5.1	2.6-10.5	0.3-102.1

Protales lobes are the most common morphological class, representing 67.4 % of all rock glaciers and 51.6 % of the total rock glacier area (Fig. 5.6). Spatulate and tongue-shaped rock glaciers include the largest rock glaciers. Together they represent 13.3 % of all rock glaciers and 29.4 % of the rock glacier area. Morainic debris rock glacier are distributed at the highest altitude with a median elevation of 5478 m. Protales lobes and protalus ramparts display the lowest velocity with only 11.5 % of the former and none of the latter being active. Of the 24 spatulate rock glaciers 12 (50 %) are active and of the 166 tongue-shaped rock glaciers 65 (39.2 %) are active. Spatulate rock glaciers are only present south of the water divide.

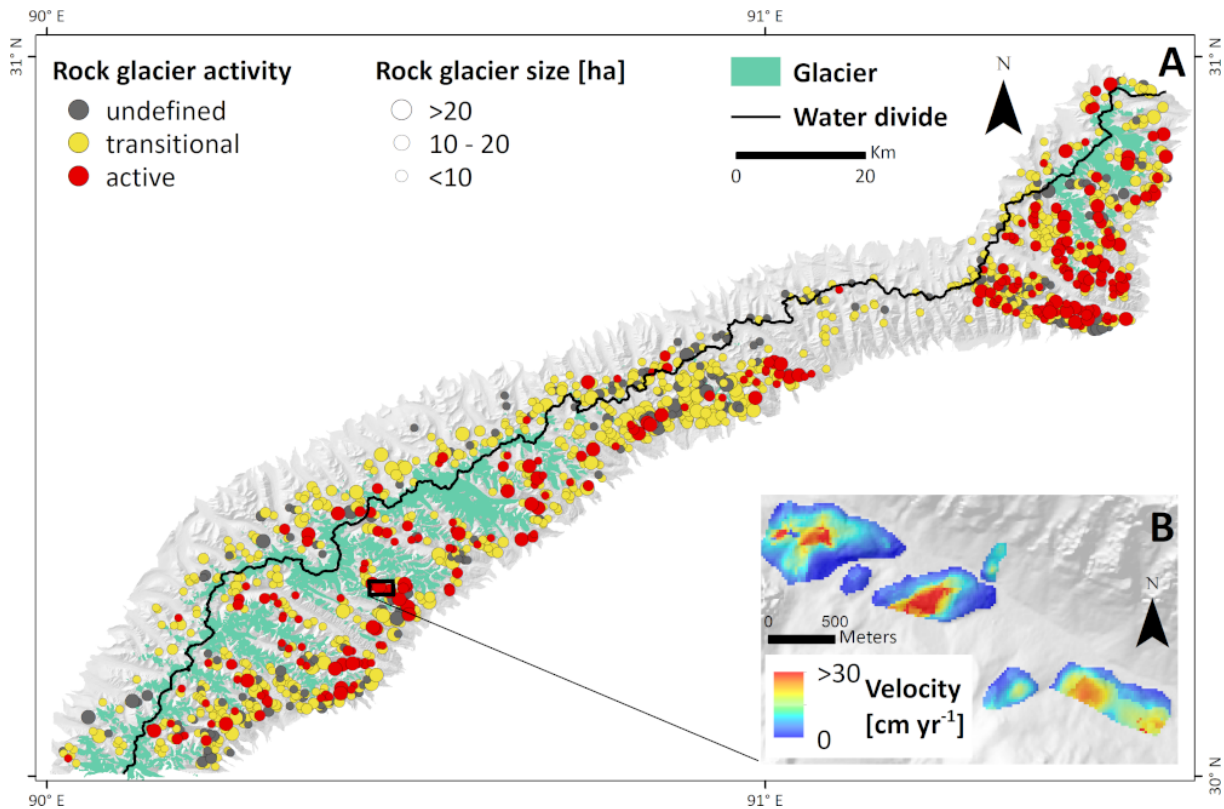


Figure 5.5: Overview of the manually determined rock glacier inventory. (A) Displays all rock glaciers mapped in the study area. Rock glacier activity is based on their median surface velocity of 2016 to 2019. The activity classification follows the IPA guidelines. Rock glaciers with surface velocity of 1 to 10 cm yr^{-1} are considered transitional and faster rock glaciers are considered active. (B) Shows a valley with active rock glaciers and their downslope velocity in greater detail (©Copernicus Sentinel data 2016-2019, processed by ESA; ©DLR, 2017).

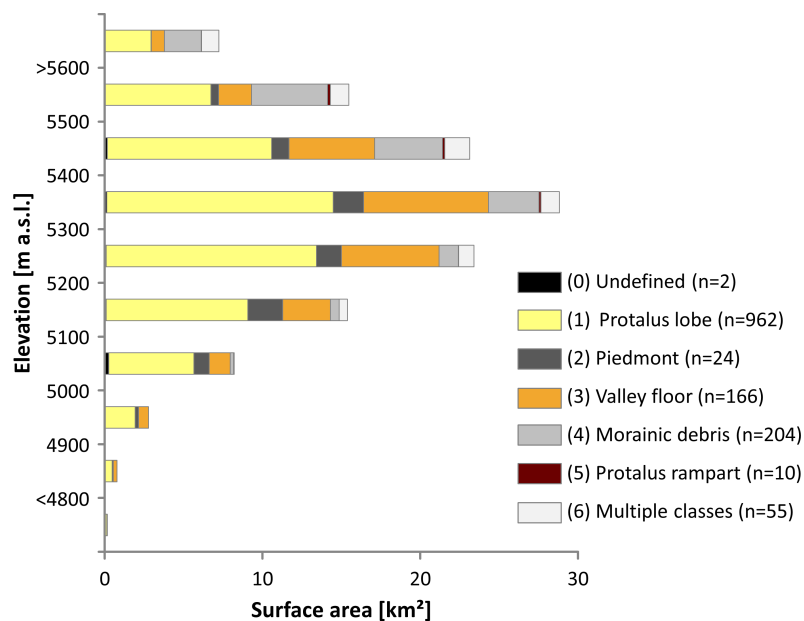


Figure 5.6: Elevation distribution of rock glacier area divided into their respective morphological classes. Numbers in parenthesis refer to the different classes of rock glaciers (found in the inventory as the attribute 'morph_clas').

5.4.3 Maximum likelihood estimation

The best result was achieved by combining the following nine features: Downslope velocity, elevation, slope, NDVI, slope variability, height error, TPI with 200 m radius and Sentinel-2 bands 2 and 3. We give an overview of these features in Table 5.2. 84.0 % of the pixels in the 15 validation rock glaciers were correctly classified with this combination. 3.2 % of the pixels in the 20 non rock glacier areas were falsely classified as rock glaciers. The true positive rate is therefore 84.0 % and the false positive rate is 3.2 % for our validation areas.

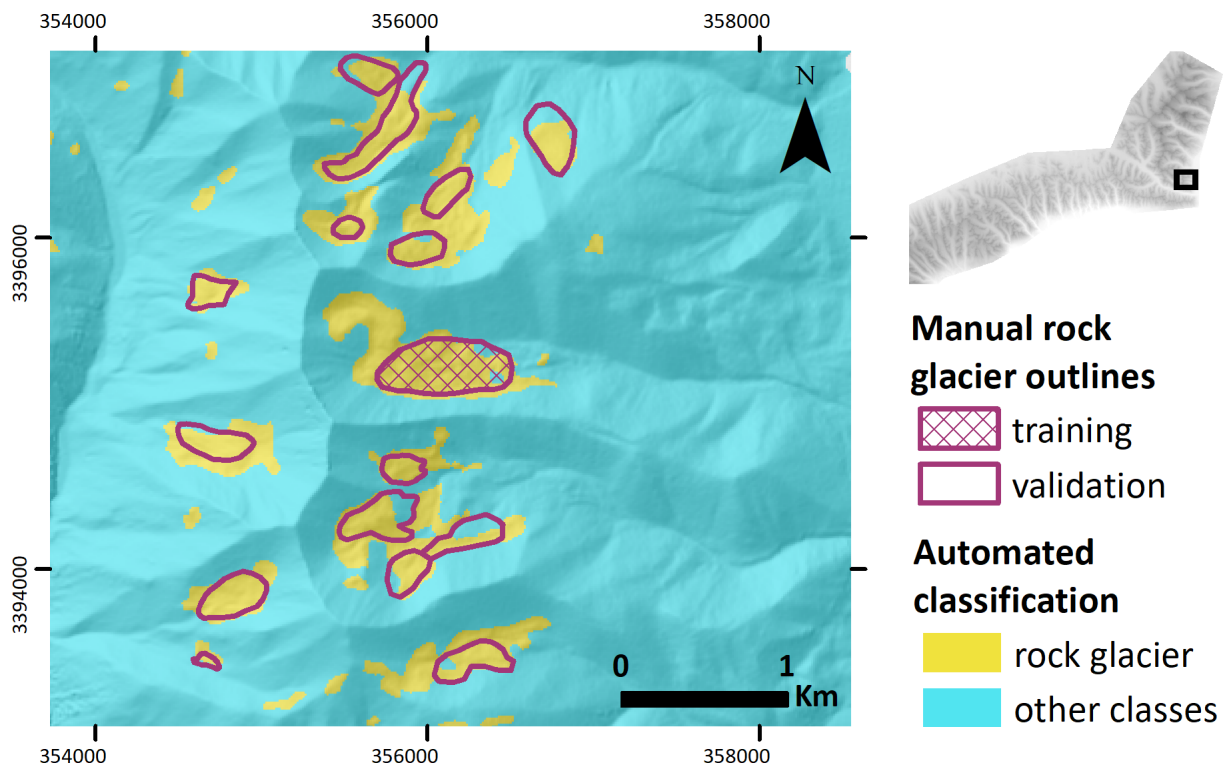


Figure 5.7: Example of the automated classification results compared to the manual rock glacier outlines. Yellow areas were classified as rock glacier and turquoise areas received other classes e.g debris slope, gully, ridge etc. (©Copernicus Sentinel data 2016-2019, processed by ESA; ©DLR TanDEM-X, 2017; Landsat-8 2014-2019 courtesy of U.S. Geological Survey).

Table 5.4: True positive rate (TP) and object identification (OI) of the automated classification for different size and activity classes.

Rock glacier classes		TP [%]	OI [%]
Entire inventory		69.5	87.8
Surface area	<10 ha	66.5	85.9
	10 - 20 ha	70.0	91.6
	>20 ha	69.3	96.5
Activity	Active	75.3	97.3
	Transitional	63.1	85.1
	Undefined	69.9	87.8

After identifying the most suitable features for the classification, we evaluated the performance of the automated classification compared to the entire manually created rock glacier inventory. We use three metrics to evaluate the performance: True positive rate (TP), false positive rate (FP) and object identification (OI). TP describes the percentage of pixels within the manual rock glacier outlines, which were correctly classified as rock glacier. FP refers to the percentage of pixels outside the manual outlines, which were falsely classified as rock glacier. OI describes the percentage of manual outlines with a TP of at least 30.0 %. 87.8 % of all rock glaciers were correctly identified by the OI (Table 5.4). Smaller rock glaciers are less likely to be identified. 85.9 % of rock glaciers smaller than 10 ha were identified, compared to 96.5 % for rock glaciers larger than 20 ha. 97.3 % of active rock glaciers, 85.1 % of transitional rock glaciers and 87.8 % of rock glaciers with undefined activity were identified. The entire inventory displays a TP of 69.5 % and a FP of 10.4 % (example area in Fig. 5.7). In total the automated classification predicts a combined rock glacier area of 428.4 km². This is equivalent to an overestimation of 243.0 % when compared to the 124.9 km² of manually outlined rock glaciers. After checking the manual outlines against the automatic classification we identified 18 additional rock glaciers. To assess the relative importance of the features to each other, we repeated the classification with only eight of the nine features (leaving out a different feature every time). The resulting feature ranking is presented in Table 5.5.

Table 5.5: Feature ranking showing the change in true positive rate (TP), false positive rate (FP) and object identification (OI) if a feature is excluded from the classification process. The three features with highest impact in each column are shown in bold letters.

Omitted feature	TP [%]	FP [%]	OI [%]
Downslope velocity	-1.9	+2.2	-0.9
TPI	-12.6	-4.2	-9.8
Slope variability	-9.6	-0.2	-10.1
Slope	-6.6	-2.8	-3.8
NDVI	-1.6	-0.1	-0.6
Height error	-4.6	-1.7	-4.3
Elevation	-3.5	-2.3	-1.3
Sentinel-2 Band 2	-4.4	-1.3	-3.8
Sentinel-2 Band 3	-5.9	-1.4	-4.7

5.5 Discussion

5.5.1 InSAR limitations

While InSAR time series techniques have great potential to monitor slow surface velocity over time, they are not without considerable limitations. These limitations include the low sensitivity towards displacement with a strong north or south component, the maximum detectable displacement between two SAR acquisitions, decorrelation due to changing surface properties and the influence of atmospheric delay.

The issue of InSAR sensitivity is well known and causes issues especially for landforms with very low displacements. Projecting the LOS displacement into the assumed direction of motion (i.e. along the steepest slope) does produce more representative results (Notti et al., 2014) but their velocities are likely still underestimated to some extent. Rock glaciers in areas with poor InSAR sensitivity are included in the inventory even if their LOS velocity is $<1 \text{ cm yr}^{-1}$ for that reason. Their activity is classified as ‘undefined’. Other rock glaciers with slightly higher LOS velocity but also located in areas where InSAR sensitivity is poor received the same classification. A map displaying the approximate InSAR sensitivity to downslope motion for each pixel is included in the supplement files.

The maximum detectable displacement between two SAR acquisitions is equal to half the wavelength of the emitting satellite, i.e. $\sim 2.8 \text{ cm}$ for Sentinel-1. Larger displacements cannot be unwrapped reliably and even displacements greater than a quarter of

the wavelength, or 1.4 cm for Sentinel-1, may lead to aliasing effects (Crosetto et al., 2016). Most of the interferograms used for our analysis have temporal baselines of either 12 or 24 days but a small number have much larger baselines of up to 72 days. This is due to temporal data gaps of the descending Sentinel-1 data set in summer 2017. The maximum detectable LOS velocity is 17.0 cm yr^{-1} in ascending and 14.2 cm yr^{-1} in descending geometry. An underestimation of the velocity due to aliasing effects may occur where the LOS velocities exceeds 8.5 cm yr^{-1} in ascending and 7.1 cm yr^{-1} in descending geometry. Most transitional rock glaciers display LOS velocities below these thresholds but the velocity of active rock glaciers is likely underestimated in this study. Rock glaciers with a maximum LOS velocity very close to 10 cm yr^{-1} were therefore classified as active to compensate for this underestimation.

Vegetation growth, snow fall and soil moisture variations between two SAR acquisitions may cause decorrelation or misinterpretation of InSAR data (Eriksen et al., 2018; Sowter et al., 2013; Bateson et al., 2015; Zwieback et al., 2017). The high altitude of our study area means that large vegetation, such as trees, are not a problem. Actively moving rock glaciers are sparsely vegetated, and we therefore consider vegetation to have little impact on our InSAR results (Cannone and Gerdol, 2003). The winter climate in our study area is semi-arid (Yao et al., 2013). Optical satellite imagery shows that snow fall occurs mainly between autumn and spring but our field work has shown that it may also occur in summer. We observe the lowest overall coherence during the spring and autumn months, which we attribute to the transition between frozen and unfrozen ground. The overall coherence is highest in winter, when the frozen ground leads to stable backscatter conditions. We chose a coherence threshold of 0.2 and employed the intermittent SBAS algorithm to perform temporal interpolation for pixels with lower coherence values in up to 40 % of interferograms. These thresholds are lenient compared to most InSAR applications but they are necessary to achieve the aims of this study. We use the surface velocity to help with the manual identification of active rock glaciers and as a feature in the automated classification. We use only the median surface velocity from 2016 to 2019. The need for good spatial coverage therefore justifies the large amount of temporal interpolation in our opinion.

Varying types of atmospheric properties may delay the microwave emitted from the satellite, leading to major uncertainties in InSAR analysis (González and Fernandez, 2011). The two dominant types we observe in our study area are turbulent delay and seasonal stratified delay. Turbulent delay is associated with short term variations in the atmosphere and can be considered random in time. We observe the effect of turbulent delay in our individual interferograms, where they lead to false identification of surface displacement of up to half a phase cycle. As turbulent delay is random in time, its effect

on longer observation periods becomes negligible. We therefore consider the effect of turbulent delay on our time series results to be relatively small. Seasonal stratified delay may lead to an apparent seasonal cycle in the surface displacement if there is a large elevation difference between the reference points and the area of interest (Dong et al., 2019). This does not affect the inter-annual surface velocity and we therefore expect its effect to be negligible for this study.

5.5.2 Rock glacier inventory

In this section we discuss the general characteristics of the rock glacier inventory and compare it to similar inventories of other studies. We also provide suggestions regarding the underlying climatic drivers. 65.9 % are classified as transitional with velocities of 1 to 10 cm yr⁻¹ and 18.5 % are considered active with velocities >10 cm yr⁻¹. Rock glaciers are more numerous and more active on the southern side of the mountain range, which contains 91.3 % of all active rock glaciers. The majority of the moisture available in this region is delivered by the Indian Monsoon from the south and south-east (Wünnemann et al., 2018). The southern (windward) side receives most of this moisture, which results larger glaciers compared to the northern side (Zhang et al., 2013b). It is likely that the higher moisture availability also facilitates the higher number and activity of rock glaciers.

Similar rock glacier inventories using comparable methods based around InSAR velocity were published for the Swiss Alps, the dry Andes, the Sierra Nevada and the Northern Tien Shan (Table 1). Rock glaciers velocities range from 2.2 to 170 cm yr⁻¹ in the Andes and from 14 to 87 cm yr⁻¹ in the Sierra Nevada (Villarreal et al., 2018; Liu et al., 2013). The study in the Andes of Villarreal et al. (2018) used InSAR velocity only to detect active rock glaciers and does not quantify their individual velocities. Rock glacier velocities in the Tien Shan reach 114 cm yr⁻¹ in China and 6.5 m yr⁻¹ near the border between Kazakhstan and Kyrgyzstan (Kääb et al., 2021; Wang et al., 2017). We observe slower velocities for most rock glaciers in the western Nyainqêntanglha Range. This can be attributed to the limitations of different InSAR techniques used to estimate the velocity. The SBAS time series technique applied in this study is well suited to display the inter-annual velocity of transitional rock glaciers but underestimates the velocity of active rock glaciers (discussed in Section 5.5.1). These other studies use individual interferograms or short periods of consecutive interferograms to determine surface displacement. In individual interferograms, small displacements are often difficult to distinguish from short term atmospheric signals. It is therefore likely that the displacement of some slow moving rock glaciers could not be identified clearly, leading to an underrepresentation of slow moving rock glaciers in these other studies. We use 74 to 80 consecutive acquisitions over

a period of three years to calculate rock glacier velocity. This allows us to filter out temporally random atmospheric signals and also identify small displacements on slow moving rock glaciers. Three of these other studies based their velocity estimations exclusively on summer acquisitions due to snow cover during spring and winter. Rock glaciers generally move faster during summer and autumn due to the increased temperature and moisture availability (Sorg, Annina and Kääh, Andreas and Roesch, Andrea and Bigler, Christof and Stoffel, Markus, 2015; Wirz et al., 2016; Strozzi et al., 2020). Deriving the annual velocity of a rock glacier solely from summer and autumn is therefore likely to lead to an overestimation. We include the often slower winter and spring seasons, leading to a lower inter-annual velocity of rock glaciers in our inventory. The likely velocity overestimation of these other studies combined with the underestimation of active rock glaciers in our study can therefore explain the difference in observed velocity.

5.5.3 Semi-automatic classification

The classification algorithm used in this study is a supervised maximum likelihood classification. Initial testing had shown that this algorithm performs better than other classification algorithms of the ENVI environment in our study area. We did not assess the performance of other classification algorithms outside the ENVI environment. ENVI is a popular remote sensing environment and easy to use without in-depth machine-learning knowledge. However, this also precludes the use of more sophisticated machine learning algorithms. The algorithm used in this study performs the classification based on individual pixel values. Other algorithms, such as convoluted neural networks, take into account more complex patterns and textures (Robson et al., 2020; Marcer, 2020). These algorithms would likely perform better to separate rock glaciers from other debris-covered landforms, such as debris-covered glaciers.

The following features are used for the automated classification: Downslope velocity, elevation, slope, height error, slope variability, terrain position index (TPI) with 200 m radius, NDVI and Sentinel-2 bands 2 and 3. The TPI represents the elevation of a pixel relative to its surrounding. The search radius by which the surrounding is defined is determined by the analyst and therefore subjective. We performed the automated classification with different feature combinations including TPI with different search radii (200 m and 800 m). The classification performed slightly better with a TPI of 200 m search radius. The true positive rate (TP) was 1.4 % higher compared to using a TPI with radius 800 m. We therefore conclude that the impact of the subjectively chosen search radius is relatively small. TPI, height error, slope and slope variability have the largest impact on the TP and object identification (OI). This partially agrees with similar studies who

determined NDVI and slope to be most important in their study areas (Brenning, 2009; Brenning et al., 2012). Elevation and NDVI were the most important features in the study of Kofler et al. (2020) evaluating different classification algorithms to differentiate between intact and relict rock. NDVI is the least impactful feature in our classification. The high elevation of our study area prevents large vegetation from growing and our field work has shown that even smaller shrubs are rare. This leads to a low NDVI on the debris material surrounding the rock glacier and may explain why NDVI was not very impactful for this study. Excluding features from the automated classification leads to a lower false positive rate (FP) in some cases, especially in the case of TPI. These features are still worth including as they improve the OI metric, which we consider most important to generate a complete inventory.

Using InSAR surface velocity reduces FP from 12.6 % to 10.4 % but it also imposes the limitations associated with InSAR onto the automated classification. We discuss these limitations in detail in section 6.1 and will therefore focus here on the most important limitations: InSAR sensitivity and spatial data coverage. InSAR techniques have poor sensitivity towards displacement with a strong north or south component. Rock glaciers moving mainly into those directions are therefore likely excluded from the classification if their overall velocity is slow or if they are inactive. High spatial coverage of InSAR surface velocity data is necessary to apply our approach to a study area. This can be difficult to achieve in high mountain areas, where heavy snow fall may lead to decorrelation of InSAR in winter (Eriksen et al., 2018). Using exclusively snow-free summer acquisitions or exploiting the low coherence associated with moving landforms could be an alternative in those regions (Bertone et al., 2019). Our automated classification approach is likely to work well in other regions with dry winter climates, like the central and northern TP. Stable winter conditions in the northern Tien Shan make this region another potential candidate (Kääb et al., 2021).

The supervised maximum likelihood classification produced a TP of 69.5 % when compared with the entire manual rock glacier inventory. Rock glaciers >20 ha are identified with good accuracy (OI = 96.5 %). Rock glaciers ≤5 ha are overlooked more frequently (OI = 85.9 %). This is likely due to the large pixel size relative to the size of small rock glaciers. The recent study of Robson et al. (2020) correctly identified 108 of 120 rock glaciers with their automated detection approach in Chile and the Central Himalaya using Convolutional Neural Networks (CNN) and object-based image analysis. They also observe good results for large rock glaciers and less accurate predictions for small rock glaciers. They observe an increase from 62.9 to 72.0 % in their TP by using optical satellite data with 2 m resolution instead of 10 m. The preliminary study of Marcer (2020) used CNN to identify rock glaciers in the French Alps based on SPOT-6 orthoimages. Similar to our

study, they identified the majority of rock glaciers (60-70 %), with better results for large landforms. They achieved a good TP (89 %) but with a large number of FP (21 %). We expect that a better resolution would also improve our classification results, especially for small rock glaciers. The automated classification overestimates the total rock glacier area by 243.0 %. FP are located on relict rock glaciers, debris-covered glaciers and in glacial foreland. The pixel-based algorithm we employ is not able to identify larger patterns, such as the ridge-and-furrow structure of rock glaciers. This leads to a large number of FP on landforms with similar pixel properties as rock glaciers, such as debris-covered glacier or creeping debris-covered slopes. We identified 18 additional rock glaciers after comparing the automated classification to the manual outlines. These results indicate that the automated classification is a useful tool to help the analyst but it cannot replace their expertise. Rock glaciers should still be outlined manually. The automated classification identifies areas where the presence of a rock glacier is likely and helps to generate a more complete inventory.

5.6 Conclusion

We combine an automated classification approach with manual outlines to create the first rock glacier inventory of the western Nyainqêntanglha Range on the Tibetan Plateau. We identified 1433 rock glaciers, 65.9 % are classified as transitional and 18.5 % as active. The activity of the remaining 15.6 % of rock glaciers is undefined, as InSAR displays poor sensitivity to downslope motion in those areas. This classification is based on their median velocities of 2016 to 2019 derived from Sentinel-1 time series analysis. The automated classification correctly identified 87.8 % of all rock glaciers at a true positive rate of 69.5 % and a false positive rate of 10.4 %. 18 additional rock glaciers were added to the inventory after reviewing the automated classification results. We conclude that the automated classification is useful to generate a complete inventory but cannot replace the manual outlining process. Rock glaciers on the southern (windward) side of the mountain range are more numerous, distributed over a greater range of elevations and are more active. Higher moisture availability from monsoon precipitation on the southern side may be the cause of this. However, a more detailed analysis of rock glacier geomorphology is required to corroborate this assumption.

Data availability

The rock glacier inventory is available on the Pangaea database at <https://doi.org/10.1594/PANGAEA.928971>. Examples of different rock glaciers in the study area, the outlines of

the free ice areas of glaciers and data related to the downslope velocity of all rock glaciers are included in the supplementary files of this manuscript.

Supplement

The supplementary material to this manuscript includes spatial information regarding InSAR-derived surface velocity, free-ice glacier extent and examples for each morphological rock glacier class.

Competing interests

The authors declare no conflicts of interest.

Acknowledgements

We would like to thank the DLR for providing us with the high-resolution TanDEM-X DEM for our data processing (Proposal ID DEM_HYDR1727) and the ESA and the Copernicus program for making Sentinel-1 and Sentinel-2 data freely available to the public. We thank our Chinese colleagues, who have worked tirelessly to support us before and during our field work. We also thank Michaela Tille for her work to identify and outline rock glaciers. We thank also Xavier Bodin and the anonymous reviewers for reviewing our manuscript, as well as the editor of *Permafrost and Periglacial Processes*. We are especially grateful to the Open Access Publication Funds of the Technische Universität Braunschweig. This research is a contribution to the International Research Training Group ‘Geo-ecosystems in transition on the Tibetan Plateau’ (TransTiP), funded by Deutsche Forschungsgemeinschaft (DFG grant 317513741 / GRK 2309).

Financial support

This research has been supported by the Deutsche Forschungsgemeinschaft (grant no. GRK 2309/1). This open-access publication was funded by Technische Universität Braunschweig.

Bibliography

- Anderson, R. S., Anderson, L. S., Armstrong, W. H., Rossi, M. W., and Crump, S. E. (2018). Glaciation of alpine valleys: The glacier–debris-covered glacier–rock glacier continuum. *Geomorphology*, 311:127–142.
- Anslan, S., Azizi Rad, M., Buckel, J., Echeverria Galindo, P., Kai, J., Kang, W., Keys, L., Maurischat, P., Nieberding, F., Reinosch, E., et al. (2020). Reviews and syntheses: How do abiotic and biotic processes respond to climatic variations in the Nam Co catchment (Tibetan Plateau)? *Biogeosciences*, 17(5):1261–1279.
- Azócar, G. and Brenning, A. (2010). Hydrological and geomorphological significance of rock glaciers in the dry Andes, Chile (27–33 S). *Permafrost and Periglacial Processes*, 21(1):42–53.
- Barboux, C., Delaloye, R., and Lambiel, C. (2014). Inventorying slope movements in an Alpine environment using DInSAR. *Earth surface processes and landforms*, 39(15):2087–2099.
- Barsch, D. (1996). *Rockglaciers: indicators for the present and former geoecology in high mountain environments*, volume 16. Springer Science & Business Media.
- Bateson, L., Cigna, F., Boon, D., and Sowter, A. (2015). The application of the Intermittent SBAS (ISBAS) InSAR method to the South Wales Coalfield, UK. *International Journal of Applied Earth Observation and Geoinformation*, 34:249–257.
- Berardino, P., Fornaro, G., Lanari, R., and Sansosti, E. (2002). A new algorithm for surface deformation monitoring based on small baseline differential SAR interferograms. *IEEE Transactions on geoscience and remote sensing*, 40(11):2375–2383.
- Berthling, I. (2011). Beyond confusion: Rock glaciers as cryo-conditioned landforms. *Geomorphology*, 131(3-4):98–106.
- Bertone, A., Zucca, F., Marin, C., Notarnicola, C., Cuzzo, G., Krainer, K., Mair, V., Riccardi, P., Callegari, M., and Seppi, R. (2019). An unsupervised method to detect rock glacier activity by using Sentinel-1 SAR interferometric coherence: a regional-scale study in the Eastern European Alps. *Remote Sensing*, 11(14):1711.
- Bolch, T. and Gorbunov, A. P. (2014). Characteristics and origin of rock glaciers in northern Tien Shan (Kazakhstan/Kyrgyzstan). *Permafrost and Periglacial Processes*, 25(4):320–332.

- Brardinoni, F., Scotti, R., Sailer, R., and Mair, V. (2019). Evaluating sources of uncertainty and variability in rock glacier inventories. *Earth Surface Processes and Landforms*, 44(12):2450–2466.
- Brenning, A. (2009). Benchmarking classifiers to optimally integrate terrain analysis and multispectral remote sensing in automatic rock glacier detection. *Remote Sensing of Environment*, 113(1):239–247.
- Brenning, A., Long, S., and Fieguth, P. (2012). Detecting rock glacier flow structures using Gabor filters and IKONOS imagery. *Remote Sensing of environment*, 125:227–237.
- Brighenti, S., Tolotti, M., Bruno, M. C., Wharton, G., Pusch, M. T., and Bertoldi, W. (2019). Ecosystem shifts in Alpine streams under glacier retreat and rock glacier thaw: a review. *Science of the Total Environment*, 675:542–559.
- Buckel, J., Reinosch, E., Hördt, A., Zhang, F., Riedel, B., Gerke, M., Schwalb, A., and Mäusbacher, R. (2021). Insights in a remote cryosphere: A multi method approach to assess permafrost occurrence at the Qugaqie basin, western Nyainqêntanglha Range, Tibetan Plateau. *The Cryosphere*, 15:149–168.
- Burger, K., Degenhardt Jr, J., and Giardino, J. (1999). Engineering geomorphology of rock glaciers. *Geomorphology*, 31(1-4):93–132.
- Cannone, N. and Gerdol, R. (2003). Vegetation as an ecological indicator of surface instability in rock glaciers. *Arctic, Antarctic, and Alpine Research*, 35(3):384–390.
- Cicoira, A., Beutel, J., Faillettaz, J., and Vieli, A. (2019). Water controls the seasonal rhythm of rock glacier flow. *Earth and Planetary Science Letters*, 528:115844.
- Colucci, R. R., Forte, E., Žebre, M., Maset, E., Zanettini, C., and Guglielmin, M. (2019). Is that a relict rock glacier? *Geomorphology*, 330:177–189.
- Crosetto, M., Monserrat, O., Cuevas-González, M., Devanthéry, N., and Crippa, B. (2016). Persistent scatterer interferometry: A review. *ISPRS Journal of Photogrammetry and Remote Sensing*, 115:78–89.
- Cuo, L. and Zhang, Y. (2017). Spatial patterns of wet season precipitation vertical gradients on the Tibetan Plateau and the surroundings. *Scientific reports*, 7(1):1–10.
- Delaloye, R., Barboux, C., Bodin, X., Brenning, A., Hartl, L., Hu, Y., Ikeda, A., Kaufmann, V., Kellerer-Pirklbauer, A., Lambiel, C., et al. (2018). Rock glacier inventories and kinematics: A new IPA Action Group. In *Proceedings of the 5th European Conference on Permafrost (EUCOP5-2018), Chamonix, France*, volume 23.

- Delaloye, R. and Echelard, T. (2020). Towards standard guidelines for inventorying rockglaciers – Baseline concepts (Version 4.1). <https://www3.unifr.ch/geo/geomorphology/en/research/ipa-action-group-rock-glacier/>. [Accessed November 13, 2020].
- Dong, J., Zhang, L., Liao, M., and Gong, J. (2019). Improved correction of seasonal tropospheric delay in InSAR observations for landslide deformation monitoring. *Remote Sensing of Environment*, 233:111370.
- Drusch, M., Del Bello, U., Carlier, S., Colin, O., Fernandez, V., Gascon, F., Hoersch, B., Isola, C., Laberinti, P., Martimort, P., et al. (2012). Sentinel-2: ESA’s optical high-resolution mission for GMES operational services. *Remote sensing of Environment*, 120:25–36.
- Eriksen, H., Rouyet, L., Lauknes, T., Berthling, I., Isaksen, K., Hindberg, H., Larsen, Y., and Corner, G. (2018). Recent acceleration of a rock glacier complex, Adjet, Norway, documented by 62 years of remote sensing observations. *Geophysical Research Letters*, 45(16):8314–8323.
- French, H. M. (2017). *The periglacial environment*. John Wiley & Sons.
- González, P. J. and Fernandez, J. (2011). Error estimation in multitemporal InSAR deformation time series, with application to Lanzarote, Canary Islands. *Journal of Geophysical Research: Solid Earth*, 116(B10).
- Haerberli, W., Hallet, B., Arenson, L., Elconin, R., Humlum, O., Käab, A., Kaufmann, V., Ladanyi, B., Matsuoka, N., Springman, S., et al. (2006). Permafrost creep and rock glacier dynamics. *Permafrost and periglacial processes*, 17(3):189–214.
- Halla, C., Blöthe, J. H., Tapia Baldis, C., Trombotto Liaudat, D., Hilbich, C., Hauck, C., and Schrott, L. (2021). Ice content and interannual water storage changes of an active rock glacier in the dry Andes of Argentina. *The Cryosphere*, 15(2):1187–1213.
- Hamilton, S. J. and Whalley, W. B. (1995). Rock glacier nomenclature: a re-assessment. *Geomorphology*, 14(1):73–80.
- Humlum, O. (1982). Rock glacier types on Disko, central West Greenland. *Geografisk Tidsskrift-Danish Journal of Geography*, 82(1):59–66.
- Jarvis, A., Reuter, H. I., Nelson, A., Guevara, E., et al. (2008). Hole-filled SRTM for the globe Version 4. available from the CGIAR-CSI SRTM 90m Database (<http://srtm.csi.cgiar.org>), 15:25–54.
- Jones, D., Harrison, S., Anderson, K., and Betts, R. (2018). Mountain rock glaciers contain globally significant water stores. *Scientific reports*, 8(1):2834.

- Jones, D. B., Harrison, S., Anderson, K., and Whalley, W. B. (2019). Rock glaciers and mountain hydrology: A review. *Earth-science reviews*, 193:66–90.
- Kääb, A., Frauenfelder, R., and Roer, I. (2007). On the response of rockglacier creep to surface temperature increase. *Global and Planetary Change*, 56(1-2):172–187.
- Kääb, A., Strozzi, T., Bolch, T., Caduff, R., Trefall, H., Stoffel, M., and Kokarev, A. (2021). Inventory and changes of rock glacier creep speeds in Ile Alatau and Kungöy Ala-Too, northern Tien Shan, since the 1950s. *The Cryosphere*, 15(2):927–949.
- Kang, S., Xu, Y., You, Q., Flügel, W.-A., Pepin, N., and Yao, T. (2010). Review of climate and cryospheric change in the Tibetan Plateau. *Environmental research letters*, 5(1):015101.
- Keil, A., Berking, J., Mügler, I., Schütt, B., Schwalb, A., and Steeb, P. (2010). Hydrological and geomorphological basin and catchment characteristics of Lake Nam Co, South-Central Tibet. *Quaternary International*, 218(1-2):118–130.
- Kellerer-Pirklbauer, A. and Kaufmann, V. (2012). About the relationship between rock glacier velocity and climate parameters in central Austria. *Austrian Journal of Earth Sciences*, 105(2):94–112.
- Kenner, R., Pruessner, L., Beutel, J., Limpach, P., and Phillips, M. (2020). How rock glacier hydrology, deformation velocities and ground temperatures interact: Examples from the Swiss Alps. *Permafrost and Periglacial Processes*, 31(1):3–14.
- Knight, J., Harrison, S., and Jones, D. B. (2019). Rock glaciers and the geomorphological evolution of deglaciating mountains. *Geomorphology*, 324:14–24.
- Kofler, C., Steger, S., Mair, V., Zebisch, M., Comiti, F., and Schneiderbauer, S. (2020). An inventory-driven rock glacier status model (intact vs. relict) for South Tyrol, Eastern Italian Alps. *Geomorphology*, 350:106887.
- Lei, Y., Yao, T., Bird, B. W., Yang, K., Zhai, J., and Sheng, Y. (2013). Coherent lake growth on the central Tibetan Plateau since the 1970s: Characterization and attribution. *Journal of Hydrology*, 483:61–67.
- Li, B., Zhang, J., Yu, Z., Liang, Z., Chen, L., and Acharya, K. (2017). Climate change driven water budget dynamics of a Tibetan inland lake. *Global and Planetary Change*, 150:70–80.
- Li, Z., Zhao, R., Hu, J., Wen, L., Feng, G., Zhang, Z., and Wang, Q. (2015). InSAR analysis of surface deformation over permafrost to estimate active layer thickness based on one-dimensional heat transfer model of soils. *Scientific reports*, 5:15542.

- Lilleøren, K. S. and Etzelmüller, B. (2011). A regional inventory of rock glaciers and ice-cored moraines in Norway. *Geografiska Annaler: Series A, Physical Geography*, 93(3):175–191.
- Liu, L., Millar, C. I., Westfall, R. D., and Zebker, H. A. (2013). Surface motion of active rock glaciers in the Sierra Nevada, California, USA: inventory and a case study using InSAR. *The Cryosphere*, 7: 1109-1119, 7:1109–1119.
- Luo, W., Zhang, G., Chen, W., and Xu, F. (2020). Response of glacial lakes to glacier and climate changes in the western Nyainqentanglha range. *Science of the Total Environment*, 735:139607.
- Marcer, M. (2020). Rockglacier evolution by ground-truthing the state and possible fate in semiarid climate in the Nyainqentanglha range, Tibetan Plateau. *Permafrost and Periglacial Processes*, 31(4):561–566.
- Marcer, M., Serrano, C., Brenning, A., Bodin, X., Goetz, J., and Schoeneich, P. (2019). Evaluating the destabilization susceptibility of active rock glaciers in the French Alps. *The Cryosphere*, 13(1):141–155.
- Matsuoka, N. (2001). Solifluction rates, processes and landforms: a global review. *Earth-Science Reviews*, 55(1-2):107–134.
- Millar, C. I., Westfall, R. D., and Delany, D. L. (2013). Thermal and hydrologic attributes of rock glaciers and periglacial talus landforms: Sierra Nevada, California, USA. *Quaternary International*, 310:169–180.
- Monnier, S. and Kinnard, C. (2015). Reconsidering the glacier to rock glacier transformation problem: New insights from the central Andes of Chile. *Geomorphology*, 238:47–55.
- Neckel, N., Kropáček, J., Bolch, T., and Hochschild, V. (2014). Glacier mass changes on the Tibetan Plateau 2003–2009 derived from ICESat laser altimetry measurements. *Environmental research letters*, 9(1):014009.
- Necsoiu, M., Onaca, A., Wigginton, S., and Urdea, P. (2016). Rock glacier dynamics in Southern Carpathian Mountains from high-resolution optical and multi-temporal SAR satellite imagery. *Remote sensing of environment*, 177:21–36.
- Notti, D., Herrera, G., Bianchini, S., Meisina, C., García-Davalillo, J. C., and Zucca, F. (2014). A methodology for improving landslide PSI data analysis. *International journal of remote sensing*, 35(6):2186–2214.

- Obu, J., Westermann, S., Bartsch, A., Berdnikov, N., Christiansen, H. H., Dashtseren, A., Delaloye, R., Elberling, B., Etzelmüller, B., Kholodov, A., et al. (2019). Northern Hemisphere permafrost map based on TTOP modelling for 2000–2016 at 1 km² scale. *Earth-Science Reviews*, 193:299–316.
- Osmanoglu, B., Sunar, F., Wdowinski, S., and Cabral-Cano, E. (2016). Time series analysis of InSAR data: Methods and trends. *ISPRS Journal of Photogrammetry and Remote Sensing*, 115:90–102.
- Otto, J.-C., Prasicek, G., Blöthe, J., and Schrott, L. (2018). GIS applications in geomorphology. *Comprehensive Geographic Information Systems; Huang, B., Ed.; Elsevier Inc.: Bonn, Germany*, pages 81–111.
- Ran, Z. and Liu, G. (2018). Rock glaciers in Daxue Shan, south-eastern Tibetan Plateau: an inventory, their distribution, and their environmental controls. *Cryosphere*, 12(7).
- Rangecroft, S., Harrison, S., and Anderson, K. (2015). Rock glaciers as water stores in the Bolivian Andes: an assessment of their hydrological importance. *Arctic, Antarctic, and Alpine Research*, 47(1):89–98.
- Reinosch, E., Buckel, J., Dong, J., Gerke, M., Baade, J., and Riedel, B. (2020). InSAR time series analysis of seasonal surface displacement dynamics on the Tibetan Plateau. *The Cryosphere*, 14(5):1633–1633.
- Ren, S., Menenti, M., Jia, L., Zhang, J., Zhang, J., and Li, X. (2020). Glacier mass balance in the Nyainqentanglha Mountains between 2000 and 2017 retrieved from ZiYuan-3 stereo images and the SRTM DEM. *Remote Sensing*, 12(5):864.
- Robson, B. A., Bolch, T., MacDonell, S., Hölbling, D., Rastner, P., and Schaffer, N. (2020). Automated detection of rock glaciers using deep learning and object-based image analysis. *Remote Sensing of Environment*, 250:112033.
- Scotti, R., Brardinoni, F., Alberti, S., Frattini, P., and Crosta, G. B. (2013). A regional inventory of rock glaciers and protalus ramparts in the central Italian Alps. *Geomorphology*, 186:136–149.
- Scotti, R., Crosta, G. B., and Villa, A. (2017). Destabilisation of creeping permafrost: The Plator rock glacier case study (Central Italian Alps). *Permafrost and Periglacial Processes*, 28(1):224–236.
- Sorg, Annina and Kääb, Andreas and Roesch, Andrea and Bigler, Christof and Stoffel, Markus (2015). Contrasting responses of central asian rock glaciers to global warming. *Scientific reports*, 5(1):1–6.

- Sowter, A., Bateson, L., Strange, P., Ambrose, K., and Syafiudin, M. F. (2013). DInSAR estimation of land motion using intermittent coherence with application to the South Derbyshire and Leicestershire coalfields. *Remote Sensing Letters*, 4(10):979–987.
- Strozzi, T., Caduff, R., Jones, N., Barboux, C., Delaloye, R., Bodin, X., Käab, A., Mätzler, E., and Schrott, L. (2020). Monitoring Rock Glacier Kinematics with Satellite Synthetic Aperture Radar. *Remote Sensing*, 12(3):559.
- Strozzi, T., Käab, A., and Frauenfelder, R. (2004). Detecting and quantifying mountain permafrost creep from in situ inventory, space-borne radar interferometry and airborne digital photogrammetry. *International Journal of Remote Sensing*, 25(15):2919–2931.
- Tian, K., Liu, J., Kang, S., and Li, C. (2006). A Primary Study on the Environment of Frozen Ground in the Nam Co Basin, Tibet. *Advances in Earth Science*, 21(12):1324–1332.
- Villarroel, C. D., Tamburini Beliveau, G., Forte, A. P., Monserrat, O., and Morvillo, M. (2018). DInSAR for a Regional Inventory of Active Rock Glaciers in the Dry Andes Mountains of Argentina and Chile with Sentinel-1 Data. *Remote Sensing*, 10(10):1588.
- Wang, X., Liu, L., Zhao, L., Wu, T., Li, Z., and Liu, G. (2017). Mapping and inventorying active rock glaciers in the northern Tien Shan of China using satellite SAR interferometry. *Cryosphere*, 11(2).
- Wang, X., Siegert, F., Zhou, A.-g., and Franke, J. (2013). Glacier and glacial lake changes and their relationship in the context of climate change, Central Tibetan Plateau 1972–2010. *Global and Planetary Change*, 111:246–257.
- Weiss, A. (2001). Topographic position and landforms analysis. In *Poster presentation, ESRI user conference, San Diego, CA*, volume 200.
- Wirz, V., Gruber, S., Purves, R. S., Beutel, J., Gärtner-Roer, I., Gubler, S., and Vieli, A. (2016). Short-term velocity variations at three rock glaciers and their relationship with meteorological conditions. *Earth Surface Dynamics*, 4(1):103–123.
- Wünnemann, B., Yan, D., Andersen, N., Riedel, F., Zhang, Y., Sun, Q., and Hoelzmann, P. (2018). A 14 ka high-resolution $\delta^{18}\text{O}$ lake record reveals a paradigm shift for the process-based reconstruction of hydroclimate on the northern Tibetan Plateau. *Quaternary Science Reviews*, 200:65–84.
- Yagüe-Martínez, N., Prats-Iraola, P., Gonzalez, F. R., Brcic, R., Shau, R., Geudtner, D., Eineder, M., and Bamler, R. (2016). Interferometric processing of Sentinel-1 TOPS data. *IEEE Transactions on Geoscience and Remote Sensing*, 54(4):2220–2234.

- Yao, T., Masson-Delmotte, V., Gao, J., Yu, W., Yang, X., Risi, C., Sturm, C., Werner, M., Zhao, H., He, Y., et al. (2013). A review of climatic controls on $\delta^{18}\text{O}$ in precipitation over the Tibetan Plateau: Observations and simulations. *Reviews of Geophysics*, 51(4):525–548.
- Zhang, B., Wu, Y., Lei, L., Li, J., Liu, L., Chen, D., and Wang, J. (2013a). Monitoring changes of snow cover, lake and vegetation phenology in Nam Co Lake Basin (Tibetan Plateau) using remote sensing (2000–2009). *Journal of Great Lakes Research*, 39(2):224–233.
- Zhang, G., Kang, S., Fujita, K., Huintjes, E., Xu, J., Yamazaki, T., Haginoya, S., Wei, Y., Scherer, D., Schneider, C., et al. (2013b). Energy and mass balance of Zhadang glacier surface, central Tibetan Plateau. *Journal of Glaciology*, 59(213):137–148.
- Zhang, G., Kang, S., Fujita, K., Huintjes, E., Xu, J., Yamazaki, T., Haginoya, S., Wei, Y., Scherer, D., Schneider, C., et al. (2013c). Energy and mass balance of Zhadang glacier surface, central Tibetan Plateau. *Journal of Glaciology*, 59(213):137–148.
- Zhang, G., Li, J., and Zheng, G. (2017). Lake-area mapping in the Tibetan Plateau: an evaluation of data and methods. *International journal of remote sensing*, 38(3):742–772.
- Zhu, L., Xie, M., and Wu, Y. (2010). Quantitative analysis of lake area variations and the influence factors from 1971 to 2004 in the Nam Co basin of the Tibetan Plateau. *Chinese Science Bulletin*, 55(13):1294–1303.
- Zink, M., Bachmann, M., Brautigam, B., Fritz, T., Hajnsek, I., Moreira, A., Wessel, B., and Krieger, G. (2014). TanDEM-X: The new global DEM takes shape. *IEEE Geoscience and Remote Sensing Magazine*, 2(2):8–23.
- Zou, D., Zhao, L., Yu, S., Chen, J., Hu, G., Wu, T., Wu, J., Xie, C., Wu, X., Pang, Q., et al. (2017). A new map of permafrost distribution on the Tibetan Plateau. *The Cryosphere*, 11(6):2527.
- Zwieback, S., Hensley, S., and Hajnsek, I. (2017). Soil moisture estimation using differential radar interferometry: Toward separating soil moisture and displacements. *IEEE Transactions on Geoscience and Remote Sensing*, 55(9):5069–5083.

Chapter 6

Summary and conclusions

In this chapter we summarize the most important findings of chapters 2 to 5 and present our conclusions regarding our research aims. These aims and their related research questions are explained in greater detail in chapter 1. Here, we present a short summary of the research questions for the reader's convenience. Each research question is then addressed individually in the following sections. The aim of this thesis is to fill the current gap in knowledge regarding the distribution and the activity of periglacial landforms, especially rock glaciers, in the western Nyainqêntanglha Range on the Tibetan Plateau (TP). To reach our aim we need to answer the following research questions:

1. How potent is InSAR time series analysis for the study of the periglacial landscape?
2. Which displacement patterns can we observe via remote sensing and how are they related to sediment transport?
3. Where are rock glaciers distributed and how active are they?
4. How does the local monsoon climate affect surface displacements on different landforms?
5. Can we assess the influence of climate change on this periglacial environment?

6.1 Potential and limitations of InSAR remote sensing to study the periglacial landscape

We used three different types of remote sensing products to study periglacial landforms in the study area: The TanDEM- X digital elevation model (DEM) and derived data sets, optical satellite imagery and microwave satellite acquisitions used to derive the surface displacement with Interferometric Synthetic Aperture Radar (InSAR) techniques. Here, we focus on the potential of InSAR time series analysis for the study of the periglacial landscape. While InSAR time series techniques have great potential to monitor slow surface velocity over time, they are not without considerable limitations. These limitations include (1) decorrelation due to changing surface properties, (2) the low sensitivity towards displacement with a strong north or south component, (3) the maximum detectable displacement between two SAR acquisitions and (4) the influence of atmospheric delay.

Vegetation growth, snow fall and soil moisture variations between two SAR acquisitions may cause decorrelation or misinterpretation of InSAR data (Osmanoğlu et al., 2016; Zwieback et al., 2017). The high altitude of our study area means that large vegetation, such as trees, are not a problem. Actively moving rock glaciers are sparsely vegetated, and we therefore consider vegetation to have little impact on our InSAR results. We observe an apparent uplift of up to a few centimeters per year in many regions near water bodies, such as the main stream of Qugaqie basin (Fig. 4.3). This is likely connected to a misinterpretation of moisture changes, rather than representing actual surface displacement. The winter climate in our study area is semi-arid. Optical satellite imagery shows that snow fall occurs mainly between autumn and spring but our field work has shown that it may also occur in summer. We observe the lowest overall coherence during the spring and autumn months, which we attribute to the transition between frozen and unfrozen ground. Overall, the coherence in our study area is good.

InSAR techniques are insensitive to displacements with a direction orthogonal to the line-of-sight (LOS) of the satellite. In the case of Sentinel-1, this affects especially displacements towards the north or south. To compensate for this insensitivity, we project the observed LOS displacement into the assumed direction of motion. In the case of rock glaciers, we assume that they move in the direction of the steepest slope, as their motion is driven by gravitational pull. This produces more representative results but velocities of rock glaciers towards the north or south have a higher uncertainty and are likely still underestimated to some extent. Rock glaciers in areas with poor InSAR sensitivity are included in the rock glacier inventory but are classified as *undefined* in regards to their activity. A total of 224 rock glaciers (15.6 %) have an undefined activity.

The maximum detectable displacement between two SAR acquisitions is equal to half the wavelength of the emitting satellite, i.e. ~ 2.8 cm for Sentinel-1. Larger displacements cannot be unwrapped reliably and even displacements greater than a quarter of the wavelength may lead to aliasing effects (Crosetto et al., 2016). We discarded older Sentinel-1 acquisitions of 2014 and 2015 as the temporal baselines were longer than in subsequent years. Most of our interferograms have temporal baselines of either 12 or 24 days but a small number have larger baselines due to temporal data gaps in the summer months of 2016 or 2017. The maximum detectable LOS velocity for the rock glacier inventory is 17.0 cm yr^{-1} in ascending and 14.2 cm yr^{-1} in descending geometry. An underestimation of the velocity due to aliasing effects may occur where the LOS velocities exceeds 8.5 cm yr^{-1} in ascending and 7.1 cm yr^{-1} in descending geometry. Most transitional rock glaciers display LOS velocities below these thresholds but the velocity of active rock glaciers is likely underestimated in our rock glacier inventory. Consequently, it may be advisable to prioritize shorter time series without temporal data gaps over longer time series with gaps to increase the maximum detectable velocity.

Varying types of atmospheric properties may delay the microwave emitted from the satellite, leading to major uncertainties in InSAR analysis. The two dominant types we observe in our study area are turbulent delay and seasonal stratified delay. Turbulent delay is associated with short term variations in the atmosphere and can be considered random in time. We observe the effect of turbulent delay in our individual interferograms, where they lead to false identification of surface displacement of up to half a phase cycle. As turbulent delay is random in time, its effect on longer observation periods becomes very minor. Seasonal stratified delay may lead to an apparent seasonal cycle in the surface displacement if there is a large elevation difference between the reference points and the area of interest (Dong et al., 2019). For our analysis of seasonal displacement processes in Qugaqie basin and Niyaqu basin, we selected reference points with similar elevations as the landscape we observed. This reduces the impact of seasonal stratified delay but we cannot be certain that it has been removed from the time series entirely without additional data sources for ground truth. The time series results of many rock glaciers of the large-scale analysis show the effects of seasonal stratified delay clearly. The reference points for the large-scale analysis had to be placed at the outskirts of the mountain range to achieve the best possible coherence. They are therefore located at about 300 to 500 m lower elevations than most rock glaciers, which leads to an apparent seasonal cycle in the surface velocity. We could confirm this seasonal cycle to be caused by atmospheric delay by choosing reference points at higher elevations. This reduced the apparent seasonal cycle on many rock glaciers but resulted in a much reduced coherence overall. For the large-scale analysis of rock glacier activity, we therefore focus on inter-annual velocity,

which is unaffected by seasonal stratified delay.

We conclude, that InSAR time series analysis is a suitable technique to study the various displacement processes of this periglacial landscape. It is, however, a complex technique with considerable limitations depending on the displacement direction, the velocity of observed landforms and the local environment. We must be very careful and critical when interpreting InSAR data, as apparent displacement signals may be caused by other effects rather than actual surface displacement.

6.2 Different surface displacement patterns and their contribution to sediment transport

Our next aim was to identify other processes associated with surface displacement and to assess their contribution to sediment transport (Chapter 4). The Qugaqie basin features steep debris-covered slopes and is fed by two glaciers. It represents well the geomorphology of central and southern catchments of our study area. The northern central part of our study area and the regions north and west of the Nam Co display a different morphology. Only a few small glaciers can be found there and the overall topography is more subdued. We therefore included the Niyaqu basin in our study of seasonal and inter-annual surface displacements, to represent these areas. We created multiple models to investigate seasonal displacement patterns and inter-annual surface velocity. On slopes we assume displacement to occur mainly in the direction of the steepest slope, due to gravitational pull. In flat terrain, such as valley floors, we assume that displacement is mainly vertical. We projected the LOS displacement of our InSAR time series into those directions and analyzed seasonal and inter-annual patterns.

The majority of flat terrain ($<10^\circ$) is relatively stable in both the Niyaqu and the Qugaqie catchment. We observe some areas with minor subsidence (Fig. 6.1B), the cause of which is not clear. Many areas of the Qugaqie catchment near water bodies display apparent uplift. This is likely due to interference from soil moisture changes, rather than actual surface displacement (Zwieback et al., 2017). Flat terrain displays a heave-subsidence cycle, caused by freezing and thawing of the ground. This displacement is most noticeable near rivers and wetlands, where more moisture is stored in the ground, leading to a larger displacement during the freezing process. The vertical amplitude of this heave-thaw cycle is 3 to 8 mm for most areas and 8 to 15 mm for areas near water bodies (Fig. 4.5). Neither the inter-annual subsidence nor the seasonal heave-thaw cycle contributes to sediment transport directly. Increased sediment transport could be a consequence, if the inter-annual subsidence is caused by permafrost degradation (Etzelmüller

and Frauenfelder, 2009).

Displacement on steeper terrain ($>10^\circ$) was projected along the direction of the steepest slope, as we assume it to be gravity-driven surface creep. Rock glaciers are the fastest common periglacial landform. Active rock glaciers make up 18.5 % of all inventoried rock glaciers with velocities of mostly 10 to 30 cm yr^{-1} (Fig. 5.5). The mean downslope velocity of all non-glaciated, non-rock glacier slopes steeper than 20° (45.5 % of the entire study area) is 1.05 cm yr^{-1} . This includes sparsely vegetated slopes, debris-covered slopes and frozen moraines. Vegetated slopes on the outskirts of the mountain range and near the Nam Co display surface creeping of up to 2 cm yr^{-1} . The slopes of the mountain range itself are covered by debris and only sporadic vegetation. They creep at mostly 1 to 5 cm yr^{-1} and in some cases up to 10 cm yr^{-1} (Fig. 4.3). Debris on slopes within the contribution area of rock glaciers moves about 30 % faster than on other slopes. Moraines on the outskirts of the mountain range are generally stable and we use them as stable reference points for InSAR processing. Frozen moraines at similar elevations as rock glaciers display surface creep of up to 5 cm yr^{-1} . This could be an indication of an ice-core in their subsurface and they may evolve into morainic debris rock glaciers in the future (Knight et al., 2019). On steep terrain we observe decorrelation of InSAR data most commonly above ice glaciers or at glacier forefields. This decorrelation is likely caused by rapid paraglacial slope failure, such as rock falls or rock slides. Paraglacial processes are part of the transition from glacial conditions to non-glacial conditions (McColl, 2012). Glacial erosion creates steep slopes along the glacier margins. Deglaciation may subsequently destabilize these steep slopes, leading to rapid events such as rock falls or slower gravitational slope deformations (i.e. slow landslides). We observe such slope deformations at a small number of locations (example in Fig. 6.1A). They lead to similar surface velocities as active rock glaciers but they are much less frequent. Their impact on the overall sediment transport of the region is therefore likely smaller.

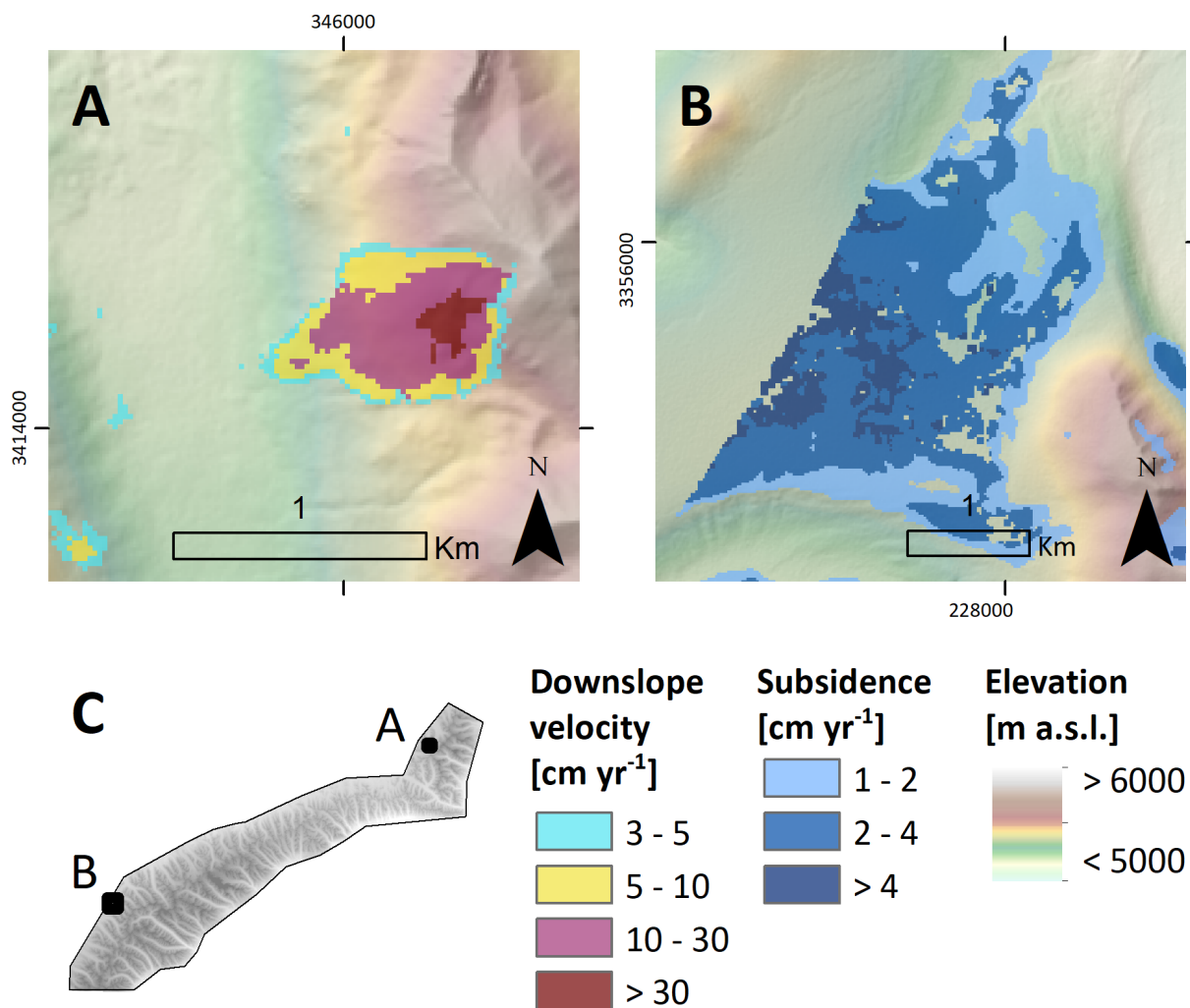


Figure 6.1: Inter-annual surface velocity of two regions. (A) Downslope velocity (2016 – 2019) of a landslide near the northern end of the study area. (B) Mean subsidence (2015 – 2019) of a flat region on the northern side of the mountain range. (C) Overview map of the study area indicating the locations of (A) and (B).

It is difficult to ascertain whether creep on rock glaciers or on debris-covered slopes contributes more to the sediment transport. For both landforms we could only determine the surface velocity and not the velocity of material in the subsurface, the thickness of the moving layer or the subsurface ice content. Further field studies are necessary to investigate those parameters, as no such information is available for our study area. Furthermore, it is necessary to evaluate sediment sinks to determine to what extent and in which areas surface creep affects sediment transport in streams. Our large-scale model of surface creep is an important step towards determining the sediment transport in the western Nyainqêntanglha Range.

6.3 Rock glacier distribution and the implications for permafrost extent

The motion of rock glaciers is facilitated by the ice within these landforms. Permafrost conditions are necessary to form and maintain this ice. Moving rock glaciers can therefore be seen as large visible expressions of permafrost conditions (Berthling, 2011). It is important to note, however, that the blocky debris of a rock glacier insulates the ice within the landform (Gorbunov et al., 2004). This helps to maintain permafrost conditions within the landform and enables rock glaciers to extend into areas where permafrost conditions are unlikely outside the rock glacier itself (Bolch and Gorbunov, 2014). In our detailed rock glacier studies we combined InSAR surface velocity data and Electrical Resistance Tomography (ERT) subsurface measurements (Chapters 2 and 3). This study shows that surface velocity of at least a few centimeters per year is a strong indication of ice and therefore permafrost conditions the rock glacier’s subsurface.

We created a rock glacier inventory in order to assess large-scale permafrost distribution in the western Nyainqêntanglha Range (Chapter 5). To create this inventory, we combined the manual approach recommended by the International Permafrost Association (IPA) with an automated classification approach. The classification algorithm we used to automatically identify rock glacier areas is a pixel-based supervised maximum likelihood classification. We trained the algorithm on 25 active rock glaciers of the manual inventory using the following spatial data sets:

1. Median downslope velocity of 2016 to 2019 based on Sentinel-1 SAR data (©Copernicus, 2016-2019).
2. Elevation, slope, height error, slope variability and terrain position index derived from the TanDEM-X DEM (©DLR, 2017).
3. Mean normalized difference vegetation index of seven Landsat 8 acquisitions of 2014 to 2019 from May to September (©USGS, 2014-2019).
4. Bands 2 and 3 of a Sentinel-2 acquisition from January 2018 (©Copernicus, 2018).

The classification produced a true positive rate (TP) of 69.5 % when compared with the entire manual rock glacier inventory, meaning that 69.5 % of the manually identified rock glacier area was correctly classified as rock glacier by the automated classification. The main purpose of the automated classification is to identify rock glaciers that were overlooked during the manual outlining process. We identified 18 additional rock glaciers after comparing the automated classification to the manual outlines. Large rock glaciers

(>20 ha) are more frequently identified correctly than small rock glaciers (<5 ha). Of the large rock glaciers, 96.5 % achieved a TP >30 %, while only 85.9 % of small rock glaciers achieved a TP >30 %. This is likely due to the large pixel size of the training data sets relative to the size of small rock glaciers. Other studies also observe better automated classification results for large rock glaciers (Robson et al., 2020). They achieve similar classification accuracies as our studies but employ more sophisticated algorithms, such as convoluted neural networks, which take into account more complex patterns and textures (Robson et al., 2020; Marcer, 2020). These algorithms would likely perform better to separate rock glaciers from other debris-covered landforms with similar surface characteristics but different surface patterns, such as debris-covered glaciers. The automated classification overestimates the total rock glacier area by 243 %. These false positives are located on relict rock glaciers, debris-covered glaciers and in glacial foreland areas. Paraglacial processes and solifluction may lead to displacement of debris material with similar pixel properties as rock glaciers leading to a false classification. Our results indicate that the automated classification is a useful tool to help the analyst but it cannot replace their expertise. Rock glaciers should still be outlined manually. The automated classification identifies areas where the presence of a rock glacier is likely and helps to generate a more complete inventory.

The rock glacier inventory contains 1433 rock glaciers classified according to their activity (i.e. surface velocity) following the guidelines of the action group of *Rock glacier inventories and kinematics* of the IPA (Delaloye and Echelard, 2020). The majority (65.9 %) of all rock glaciers is classified as *transitional* with velocities of 1 to 10 cm yr⁻¹. 18.5 % of all rock glaciers are classified as *active* with velocities >10 cm yr⁻¹. The activity of the remaining 15.6 % is *undefined*, as they are located in areas where InSAR is insensitive to downslope motion (Fig. 5.5). Rock glaciers seem to be less active compared to similar rock glacier inventories of the Sierra Nevada, the Tien Shan or the Andes (Liu et al., 2013; Wang et al., 2017; Villarroel et al., 2018; Kääh et al., 2021). However, this is most likely caused by the limitations of the InSAR time series technique, which underestimates the velocity of active rock glaciers (discussed in Section 6.1). The western Nyainqêntanglha Range can be separated along its water divide into a northern and a southern side (Fig 5.1). Catchments on the northern side drain northward into the endorheic Nam Co and other smaller lakes. Catchments on the southern side drain southwards into the Yangbajain-Damxung Valley as part of the Tsangpo-Brahmaputra River system. The elevation of the northern side ranges from 4721 to 6427 m (median is 5319 m). It represents 41.1 % of the study area but contains only 300 rock glaciers (20.9 %), only 7.7 % of which are active. The elevation of the southern side ranges from 4276 to 7152 m (median is 5411 m). It represents 58.9 % of the study area and contains 1133 rock glaciers (79.1 %), 21.4 % of which are active. Spatulate and tongue-shaped rock

glaciers are the largest and most active rock glaciers (see Section 5.3 for an explanation). Together they represent 13.3 % of all rock glaciers, 29.4 % of the rock glacier area and 29.1 % of all active rock glaciers.

Following the approach described by Jones et al. (2018b) and others, we can estimate the amount of fresh water stored within rock glaciers. To that end, we estimate the rock glacier thickness according to the following empirical rule established by Brenning (2005):

$$\text{Mean rock glacier thickness} = 50 \times (\text{surface area [km}^2\text{)})^{0.2}$$

Geophysical studies in our region are rare and focus on ice detection, rather than subsurface ice content (Buckel et al., 2021). We therefore assume ice to represent 40 to 60 % of a rock glacier’s volume (Barsch, 1996). For the lower estimate we assume all rock glaciers with undefined activity to be relict (i.e. ice-free) and all other rock glaciers to contain 40 % ice. For the upper estimate we assume all rock glaciers, including those with undefined activity, to contain 60 % ice. We calculate the water equivalent volume of the ice storage using an ice density conversion factor of 900 kg m^{-3} . The resulting estimate for water stored in rock glaciers of the western Nyainqêntanglha Range is 1.32 to 2.32 km^3 . Only 0.18 to 0.36 km^3 is stored in rock glaciers within the catchment of the Nam Co. No studies of glacier volume are available for this region. The free ice glacier area of 575.7 km^2 of January 2018 (Reinosch et al., 2021) suggests that the water stored in glacial ice is at least one magnitude larger than the water stored in rock glaciers. However, glacial area shrinks at a rate of $\sim 4 \text{ km}^2 \text{ yr}^{-1}$ in this mountain range (Luo et al., 2020). Rock glaciers are more climate resistant water storages (Jones et al., 2018a) and we expect their importance to increase as glaciers recede.

The distribution of rock glaciers is controlled, amongst other environmental parameters, by ground temperature (i.e. occurrence of permafrost conditions) and precipitation (Cicoira et al., 2019). Our field studies corroborate that moving rock glaciers are indicative of permafrost conditions. Rock glaciers form under permafrost conditions but may exist in areas where permafrost is unlikely outside the rock glacier itself (Bolch and Gorbunov, 2014). Their blocky material creates favorable conditions for permafrost and their debris may be several degrees colder than their surrounding (Gorbunov et al., 2004). The absence of rock glaciers does not necessarily indicate the absence of permafrost conditions, as a lack of slope, moisture availability or debris material may prevent their formation as well (Haeberli et al., 2006). Using rock glacier distribution as an indicator for permafrost extent is therefore limited. We cannot determine an exact distribution of permafrost but we can estimate the lower boundary of discontinuous permafrost from the median elevation of the rock glacier fronts (Scotti et al., 2013). Ran and Liu (2018) published the only

other rock glacier inventory on the TP. In their study of Daxue Shan on the south-eastern TP, they deduce permafrost to be probable above 4352 m.

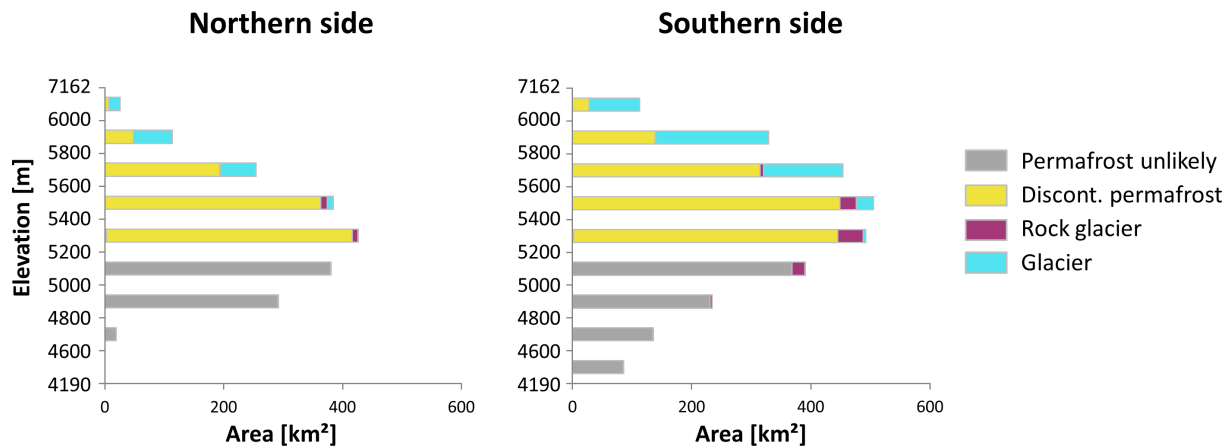


Figure 6.2: *Altitudinal distribution of the glacial and periglacial landscape of the western Nyainqêntanglha Range.*

The high number of rock glaciers on the southern side compared to the northern side highlights the dependency of rock glacier formation on other parameters, such as moisture availability. Permafrost distribution is only dependent on the average ground temperature, which must be below 0 °C for at least 2 consecutive years (French, 2017). Consequently, in order to use the rock glacier inventory to infer permafrost distribution, we must exclude all rock glaciers with a low activity due to limiting environmental parameters. We therefore only consider the 265 rock glaciers classified as active (faster than 10 cm yr⁻¹) to estimate permafrost distribution. We follow the method of Scotti et al. (2013) and Ran and Liu (2018) to infer the lower limit of discontinuous permafrost (50 to 90 % chance of permafrost). Our resulting estimation for the lower limit of discontinuous permafrost is 5202 m in the western Nyainqêntanglha Range. The altitudinal distribution of discontinuous permafrost, rock glaciers and ice glaciers is shown in Figure 6.2. Our remote sensing permafrost assessment agrees well with the ERT measurements performed by Buckel et al. (2021) in the Qugaqie basin. They detect no permafrost at 5100 to 5200 m, individual ice lenses at 5450 m and ice within the rock glacier at 5500 m (Fig. 3.8).

The two most recent maps of permafrost distribution on the TP are described by Zou et al. (2017) and Obu et al. (2019). The former focuses on the TP, while the latter includes the entire northern hemisphere. Both use a variety of remote sensing data, such as ground surface temperature and land cover maps, to model the distribution of permafrost. Their resolution is approximately 1 × 1 km and both predict permafrost for the majority of our study area. Zou et al. (2017) predict permafrost above ~5100 m. They only distinguish between seasonally frozen ground and permafrost and not between discontinuous and continuous permafrost. Obu et al. (2019) predict continuous permafrost (>90 % chance of

permafrost) above ~ 5000 m.

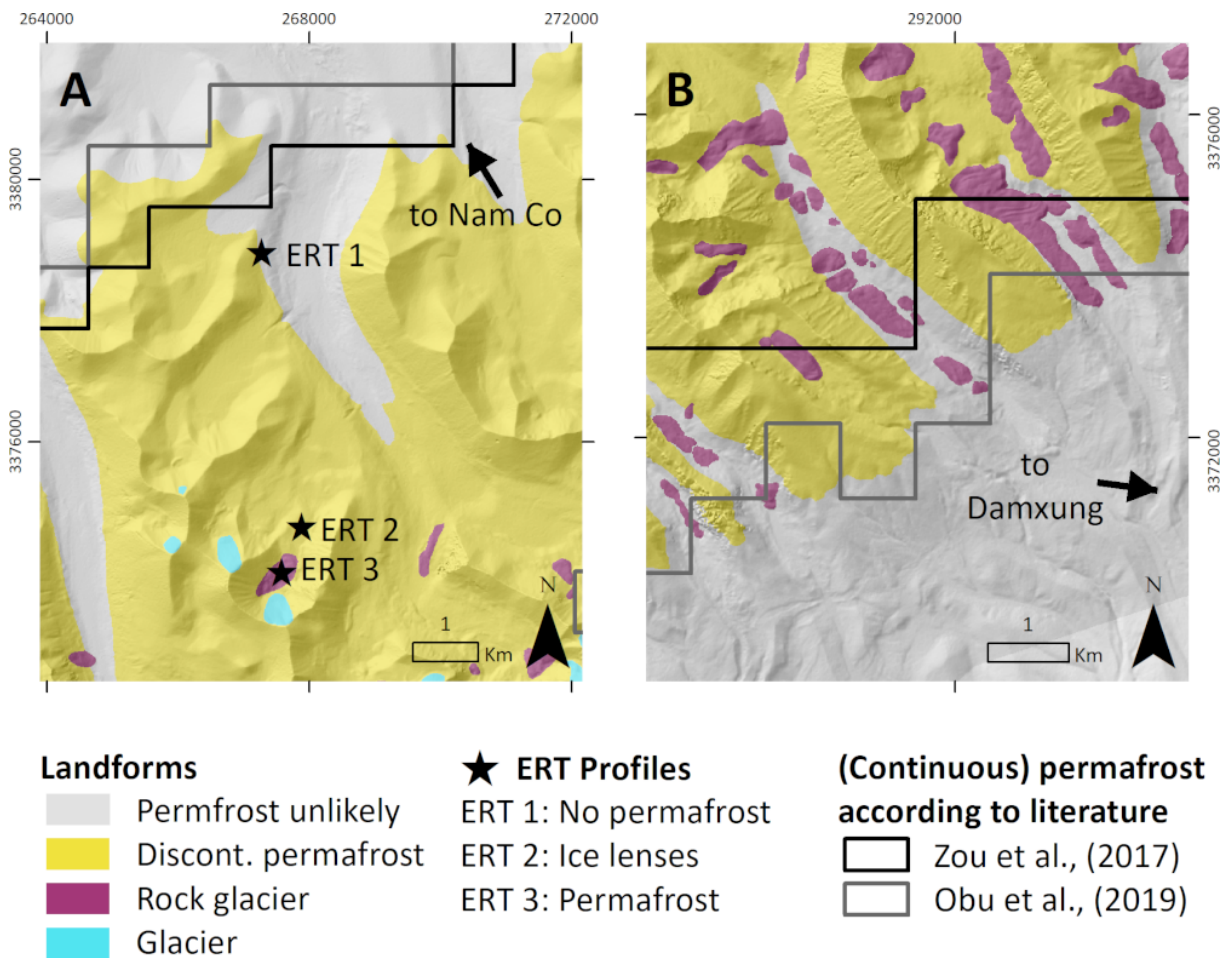


Figure 6.3: Comparison of the landform distribution generated for this thesis and our ERT field measurements with the modelled extent of permafrost (Zou et al., 2017) and continuous permafrost (Obu et al., 2019). Zou et al. (2017) do not distinguish between discontinuous and continuous permafrost, only between seasonally frozen ground and permafrost. (A) Displays the Qugaqie basin on the northern side and (B) displays catchments on the southern side of the mountain range.

The modelled predictions for continuous permafrost of Obu et al. (2019) do not agree well with our field measurements and the rock glacier distribution (Fig. 6.3A). They predict continuous permafrost above ~ 5000 m, while we predict discontinuous permafrost above ~ 5200 m. Borehole data of the eastern TP suggests that their model underestimates the mean annual ground temperature by 1.5 °C, which would lead to an overestimation of the permafrost extent in that region. This could explain the discrepancy between our permafrost predictions and theirs. However, these boreholes are located several hundreds of kilometers north of our study area and more closely located boreholes would be required to corroborate this assessment. The permafrost model of Zou et al. (2017) shows better agreement with our findings. They predict permafrost above an elevation of ~ 5100 m, compared to our prediction of ~ 5200 m. Their borehole data suggests that the model is

most reliable in regions with steep terrain, such as our study area, though all their borehole sites are located in different parts of the TP. While our ERT measurements agree well with our permafrost prediction, further field research on both sides of the mountain range is necessary to assess their accuracy.

6.4 Effect of the monsoonal climate on surface displacement

The Indian Summer Monsoon (ISM) affects surface displacement in the study area in two ways: (1) Seasonal acceleration of surface creeping in late summer and autumn and (2) higher inter-annual velocity of rock glaciers on the southern side of the mountain range. We observe the seasonal acceleration on many debris-covered slopes in the Qugaqie basin and the Niyaqu basin. The velocity of debris-covered slopes is often negligible in winter but accelerates to 10 to 20 cm yr⁻¹ from August to November (Fig. 4.6C). This acceleration is likely enabled by the thawing of the frozen debris during the summer months and driven by the high precipitation from June to September. This freeze-thaw induced downslope displacement is referred to as solifluction (Matsuoka, 2001). Similar seasonal variations have been observed for rock glaciers in the Andes Mountains, Greenland and the European Alps (Strozzi et al., 2020). These seasonal velocity variations appear to be controlled mainly by precipitation and snow melt. Temperature also affects this process, though this occurs indirectly through snow melt in spring and summer, rather than directly through conductive heat transfer (Kenner et al., 2017; Cicoira et al., 2019). Our investigations of rock glaciers in the Qugaqie basin did not display such seasonal accelerations (Fig. 3.10). The time series of many rock glaciers included in the rock glacier inventory display an apparent acceleration in late summer and autumn. However, this is caused by seasonal stratified delay rather representing an actual acceleration of surface velocity (Section 6.1; Dong et al., 2019). Consequently, we cannot be certain to what extent rock glaciers in the western Nyainqêntanglha Range accelerate seasonally.

Only one weather station in the mountain range itself was active from 2009 to 2011 at the Zhadang glacier on the northern side (Fig. 5.2; Zhang et al., 2013a). It displays a higher annual precipitation than weather stations at NAMORS or Damxung. No meteorological data from inside the southern side of the mountain range is available for comparison. The High Asia refined analysis model (HAR) predicts a mean precipitation of ~ 900 mm yr⁻¹ on the northern side and ~ 1100 mm yr⁻¹ on the southern side between 2014 and 2018 (Wang et al., 2021). Rock glaciers on the southern side of the mountain range are more numerous, more elongated and more active than on the northern side.

The southern side hosts 79.0 % of all rock glaciers included in the inventory and 91.3 % of all active rock glaciers. The most likely explanation for this is a difference in mean annual precipitation. The ISM delivers most of the annual precipitation from the south and south-east. The southern side of the mountain range is therefore on the windward side and receives most of the precipitation (Zhang et al., 2013b). The northern side of the mountain range represents the leeward side and likely receives less precipitation, especially at lower elevations. This allows ice glaciers and debris-covered glaciers on the southern side to grow larger and extend to lower elevation. Similarly it also appears to increase the overall activity of rock glaciers (i.e. their surface velocity), which is dependent on water availability through precipitation or snow melt (Cicoira et al., 2019). Rock glaciers on the southern side also tend to be more elongated along their motion direction and therefore extend to lower altitudes. Rock glaciers on the southern side are therefore more likely to move beyond the extent where permafrost is likely outside of the rock glacier itself. We conclude, that the rock glacier distribution in the western Nyainqêntanglha Range is a function of both precipitation controlled by the ISM and ground temperature (i.e. permafrost occurrence) controlled by elevation and aspect.

6.5 Influence of climate change on the study area

Recent studies of rock glacier velocities have observed accelerated inter-annual velocities in Norway, the European Alps and the Tien Shan over the last decades (Eriksen et al., 2018; Kenner et al., 2017; Kääb et al., 2021). This has been attributed to rising ground temperatures and increasing water availability due to climate change. In some cases, may lead to a hazardous destabilization of the rock glacier (Scotti et al., 2017; Marcer et al., 2019). Our surface velocity time series is too short to reliably infer changes to the inter-annual surface velocity. Furthermore, seasonal variations associated with seasonal stratified delay overprint the inter-annual signal. A longer Sentinel-1 time series of at least 5 to 10 years starting from autumn of 2016 or even spring of 2017 may be able to address this topic. Older Sentinel-1 acquisitions should not be used, as their longer temporal baseline would result in the underestimation of the surface velocity before 2017. We observe subsidence in some areas of discontinuous permafrost, which may be an indication of permafrost degradation (Fig. 6.1B). These areas are mostly located in the outskirts of the northern side of the mountain range at an elevation of 5200 to 5400 m. Subsidence in these areas is up to 5 cm yr⁻¹. Without further investigation it will remain unclear if this subsidence is related to permafrost degradation.

6.6 Outlook

Further research is necessary to understand the hydrology and sediment flux of this region and to assess the impact climate change has on this environment. We suggest that future research in this region should focus on the following topics:

1. Moisture availability controls the formation of rock glaciers, their velocity and the formation of seasonal and perennial ice in the subsurface (Chapters 4 and 5). Meteorological data of this mountainous region is sparse. Only one weather station within the mountain range was active from 2009 to 2011, while the nearest active weather stations are located at the Nam Co and in the Damxung valley. Precipitation must therefore be modelled based on sparse data or inferred from indirect proxies such as glacier distribution or river discharge. The influence of the monsoon system on soil moisture in the mountain range and the difference between the northern (leeward) side and the southern (windward) side is therefore difficult to assess. Applying remote sensing techniques to determine soil moisture could help to improve our understanding of this region's high mountain hydrology.
2. Rising ground temperatures have led to the acceleration and in some cases destabilization of rock glaciers in the European Alps, Norway and the Tien Shan. Velocity time series of multiple decades are generally used to infer this acceleration. No such long-term velocity data is available for rock glaciers in our study. Our time series of 3 to 4 years are too short to assess reliably whether the inter-annual velocity increases. Revisiting this topic once the Sentinel-1 time series is longer may answer this question.
3. Our large-scale analysis of surface displacements is an important step towards assessing the sediment transport of this region. However, more research is necessary to complete the assessment. Little is known about sediment sinks, the thickness of debris and the subsurface ice content of active landforms in this region. These parameters can only be studied to a limited extent with remote sensing and likely require further field work.

Bibliography

- Barsch, D. (1996). *Rockglaciers: indicators for the present and former geocology in high mountain environments*, volume 16. Springer Science & Business Media.
- Berthling, I. (2011). Beyond confusion: Rock glaciers as cryo-conditioned landforms. *Geomorphology*, 131(3-4):98–106.
- Bolch, T. and Gorbunov, A. P. (2014). Characteristics and origin of rock glaciers in northern Tien Shan (Kazakhstan/Kyrgyzstan). *Permafrost and Periglacial Processes*, 25(4):320–332.
- Brenning, A. (2005). Climatic and geomorphological controls of rock glaciers in the Andes of Central Chile. *Humboldt-Universität zu Berlin, Mathematisch-Naturwissenschaftliche Fakultät II*.
- Buckel, J., Reinosch, E., Hördt, A., Zhang, F., Riedel, B., Gerke, M., Schwalb, A., and Mäusbacher, R. (2021). Insights in a remote cryosphere: A multi method approach to assess permafrost occurrence at the Qugaqie basin, western Nyainqêntanglha Range, Tibetan Plateau. *The Cryosphere*, 15:149–168.
- Cicoira, A., Beutel, J., Faillettaz, J., and Vieli, A. (2019). Water controls the seasonal rhythm of rock glacier flow. *Earth and Planetary Science Letters*, 528:115844.
- Crosetto, M., Monserrat, O., Cuevas-González, M., Devanthéry, N., and Crippa, B. (2016). Persistent scatterer interferometry: A review. *ISPRS Journal of Photogrammetry and Remote Sensing*, 115:78–89.
- Delaloye, R. and Echelard, T. (2020). Towards standard guidelines for inventorying rockglaciers – Baseline concepts (Version 4.1). <https://www3.unifr.ch/geo/geomorphology/en/research/ipa-action-group-rock-glacier/>. [Accessed November 13, 2020].
- Dong, J., Zhang, L., Liao, M., and Gong, J. (2019). Improved correction of seasonal tropospheric delay in InSAR observations for landslide deformation monitoring. *Remote Sensing of Environment*, 233:111370.
- Eriksen, H., Rouyet, L., Lauknes, T., Berthling, I., Isaksen, K., Hindberg, H., Larsen, Y., and Corner, G. (2018). Recent acceleration of a rock glacier complex, Adjet, Norway, documented by 62 years of remote sensing observations. *Geophysical Research Letters*, 45(16):8314–8323.

- Etzelmueller, B. and Frauenfelder, R. (2009). Factors controlling the distribution of mountain permafrost in the Northern Hemisphere and their influence on sediment transfer. *Arctic, Antarctic, and Alpine Research*, 41(1):48–58.
- French, H. M. (2017). *The periglacial environment*. John Wiley & Sons.
- Gorbunov, A. P., Marchenko, S. S., and Seversky, E. V. (2004). The thermal environment of blocky materials in the mountains of Central Asia. *Permafrost and Periglacial Processes*, 15(1):95–98.
- Haerberli, W., Hallet, B., Arenson, L., Elconin, R., Humlum, O., Kääh, A., Kaufmann, V., Ladanyi, B., Matsuoka, N., Springman, S., et al. (2006). Permafrost creep and rock glacier dynamics. *Permafrost and periglacial processes*, 17(3):189–214.
- Jones, D., Harrison, S., Anderson, K., and Betts, R. (2018a). Mountain rock glaciers contain globally significant water stores. *Scientific reports*, 8(1):2834.
- Jones, D., Harrison, S., Anderson, K., Selley, H., Wood, J., and Betts, R. (2018b). The distribution and hydrological significance of rock glaciers in the Nepalese Himalaya. *Global and Planetary Change*, 160:123–142.
- Kääh, A., Strozzi, T., Bolch, T., Caduff, R., Trefall, H., Stoffel, M., and Kokarev, A. (2021). Inventory and changes of rock glacier creep speeds in Ile Alatau and Kungöy Ala-Too, northern Tien Shan, since the 1950s. *The Cryosphere*, 15(2):927–949.
- Kenner, R., Phillips, M., Beutel, J., Hiller, M., Limpach, P., Pointner, E., and Volken, M. (2017). Factors controlling velocity variations at short-term, seasonal and multiyear time scales, Ritigraben rock glacier, Western Swiss Alps. *Permafrost and Periglacial Processes*, 28(4):675–684.
- Knight, J., Harrison, S., and Jones, D. B. (2019). Rock glaciers and the geomorphological evolution of deglaciating mountains. *Geomorphology*, 324:14–24.
- Liu, L., Millar, C. I., Westfall, R. D., and Zebker, H. A. (2013). Surface motion of active rock glaciers in the Sierra Nevada, California, USA: inventory and a case study using InSAR. *The Cryosphere*. 7: 1109-1119, 7:1109–1119.
- Marcer, M. (2020). Rockglacier evolution by ground-truthing the state and possible fate in semiarid climate in the Nyainqêntanglha range, Tibetan Plateau. *Permafrost and Periglacial Processes*, 31(4):561–566.
- Marcer, M., Serrano, C., Brenning, A., Bodin, X., Goetz, J., and Schoeneich, P. (2019). Evaluating the destabilization susceptibility of active rock glaciers in the French Alps. *The Cryosphere*, 13(1):141–155.

- Matsuoka, N. (2001). Solifluction rates, processes and landforms: a global review. *Earth-Science Reviews*, 55(1-2):107–134.
- McColl, S. T. (2012). Paraglacial rock-slope stability. *Geomorphology*, 153:1–16.
- Obu, J., Westermann, S., Bartsch, A., Berdnikov, N., Christiansen, H. H., Dashtseren, A., Delaloye, R., Elberling, B., Etzelmüller, B., Kholodov, A., et al. (2019). Northern Hemisphere permafrost map based on TTOP modelling for 2000–2016 at 1 km² scale. *Earth-Science Reviews*, 193:299–316.
- Osmanoğlu, B., Sunar, F., Wdowinski, S., and Cabral-Cano, E. (2016). Time series analysis of InSAR data: Methods and trends. *ISPRS Journal of Photogrammetry and Remote Sensing*, 115:90–102.
- Ran, Z. and Liu, G. (2018). Rock glaciers in Daxue Shan, south-eastern Tibetan Plateau: an inventory, their distribution, and their environmental controls. *Cryosphere*, 12(7).
- Reinosch, E., Gerke, M., Riedel, B., Schwalb, A., Ye, Q., and Buckel, J. (2021). Rock glacier inventory of the western Nyainqêntanglha Range, Tibetan Plateau, supported by InSAR time series and automated classification. *Permafrost and Periglacial Processes*.
- Robson, B. A., Bolch, T., MacDonell, S., Hölbling, D., Rastner, P., and Schaffer, N. (2020). Automated detection of rock glaciers using deep learning and object-based image analysis. *Remote Sensing of Environment*, 250:112033.
- Scotti, R., Brardinoni, F., Alberti, S., Frattini, P., and Crosta, G. B. (2013). A regional inventory of rock glaciers and protalus ramparts in the central Italian Alps. *Geomorphology*, 186:136–149.
- Scotti, R., Crosta, G. B., and Villa, A. (2017). Destabilisation of creeping permafrost: The Plator rock glacier case study (Central Italian Alps). *Permafrost and Periglacial Processes*, 28(1):224–236.
- Strozzi, T., Caduff, R., Jones, N., Barboux, C., Delaloye, R., Bodin, X., Käab, A., Mätzler, E., and Schrott, L. (2020). Monitoring Rock Glacier Kinematics with Satellite Synthetic Aperture Radar. *Remote Sensing*, 12(3):559.
- Villarroel, C. D., Tamburini Beliveau, G., Forte, A. P., Monserrat, O., and Morvillo, M. (2018). DInSAR for a Regional Inventory of Active Rock Glaciers in the Dry Andes Mountains of Argentina and Chile with Sentinel-1 Data. *Remote Sensing*, 10(10):1588.
- Wang, X., Liu, L., Zhao, L., Wu, T., Li, Z., and Liu, G. (2017). Mapping and inventorying active rock glaciers in the northern Tien Shan of China using satellite SAR interferometry. *Cryosphere*, 11(2).

- Wang, X., Tolksdorf, V., Otto, M., and Scherer, D. (2021). WRF-based dynamical downscaling of ERA5 reanalysis data for High Mountain Asia: Towards a new version of the High Asia Refined analysis. *International Journal of Climatology*, 41(1):743–762.
- Zhang, G., Kang, S., Fujita, K., Huintjes, E., Xu, J., Yamazaki, T., Haginoya, S., Wei, Y., Scherer, D., Schneider, C., et al. (2013a). Energy and mass balance of Zhadang glacier surface, central Tibetan Plateau. *Journal of Glaciology*, 59(213):137–148.
- Zhang, G., Kang, S., Fujita, K., Huintjes, E., Xu, J., Yamazaki, T., Haginoya, S., Wei, Y., Scherer, D., Schneider, C., et al. (2013b). Energy and mass balance of Zhadang glacier surface, central Tibetan Plateau. *Journal of Glaciology*, 59(213):137–148.
- Zou, D., Zhao, L., Yu, S., Chen, J., Hu, G., Wu, T., Wu, J., Xie, C., Wu, X., Pang, Q., et al. (2017). A new map of permafrost distribution on the Tibetan Plateau. *The Cryosphere*, 11(6):2527.
- Zwieback, S., Hensley, S., and Hajnsek, I. (2017). Soil moisture estimation using differential radar interferometry: Toward separating soil moisture and displacements. *IEEE Transactions on Geoscience and Remote Sensing*, 55(9):5069–5083.